THESIS

A FINE RESOLUTION CFD SIMULATION APPROACH FOR BIOMASS COOK STOVE DEVELOPMENT

Submitted by

Daniel David Miller-Lionberg

Department of Mechanical Engineering

In partial fulfillment of the requirements

For the Degree of Master of Science

Colorado State University

Fort Collins, Colorado

Spring 2011

Master's Committee:

Advisor: Bryan Willson

Morgan DeFoort
Hiroshi Sakurai
John Volckens

ABSTRACT

A FINE RESOLUTION CFD SIMULATION APPROACH FOR BIOMASS COOK STOVE DEVELOPMENT

More than half of the world's population meets cooking and heating needs through small-scale biomass combustion. Emissions from these combustion processes are a major health hazard and air pollution concern. Simple improvements over traditional cooking fires have been shown to increase combustion and heat transfer efficiency while reducing physically harmful gaseous and particulate matter (PM) emissions. Over approximately 30 years of modern stove development history, designs have largely been based on empirical guidelines, and attempts at improvements have been made through an iterative, trial-and-error approach. Feedback in this design process is typically attained through bulk measurements made during experimental testing of prototypes. While important for assessing the performance of a stove, such testing offers no information on the fine spatial or temporal scales of phenomena within the stove, leaving it a "black box" in the view of the designer. Without higher resolution information, the rate and ultimate level of design improvement may be limited.

In response, a computational fluid dynamic (CFD) simulation of a common, production cook stove is conducted using ANSYS FLUENT 13.0 software. Aspects critical to achieving high spatial and temporal resolution flow and temperature field results are included, enabled by necessary simplifications to less important elements. A model for the steady, time-averaged drying and pyrolysis of wood stick fuel is used in conjunction with a consideration for the

simultaneous oxidation of the resulting char, to generate gas-phase fuel boundary conditions for the simulation.

Fine spatial and temporal resolution are simultaneously possible in an unsteady formulation with the use of the simplified fuel condition, reduced-mass solid boundaries, and abbreviated runtimes. Employment of a large eddy simulation (LES) turbulence model is proposed as necessary to realistically consider the larger scales of gas mixing. Combustion heat release is approximated by reactions dictated by a mixture fraction formulation, assuming equilibrium conditions in a non-adiabatic system, affected by turbulent fluctuations through a probability density function (PDF). Sensitivity studies are conducted on grid parameters, boundary condition assumptions, and the duration of simulation runtime necessary to achieve result significance. A model for particulate emission formation is secondarily explored.

A thermocouple-instrumented stove is used in an experiment to generate internal gas temperature profiles for the validation of the CFD simulation through comparable results. Likewise, a heat-exchanger integrated into a cooking pot is employed with the instrumented stove to measure short time-scale heat transfer values that are compared to the CFD simulation results, as well as to benchmark test data from the production stove. Recommendations for future efforts in stove simulation are made.

ACKNOWLEDGEMENTS

This work is supported by Colorado State University and the Engines and Energy Conversion Laboratory of the Department of Mechanical Engineering. Envirofit International, Ltd. continues to be a consistent partner in development. I could not have concluded this work without the help of everyone at the EECL, but would like to especially mention Josh Agenbroad, Christian L'Orange, Cory Kreutzer, Jason Prapas, Melanie Sloan, and Dan Zube, with whom I have worked very closely. I would like to thank my committee for offering me wisdom, and specifically Morgan DeFoort for being a very understanding boss. I will always look upon my time at the EECL with great fondness – it truly is a wonderful and unique place to work, learn, and find friends.

TABLE OF CONTENTS

LIST OF TABLES

LIST OF FIGURES

1. Introduction

This thesis proposes a new set of advanced engineering tools for improved cook stove design. The background section defines the scope of the real-world problem, giving details on the negative effects of indoor air pollution (IAP), deforestation and anthropogenic global warming (AGW) on the human condition, so that stove efficiency and emissions have practical meaning. The discussion of cultural and societal aspects as well as a history of the "modern stove movement" will explain the origins of certain design constraints that might otherwise not be intuitive to those unfamiliar with biomass cook stove markets. Physical fundamentals are explained to a level and in a manner such that justifications of mathematical models and simulation schemes can be understood, and the meaningfulness of the testing and validation approach is communicated. Description of a reasonably comprehensive range of options for possible mathematical models is given so that the choices of the models proposed herein are further understood. Finally, the conclusion contains an assessment of the validity of the proposed concept, again with the goal of advancing the tools available to the stove designer.

1.1 The world challenge posed by domestic biomass combustion

Roughly half of the world's population relies on the combustion of solid biomass fuels for small-scale cooking and heating energy needs. These fuels commonly include wood, crop waste, dung, and also charcoal derived from these primary fuels. Biomass combustion accounts for approximately half of the total domestic energy use in many countries, and as much as 95% of use in the poorest countries [1]. Cooking is frequently done indoors over a crude open fire or in a traditional cook stove, producing significant amounts of harmful indoor air pollution (IAP). IAP

exposure is conservatively estimated to be the base cause for at least 4% of global disease and more than 2 million annual deaths [2], with some studies suggesting these figures significantly underestimate the extent of this problem [3]. Due to domestic arrangements, women and young children are disproportionately exposed to IAP, with IAP being the leading contributor to deaths of children under 5 years of age, worldwide [2].

Populations using biomass as their primary energy source are considered as living in a state of energy poverty, defined by the UNDP as "inability to cook with modern cooking fuels and the lack of a bare minimum of electric lighting to read or for other household and productive activities at sunset" [4]. Electrification does not necessarily cause a significant reduction in the use of biomass fuels however, due to the higher cost of electrical energy [2]. Indeed, there is a wide range of relative wealth among those using biomass.

In contrast to the general trend for developed nations to move away from the use of crude biomass toward cleaner fuel sources, evidence shows that biomass fuel use in developing countries is actually increasing [2]. The development of clean cook stoves, therefore, affects a population that is both gargantuan and growing. The World Health Organization (WHO) submitted an ambitious, sweeping vision for eliminating specific elements of poverty in the first 15 years of this third millennium entitled the Millennium Goals. Dissemination of clean-burning, efficient, durable and safe improved cook stoves has been identified as key in achieving four of the eight WHO Millennium Development Goals [5][6].

Lastly, parallel challenges are posed by the very success of such unarguably benevolent development as improved cook stove dissemination. K.R. Smith, Director of the Global Health and Environmental Program School of Public Health at the University of California, Berkeley, provides some numbers to the popularly intuitive trend; As fuel-poor countries develop and acquire cleaner-burning biomass stoves, the next step is that they acquire access to cleaner energy

(i.e. petroleum, electricity), and begin to use larger amounts of it, generally leading to an increase in carbon dioxide production [7].

1.2 Cook stove background

"Stove" is a term loosely referring to the physical structure that serves to contain combustion and then to direct the resulting heat towards a "cooking target". Typically, this is a pot, pan, plancha griddle, etc. Other uses of the stove include providing interior heating and lighting. The same device often serves all of these functions.

One desires a stove to provide additional utility over a plain fire, such as enhanced overall thermal efficiency, reduced production of harmful emissions, and improved safety. Increased thermal efficiency translates to lower fuel consumption and hence lower consumer energy costs. A stove may have a chimney to remove exhaust from the dwelling the stove is installed within, but often this is not the case.

Stove designs vary significantly worldwide due to the wide range of cooking practices, cultural and social cues, and available fuel. Popular traditional stoves include the wood-burning *chulha* (southeast Asia), and *plancha* (central and south America) types, and the charcoal-burning *jiko* (Africa). Traditional stoves have evolved over thousands of years, and are the widely accepted status quo. It cannot be understated how significantly cultural practices and societal views of cooking affect decisions regarding stove design, purchase, and use.

Underscoring all these points is the fact that a widely adoptable stove must have a low enough cost that people can afford to purchase it. Like most situations in the real world, this sets up the case for design optimization vs. utility maximization.

1.3 Fuel background

As would be expected, traditional stoves have evolved to utilize the locally available fuels. Indeed, cooking customs and related cultural identity themselves probably evolved in consideration of these fuels. If a stove does not function well with locally available fuels, it will likely not be used and be considered a failure. To complicate the issue further, the fuels available in many regions today have changed over time, and are likely to continue to do so. For example, parameters of available fuel may change with a switch in supply of wood from old growth forest to that of wood from commercial tree plantations, or to pelletized crop waste brought by the initiation of a government fuel program. Fuel parameters pose serious implications to the design and use of a stove. For example, a stove that functions well burning large-diameter sticks of Eucalyptus wood may perform poorly when burning granular crop waste, and vice-versa.

Primary biomass is the biological material of a living or recently deceased organism, including that of both plants and animals. The designation of *primary biomass* defines biomass that has not been substantially processed beyond the mechanisms associated with harvest, such as chord firewood (wood that is left in the original condition with bark, etc, and has only been processed in being cut to length, split, etc). The designation of *secondary biomass fuel* introduces much more ambiguity. Examples of these include industrial waste wood sawdust and pelletized crop waste. In a more extreme case chemical and even elemental composition of a biomass may be changed in the processes that convert a primary biomass fuel to a *secondary* biomass fuel. As is perhaps intuitively known, any processing of virgin biomass that is conducted to create the final biomass fuel likely alters physical properties, which in turn, can significantly affect the way that fuel burns. For example, dry fuel wood has a higher heating value (HHV) typically in the range of 18-24 MJ/kg, whereas charcoal made from this wood possesses approximately 32 MJ/kg [8]. The important connection to this study is that cook stoves around the world commonly burn

both primary and secondary biomass fuels of widely ranging properties that need to be taken into account in the design of the stove.

Common primary biomass fuels include full stick or cut and split wood, stalks of woody plants (often crop waste), and depending on the parlance perhaps pure animal dung. Common secondary biomass fuels include granular crop waste product (such as rice hulls), and the very common, significantly processed charcoal. Additionally, more complex secondary fuels can be created by amalgamation of various primary and secondary biomass fuels. For example, animal dung, crop waste and charcoal can be mixed with water and cast or pressed into briquettes, demonstrating that materials which don't burn very well on their own can be made significantly more useful when compounded with other substances.

Plants, trees and crops are formed of cellular structures composed of lignocellulosic material components including cellulose, hemicellulose, and lignin, along with minor extractive and inorganic components [9], having inconsistent proportions. One study by Demirbas [10] reports that across ten various types of crop wastes and woods, hemicellulose, cellulose and lignin ranged from 19.9 to 39.4%, 25.6 to 50.7%, and 15.0 to 52.3% dry weight, respectively, with no obvious trend of one component to another amongst crop waste shells, seeds, corn cobs or wood. There is, however, tighter agreement among the ultimate composition of these fuels, with Demirbas again reporting percent dry weight carbon and oxygen as 42-54% and 35-45%, respectively [10]. Other researchers report similar ranges for both material component and elemental composition as percent dry weight [11-16]. Compared to fossil fuels such as coal, all biomass has considerably higher percent oxygen. The diverse and complex composition of fuel further reinforces the point that it must be taken into account in stove design.

1.4 The "modern stove movement"

The so-called "modern stove movement" began with non-governmental organizations (NGOs) in developed countries working either through governments in developing countries, or directly [17]. Since then, a wider variety of mechanisms of technology diffusion and project initiation have come into use, with organizations waging efforts to bring improved stoves to areas lacking them. Some stove proliferation efforts do not include bringing modern fuels to these areas, as those fuels are too expensive to be supported by a free market in such cases, and are not locally available. The difficulty of disseminating improved cook stoves is evidenced by a history filled with many such projects failing: by way of poorly-designed stoves, lack of cultural sensitivity, or flawed economics [18]. The intentions and efforts of partners to disseminate improved cook stoves have come in three distinct phases.

The first of these phases was motivated by a concern that high biomass fuel consumption would lead to deforestation and intensified poverty. In the 1970's, non-governmental organizations projected that rapidly increasing populations would consume biomass fuels (chiefly wood from forests) at an unsustainable rate, resulting in the approach of a hard limit to fuel availability, supply/demand mismatch, and subsequent poverty. The motivation in this era was to reduce the rate of deforestation through improved cook stove dissemination and forestry policy interventions in specific developing areas. By the 1980s better data on deforestation rates became available, and the commonly held opinion changed to hold that deforestation was a much lower risk than originally projected [19], [20], removing some of the pressure for a deforestation-mitigation motivated policy. Recently however, deforestation associated with domestic biomass use is coming back into the focus of concern as new data suggests that deforestation rates may be truly significant [19].

The second phase focused on removing poverty by reducing disease associated with indoor air pollution from domestic biomass use. Beginning in the 1980s, epidemiologists and

public health scientists widely began to consider disease correlated with traditional, unimproved domestic biomass fuel use and the associated loss of productivity as a significant cause of poverty [21]. This represents a significant switch in interpretation.

A third phase brings together additional environmental concerns with the need to balance these previous motivations by improving understanding of the underlying causes of health impacts, deforestation, fuel expense and now anthropogenic global warming (AGW) [22-24].

Incomplete combustion of nearly any fuel will generate emissions harmful to humans, with some fuels being significantly worse than others in this respect. Stove design has an enormous affect on the emissions formed. The interaction of these factors is a complex, temporally varying relation of a seemingly chaotic nature.

2. Modern stove design process

The process of designing an improved cook stove does not have a closed or well defined form. To date, no straightforward procedure or system of equations have been assembled which can define a highly performing stove. A low-cost biomass cook stove does not feature any sort of control system or even uncontrolled stabilizing device such as a fan to drive air flow (more elaborate stove designs can include such elements). The function of an improved cook stove is to provide some stabilization of, and limitation to the ranges of physical phenomena in a way that improves efficiency, utility, and emission production. Although it is the fundamental goal of a stove designer to add such stabilization, only relatively minor amounts are possible due to the low amounts of energy that can be utilized.

Biomass combustion in low-technology domestic devices is complex for two broad reasons. Firstly, the scope of the associated physical phenomena is very large, with incredibly complex coupling. Secondly, these devices are not actively controlled or highly stabilized (as industrial biomass combustion devices can be), and hence there is inherent instability and thus a significant stochastic element. It also cannot be ignored that there is relatively little interest from industry in understanding and modeling these phenomena at high levels due to the limited commercial interest they command in the developed world. The result of these realities is that to date there are no simple, practical procedures for optimizing residential biomass stove designs. The most common approach of employing advanced engineering tools to stove improvement thus far, has been to integrate them into a traditional design path, in the utility of modeling specific elements and functions of a stove.

2.1 Empirically-based stove design

When designing a stove, one will often start with a prior-art stove design and experimentally vary some parameters. There are, however, instances in the literature describing individual stoves, providing rough guidelines for producing substantially similar stoves, or stoves in general [25]. Through experimentation, the geometric proportions of the so-called "rocket stove" have been found [26], [27], and in one case these design criteria included in a design tool software program [28]. Out of the desire to come up with the best possible initial specification, the stove designer may also consult any of the experimentally-based empirical design guidelines that have been developed [29], [25], [27], [26].

Once a design has been determined, a physical prototype is fabricated and then evaluated through whatever testing procedure is available to the developer. The resolution and quality of available data from this testing may range from qualitative human sensory observation to cutting-edge optical diagnostics. Whatever the case may be, the designer must still make an interpretation as to how various parameters of the stove affect performance. These interactions are often not very intuitive and in fact sometimes quite counterintuitive. Still, the more and better the data that is available, the more information potentially available for the designer to form a realistic understanding from. Based on the assessment of this data the designer may decide to make parametric changes to the stove design, prototype the design anew and then retest and reevaluate. This design-test-evaluate cycle forms an iterative, trial-and-error design improvement process that is represented in Figure 1. This is essentially the same procedure that has been used to design stoves throughout all of human history, with stove designs improving with increases in the understanding of science and the resolution of data available from the testing. The traditional stove design cycle is fairly effective, but can be lengthy in development time and high in cost.

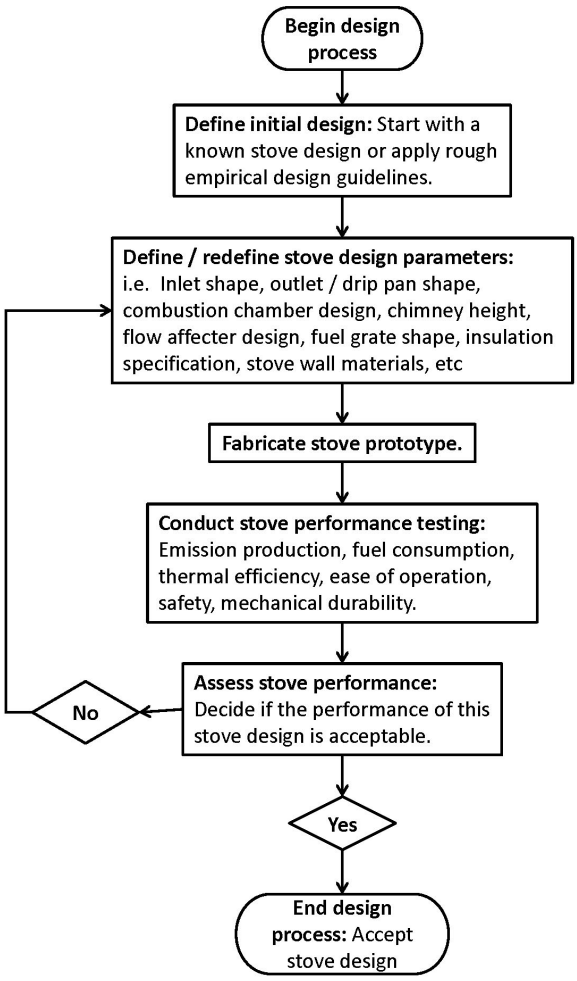

Figure 1: Iterative stove design process

Much improvement in stove design can be had by simple trial-and-error approaches. In fact, nearly all development of stoves to date was done using this sort of approach. Furthermore, considering the relative difficulty of applying any type of advanced engineering tools to stove design, these more traditional design processes are quite attractive.

Traditional testing as described above gives mostly measures of *bulk, time-averaged* performance metrics. The stove is treated as a black box in so far as one can only measure what goes in and goes out by balance, without very good insight into what happens within. Hence, the feedback that drives the variation built into the next design revision is not particularly explicit.

Another way to look at this is that the stove designer must apply any available knowledge into correlating some aspect or parameter of the stove design to some item of its bulk performance. It becomes very obvious to a beginner stove designer that the system of these relations is extremely complex, and that these relations are often very sensitive and perhaps counterintuitive. This approach essentially combines basic knowledge of the nature of fluid flow, combustion, and heat transfer with a kind of learned, system-level intuitive understanding of complexly related phenomenological trends. Thus, a stove designer must devise a very careful system for experimental variation lest they slip into nearly blind, random experimentation.

While it is likely that traditional stoves were designed in essentially the same manner for millennia, formal documentation of this process is not found. There are also few modern, comprehensive considerations of small biomass cook stoves. This is likely a function of there being limited commercial and industrial interest in such stoves. Baldwin [29], and Burnham-Slipper [30], [31], offer consideration of the major aspects of stoves, giving a substantial background on the human health and fuel saving motivations, developing the governing equations of most related physical phenomena, proposing design guidelines, estimating stove costs, and in the case of Burnham-Slipper even developing computational codes for geometry optimization.

2.2 Experimental stove performance testing

It is obvious that the stove user has little interest in the functions occurring within the stove as long as stove performance in the areas of efficiency, fuel consumption, emissions and usability are satisfactory. In order for the stove designer to design a stove that achieves these functions, they often need to evaluate conditions at, on, or within the stove. The goal of experimental testing is to give the stove designer a tool by which to evaluate the performance of the experimental stove, providing information that will help guide the next design iteration. Without such experimental procedures, the iterative design process would be impossible.

The stove designer may design experiments to yield information useful in evaluation of the effects of specific design parameters. Such utility has historically been difficult to achieve with biomass cook stoves because of the large operational variation due to uncontrolled or difficult to control elements. These unintended confounding elements become experimental variables, thus complicating experimentation. Testing conducted by different people, with different interests, for different purposes takes on different forms. Some testing is conducted to gain information about the behavior of detailed phenomena within the stove (e.g. where the flame sheet stands, what the temperature field looks like), while other testing is done to gauge overall performance (fuel use, total CO emissions, etc.).

2.2.1 Standardized performance testing

With the goal of increasing the ability to conduct meaningful and accurate assessments of how a stove will function in actual field use, and hence the ability to compare the performance of stove prototypes, attempts have been made to provide some level of test standardization. While such protocols have significant differences, they share the common goals of reducing confounding elements, and standardizing test parameters such that results attained from one stove designer can be compared to those of another. Such tests have been designed by a number of major members in the modern stove movement. The efforts of the Volunteers in Technical Assistance (VITA) beginning in 1982 and continuing to this day have defined and continuously refined a test that came to be commonly known as the “Water Boil Test” (WBT), which sought to mimic the actual use of a stove to gauge thermodynamic efficiency [32]. Other noteworthy developments of stove testing protocols were made by the government of India through the Bureau of Indian Standards (BIS), and the Chinese government through the National Improved Stove Programme (NSP) [33].

Significant investigations into the sensitivity of the WBT protocol to test parameter variation have been conducted at the Clean Cook Stove Laboratory of Colorado State University [33], [34]. For instance, in an investigation of the effects of variation of fuel moisture content and geometry, it is found that moisture content significantly affects operation, and the fuel geometry less so. Proposed changes to the protocol have proven reductions in uncertainty and increased robustness. Understanding the logic and statistical justifications that went into forming such testing protocols is useful in consideration of how advanced engineering tools may be applied to stove design.

Most such testing methods evaluate the behavior of the stove in "bulk" ways, treating the stove as a lumped device (i.e. a "black box") by collecting data that is spatially and temporally averaged. In fact, this is for good reason because after all, that is the way the user interacts with the stove – by experiencing time-averaged stove performance and by exposure to emissions with application-specific averaging, in which gas dilution and aerosol dynamics are quite important. Indeed, the averaging that occurs in these tests is absolutely critical.

2.2.2 Precision physical sampling

It is sometimes quite useful to gain detailed physical information from some zone in or around the stove. Such information often comes in the form of data from finer spatial and temporal scales. Stove designers needing finer resolution data regarding internal function must develop other tools including fine-scale physical sampling and CFD simulations of internal stove phenomena.

For example, a stove designer interested in the source of a high carbon monoxide (CO) emission may utilize a small point probe emission-measuring device to attempt to find the region at the stove outlet where the CO molar concentrations are the highest, knowing that locations upstream from that location are contributing to the high emission value. The following devices

and techniques can be used in similar methods. Fine-resolution optical techniques can be used to evaluate highly local soot volume fraction in a non-invasive manner [35]. Relatively low-cost Schlieren imaging can be used to evaluate the temperature and flow field within the space of a thin plane of fluid, such as the hot gas emerging from the pot gap [36], [37]. Microprobes can extract fluid from a precise location in or around a flame, and halt any ongoing chemical reactions before compositional analysis [38]. Extremely thin passive wires may be suspended across a combustion chamber and with line-of-sight access a traditional camera may be used to gather image data that is post-processed to yield the temperature field through pyrometry [39]. In the method used in the work reported by this thesis, traditional fine-wire thermocouples are used to evaluate the temperature field.

While being attractively practical on description, there are considerable downsides to precision sampling methods. They are often tedious and expensive and the measurement can be invasive, typically affecting fluid or heat flow. The very nature of precision sampling increases the concern of data relevance, as there is less damping of periodic or stochastic elements.

Precision sampling can be used to validate elements of CFD simulations, in similar methods as the work reported in this thesis. Once adequate validation and desensitization of CFD simulations have been achieved via detailed physical sampling, CFD models can be used in lieu of such tedious methods.

3. Background on related physical phenomena

This thesis focuses on related physical phenomena in a narrow scope, and addresses them in a way practical to the end goal of formulating a stove modeling and design approach. An emphasis is made on discussing relatively large water-containing wood particles, burned in continuously fed stoves dominated by diffusion flame combustion. Most of the topics discussed here also apply to other stove types, including gasifiers/semi-gasifiers, and those featuring heterogeneous-phase dominant combustion (i.e. charcoal stoves), however the distinctions must be regarded.

There exists technical jargon associated with biomass combustion. Some terms are used counterintuitive to their literal definition, and most terms have multiple meanings across different zones and phases. A brief explanation of some key terms follows.

- *Homogeneous-phase* or *gas-phase* refers to the fluid (gas) phase space (domain) and related phenomena occurring exclusively within the fluid (gas) domain of the stove. Strictly speaking, these phenomena include bulk and turbulent gas transport, and gaseous combustion reactions.
- *Homogeneous-phase combustion* (i.e. *flaming combustion*) refers to the first major mode of combustion, in which the gas resulting from pyrolysis and air combust in non-premixed diffusion flames.
- *Solid-phase* or *condensed-phase* refers to the solid phase space (domain) and related phenomena involving only solids, including conduction heat transfer, and solid-phase chemical reactions.

- *Heterogeneous-phase* or *Multi-phase* refers to the gas-solid or gas-liquid boundary, and related phenomena such as water evaporation, solid or liquid thermolysis (torrefaction, pyrolysis, gasification, etc.), soot formation and transport, and conjugate fluid-solid convection and radiation heat transfer.
- *Heterogeneous-phase combustion* (i.e. *smoldering combustion*) refers to the second major mode of combustion, in which oxidation of carbon occurs at the surface of the fuel (an important step in charcoal combustion).

While stoves can be categorized by the *type* of fuel they are designed to burn, they can also be described by the *way* they burn that fuel. There are two highly *generalized modes* of combustion relating to stoves (defined above), commonly and in the rest of this thesis referred to as *flaming* and *smoldering* combustion. All stoves burning biomass will support combustion that includes a proportion of both of these types. This proportion will vary with fuel parameters, stove design (geometry), temporally over the duration of the fire, according to the intentionally specified condition (such as intended firepower), and in many other ways that are very complex and outside the scope of this discussion. It may be more useful to think of a stove as burning fuel in a *more flaming* manner or a *more smoldering* manner. Both overall reaction modes can be generally described in a cascade of successive steps, as follows:

Charcoal burning in a stove designed for that fuel will foster combustion that is nearly all of in the smoldering mode, with only a small portion of the flaming mode. Wood burning in a stove that was designed to burn wood will foster a high proportion of flaming combustion during the majority of the use cycle, with the proportion of smoldering combustion increasing with time due to char accumulation, and becoming the exclusive type during burnout. Conversely, a wood stove does not exclusively foster flaming gas-phase combustion, nor does a charcoal stove exclusively foster surface-oxidation. It is therefore inappropriate to differentiate between stove types as if the modes of combustion were exclusive. These two generalized combustion *modes*

are termed as such because they are actually a set of physical phenomena. Both modes contain many of the same general phenomena, albeit in different proportions and with different parameters and through different chemical reactions.

3.1 Heating and drying of wood

All ligneous cellulosic (i.e. woody) solid fuels stored in open air include water in amounts depending on how recently the source plant was harvested, and the conditions of storage. The amount of water can vary from over half of the total fuel mass in fresh, "green" wood, to trace amounts in well-dried wood [8]. Intrinsic water does not contribute to any exothermic reaction and in fact requires substantial energy to be heated, separated from solid-liquid bounds, and evaporated. The presence of water serves to lower the mass specific heating value and thermal efficiency. This water remains trapped within the cellular structure of the fuel until vaporization and egression from the solid occurs. Pressure rises according to the expansion of this phase change and forces the gas and cooler, trapped liquids towards the fuel surface along the porous structure of the ex-plant's vascular phloem and xylem. The mode of this transport is highly affected by the heating rate and the structural morphology of the fuel [40]. This porous structure is highly anisotropic, with key parameters such as thermal conductivity and permeability varying by around an order of magnitude whether along the lines of these tubular structures or across them. The presence of remaining liquid with its relatively large heat of vaporization poses a significant heat sink that remains at the boiling temperature of the liquid until all has vaporized. Fuel water content and structural morphology can have a large affect on the pre-combustion response of the fuel and hence newly added fuel can significantly affect previously developed combustion. It is significant that the water trapped inside the structures of the plant requires more energy to evaporate than expected through simply the specific heat and heat of vaporization of water. This is due to the significant energy associated with the solid-liquid bounds [41].

3.2 Pyrolysis

Following the drying process, solid and gas temperatures increase above the liquid boiling temperature in the absence of remaining liquid. As the temperature of the solid is raised above a lower critical temperature, chemical reactions, phase changes and physical transport begin to convert the dry virgin fuel to something that can actually burn. These processes occur somewhat conjugately, and are thus frequently referred to interchangeably as pyrolysis, torrefaction, gasification and devolatilization, but have distinct literal definitions. Devolatilization implies the thermally-driven breakdown of biomass in the presence of air/oxygen. Pyrolysis is the pure thermal breakdown of biomass in the absence of oxygen. Torrefaction refers to pyrolysis at the very low end of the temperature range. Gasification simply refers to the process of changing the fuel from solid to gas phase and thereby contains the other three definitions. Other related processes include complex chemical reaction mechanisms, including polymerization. Also occurring in small amounts simultaneously with pyrolysis, even in the absence of atmospheric air, is a small portion of surface oxidation of char, consuming the oxygen contained in the original composition of dry biomass. This thesis will refer to these processes collectively as pyrolysis.

What happens in these processes is extremely complex, with details beyond the scope of this thesis. Pyrolysis products are produced by reactions of chemical breakdown which are hard to evaluate due to their detailed interaction with the closed structures of the wood [42]. Primary biomass fuels have very complex physical structures and chemical compositions, all of which affect the pyrolysis process. Cellulose, hemicelluloses and lignin all have competing exothermic and endothermic paths of reaction leading to final devolatilization, occurring in the temperature ranges given in Table 1.

Table 1: Structural compounds and corresponding pyrolysis temperatures

Structural compound	Pyrolysis temperature range (K)
Hemicellulose or xylan	500-600
Cellulose	550-650
Lignin	575-675

This cascade of reactions starts with waterless solid fuel of the original chemical composition and proceeds to the production of pyrolysis gas, high-viscosity tar and solid char. These steps of conversion can be grouped into single and multi-component global reaction sets. The global reaction set seen in Figure 2 represents the major processes of pyrolysis of dry wood. Some of the dry wood converts through immediate reaction steps directly to primary pyrolysis gas while the rest proceeds to either tar or char.

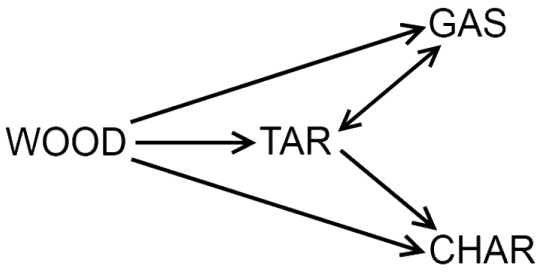

Figure 2: Global reaction mechanism for pyrolysis of wood

The makeup of the tar is mostly phenols, aromatics, and both saturated and unsaturated C_2 hydrocarbons, formed both through solid-liquid synthesis and gas-phase condensation [43]. Tar can condense from gas and can re-volatilize back to gas or polymerize to char.

Char (i.e. charcoal) is a final, non-volatile solid that cannot be volatilized, directly. The proportion of solid fuel that is initially leftover as char vary significantly as a function of the chemical composition, structural morphology, water content, geometry, the heating rate (indirectly the incident radiation heat flux), and to a lesser degree, the local ambient gas composition [44]. The composition and morphology of the char itself is also a function of the heating rate, structure, and chemical composition [45]. Under high-heat combustion, and not

gasification process incident heat fluxes and environment, wood yields between 10-25% char on a dry mass basis.

The proportion of these major product types as well as their chemical composition can be related by chemical kinetic function of the temperature of the solid during formation, the residence time of the solid at this temperature, and thus ultimately of the heating rate of the fuel . Reaction mechanism formulation and reaction rate equation coefficient specification are achieved through empirical evaluation of isothermal [16] and transient [46] thermogravimetric measurements, and also through experimentally-calibrated numerical methods [15]. These chemical kinetic reactions are a strong function of temperature.

A schematic diagram of the overall processes of drying, heating and now pyrolysis occurring on a sample cross-section of wood is provided in Figure 3 [47]. The outer surface of the fuel is depicted as having converted to char. A plot of the relative temperatures present through the cross-section implies different rates of conductivity and the thermal sinks of water evaporation. The final gas produced in the balance of these global mechanisms includes mostly light hydrocarbons, CO2, CO, and small fractions of heavier hydrocarbons and hydrogen. Diffusion driven by gradients of pressure, concentration, and temperature drive the final gas towards the outer surfaces of the biomass.

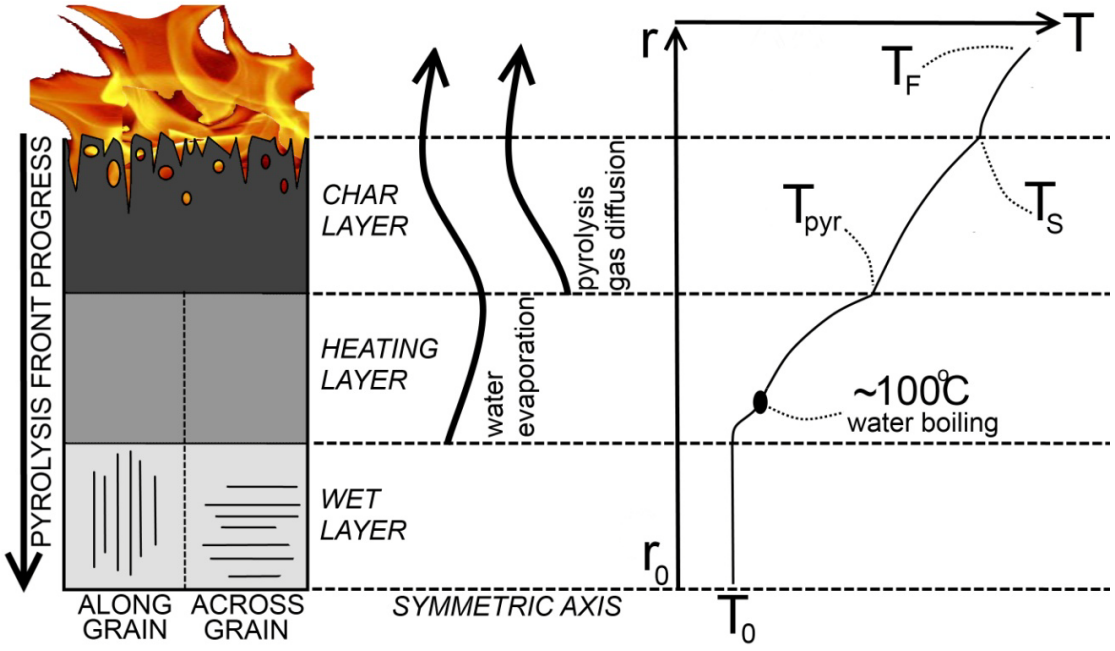

Figure 3: Schematic of the processes of drying, heating, and pyrolysis of wood

3.3 Heterogeneous-phase surface oxidation of char

Smoldering combustion is a complex reaction which is idealized to occur as an interaction occurring at the gas/solid interface, as seen in Figure 4. In actuality, the first step of the overall reaction happens at this interface and the second part occurs in the gas phase, ideally very *near* the solid surface. So in actuality, there is a homogeneous gas-phase reaction sheet standing off very close to the surface (much closer to the char surface than the analogous diffusion flame in a flaming combustion example).

Char is largely pure carbon, arranged in a structure that depends on the virgin fuel cellular structure and the heating rate during pyrolysis (either for char formed during flaming combustion of virgin biomass, or for char formed in an intentional charcoal-forming process) [45]. Pre-reacted, secondary fuels such as charcoal are almost exclusively composed of char. Virgin biomass such as wood and crop waste that has not yet been heated contain no char initially. Char forms on the outer fuel surface as a residual product as soon as the pyrolysis reaction begins.

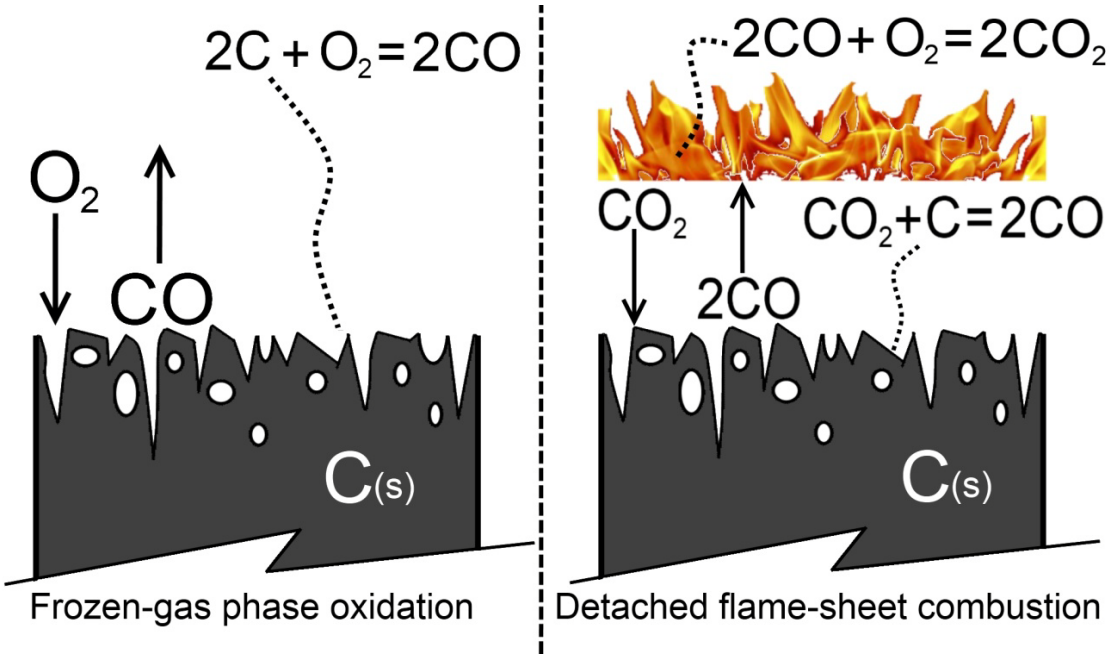

Figure 4: A schematic of the two simplified mechanisms for surface oxidation

3.4 Homogeneous-phase flow and combustion

Idealizing flaming combustion to a one-dimensional case, fuel gas species exist on one side of the flame reaction sheet and oxidizer species on the other. Transport processes including bulk and turbulent motion, as well as diffusion bring the fuel and oxidizer together. Thermal phenomena occurring in the gas phase include the obvious heat release from reaction and then heat transfer via convection and radiation. Conjugate heat transfer also exists between the solid and gas phases (between gas, solid fuel and solid structures of the stove). Heating leads to dramatic changes in density and subsequent expansion, giving rise to buoyancy effects and setting up complex flow fields.

In typical operation, nearly quiescent ambient air is induced into the combustion chamber inlet via buoyantly-driven bulk motion, and flows for some distance in a laminar fashion before transitioning to turbulent through the influence of shear or by the presence of intense, uneven heating by the combustion reaction. The “dancing” or “searching” diffusion flames of a relatively high-intensity fire feature a range of turbulent scales from large-scale eddies or the order of size

of the chamber itself, cascading down through turbulent dissipation to the miniscule Kolmogorov scales.

This combustible pyrolysis gas along with the already formed liquid vapor (largely water) is emitted from the porous, outer surface of the fuel at locations and through structures determined by fuel structural morphology and again, heating rate. Through mechanisms of convection and diffusion aided by unsteady, low-turbulence flow components, this gas travels towards the reaction zone of the off-standing flame. In the case of a fairly intense fire (radiation fluxes >25 $W \bullet m^{-2}$), the advection of energy with this outgoing gas is significant and must be considered for the concern of the thermal condition of the solid fuel [48].

As the fuel approaches the reaction zone of the flame, it is further heated, and the chemical reactions of classical non-premixed diffusion-flame combustion occur. The position of the reaction zone of the flame is determined by an equilibrium point in the local energy and momentum balances. The flame essentially "seeks" out this location, which is a function of flow field parameters such as chemical species concentration. Reactants and intermediate products proceed towards their final chemistry, be that products of incomplete combustion (PIC), or the final idealized product, carbon dioxide. PIC also include solid-phase particulate matter commonly known as soot. A detailed description of non-premixed combustion specifically associated with these fuel types is outside the scope of this thesis, but details associated with flame behavior are considered in coming sections. A constant Lewis number is assumed for the use of a mixture fraction model in the approximation of the combustion reaction in the CFD simulation, described in more detail in section 5.4.

Heat release from the highly energetic reaction at the flame causes a significant reduction in gas density. The effect of buoyancy now propels this lower density gas upwards by a classic phenomenon commonly identified as the *chimney effect*. Bulk parameters such as mass flow rate, excess air ratio, average gas temperature, and even production of CO and PM emissions can be

calculated as strong functions of very general stove geometry and average firepower [49]. In a more detailed sense, the buoyantly-affected flow field tends to stretch the reaction zone of the flame upwards, making for the classical, vertically distorted shape of biomass combustion flames. Buoyancy effects are certainly non-trivial, creating fluctuations, and complicated mechanisms of entrainment [50][51][52]. These phenomena are in fact likely key aspects to the reactions occurring in the stove, and accurate modeling of them is important for realistic CFD simulations [53][54].

Hot gas and suspended particles take part in the transfer of heat through the gas via convection and radiation [55]. They are very active in emitting, refracting and absorbing radiated energy, influencing flame stretch, combustion zone shrinkage and in extreme cases the outright stoppage of homogeneous-phase combustion, known as flame extinction [56]. The balance of radiation transfer between surrounding gas, particles and combustion chamber is a very important factor for the pyrolysis rate. Radiation transfer to combustion chamber walls can significantly affect flow and flame behavior but is unfortunately often ignored or overly simplified due to the fact it is quite complicated [57].

3.5 Thermal energy feedback

In all forms of combustion the hot post-combustion gases, any soot particles, and hot solid surroundings are available to transfer thermal energy back into the fuel, driving the endothermic processes of fuel heating, water-drying, and pyrolysis, as depicted in Figure 5. Heat from these nearby flames is transferred by radiation and convection within the gas phase and to the solid fuel, and via conduction within the solid fuel. Radiation heat transfer occurs between glowing soot particles suspended in the gas stream just downstream of the flame, from the hot solid surfaces of nearby stove body and fuel solids, as well as minor emissions from the hot gas itself. These surfaces are both sources and sinks, with net heat transfer as the balance between the

two. Convection heat transfer from flame to fuel is limited over much of the surface due to the fact that pyrolysis gasses escaping from the fuel pose an outgoing convection that counteracts any inwardly convection of hot gases. Since flows are typically unsteady considerable convection does occur. Solid fuel is acted on by a number of solid phase processes, namely heating, drying, pyrolysis and surface oxidation. The temperature difference between the warming surface of the fuel and the cooler interior sets up inwards heat conduction.

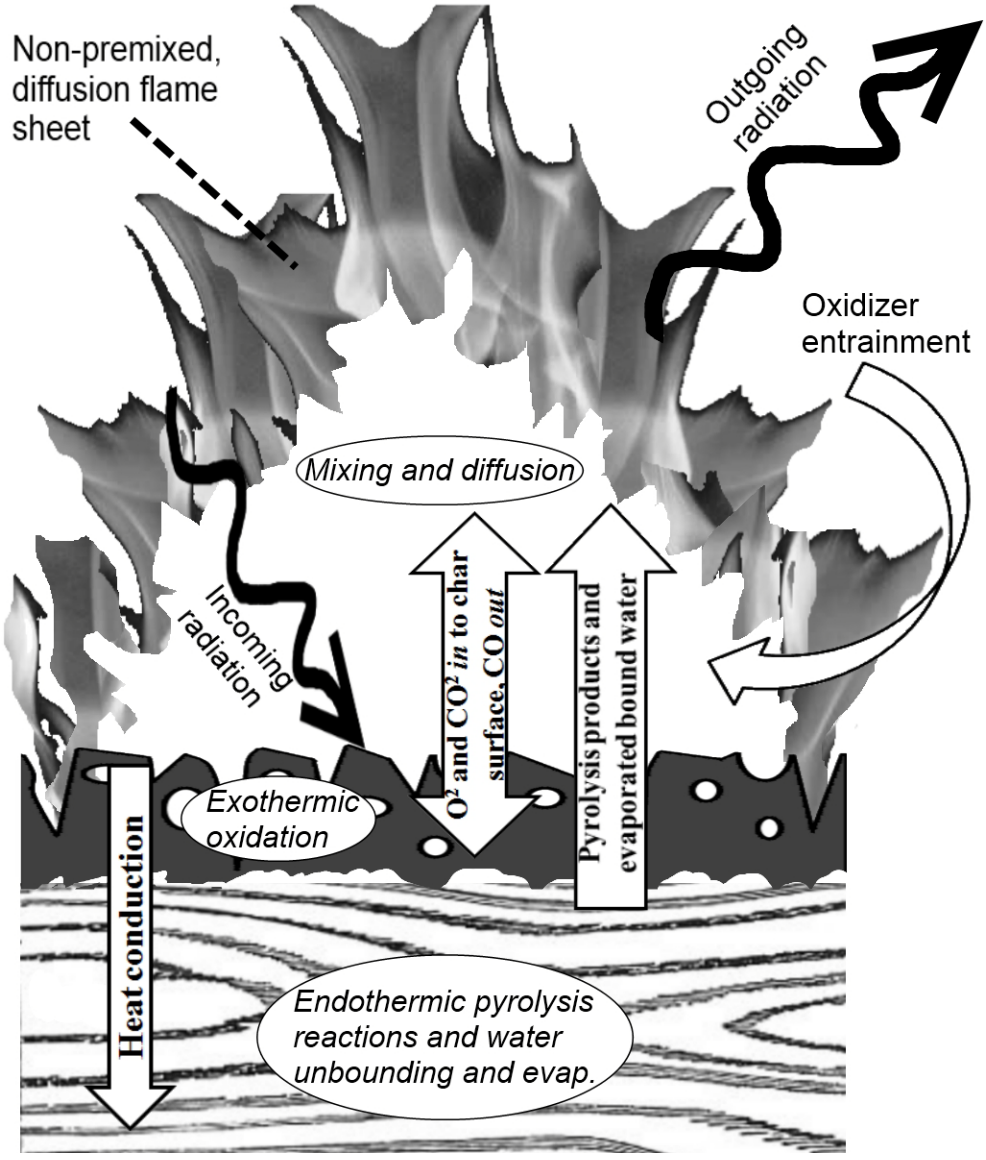

Figure 5: Simplified processes of endothermic pyrolysis

4. The case for the use of CFD simulation in cook stove design

4.1 Overview of the concept

It is abundantly clear that designing improved biomass cook stoves is considerably difficult. CFD simulation can advance the stove design process through two major utilities:

- *CFD simulation enables the evaluation of phenomena within a stove that cannot be visually observed or quantitatively measured through the bulk testing typically conducted on traditional cook stoves, giving powerful insight to the designer.*
- *Once the use of CFD simulation is learned and validated, it can be predictive, replacing a significant amount of physical prototyping and testing.*

The approach proposed by the author is an effort to minimize the difficulties and shortcomings typical to the process of designing an improved biomass cook stove. This process is pursued through the application of a CFD simulation and three supporting advanced design tools. These elements were researched, developed, and evaluated in the course of the author's graduate study, and then reported in this thesis.

1. A CFD simulation of an existing, common cook stove, with major elements including:
    - Unsteady flow with fine spatial and temporal resolution.
    - A mixture-fraction approximation for gas-phase combustion.
    - A large-eddy simulation (LES) of turbulence
2. A lumped-reaction fuel model that calculates a realistic, yet computationally practical approximation for the naturally complex and unsteady reactions of fuel pyrolysis, charring and smoldering oxidation – to be used as the fuel boundary condition in the

CFD simulation. Inputs include the virgin solid fuel geometry and empirical composition.

3. The construction of a thermocouple-instrumented stove, and its use to experimentally validate the zonal heat release and flow field behavior predicted by the CFD simulation.
4. The construction of a heat-exchanger cooking pot, and its use in experimentally validating the heat transfer to the pot as predicted in the CFD simulation.

4.2 Prior use of CFD simulation of biomass stoves

Computational fluid dynamic (CFD) simulations have been used extensively across industries to simulate fluid flow, heat transfer, pyrolysis, and solid and gaseous chemical reactions. These aspects have all been explored individually, or in groups, for conditions similar to those in a biomass stove. While modeling a stove with these comprehensive physics is theoretically possible as they are relatively well understood, it has yet to be completed due to practical computational limits and a lack of industrial interest. Advanced design tools such as CFD provide higher resolution information that can allow the stove designer to further improve a stove design. The tools and techniques proposed in this thesis essentially give additional insight into the "black-box" of the stove. They give the designer an ability to correlate small phenomenon occurring within the stove to the resulting performance, allowing finer, more informed design iteration.

This thesis focuses on multidimensional CFD modeling, where the geometry of the stove is spatially resolved in detail via the finite volume method (FVM) or finite element method (FEM). It is worth mentioning that there are also non-dimensional or one-dimensional numerical simulations of stoves which may be very useful to the stove designer. The thesis of Agenbroad [49] reports the development of a first-law of thermodynamics-based relation of stove

performance in firepower, thermal efficiency and emission production as a strong function of simple stove geometry. The work of Kausley and Pandit [58] presents the development of a comprehensive set of numerical phenomenological models related to a stick wood burning domestic cook stove, solved without the spatial resolution of a finite-method analysis.

There are numerous approaches that can be taken with biomass stove simulation, each having a different computational costs and utility, as discussed in the following sections. This section discusses previous, directly related approaches to simulating biomass cook stoves. There are many academic papers containing general information pertinent to the CFD simulation of cook stoves, however very few works clearly discussing reasoning behind model specification decisions and scant documentation of the actual application of CFD. There are no clear reasons for this, however one may cite the difficulty and complexity of the task combined with the relatively low profitability assumed in the commercialization of low cost biomass cook stoves. Simulations of a comprehensive range of phenomena related to biomass stoves have been conducted in industry, however a general discussion on this work is outside the scope of this thesis. Following are specific examples of CFD simulations applied to small-scale biomass combustion devices that are helpful in understanding the approaches that can be applied, and why.

4.2.1 Non-reacting thermal vs. reaction approximation simulations

The decision of whether to consider chemical reactions or not is based on the desired function of the model and practical computational limitations. Simulations employing non-reacting thermal approximations of combustion heat release can be several orders of magnitude less complex and computationally expensive than simulations featuring chemical reactions. Despite the fact that unsteady, transitioning, buoyant thermal or flaming flows contain extremely complex physics, non-reacting representations of combustion sources are useful for visualization

of gas flow path and heat transfer approximation, including many of the fine details seen in much more complex reactive models. The obvious shortcomings of this representation are the lack of chemical realism, and the inaccuracy of the heat release zone.

Some important phenomena associated with a biomass stove are not strong functions of the fine details of zonally-realistic heat release, and thus can be modeled in a simulation that does not consider complex combustion approximation models. Examples include the optimization of heat transfer even a short distance away from the ends of any flames. Such *chemically passive* simulations typically include models for major physical functions such as bulk heat and mass convection and viscous dissipation, but do not include the modeling of chemical reactions of combustion and emission formation. Consideration of chemical and thermal species transport is also typically ignored since such details are minor compared to the major effect the combustion reaction would have. This simplification results in the absence of a number of conservation and transport equations from calculation, thus significantly reducing computational demands.

There are two typical methods of adding heat of combustion to a non-reacting thermal simulation:

- Model heat advection through a "blowing" (bulk advection) mass-flow boundary condition at the approximate location and area of the solid fuel bed. The desired enthalpy introduction is defined as a mass flow equivalent to the stoichiometric product mass stream, at an adiabatic or other calculated temperature. The analytical and empirical development of these methods of hot plume flame approximation is reported by Heskestad [51].
- Model a volumetric heat source (VHS) to a fluid-domain control volume just above the solid fuel bed. This constant-pressure, heat addition zone is often given a thin, conical or wedge-like shape in an attempt to add zonal realism to the flame-approximation plume. No additional boundary-condition flow element is needed at

the boundary, as local air is entrained into the heat addition zone. The VHS model is specified as a function of fuel and desired firepower parameters [59], [60].

The VHS method has been successfully used across a wide range of fire simulation applications [61]. The heat advection method was used by the author in an initial case study reported in the results section of this thesis. The method has also been used for fire representation in two heat transfer improvement studies in wood combustion devices, reported by Menghini, et al. [62], [63], described in more detail in section 4.2.4.

A chemically-reactive simulation includes any model(s) addressing the chemical reactions occurring in the fluid or solid phases. There are a number of methods for taking this into account, ranging from mixture-fraction formulations to detailed chemistry through chemical kinetics. These are considerably more complex than either typical non-reacting combustion heat approximation, and are introduced in section 5.4 of this thesis.

4.2.2 Steady-state vs. transient simulations

As introduced previously, fluid flow, fuel consumption, heat release, and some boundary conditions are in most cases all very strong functions of time in biomass cook stoves. For example, instability in the flow field and flame position in a biomass stove may have characteristic flame flicker frequencies of around 3-10 Hz [50], but the characteristic time of the consumption of a single stick of wood fuel can be around five minutes. Likewise, the thermal time constant for a stove combustion chamber experiencing a significant boundary condition change may be around one hour. CFD simulations can be designed with some of these elements modeled in a higher-fidelity transient formulation, or approximated as steady-state, at the expense of computational resource cost. It is however, practically impossible to resolve all these scales. The choice of temporal resolution and scale is a balance of fidelity, meaning, and computational

cost. Due to limits of practicality, there has not yet been a report in the literature on any CFD simulation of a cook stove containing resolution of a wide range of time scales.

Steady, laminar flow has parallel streamlines that do not vary significantly in time and space, and hence a steady simulation that has no functions of time is appropriate for such flows. Unsteady laminar flow and all turbulent flow inherently vary in time and space and hence a transient simulation, or at least an attempt to consider these effects in a steady solution, is necessary. Fluid flow in small, passive, biomass-burning domestic cooking/heating devices feature an initial zone of significantly steady laminar flow, followed by a time-varying laminar zone, and then near turbulent or weakly turbulent flow at the flame zone and thereafter, again requiring a careful approach. These relations are different for different combustion modes in different devices. The proportion and importance of the unsteady elements within the flow field are critical in determining if the flow may be approximated as steady [53].

Steady CFD simulations can provide some meaningful results in circumstances of largely uninterrupted and steady flow, such as in the fire of a candle, in packed sawdust rocket elbow stoves where the combustion chamber "walls" are actually the fuel [64], [65], or in devices where gas is forcefully injected in a stabilizing manner like as in a laminar-flow gas burner (i.e. gasifiers and semi-gasifiers). The flows in such cases do not have significant unsteady elements such as eddy-flow entrainment and significantly-flickering diffusion flames, and hence can be modeled in a steady formulation. However, such formulations are less practical for the additional unsteady complexities of continuously-fed stoves (i.e. wood stick-fuel rocket elbows), in which flow eddies and flame flicker are critical to mixing and combustion behavior.

While the unsteady nature of the fluid domain is visible and thus superficially understandable, temporal changes to the solid fuel are not easy to comprehend. The intensive and extensive fuel condition changes described in some detail in chapters 3 vary on time scales

typically longer than the key phenomena of the associated fluid domain, making for an interesting dilemma of how they should be treated.

4.2.3 Explicitly specified simulations vs. optimization schemes

All engineering development CFD simulations where geometry is explicitly specified a priori are essentially trial-and-error method design experiments, requiring a manual cycle of results interpretation and possible redesign. This has typically been the traditional case, most likely due to the difficulty of defining governing phenomenological models and boundary conditions in a way they can be automatically iterated for a an optimization scheme. One-off, stove-specific simulations are defined as the modeling of a particular, specific stove geometry (a range of boundary conditions is understood). The goal of such simulations is to give the stove designer an assessment of the operation of a stove whose geometry has already been defined and boundary conditions determined so that the design can be further refined. There are very few scientific papers outlining attempts at this type of simulation, described in the following section.

An optimization scheme has a critically different goal compared to an explicitly specified simulation. This subset of computer modeling attempts to experimentally evolve a set of stove parameters in numerical code, in the interest of automatically defining stove geometry optimized for predetermined performance metrics. This approach essentially recreates the trial-and-error process a human repeats in traditional, experimental design, except the process is faster and not prone to human error in measurement or perhaps biased judgment. A subset of this approach that has been applied to cook stoves is the employment of evolutionary algorithms, specifically genetic algorithms, to perform the optimization. There are some specific examples of genetic algorithms applied to cook stoves given in the following section.

4.2.4 Biomass stove CFD simulation examples

Two works of Menghini et al. [62], [63], report a CFD simulation approach applied to a domestic wood-burning fireplace. The stated goal of the authors for performing this simulation was to optimize heat transfer to an internal heat exchanger and as such no combustion reaction is modeled, and no emission results considered. The reported simulation is an example of the use of non-reacting hot advecting flow to approximate combustion heating, as described in section 4.2.1. Bulk-averaged temperature and mass flow values were experimentally acquired from a similar test stove, and then prescribed as boundary conditions above the fuel bed zone. Turbulent effects were approximated with a steady formulation of a Reynolds-Averaged Navier Stokes (RANS) k-ε model. In this case the much faster solving steady formulation is suitable since the goals were to consider approximate heat transfer only. The computation time of a CFD simulation must always be considered, especially in work with a goal of optimization, requiring iterations. Relative inaccuracies associated with the lack of combustion model are likely on the order of those associated with the lack of an unsteady flow formulation, and as such a steady flow formulation is probably justifiable. Manual iteration of the device geometry and the repeated computation of a simulation are laborious and time consuming. The employment of a steady formulation in this case is likely a practical one.

Ravi et al. [64], [65] develops a simulation method for a packed sawdust stove that has some important similarities to the method proposed here, but also critical differences. A packed sawdust stove is “built” anew for each use as particulate sawdust is packed into the space between the outer surface and removable plugs forming the horizontal inlet and vertical outlet sections. The plugs are then removed to leave a flow path bounded by packed sawdust. The combustion chamber of this stove is thus also the fuel, and much like the fuel inside a solid rocket motor is consumed in an outwards direction as it burns away. In a packed sawdust stove the homogeneous-phase combustion is attached to the walls which themselves supply fuel into the fluid through

advection (i.e. blowing) as the solid fuel devolatilizes. Mixing critical to non-premixed diffusion flame combustion is largely included within, and stabilized by the laminar portion of the boundary layer at that wall. This is an important distinction vs. the comparable scheme in a stick-fuel type stove, where the fuel is advected away from the wooden sticks of fuel where there is no stationary obstacle to stabilize the location of the diffusion flame front, which significantly fluctuates around the combustion chamber. Ravi et al. propose the use of a semi-empirical equation to model the pyrolysis of the sawdust purely as a function of a constant incipient heat flux between flames and surface, with pure conduction into the sawdust. The authors use an iterative process where the incident heat flux from flame back to the fuel was assumed, the heat driven pyrolysis rate calculated, and then the CFD simulation ran and the result of available heat from combustion assessed for iterative refinement. The model did include the transient condition of fuel consumption and burnout, addressing the changing operation of the stove over the burn cycle. Flow itself was modeled in a steady approximation, highlighting the assumption that it was not critical to model transient flow. Revisiting the discussion in Section 4.2.2 of this thesis, it is very important to point out that Ravi et al. chose to focus on resolving the long time scales of fuel consumption vs. the much shorter time scales of transient flow. The fact that the authors found good agreement between their model and a validation experiment highlights the importance of evaluating the nature of each transient element in a device when deciding on the scales to resolve. In common with the procedure proposed in this thesis is the use of a simplified approximation for pyrolysis. Not in common with the work presented in this thesis is the choice of Ravi et al. to use a steady flow formulation, a choice justified by the fact that the wall-stabilized combustion has less unsteady motion.

Bojko and Branc [66] present a CFD simulation of a wood-burning stove modeled in detailed geometry. The fuel is introduced as a production source term of constant mass-flow of lumped pyrolysis gas at the surface of the fuel. Heterogeneous-phase combustion is ignored and

homogeneous-phase, diffusion flame combustion is modeled using the eddy-dissipation method (EDC). Radiation transfer is modeled via discrete ordinates (DO) method. Of interest is that the air inlet boundary condition is specified as an explicitly defined mass flow based on an excess air ratio known a priori instead of naturally induced via buoyancy effects through a pressure inlet condition.

Three related works by Bryden et al. [67], [68], and Urban et al. [69], utilize graph-based evolutionary algorithms (GBEA) to optimize geometric parameters of the heat transfer surface on a plancha-type stove. Geometric limits are given to boundaries of the internal gas flow path beneath the plancha surface and the GBEA iteratively refines the path geometry. Other inputs include governing equations for flow losses and a pressure-based source of hot gas flow. The approach maximizes convective heat transfer while considering loss effects. Validations prove that these are useful methods of optimizing some major aspects of a stove, simultaneously reducing development time and increasing the likely level of improvement over baseline. This application is very limited, however, in the phenomena that they consider. The simulations did not feature the complications of a combustion model, nor unsteady flow. The steady flow formulation is justifiable because the flow field in the portion being optimized is suitably stabilized.

Burnham-Slipper [30], [31], has developed a process for using genetic algorithms (GA) to automatically optimize the entire combustion chamber of a stick-wood fired Eritrean cook stove. The author assembled a comprehensive set of governing equations and phenomenological submodels able to represent the behavior of the stove, but simplified enough that they can be solved in an optimization scheme. The overall control volume is idealized as axisymmetric in order to reduce the computational cost. Several small CFD pre-simulations and experiments are conducted in order to validate various assumptions and develop constitutive sub-models. A fuel bed composed of stacked layers of alternating perpendicular alignment is burned in a bench

combustion experiment in order to learn the mass evolution (global reaction rate), and product gas temperature and flame plume geometry. Data from this experiment is then used along with assumptions of fuel geometry and packed bed relations to define a constitutive relation approximating combustion. The model is then able to be defined in the CFD as a porous zone with pressure drop and hot product gas source term. Another CFD pre-simulation and a matching experiment are conducted to validate stagnation flow heat transfer to the pot. This set of tuned sub-models is then assembled into the overall CFD simulation, configured to a genetic algorithm for geometry evolution, and then run in iteration seeking to maximize heat transfer to the target. The author demonstrates successful use of this process but does not construct the final stove geometry to conduct a validation experiment.

4.3 Logic and assumptions

The logic of the case for the proposed simulation method is introduced as follows. The physical phenomena occurring around the biomass cook stove are complex and transient. Traditional stove design methods rely mostly on bulk measurements (spatially and/or temporally averaged), and visual inspection, limiting the usefulness of such data as an input in considering effects on finer scales. Using only bulk data, the phenomena inside the stove can only be known in crude spatial and temporal resolution. While absolutely necessary for evaluating the net performance of a stove, the coarseness of bulk data limits the stove to being a “black box” in the eyes of the designer until they learn to interpret the related complex phenomena indirectly.

These shortcomings limit both the rate and ultimate level of design improvement that can be attained by such methods. Further design improvement often requires information such as fluid flow paths, temperature ranges, residence times, zones of rich and lean stoichiometry, etc. This requires significant introspection into the stove, and the phenomena occurring therein.

Technologically advanced experimental techniques such as the use of optical diagnostics to sense temperature, chemistry and velocity are an attractive option due to their fine spatial and temporal resolution capability, but are unfortunately very costly and thus not widely available. State-of-the-art numerical models and their computational applications are capable of simulating every single physical phenomena occurring around a biomass cook stove, but such extreme approaches are many orders of magnitude too complex for application to biomass cook stoves. These conditions form an essential question: If phenomena associated with biomass stoves are so complex that low-tech design tools are not powerful enough to benefit the process, and that using highly accurate models adds too much complexity, where then is the practical and useful middle-ground of technology, that is good enough to yield reasonably accurate results but fast enough to be a *practical* design tool?

If available computer resources are finite, one must consider that all the elements of the model contribute to computational requirements. This creates the case for creating a model that is a compromise of three general terms; Phenomenological complexity, spatial/temporal resolution (linked), and model simulation duration (impacts what scale of transients can be considered). These general terms can be further broken into metrics of spatial and temporal resolution, characteristic time, behavioral complexity and impact, as related in Table 2. For example, the CFD model can either be fully complex in phenomena that are unsteady functions of relatively short characteristic times (such as unsteady flow) and have fine spatial/time resolution, or they can be crude in phenomenological model and have crude spatial/time resolution.

Table 2: Comparison of relative scales and complexity associated with various stove-related phenomena

Complex aspect	Spatial resolution	Temporal resolution	Characteristic time	Behavior complexity	Impact
Flow field details	**HIGH** - on the order of 5mm in order to resolve the smallest flow features in stoves	**HIGH** - Purely a function of the high spatial resolution and requirements for computational stability	**LOW** - Fluctuations in flows occur around the flicker frequency (1-10hz in these devices)	**HIGH** - complex, requiring special modeling tactics such as turbulence models	**HIGH** - For the fine adjustments being made in the design of stoves, good resoluction of the flow field is critical.
Solid fuel / pyrolysis reaction	**LOW** - Considering the natural uncertainty about fuel position and geometry only low resolution justified.	**LOW** - On account of the long characteristic time	**HIGH** - Sticks of fuel may take several minutes to be consumed in a small biomass stove.	**HIGH** - Pyrolysis is a very complex reaction.	**HIGH** - Many references and practical experience point to the fact that pyrolysis and the solid fuel reaction are critical to performance
Transient conjugate heat transfer / heating of boundaries	**LOW** - Peclet number considerations suggest high resolution is unnecessary	**LOW** - Due to extremely long charateristic time	**HIGH** - Even a small stove may take an hour or more to come to full temperature	**LOW** - Convection and conduction in the case of a stove are not particularly complex.	**LOW** - There are acceptable ways to get around the challenges of conjugate heat transfer

There are phenomena at particular scales that are important in the evaluation of a biomass cook stove. Fluid flow and bulk (larger scale) gas mixing occurring in buoyant, non-premixed diffusion flames (including those in stoves) are dominated by relatively large, unsteady flow fluctuations, commonly called eddies or vortices [50], [52]. Modeling these flow structures requires the model be formulated as a function of time, known as an unsteady or transient simulation. For this reason unsteady transient flow formulations are regarded as much more useful than steady ones for modeling of most buoyantly-driven diffusion-flame fires, and unsteady modeling is much more common for fire modeling [70], [71], [61], [72]. Unsteady flow is adopted in the work reported here on this basis.

Considering that unsteady flow requires fine-temporal resolution, the simulation of a fully transient fuel condition with a characteristic time on the order of minutes or hours is impossible in the foreseeable future of common computers. The fuel condition must thus be steady state, or transient with only a brief characteristic time.

Since the fuel condition varies on a relatively long characteristic time, it is practical to solve a stand-alone lumped fuel model outside of the CFD, and then model the outputs of that model as boundary conditions in the CFD. Several suitable models are found in the literature that lump the overall reactions of the solid fuel into a single step. One is selected and developed for use in coming sections.

The CFD model must be validated before it can be relied on as a tool for iterative design. Ultimately, the interest is in how well the computer model compares to an actual fuel fire in a physical prototype of the experimental stove design. Since the boundary conditions of the CFD model differ from the realities in the actual stove, such a validation is statistical and not direct. An instrumented prototype stove is used to demonstrate this procedure.

5. CFD simulation development

The development and computation of CFD simulations towards the goals of the concept outlined above are reported here. Simulations were created of an existing stove with known geometry and performance in order to have the utility of additional performance data from which to make validation comparisons. Two specific boundary condition cases are reported. One of these cases is of a stove at a relatively low firepower condition, matching the average simmer condition behavior found in experiments at the CSU Clean Cook Stove Laboratory. The other case is the simulation of a relatively high firepower condition, matching the average conditions found for "hot start" stove performance. An external model calculates a lumped fuel reaction condition a priori, to be used as a boundary condition in the simulation. The simulations include models for gas-phase combustion, radiation, turbulence and law-of-the-wall gas/solid interaction, and soot formation.

There has been considerable learning and development in the work leading up to this thesis, much of which is considered common knowledge by those in the art of CFD modeling. That work is not reported in detail here, but the important points are made clear. It is important to mention that a significant amount of modeling with other software was conducted in exploring these methods. ANSYS Gambit was the previous pre-processing software before ANSYS Workbench, which is used here. ANSYS FLUENT 12.0 was used previous for computation before version 13.0. One noteworthy implication is that cut-cell meshing was not available previous to ANSYS FLUENT 13.0 - an option that has significantly changed the modeling approach due to the ability to achieve viscous-sublayer resolution of the boundary layer with a reasonably small cell count. Significant early modeling work was also conducted using the Fire

Dynamic Simulator open-source fire-modeling CFD software available from the National Institute of Standards and Technology (NIST), but are not reported here.

The standard, academic version of ANSYS FLUENT 12.0 and 13.0 was used. As such, all governing equations, and those defining all models and submodels are as reported in the ANSYS FLUENT 13.0 Theory guide [73]. Model selections as output by ANSYS FLUENT can be seen in appendix H.

5.1 Simulation geometry and boundary conditions

As mentioned, the intent of this CFD simulation is to have comparison to a known stove, which in this case is a model G3300 stick burning wood fuel cook stove, made by Envirofit International, LLC. The conjugate heat transfer is approximated as a boundary condition and not actually physically resolved and hence the control volume (CV) includes only the void in the solid geometry and not any solid volumes. The control volume featuring critical dimensions is seen represented by the transparent volume in Figure 6. The control volume itself was created in SolidWorks CAD modeling software, around the solid model of the G3300 as seen in Figure 7. The CFD control volume also matches the geometry of the instrumented validation stove, detailed in section 6.1 and seen here in Figure 8. The control volume includes voids and boundaries where the surfaces of the stove, cooking pot, wood fuel stick approximation, and inlet and outlet reservoir boundaries have been defined.

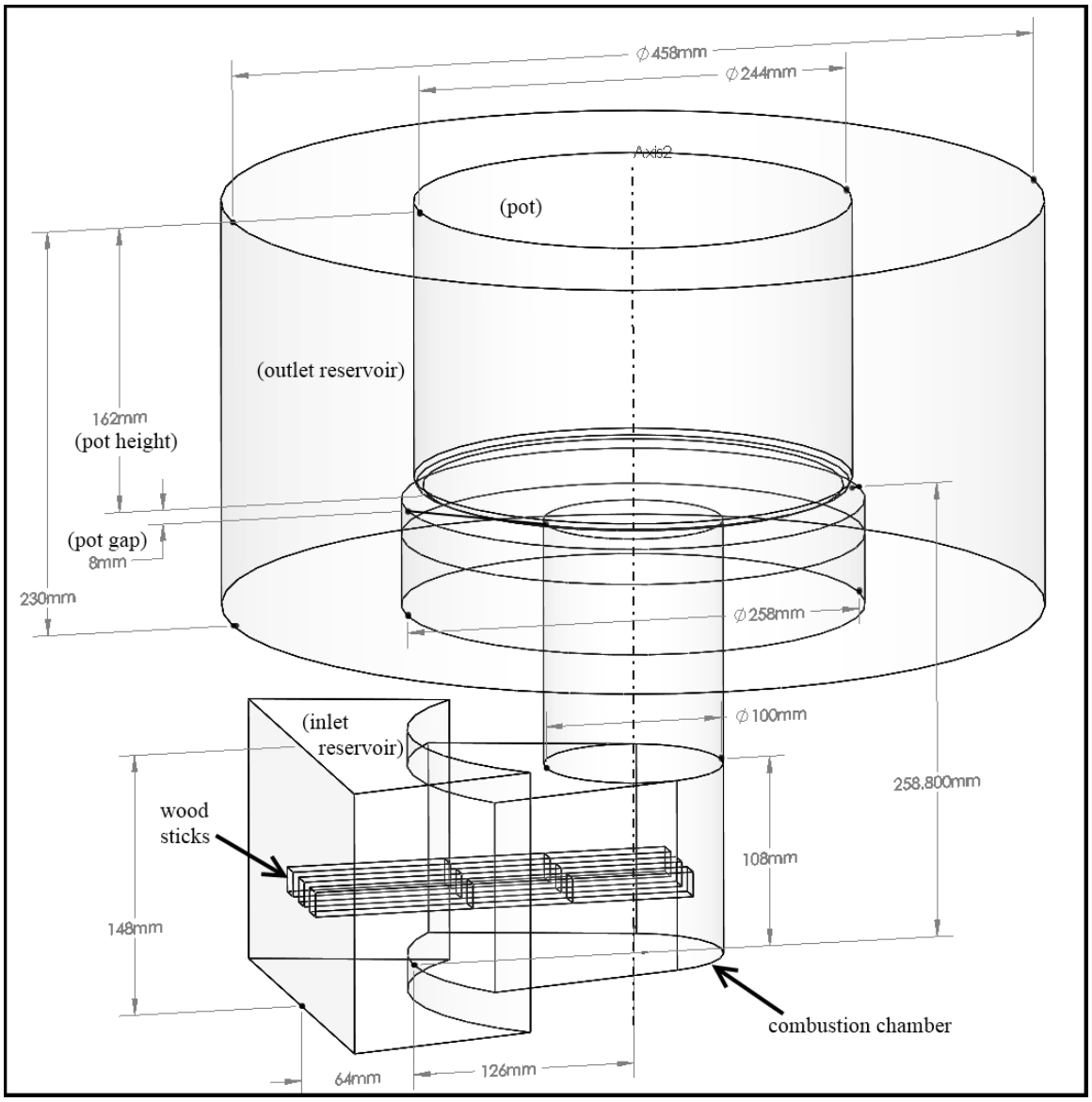

Figure 6: Control volume used in CFD modeling

The control volume features extra reservoir zones around the inlet and outlet areas. These are necessary due to some difficulties specific to the simulation of naturally-generated buoyant flows. In this case the inlet reservoir is wedge shaped, extending radially outward from the front of the stove 64mm in the shortest dimension. The outlet reservoir is an extra tube-shaped volume extending out radially from the pot and stove body, upwards to the top of the pot and downwards approximately 60mm below the gap where hot gas escapes out of between the pot and stove top. These reservoir zones exist for the following reasons:

- These reservoirs allow the generation of natural flow streamlines, important for establishing inlet velocity profiles, the growth of boundary layers on surfaces, and the turbulent transition of those boundary layers. A secondary concern of the inlet boundary is how stochastic turbulence levels are specified for the incoming flow.
- Especially in the outlet region, the boundary must be far enough away from large recirculating flow structures of interest, as to avoid interaction of the two. In the physical reality of a recirculation in flow straddling the boundary of an imaginary control volume, half of the eddy is exiting the control volume while the other half is re-entering. In a CFD simulation there is no resolution outside of the modeled domain and as such there is no mechanism to resolve that re-entering flow. If the boundary is put in a region where eddies of significant importance exist, their resolution will be lost. Since eddies are important in convection heat transfer into the side of the pot the outlet boundary needs to be far enough away so as to avoid such conflict. Even when the flow is not of interest, unsteady recirculation at a boundary generally slows computation by way of reducing convergence speed.
- The outlet reservoir allows the flow energy of any flow jets to diffuse, and turbulent energies to dissipate so that the conservation computations converge easily.

Adding these geometries enlarges the control volume by approximately 35%, adding roughly 15% more computational cells to the volume, but often actually decreasing computational time. Note that another option for handling flows external of the stove is to model the stove boundaries within a single, larger control volume (imagine the stove inside a large box), without distinct inlet and outlet regions. This method has been evaluated in the CFD simulation by the author, and found to be an unnecessary increase in computational cost.

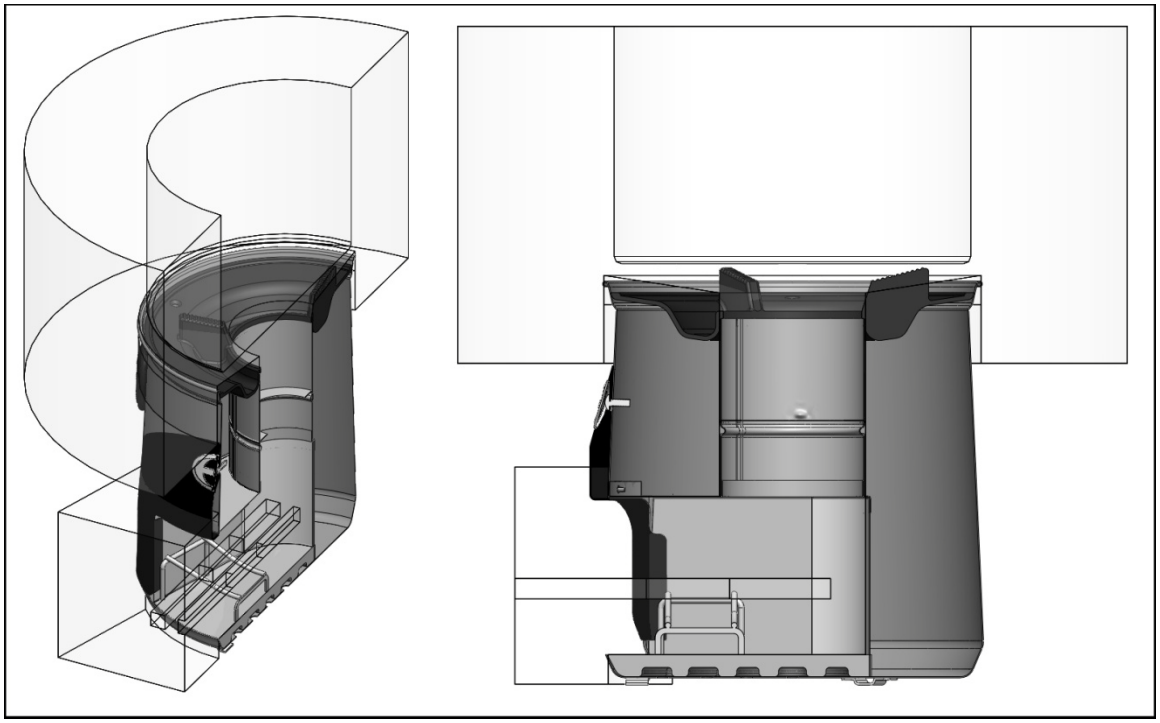

Figure 7: Cross-section of CFD control volume geometry superimposed of that of the G3300 stove model

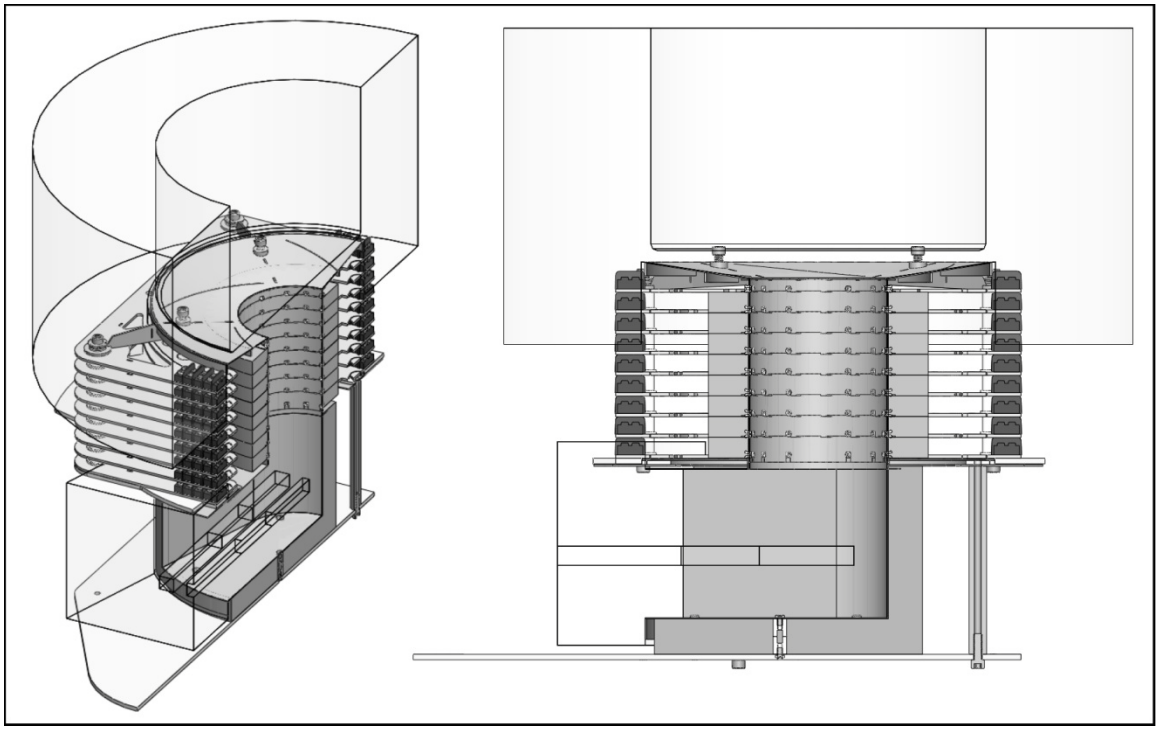

Figure 8: Cross-section of CFD control volume geometry superimposed of that of the validation stove

Boundary conditions (BC) specifically reflect many elements of the overall assumptions applied to the simulation, as reflected on in the conceptual development in sections 4.1 and 4.3. Very importantly, an emphasis has been placed on the phenomena occurring on short time scales, such as the unsteady motions of the flow field. Typical simulation run times are on the order of 3-10 seconds, which is around three orders of magnitude less time than the known duration of a cooking cycle (30-90 minutes) [74][75]. The thermal equilibrium of the stove may not be reached naturally for over an hour [76]. Towards, the goal of artificially reducing the thermal response time of the overall system, the fuel condition has been approximated as a steady, lumped reaction without driving feedback (see section 5.3). Also noteworthy, the combustion chamber walls possess reduced mass for the purpose of rapidly assuming thermal equilibrium with new flow and reaction conditions.

The key focus of these assumptions is on the realism of the accurate modeling of zonal heat release through a mixture-fraction combustion approximation, made possible by the removal or alteration of long time-frame elements. The boundary conditions of the two cases of CFD simulation are representations of the validation stove, which itself coincides with the boundary conditions of the G3300 production stove in most ways. Section 6.1 explains the physical construction of the validation stove for reference here.

The boundary conditions for the CFD simulation are defined in meaningful consideration of the G3300 physical stove. Material and layout for both the actual G3300 and the validation stove are seen in a cutaway view in Figure 9.The details of the validation stove construction are described in section 6.1. The CFD simulation makes no attempt to resolve the directional flow of heat within the insulation-filled body of the G3300. The CFD boundary scheme more replicates the validation stove, with heat modeled as a convection BC, meaning that heat flowing out of the system is only modeled as normal to the surfaces.

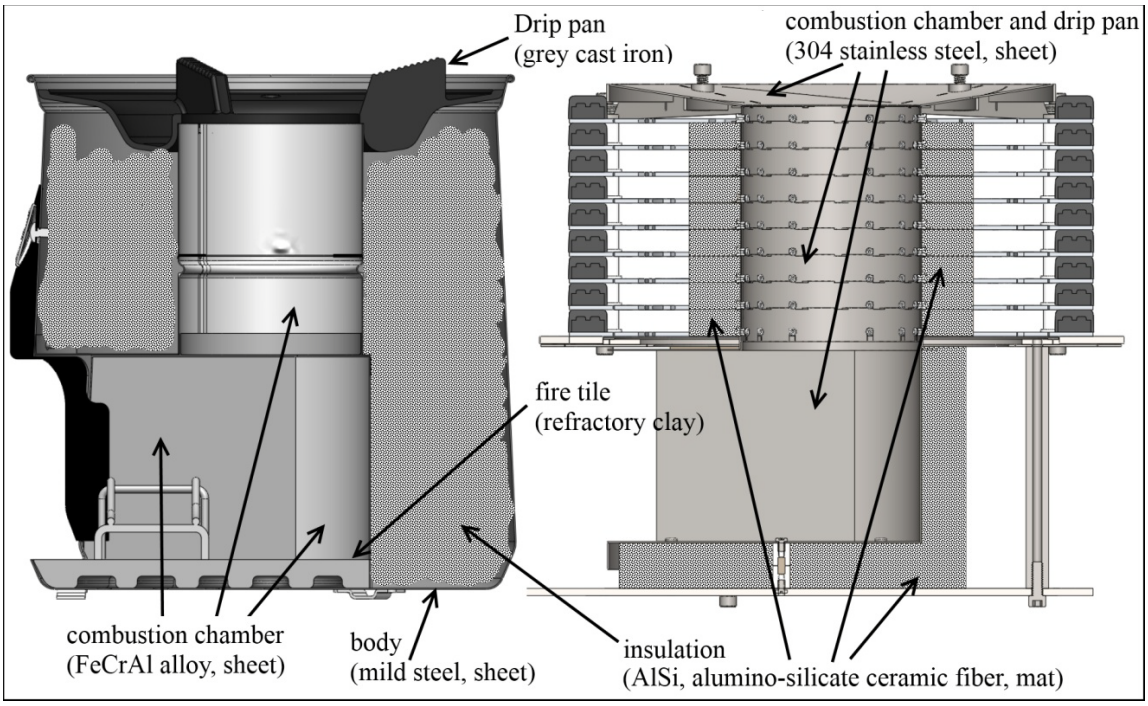

Figure 9: Materials of construction for the G3300 and validation stove

The simulation boundary conditions are listed in Table 3. The inlet is represented as a pressure inlet and the outlet as a pressure outlet, both set at zero relative pressure (85kpa absolute). The major exterior boundaries are diagrammed in Figure 10.

The fuel boundaries are setup as shown in Figure 11. There is an inert section to the end of the fuel protruding from the stove, modeled as an adiabatic wall here, and a mass-flow inlet at the idealized pyrolysis zone, representing the advecting boundary where the injection of net pyrolysis gas occurs. The pot surfaces are modeled as 0.5mm thick of 304 stainless steel with an external convection coefficient of $110 W*m^{-2}K^{-1}$ assumed for a condition of quiescent water, and a stream temperature of 325.6K. This temperature is about halfway between room temperature and boiling. The external boundary condition for the cooking pot (for the transfer from pot to water) is extremely complex due to the natural convection loops that establish in the water. It is likely that any simple, assumed convection coefficient carries significant error [77][78]. No-shear conditions are specified at all walls, a topic discussed in more detail in section 5.5.

Table 3: Boundary conditions for CFD

Boundary location	ANSYS FLUENT BC type	Parameters
inlet	pressure inlet	P=0 Pa, T=295K, emissivity=1.0
outlet	pressure outlet	P=0 Pa, T=295K, emissivity=1.0
combustion chamber walls	wall, convection	External h=10 $W*m^{-2}K^{-1}$, Tfilm = 300K, AlSi insulation 30mm thick
cooking pot	wall, convection	External convection coefficient of 110$W*m^{-2}K^{-1}$, external film temperature of 325.6K, wall thickness of 0.5mm of 304 stainless steel
inert fuel surfaces	wall, isothermal	Adiabatic, 0W heat transfer
pyrolysis fuel surfaces	mass-flow inlet	*(details given in section 5.3)*

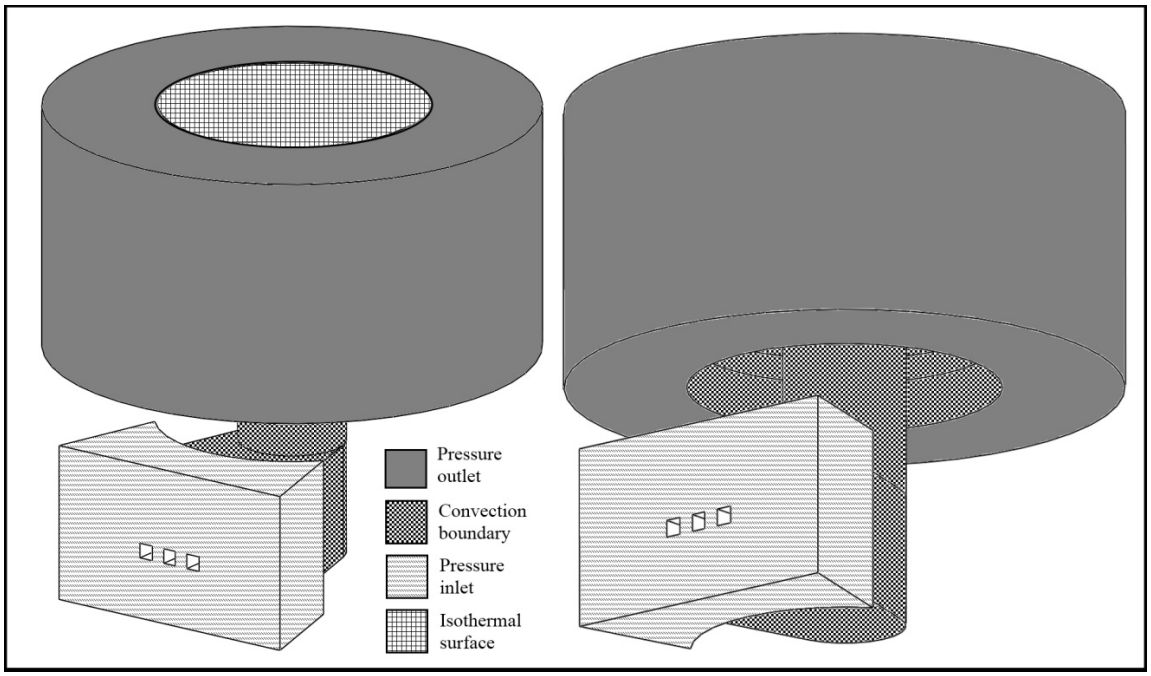

Figure 10: Depiction of major CFD control volume external boundaries

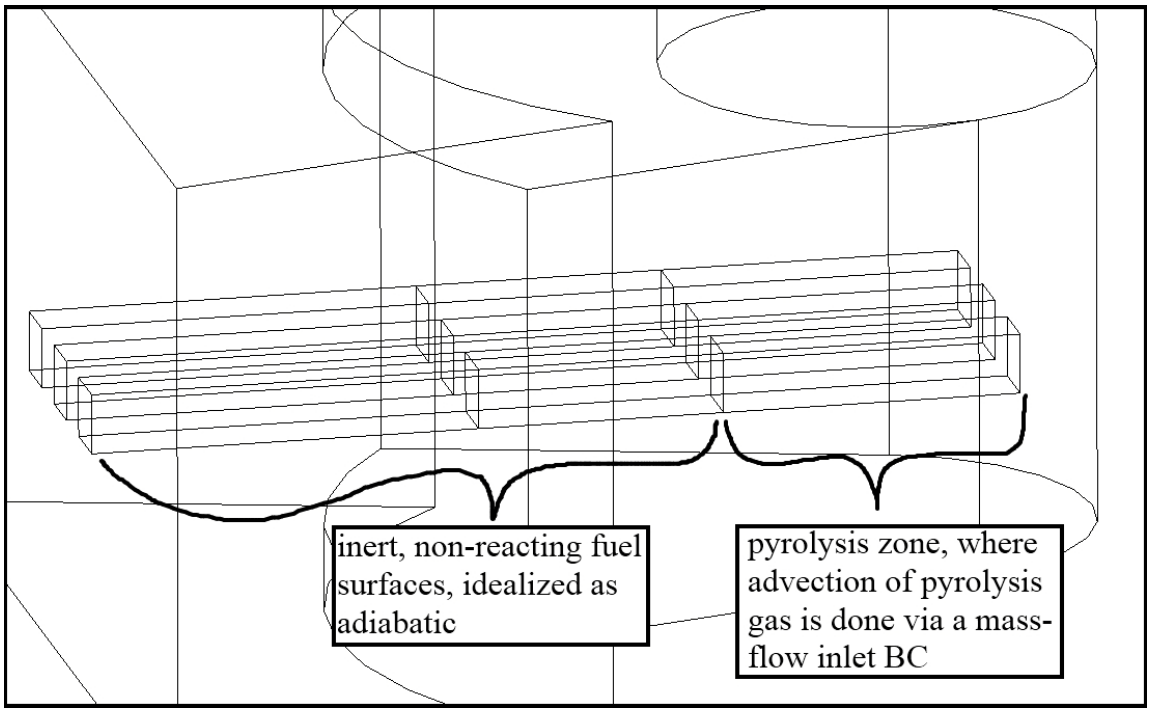

Figure 11: CFD fuel conditions

Thermal effects at the combustion chamber walls are known to have a large effect on the behavior of the stove. The temperature of these surfaces are known to be important and hence of interest in the CFD simulation. Shell conduction, or the conduction of heat along the boundary surface, has been ignored on all solid boundary surfaces. The reason for this is twofold. First, shell conduction would require realistic material densities that would contribute to long thermal response time constants, requiring simulations at least two orders of magnitude longer than those simulated here. Secondly, shell conduction is not available in ANSYS FLUENT CFD simulation software when using a mixture-fraction combustion approximation. Since mixture-fraction is strongly preferred for this initial investigation into the use of CFD on stoves, the absence of shell conduction is accepted.

As mentioned above, the thermal time constant of the combustion chamber walls is much longer than the typical simulation durations proposed here. What this means is that the combustion chamber walls would not be able to approach thermal equilibrium in the short

simulation run times if natural boundary conditions are used. An alternative tactic is thus used here. The combustion chamber wall boundaries are essentially modeled as ultra-low density insulation, but with an internal-surface emissivity matching that of the metal chamber. No report of the use of this tactic could be found in the literature. Experimentation by the author suggests that the following benefits exist:

- Bulk heat loss through the wall will at least be generally approximated, leading to the increased accuracy of radiation transfer to and from the combustion chamber walls – an element known as being important (Wall radiation interaction isn't critical for the use of mixture fraction combustion modeling, but definitely is for the future use of any combustion model relying on chemical kinetics).
- The walls will change temperature very quickly as if they were the fictitious, low-mass insulation.

The lack of significant thermal mass means the temperature can alter very quickly and unnatural transient boundary layer behavior should exist. If the material had an infinitesimally small mass then the surface would effectively follow the temperature of the flame, exactly. The use of this tactic brings behavior closer to that extreme.

The thermal aspect of the combustion chamber boundary is modeled as a convection boundary. Everything outside of the combustion chamber control volume is not resolved in the spatially-discretized computational domain and as such the external heat flow cannot be modeled in a finite volume or finite element method. The heat transfer is thus modeled using an external convection boundary condition. Required inputs include the film temperature (elevated ambient), and convection coefficient. In both CFD simulations the film temperature was set as 300K and the convection coefficient as 10 $W*m^{-2}*K^{-1}$. Since the boundary conditions are designed to match the G3300 generally, and the validation stove specifically, the external condition of the validation stove is of more interest. As described in section 6.1, the validation stove is composed of stacked

levels of combustion chamber in between fiberglass frames. The heat rejection scheme is thus actually very complex, with the device taking on the form of a vertically-aligned cylindrical heat source with horizontal heat exchange plate fins (as in a vertically-oriented electronic resistor with heat sink). The author decided addressing this in detail was outside the scope of the project and that the simplifying assumption of using an arbitrary, textbook external heat transfer coefficient would add minimal error compared to other sources. In other words, the assumption of the extremely low-mass insulation, and the necessary simplification of the combustion chamber boundaries lacking shell conduction (conduction along surface), are both sources of error at least as significant if not more so than specifying an arbitrary external convection coefficient.

Actual material thermal properties for the G3300 and validation stoves are assumed constant, as seen in Table 4 [8][76][79]. Table 5 includes the values as modeled in the CFD simulation.

Table 4: Material properties

Property	Sym.	Units	Alumino-silicate refractory ceramic fiber	FeCrAl	304 stainless steel	ductile cast iron	mild steel	wood (Douglas Fir)
Density	ρ_i	$(kg*m^{-3})$	160	7460	8000	7400	8030	530
Specific heat (CV)	$c_{p,i}$	$(J*kg^{-1}*K^{-1})$	1130	460	500	490	502	1380
Thermal conductivity	k_i	$(W*m^{-2}*K^{-1})$	0.06	16.00	16.20	36.00	16.27	0.11
Emissivity	$\in_i$	*(dimensionless)*	0.80	0.85	0.85	0.64	0.94	0.88

Table 5: Materials of stove elements

Property	Sym.	Units	Lumped chamber wall and insulation	304 stainless steel	mild steel	wood (Douglas Fir)
Density	ρ_i	($kg*m^{-3}$)	10	8000	8030	530
Specific heat (CV)	$c_{p,i}$	($J*kg^{-1}*K^{-1}$)	1130	500	502	1380
Thermal conductivity	k_i	($W*m^{-2}*K^{-1}$)	0.06	16.20	16.27	0.11
Emissivity	ϵ_i	*(dimensionless)*	0.80	0.85	0.94	0.88
Stove body					X	
Combustion chamber (inc. bottom)			X			
drip pan			X			
Wood fuel						X
Cooking pot				X		

The fuel condition is modeled as the injection of a hot (800K) net pyrolysis gas at the idealized pyrolysis surface region. The two CFD simulation cases have different gas flow rates, with details of the fuel condition given in sections 5.3, and 5.4.

5.2 Spatial discretization

The control volume domain is split into a mesh (or grid) of cells, allowing representation by a linear mathematical matrix in which the fundamental analytical and other governing equations are solved using the finite volume method. The author has pursued several different approaches to achieve a suitable mesh, spanning multiple generations of several commercial software packages. Aspects of these major approaches attempted are described generally, and the most recent and final meshing technique is reported in detail. The modeled control volume was usually limited to the fluid domain as reported here, except for some experimentation involving inclusion of solid regions in the domain for investigation of conjugate heat transfer. Meshing small biomass cook stoves in high spatial resolution is not trivial due to the range of scales requiring resolution.

The mesh must be fine enough to resolve small boundary features, such as the fuel sticks and the radius on the bottom of the pot. Cell faces are planar and as such curved surfaces are approximated as a three dimensional spline. The more elements used to represent a curved or complex surface the greater the fidelity of its reproduction. For this reason, small features of little importance are intentionally removed from the geometry before meshing.

The fluid domain mesh must also be appropriate along solid boundaries in order to take into account effects in the thermal and momentum boundary layers, either through fine, direct resolution or through a local suitable for the use of a law-of-the-wall model. In zones between boundary features, such as in the pot gap (~9mm) and the spacing around the fuel sticks (0-15mm), the above concern is complicated by the fact the boundary layers affect each other.

As has been repeated in this document, aspects of time and space cannot be separated in an unsteady simulation. The geometry of the mesh affects the simulation of an unsteady, turbulent flow quite significantly. The minimum scale of unsteady motion (here including turbulence) resolved in a simulation is a function of the local mesh size.

Specification of a mesh fine enough to resolve these features may actually be relatively easy, however as always the cell count must be held as low as possible for practicality of calculation. This means that the mesh density must decrease as it moves away from zones needing fine resolution. Meeting the requirement of adequate resolution and minimized cell count is often an exceptional challenge.

Early work using ANSYS Gambit preprocessing software yielded meshes void of any boundary layers due to the limitations of that software in controlling complex 3D boundary layers. Even though a structured hexahedral / rectilinear mesh was preferred it was not practical again due to difficulty in control. Because of these limitations in meshing control, a computationally expensive unstructured tetrahedral mesh was the only option for practical meshing. Unfortunately, the resulting mesh was not practical due to the computational demand.

The method for refining boundary layer regions into the log-law region of resolution for use of a law-of-the-wall model was to use size functions growing off of the surfaces of interest. An example of this type of meshing scheme can be seen in Figure 12. Such a meshing scheme was practically limited to log-law region boundary layer resolution (and not finer). Despite this, such meshes were still too large to be very practical. The example mesh seen in Figure 12 has over 800k elements, making it impractical for calculation on a desktop PC.

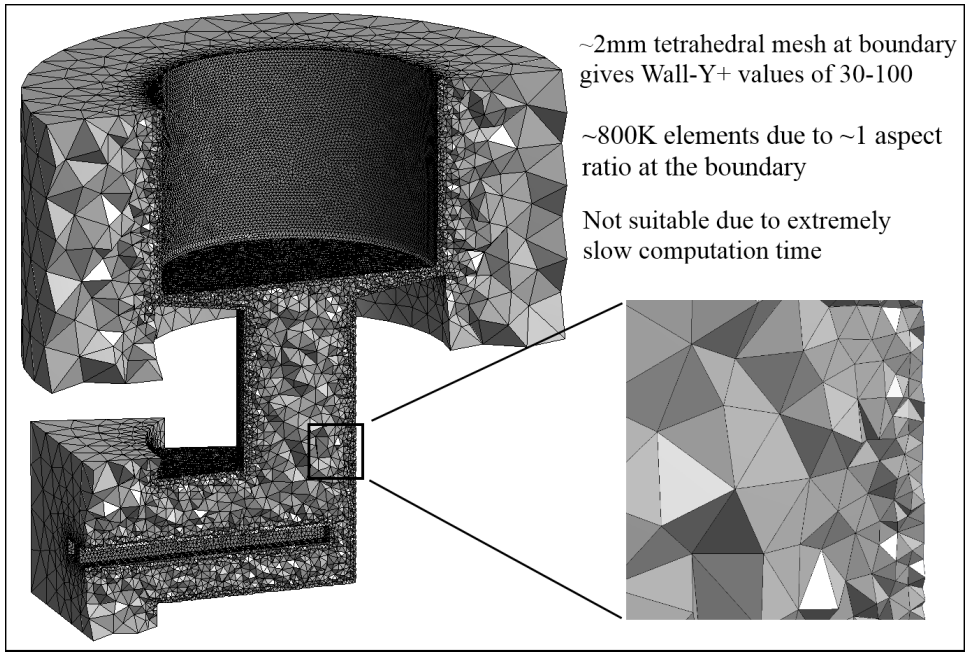

Figure 12: Cross-section view of an example of an unstructured tetrahedral mesh without explicit boundary layers.

All the meshing methods discussed as follows are created via automatic methods within ANSYS Workbench (12.0 or 13.0). The use of ANSYS Workbench 12.0 software for preprocessing allows the robust generation of a prismatic boundary layer on an unstructured tetrahedral base mesh, but it is restricted to an unstructured, or mostly unstructured tetrahedral-based core. An example of this scheme can be seen in Figure 13. This scheme allows the resolution of a boundary layer down to the viscous sublayer (wall Y^+ values ~1), but the mesh still remains large at ~500k elements. Other candidate meshing methods include the use of a hexacore mesh or combinations of these options.

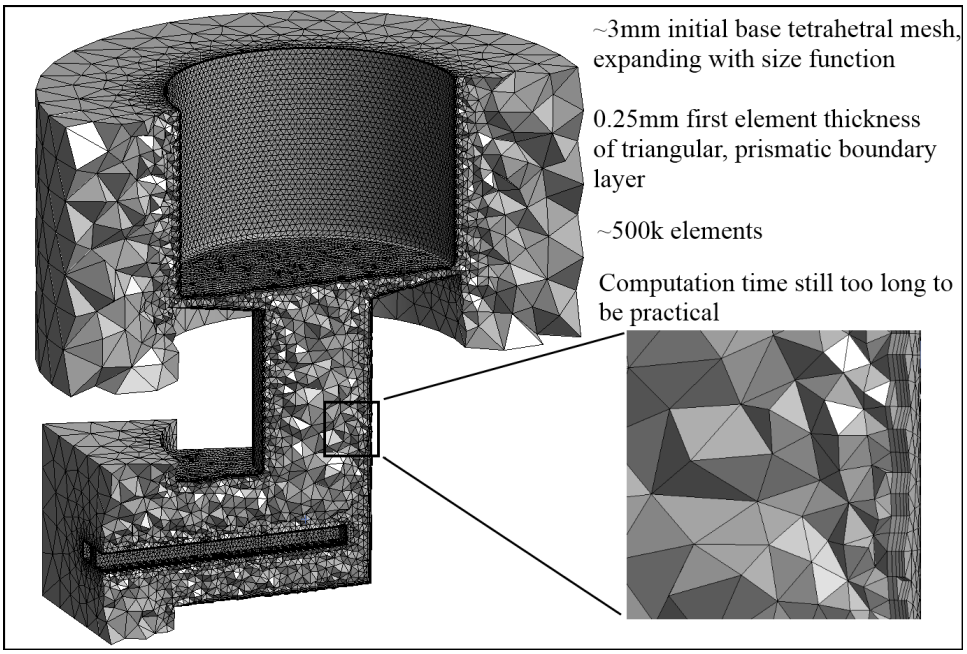

Figure 13: Cross-section view of an example of an unstructured tetrahedral mesh with explicitly prescribed prismatic boundary layer.

An upgrade to version 13.0 of ANSYS Workbench brought the ability to use a structured, hexahedral / rectilinear (cubic), cut-cell mesh in conjunction with a prismatic boundary layer, as seen in Figure 13. This was found to be far more efficient than any other option, even with a boundary layer resolved into the viscous sublayer (wall Y^+ ~1). Various size function and control schemes were experimented with until a good balance of performance was had with the meshing scheme described as follows.

The final, successful meshing scheme uses a cut-cell Cartesian mesh throughout the entire control volume, with boundary layers specified on all solid surface boundaries, as seen in Figure 14. A cut cell Cartesian mesh is easy to understand, visually. The ideal basis of this type of mesh is made of perfectly cubic hexahedral blocks. In reality the mesh is not perfectly Cartesian, but mostly rectilinear with slight element edge curvature allowed. The version of this meshing scheme employed in ANSYS Workbench V13.0 allows mixed element types along boundaries that are not aligned with the element edges. The name “cut-cell” comes from the fact the cells divide to provide higher mesh density. The mesh density is increased not by the scaling of the

size of the cubes, but by the three-dimensional quartering of them. Thus the edge sizing varies quadratically. This is achieved by dividing all edges of each discretized cube in half at once – thereby making a single cube into eight smaller cubes. This operation done twice to a single element creates 64 separate cubic elements. There major utility of this meshing type is the computational efficiency it allows. Nearly cubic blocks have an aspect ratio close to 1.0. Aspect ratios of unity allow for the easiest possible discretization of the fundamental governing differential equations, and the fastest solution through the lowest number of computational iterations. There may be important implications of the use of this mesh type on the modeling of turbulent flows with a Large Eddy Simulation, as the modeled subgrid scale rapidly changes as the flow moves from a region of one grid resolution to another. The transition between areas of two mesh densities may not be trivial.

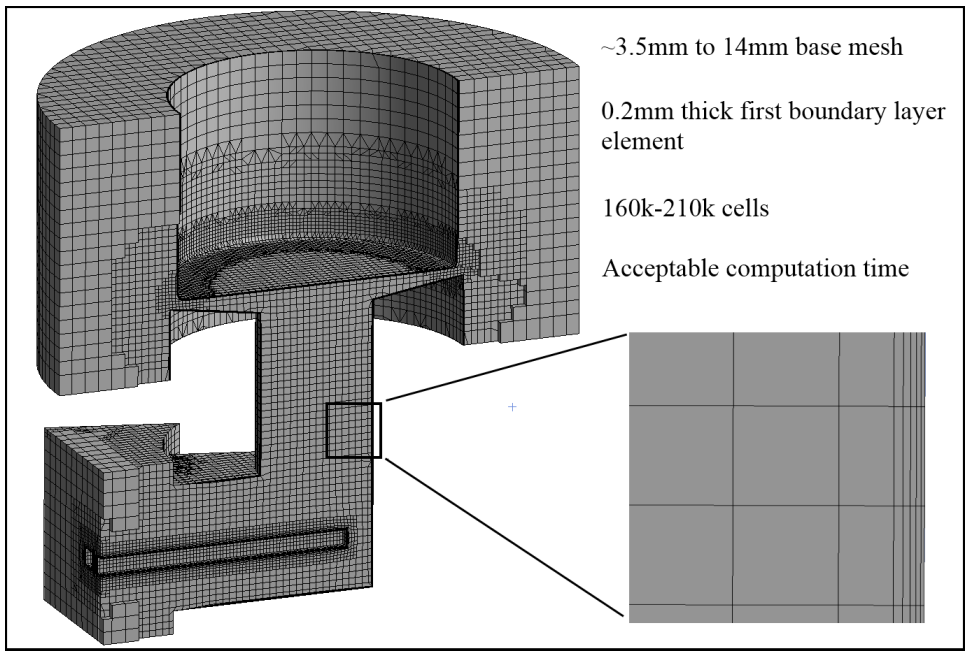

Figure 14: Cross-section view of structured cut-cell rectilinear mesh with explicitly prescribed rectilinear boundary layer.

The boundary region is the zone of the fluid domain immediately adjacent to non-moving boundaries (e.g. walls), wherein the thermal and momentum boundary layers experience the effects of this interaction of zones. Proper treatment of the thermal and momentum boundary

layers can be critical for the realism of a CFD simulation. Since the flow within a stove is weakly turbulent, as addressed in section 5.5, these boundary layers are known to be fairly complex. There are a number of other methods for handling this but a comprehensive discussion of them is out of the scope. The treatment reported here is quite simple. Since this approach uses a large eddy simulation (LES) turbulence model (discussed in section 5.5), the first mesh element away from wall must fall within what is known as the viscous sublayer of the momentum boundary layer. This is a requirement for adequate solution of the differential equations relating the flow to the wall. The viscous sublayer is the first region away from the wall as seen in Figure 15, wherein the flow is laminar. The Y^+ value is a measure of the relative, dimensionless distance away from the wall in that normal direction, and U^+ is dimensionless velocity parallel to the wall (as a function of Y^+). The plotted line in Figure 15 bears the relation between the two. LES usually requires that the wall Y^+ value of the first element be less than 3.5 in all critical areas, and preferably be near 1.0. Wall Y^+ is around 1.0 in the sample simulations developed here, with some areas deviating not above approximately 1.5. The actual, corresponding thickness of the Y+ value depends on the Reynolds number of the flow. The generally fine resolution needed to attain a first element Y^+ value of ~1.0 is computationally affordable in a stove simulation since the Reynolds number is relatively low throughout (discussed in section 5.5). Other treatments of the boundary layer use a law-of-the-wall approximation not typically recommended for use with LES.

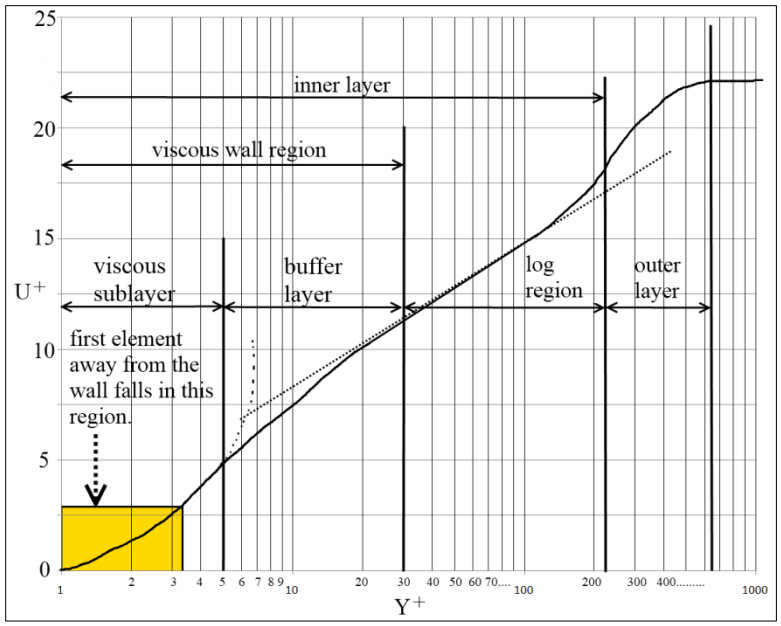

Figure 15: Diagram of the dimensionless momentum boundary layer

The procedure for achieving the Y^+ value requirement is simple. The boundary layer resolution is specified initially on a blind guess or by way of previous or other knowledge of the flow that will exist. The simulation is run and then the wall Y^+ values evaluated as contours on all critical surfaces within the ANSYS FLUENT software. If the value is seen to be too high then the first element thickness of the boundary layer must be reduced. If the value is lower than required the boundary layer resolution may be relaxed. Y^+ values are a function of the flow which of course is itself a function of the mesh. Hence, the process of tuning the boundary layer mesh resolution is iterative. Despite this, the boundary layers required in stoves can be setup in one or two rounds of iteration, and similar stoves tend to have similar requirements, further minimizing this process. It is found that the area with the most compressed (thinnest) flow boundary layer is in the stagnation region of the pot. In that area 0.2mm first-layer thickness is specified. Elsewhere 0.25-0.5mm first element thickness is acceptable. These settings achieve a wall Y^+ values near 1.0, throughout the domain. Other concerns affecting the boundary layer specification include the requirement of enough cells to accurately resolve the flow profile in constricted flow paths, such as the pot gap, which is the most compressed and critical such zone in the stove evaluated here.

Figure 16 depicts a cutaway view of the mesh in the area of the pot gap. The cut-cell Cartesian form is easily viewed here, as are the two, opposing boundary layers on the pot and drip pan (labeled).

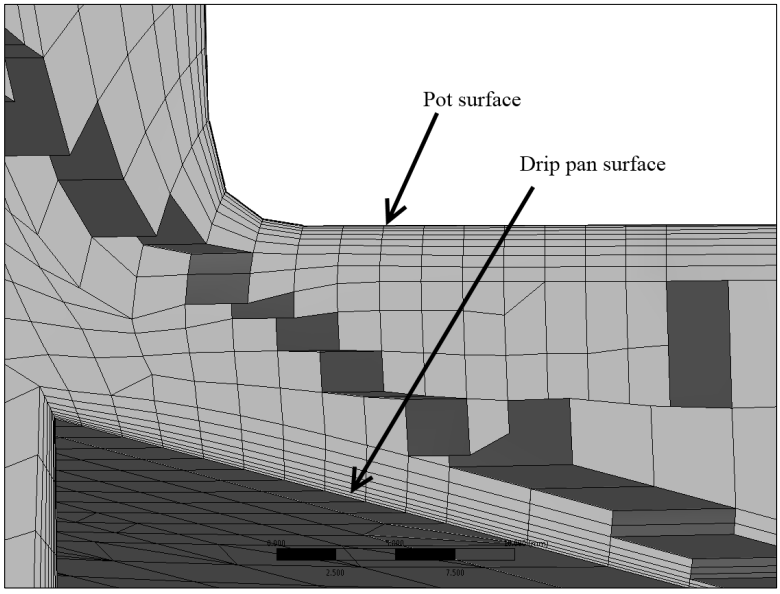

Figure 16: Cross-section view of the mesh in the pot gap region.

The final meshing scheme as seen in Figure 17 features boundary layers as mentioned above, starting off with first element thicknesses of between 0.2 and 0.5mm, extending to between 5 and 7 elements in thickness under default growth rates. The mesh beyond that rapidly expands to the finest base mesh (smallest "cubes") of ~3.5mm, then further expanding to ~7mm and then ~14mm, in the next and final sizes, respectively. Growth rates of 1.2-2.0 are used throughout. Further mesh details are provided in Appendix G.

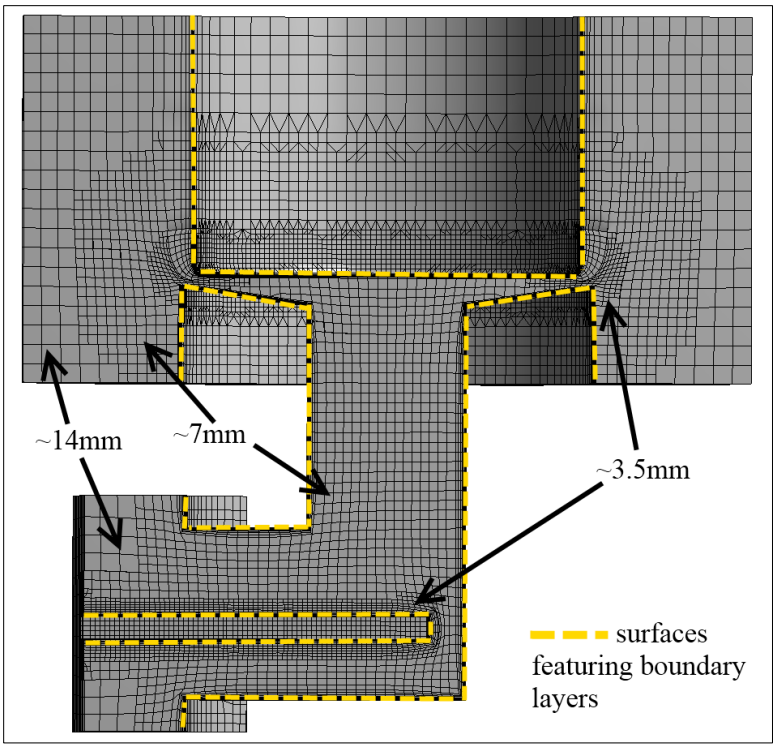

Figure 17: Cross-section view of final meshing scheme, showing element sizing

5.3 Solid fuel reaction model

As described in section 3.2, reactions of the initial (solid) fuel in a biomass stove are quite complex, and more importantly transient, and highly variant. As introduced in section 4.2, stove modelers have used various approaches in addressing fuel challenges, depending on the phenomena and scales of interest. Very detailed pyrolysis models exist [80], including some that are fully thermally and chemically transient, including fuel consumption. Most of these models treat the wood via integral equations as a one, two, or three dimensional domain with heat transfer, temperature rise, and conversion. Kinetic rates of reaction are applied, and boundary conditions are seen as quite critical to behavior. An inspection of these models gives the impression they are extremely complex. As explained in previous sections however, a meaningful steady-state fuel condition is desired so that the focus of the CFD simulation can be the fine scales of flow and heat release instead of the much longer time-scales of the fuel conversion.

The simplest approach is to specify general fuel boundary conditions based on published, experimental data from similar combustion applications. There is much literature on the gas composition measured from the total oxidation of various woods, chars, and crop wastes. These studies typically publish gas chemistry and reaction rate as a function of incident heat flux (in those cases usually by radiation), and often residence time and inlet gas conditions (e.g. nitrogen, air, or oxygen). In most cases this option is accurate enough, and the overall simulation speed will justifies its use. DiBlasi et al. [44], Miltner et al. [81], and Zanzi et al. [82] provide explicit net-pyrolysis gas compositions that are certainly realistic enough for a mixture-fraction combustion approximation. These experiments are often not completed under similar conditions as those of small biomass cook stoves – under so called fire-level incident heat flux. Furthermore, specifying the fuel composition without consideration of any fuel parameters offers no sensitivity to fuel composition, geometry, water content, etc, the effects of which may be significant. A more advanced approach is desired for situations that justify some particular sensitivity.

The work of Thunman et al. [83] reports a mixed analytical and empirical method to modeling the primary pyrolysis gas formed under fire-level heating of relatively large particles of wood fuel in either fixed or fluidized bed arrangements. Dried hardwood (birch) and softwood (spruce) samples of various sizes are pyrolyzed in an inert environment quartz-tube reactor under incident heating rates in the range of those seen in combustion (25-75kW•m^{-2}). The resulting pyrolysis gas is sampled and reported in time averaged (steady, fixed) mass ratios of the major gas components H_2, CO_2, CO, H_2O, CH_4, C_2H_4, C_2H_6, and the remaining solid char, which is not oxidized during the sampling. Thunman et al. then reports these ratios as a function of the wood type (birch hardwood or spruce softwood), and fuel particle specific area (surface area/volume), in tabular form. The author here transcribes and plots these tabular values to find polynomial fits for the ratios and relationships as functions of fuel specific area, such that the composition can be driven directly in a spreadsheet. Table 6 gives an example of these ratios, as calculated by the

method of Thunman, et al., for the high firepower case. These ratios are then systematically applied to the weighting of arbitrary masses of gas, starting with CO_2. The system is solved directly in spreadsheet form to give the primary gas composition seen in Table 7, where the fraction definition is given in the first column on the left, symbol in the second column, mass ratio value in the third column, and the aspect the ratio is a function of in the fourth column.

Table 6: Example gas composition ratios for the high firepower case, as defined by Thunman, et al.

Parameter (Y_a/Y_b)	Symbol, R_i	mass ratio (Y_a/Y_b)	Function of
Char/dry wood	R_1	2.18E-01	specific area
H_2/dry pyrolysis gas	R_2	6.00E-03	explicit
THC/CO_2	R_3	1.24E+00	specific area
(CH_4+C_2H_4)/CO_2	R_4	1.05E+00	nominal of fixed range
CH_4/C_2H_4	R_5	2.50E+00	nominal of fixed range
CO/CO_2	R_6	2.33E+00	specific area
H_2O/CO_2	R_7	9.88E-01	specific area

Table 7: Primary dry pyrolysis gas resulting from calculated ratios

	$Y_{PDG,i}$	$X_{PDG,i}$	$m\_dot_{PDG,i}$ ($g*s^{-1}$)
H_2*	0.006	0.070	1.057E-03
H_2O	0.176	0.231	3.107E-02
CH_4	0.135	0.198	2.374E-02
C_2H_4	0.054	0.045	9.495E-03
C_6H_6	0.033	0.010	5.808E-03
CO	0.416	0.350	7.331E-02
CO_2	0.180	0.096	3.165E-02
SUM:	**1.000**	**1.000**	**1.761E-01**

The inputs are limited to only the wood type and the specific area of the pyrolizing section of the wood (i.e. only the tip of a long piece of wood inserted a small distance into a fire). All testing conducted at the CSU Clean Cook Stove Laboratory makes use of uniformly cut sticks

of wood approximately 5/8” x 5/8” x 12” (16mm x 16mm x 305mm), with the longest dimension is in direction of grain. Of course the wood is consumed during combustion and hence this size reduces to zero, but the CFD simulation requires some geometry as the boundary condition and the fuel model requires a specific area. For this purpose, fuel is assumed to be of an extruded square cross-section having 13mm short sides (fixed), and of a length that varies with the relative firepower. The idea is that this represents an intermediate point of the wood geometry as it is being consumed. Aspects of the fuel geometry assumption can be seen in Table 8, including the number of wood fuel sticks activated, the length of the advecting zone, and the resulting fuel specific area. The dry wood mass consumption rate, and idealized heating firepower (LHV basis) are given for reference as well. A sensitivity analysis on this was not conducted directly, however the author’s experience suggests that the chosen geometry and position of the fuel may have significant effects on the simulation, as does the position and geometry of wood in an actual stove.

Table 8: Fuel geometry assumptions

	Mean dry wood mass burn rate ($g*s^{-1}$)	Idealized firepower, LHV basis (W)	Number of fuel sticks (n)	Length of advecting zone (m)	Fuel specific area (m^{-1})
High power (hot start):	2.253E-01	4.089E+03	3	0.09	319
Low power (simmer):	9.888E-02	1.795E+03	3	0.069	322

Thunman et al. do not consider the evaporation of the internal water or go on to model the reaction of the char. The author of this thesis adds the vaporized wood moisture to the water product in the primary pyrolysis. The average, typical moisture content found in wood at the CSU Clean Cook Stove Laboratory is around 7% on a dry mass basis, and is assumed here. The net reaction of external gaseous O_2 with the solid carbon of the char to form CO gas is then considered, with the necessary oxygen stream assumed to come from outside the control volume. This process can be viewed schematically as a steady-state process represented by the diagram seen in Figure 18. The spreadsheet used to calculate this composition is added as appendix B.

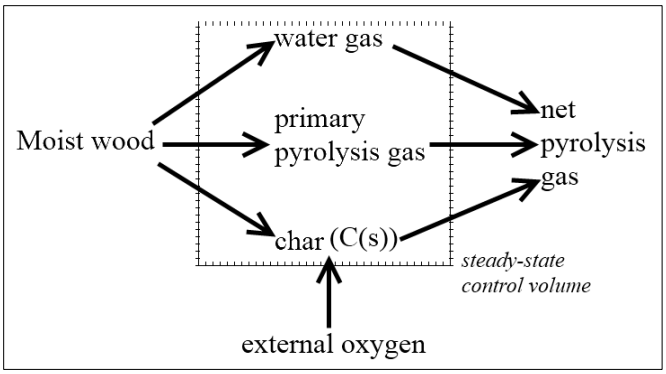

Figure 18: Lumped single-step reaction process assumed in fuel model

The lumped reaction products produced from this steady-state control volume concept is the composition specified in the CFD simulation. An example of this composition for the high firepower case is given in Table 9. The outlet mass flow rate is known through the conservation of mass of the system, as equal to the incoming mass flow rates of wet wood plus the oxygen required to convert the char to CO. The temperature of the gas is a function of the heating balance within the wood. This again, is quite complicated, but a range of 575-900K is typically used [84], [83], [85], and a value of 800K assumed in this work.

Table 9: Resulting net gas calculated through the consideration of a steady-state control volume

Net control volume gas (lumped reaction product)			
	$Y_{NCVG,i}$	$X_{NCVG,i}$	$m\_dot_{NCVG,i}$ ($g*s^{-1}$)
H_2*	0.003	0.042	1.057E-03
H_2O	0.153	0.209	4.684E-02
CH_4	0.077	0.119	2.374E-02
C_2H_4	0.031	0.027	9.495E-03
C_6H_6	0.019	0.006	5.808E-03
CO	0.613	0.539	1.880E-01
CO_2	0.103	0.058	3.165E-02
SUM:	**1.000**	**1.000**	**3.06571E-01**

The final specification required for the fuel model is the *rich flammability limit* or *upper flammability limit* (UFL) of the mixture, calculated using Le Chatlier's principle as it is applied to a gas mixture [86]. In the high firepower case, a UFL is calculated as 0.452 mol fraction fuel (in the fuel-air mixture). This is an important parameter for achieving realistic zonal heat release with

the mixture fraction combustion approximation. Since mixture fraction requires the assumption of infinite reaction rate and thus does not consider chemical kinetics or stoichiometry, the gas would begin to convert from reactants to products even at unrealistically-rich mixtures. The equilibrium chemistry assumption offers meaningful realism on the lean end of the stoichiometric range but not on the rich end. Reactions are prevented at stoichiometry richer than the UFL through its specification in the ANSYS FLUENT mixture fraction formulation.

$$(UFL)_{dilution} = \left[\frac{X_F}{(UFL)_F} + \frac{X_I}{(UFL)_I}\right]^{-1} = \frac{(UFL)_F}{X_F} \tag{5.1}$$

where

X_I is the mol fraction of the inert species

X_F is the mol fraction of the fuel species

UFL_I is the upper flammability limit for each inert species -> ∞.

UFL_F is the upper flammability limit for each fuel species.

As mentioned, the open-loop, non-feedback approach of a directly specified fuel condition is frequently quite useful enough to use for development purposes. The more complex lumped fuel model may be more appropriate when attempting to resolve phenomena that are particularly affected by chemistry, such as soot formation. It is thus likely that a designer could conduct rapid, initial design improvement iterations with the simpler fuel model, and switch to the complex model for additional refinement. Thunman et al. observes that the gaseous composition and char fraction are more strongly correlated with the wood geometry, than the incident heat rate itself (within typical fire-level conditions). This justifies the use of the open-loop process where only fuel geometry is needed to define the pyrolysis gas composition.

Some feedback may be observed though. Energy and species sinks may be applied at the surface to account for consumption of oxygen through heterogeneous surface reaction and the

endothermic heat of pyrolysis. Rigorous calculation of this is complex [42], and deemed outside the scope of this thesis. Following CFD simulations, heat flux back to the fuel boundary may be evaluated and compared with the expected values. Spearpoint and Quentiere [85] directly measure the fire-level heat of pyrolysis as $1.6 kW \bullet g^{-1}$ on end-grain surfaces and $2.9 kW \bullet g^{-1}$ on cross-grain surfaces. Heating feedback to the fuel boundary in the CFD simulation can then be compared to these simple mass-basis energy requirements, as discussed in the conclusion section of this thesis.

The gas mass flow rate (the same as the moist wood consumption rate), the net pyrolysis gas composition, the pyrolysis gas temperature, and the upper flammability limit calculated in the above procedure are the parameters specified in the CFD simulation as a mass-flow inlet at the fuel surface boundary.

5.4 Mixture fraction formulation for gas-phase combustion

The non-premixed homogeneous phase gas reaction is approximated by employment of the mixture fraction formulation, which has seen broad use in modeling non-premixed laminar and turbulent combustion alike [61], [87-90]. The mixture fraction formulation is derived from the coupling function formulation, and as such requires that all gases share a single diffusion coefficient, and that a universal Lewis number be unity [86]. This drastically simplifies the approximation such that the rate of progress of reaction from reactants to products can be tracked with a single, conserved scalar value known as the *mixture fraction, f,* as defined in equations 5.2, and 5.3 [73].

$$f \equiv \frac{\text{mass of material having an origin in the fuel stream}}{\text{total mass of mixture}} \tag{5.2}$$

$$f = \frac{Z_i - Z_{i,ox}}{Z_{i,fuel} - Z_{i-ox}} \tag{5.3}$$

where

Z_i is the mass fraction for element i

ox refers to the element mass fraction in the initial oxidizer stream

$fuel$ refers to the element mass fraction in the initial fuel stream

The mixture fraction value for a pure fuel stream is unity and for an oxidizer zero. In between those two boundary conditions however, is a *mixture*, at a particular state of progress towards product. The assumption applied to the mixture fraction formulation is that the reaction is mixing controlled, and that fuel and oxidizer coming together instantly react at an infinite speed. Thus, at any given location, the fuel and oxidizer mass fractions must equal unity, as given in equation 5.4. This makes for a very attractive combustion approximation because all the complexity of the reaction is removed and represented in the context and *space* of the mixture fraction conserved scalar domain instead of through a rigorous energy balance.

$$f_{fuel} + f_{ox} = 1 \tag{5.4}$$

Since the mixture fraction is a *conserved* scalar it must abide by the conservation law. A version of the mixture fraction conservation equation is given in equation 5.5. The mixture fraction is related by way of a mean mixture fraction here. A *mixture fraction variance* term is essentially the difference between the instantaneous mixture fraction and the mean mixture fraction. In the case of the involvement of an LES turbulence model, the mixture fraction variance term is directly calculated as a function of the gradient given in equation 5.6.

$$\frac{\partial \rho \bar{f}}{\partial t} + \nabla \cdot (\rho \vec{v} \bar{f}) = \nabla \cdot \left(\frac{\mu_t}{\sigma_t} \nabla \bar{f} \right) \tag{5.5}$$

where

ρ is fluid density

$\bar{f}$ is the mean mixture fraction

$\vec{v}$ is the flow vector

μ_t is the turbulent viscosity

σ_t is a turbulent diffusion constant, similar to Sc

$$\overline{f'^2} = C_{var} L_s^2 \nabla \bar{f}^2 \tag{5.6}$$

where

C_{var} is a constant

L_s is the local subgrid length scale, associated with the mesh dimension

When used in conjunction with an LES turbulence model, the mixture fraction variance term is able to allow fine resolution turbulence-chemistry interaction through the involvement of a probability density function, introduced in the next section. Furthermore, due to the high-fidelity associated with a flow field served by an LES turbulence model, the reaction zone approximation is known to be quite accurate [91], even with very low Reynolds number flows, where the lack of fully represented diffusion would naturally seem to be a problem. In the case of the simulations reported here, the mixture fraction variance boundary condition at the idealized pyrolysis surface was left at a value of zero.

There are some major assumptions applied in the model choices here which affect how the system functions. Equilibrium chemistry is utilized, meaning that individual species mass-fractions are solved as they would be in their equilibrium state using local thermophysical conditions and an equilibrium chemistry database. That solution is however mitigated by the inclusion of an *upper flammability limit* (UFL) as mentioned in the previous section. The inclusion of the UFL in a simulation means the gas will not react toward equilibrium state, even in the presence of some oxidizer, if it is at a higher local mass fraction than that implied by the UFL. It is known that this is a crucial selection for a relatively slow, low-energy fire such as the type common in the modeled stove, if a realistic heat release zone (i.e. flame zone) is to be simulated. The presence or not of the UFL specification does make for a visible, and measurable effect on behavior and results. Fortunately, the upper flammability limit is easy to calculate and its inclusion in the CFD simulation adds no significant computational cost.

The other major specification for the use of the mixture fraction combustion model is the selection of non-adiabatic considerations. This simply means that the thermophysical values used to lookup the equilibrium conditions of mass fractions consider the transfer of heat by way of convection and radiation. The effect of this is a sometimes significant shift in those equilibrium conditions.

5.5 Turbulence model

Some classical approaches such as the assessment of Reynolds number and consideration of turbulent entry length can be used to consider where the flow may transition to turbulent, but often such approaches are themselves too simple for such complex geometries and phenomena. A calculation of the Reynolds number and a correlation for the turbulent entry length for an idealized 0.1m diameter combustion chamber is calculated to be 2480 and 0.44m, respectively [92]. This simplification does not take into account the flow obstruction of the fuel bed, the right-

angle flow turn, the stagnation condition at the pot, or more importantly the fire heat release, and thus all the more shows the propensity of the flow to transition to turbulent. Turbulent transport is important for calculation of the location of the flame front and unsteady combustion.

Since the Reynolds number is relatively low it is practical to use a high-fidelity turbulence model, with the first element of the mesh contained in the viscous sub-layer. This is the case because the viscous sub-layer is relatively thick, and the first element is not impractically thin. The boundary layer and meshing scheme discussed in section 5.2 explains this resolution issue in detail. Furthermore, the mixture-fraction combustion formulation is itself a relatively simple model that does not require significant computational resources. Fidelity is achieved through attaining high temporal and spatial resolution, on the utility of resolving the energy transfer allowed by the non-adiabatic formulation, as explained in section 5.4. It is thus an appropriate match to utilize a high-fidelity turbulence model. More importantly, LES allows the close interaction between the resolved turbulent scales and the probability density function, for additional combustion modeling fidelity.

In short, the LES turbulence model and a mixture fraction formulation work very well together, and should be used if the high spatial resolution required for the LES can be afforded. If computationally affordable, LES is more suitable due to the lack of the inherent limitations of the averaging that occurs in Reynolds Averaged Navier-Stokes models. Original work relied on the Smagorinsky-Lilly subgrid model. Later efforts employed the WALE model due to the reported benefit of a no-slip condition possibility unavailable in the former. Significant differences were not found for these low-Reynolds flows. Similar to the condition of the mixture fraction variance, no boundary condition turbulence perturbations were set. Associated pressure inlet values were set equal to zero.

5.6 Radiation model

The Discrete Ordinates (DO) radiation model is used based on the assumption that most of the region inside the stove is thermally thin, with the flame and any soot adding thickness. The P-1 and Rosseland radiation models are rejected due to their treatment of radiation as a pseudo-diffusion, more fitting for optically thick regions. On the contrary, the discrete ordinates model is capable of handling a potentially large range of optical thickness, can model a gray-gas approximation, and has the ability to interface with the two-step soot model.

5.7 Soot model

The Moss-Brookes [93], two step soot model was used to simulate particulate matter formation. This model was selected due to its success predicting soot formation in turbulent and laminar methane flames [94].This model works on the theory of particle nucleation off of gaseous precursor series, and as such ties in well with the turbulence-enhanced progress variable methodology of the PDF mixture fraction model. This is important since experiments have established that the formation of soot is driven by small-scale flow strain rates, which can be taken into some account by the PDF relation, in conjunction with the LES turbulence model [55]. Benzene and ethylene are specified as precursors, and Fenimore-Jones soot oxidation model used.

5.8 Computation

Experience modeling several typical stoves in the proposed manner suggests to the author that statistically meaningful results can be found in post-stabilization run durations in the range of five to ten seconds, using some special tactics. Using a commonly available, commercial-level workstation computer, these simulations require on the order of one to several days of calculation time. Additional time is then required to post-process and interpret results. A procedure has been

developed to accelerate the initialization and processing of the model. A new simulation run requires the following phases:

1. Initialization: The model is initialized and the normal pressure inlet boundary condition is replaced with a mass-flow inlet condition, set for a mass flow rate typically found in standard operation. The goal of this switch is to establish upwards flow, avoiding the costly alternative of a "flashover" initiation, with flames leaping out of the inlet (and taking up to 5 seconds to get pulled into the chamber). Approximately one second of initialization time is required to establish flow. If an appropriate interpolation file exists, it can be used to help accelerate the initialization phase.
2. Flow normalization: The inlet boundary condition is returned to the standard pressure inlet. If the initialization mass flow value was well-specified, the normalization period takes less than a few seconds of runtime.
3. Statistical runtime: After mass or volume flow rate monitors stabilize, statistics can be recorded. Monitors are initialized and unsteady statistics activated. This is the part of the simulation from which meaningful data is acquired. The statistical runtime varies depending on the stove and fire, but is typically in the range of three to ten seconds.

Figure 19 depicts the evolution of gas temperature from startup (@t=0s), for one of the thermocouple locations in the high-firepower CFD simulation, and can be used to make points about the three phases introduced above. This particular run was started off an *interpolation* file, which defines all initial scalars as those exported from a previous run at fully-established conditions. In this case the initialization phase is just the start itself, with the run heading directly into the normalization phase. Even so, instability exists for the first few seconds. The black line is the running average from that start, showing how in this case, 5 seconds of runtime is enough to

begin to get to an approximate, asymptotic, steady time-average. Statistical runtime can begin by the end of this sample. Every location in the combustion chamber will have a different settling time.

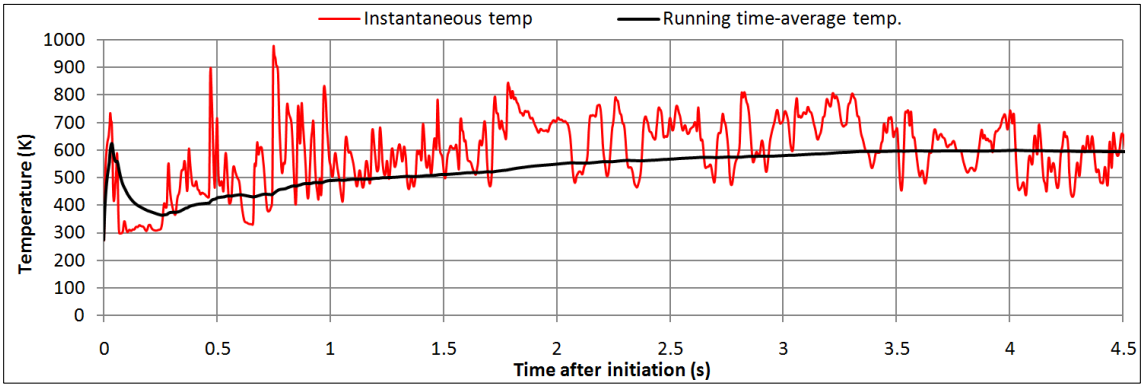

Figure 19: Evolution of instantaneous and running average temperature at a thermocouple location in the CFD simulation.

5.8.1 Computer hardware

Multiple operating systems, computer types, and individual computers are used in these studies. Initial experiments were conducted in parallel mode on individual CSU Engineering computer laboratory PC computers. In an effort to gain more speed LINUX-based compute-servers were used but connection and stability problems ended their use. Finally, two fast desktop workstations, a Hewlitt-Packard Z-600 and a Z-400 were made available, and were used for the majority of the project work. These machines operated on Microsoft Windows 7 x64 operating system and feature dual quad-core Intel processors (2.79GHz), and 16GB of RAM. This final arrangement was found to be superior due to the ease of local access and control, as well as stability.

Simulations are always run on parallel processors, with up to 16 parallel threads per machine used. It was found that there was no significant advantage to running 16 threads via processor hyper-threading vs. conventional processor access (8 processors), on up to all 8 processors. Furthermore, additional stability with very minor reductions in speed are found when

multitasking on these machines, if reducing the parallel thread count to 6 threads (leaving 2 processors for other use). The author finds the greatest utility in good speed, minimal license usage, computer stability, and ability to multitask in the employment of no more than 6 parallel threads.

5.8.2 Sensitivity studies of combustion simulations

Very complex models yield results equivalently complex in relation to many model parameters – hence the simulation itself now requires experimental perturbation to find these relations. It is well documented why these sensitivity studies must be conducted. Depending on the model, significant error can be included in a system that has not been desensitized. Since there are many phenomena that need to be modeled, and many of these models require desensitization, a modeler can very quickly create a simulation that becomes a significant experiment in itself. The sensitivity studies required to do this can quickly amount to so much work they detract from the entire goal of finding a tool to gain insight into the stove and increase the rate of learning.

CFD simulation mesh sensitivity studies have been conducted for a range of parameters important for modeling stoves in general and the final validation simulations specifically. The procedure of conducting such sensitivity studies is classic in the art of CFD simulation. The early painstaking and troublesome practice of conducting these simulations also gave the author the skills and knowledge necessary to conduct the final validation simulations. The sensitivity cases bear critical resemblance to the final validation despite obvious differences.

Mesh resolution is the meta-sensitivity for CFD, since all aspects are inherently affected by the spatial discretization of the physical domain. Early in the process of forming this thesis a mesh sensitivity was performed involving twenty-five independent, full scale models. A table containing parameters of this study can be found in appendix C. While the geometry and case were slightly different than the final cases reported here, they were valuable for providing

lessons. Note that the pieces of data recorded were not consistent as it was taken at a time when the author was learning what items to evaluate.

Model grid or mesh sizing requirements (spatial resolution) are defined by the scales of flow that are intended to be resolved. While there are empirical guidelines, these scales are frequently found by desensitization. Practically, the mesh resolution is defined by the practical limits of the computer system. The process of learning these limits can be quite time-consuming. In such an unsteady simulation, the maximum time step by which the unsteady CFD model can proceed is limited by the requirements of mathematical stability, which is itself a function of the mesh resolution. Since the full model comprised of mesh-discretized governing equations must be solved at each time step, and the maximum time step is a function of the mesh size, an increase in mesh resolution can increase the computational load resources by orders of magnitude. Stoves have small geometry relative to other features. For example, small biomass stoves have gaps between pot and stove top edge as small as 8mm, compared to a vertical combustion chamber diameter of approximately 100mm. This suggests that small flow structures may develop in the tight critical areas and require resolution as they flow into other areas.

The effects of the mesh density on a complex and unsteady model do not show themselves in ways that are easy to study. In general it was found that there was no critical mesh density, per se. The mixture fraction formulation for combustion does not require resolution of the flame sheet (~1mm) as a simulation featuring a chemical kinetic homogeneous combustion model would. The mixture fraction model will always show reaction, albeit unrealistically, despite coarse resolution. Therefore, it is merely a question of optimizing the choice of mesh – finer will give greater resolution of zonal heat release while coarser will yield a faster running model. The author settled on a 6-7mm mesh in the main chamber, finer meshes adequate to give ~20 elements across the narrowest area of the pot gap region, and boundary layer first element thicknesses between 0.2-0.5mm as explained in section 5.2. Another way to explain this is that

while the boundary layer first element size (mesh resolution in boundary layer) *does* have a certain target, the mesh density of the rest of the domain does not.

The boundary layer resolution was evaluated in the sensitivity study. As seen in appendix C, consecutive simulation runs gave wall Y^+ closer to the accepted target of ~1, and by simulation run "sensitivity 17", mean values had fallen below it. Heat transfer to the pot (also seen in appendix C for some of the simulation cases) is seen to continue to climb with wall Y^+ values until a leveling-off is perceived after run "sensitivity 17". This is due to the boundary layer being adequately resolved.

The time step was also evaluated. Time steps of 0.005s, as used in most of these initial sensitivity study simulations were found to be far too high, contributing to cell Courant numbers in the range of 4-7. As indicated earlier in this section, cell Courant numbers at or below unity give better convergence for a large eddy simulation turbulence model as used here.

6. Experimental apparatus and process

This thesis has already presented the logic that a CFD simulation yielding flow field and temperature field results is useful information to the stove designer but is not available through traditional bulk performance testing. It goes on to explain that a mixture-fraction combustion approximation was chosen for the purpose of CFD modeling due to the fact that it provides a good approximation of these two aspects, with reasonable accuracy and at acceptable computational cost. Being that flow path behavior and temperature field results are the aspects of interest an attempt is made to validate them experimentally, as explained in previous sections. The temperature field is evaluated directly through employment of fine wire thermocouples and high speed data acquisition. The flow field itself is not explicitly evaluated in this work but can be considered implicitly.

Many authors have conducted tedious studies of momentum, temperature and species formation as a function of time in unsteady reacting flows. As described in section 3.4, an unsteady flow will have features spanning from large eddies down to the miniscule Kolmogorov scales. Buoyant flows, especially reacting ones, will develop large flow fluctuations at the "puffing frequency". This frequency trends inversely with the characteristic dimensions of the fire [52]. Faster fluctuations happen on the order of the frequency by which smaller flame structures move back and forth across a location. It is not clear what time-scales of fluctuations are of interest in cook stoves evaluation and design. The validation approach outlined in this thesis attempts to enable inspection of a wide range, resolving fluctuations up to a maximum frequency of approximately 10 Hz.

Data acquired on fine temporal and spatial scales can always be integrated and summed to get bulk behavior, but going the other way is usually impossible. Bulk behavior can of course not be ignored in exchange with focusing on fine scales. The ultimate purpose of a stove is in fact the harnessing of useable bulk heat, a measure that is traditionally considered in bulk on a fairly coarse time scale, and as a single spatial point. The opportunity to study fine scales within the stove motivates the author to study the transfer of useable heat in finer scales as well. This motivation leads to the development of an instrumented, heat-exchanger cooking pot that offers benefits over the traditional calculation of heat flow through measurement of the temperature rise of a full pot of water. Such measurement also allows more interesting validation of the CFD simulation. Bulk measurement of standard gaseous combustion products is also conducted for the purpose of emissions evaluation and also the calculation of instantaneous firepower.

Experimental equipment has been designed and built in order to validate the temperature field and cooking pot heat transfer results of the CFD simulations. This equipment includes:

- A rocket-elbow type wood burning stove featuring nine modular, metal combustion chamber sections, each instrumented with a row of seven fine-gauge thermocouples, creating a planar array of 63 fine-gauge thermocouples in total.
- An instrumented heat-exchanger cooking pot featuring the outside geometry of the standard cooking pot but possessing significantly lower thermal mass and the means to measure heat transfer through advection in a constant stream of water.

6.1 Thermocouple-instrumented validation wood cook stove

6.1.1 Stove and thermocouple array geometry

The thermocouple-instrumented validation stove has geometry typical to small, rocket elbow type wood-burning stoves in the <10 kW maximum firepower range. The stove features internal geometry intended to be the same as that of the G3300 cook stove manufactured by

Envirofit International, Ltd., which can be seen in Figure 20. This geometry was selected so that experimental results from the validation stove could be compared to both the CFD simulation (of the exact same geometry) and also to the significant performance data that has been compiled for the G3300 stove through testing conducted at the Colorado State University (CSU) Clean Cook Stove Laboratory (CCSL).

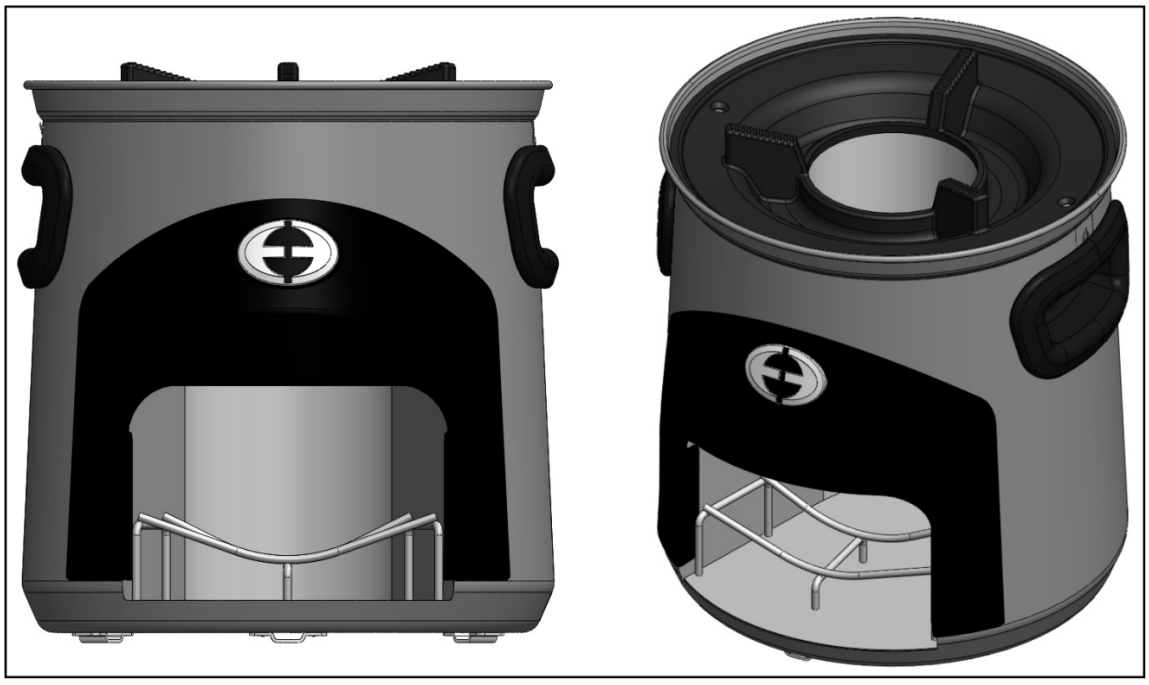

Figure 20: G3300 stove

The validation stove features internal geometry exactly the same as that modeled in the CFD simulation and within several millimeters tolerance of that of the G3300, including the known critical parameters of the inlet shape, the ~100mm diameter of the cylindrical portion of the combustion chamber, and a ~8mm minimum pot gap. Important differences include that the orifice has been neglected, there is a lack of a clay fire tile, chamber walls are of 304 stainless steel vs. FeCrAl, and that the drip pan is a plain cone as opposed to the elaborate cast part on the G3300. The G3300 stove is shown in cross-sectional view, with part labels, in Figure 21.

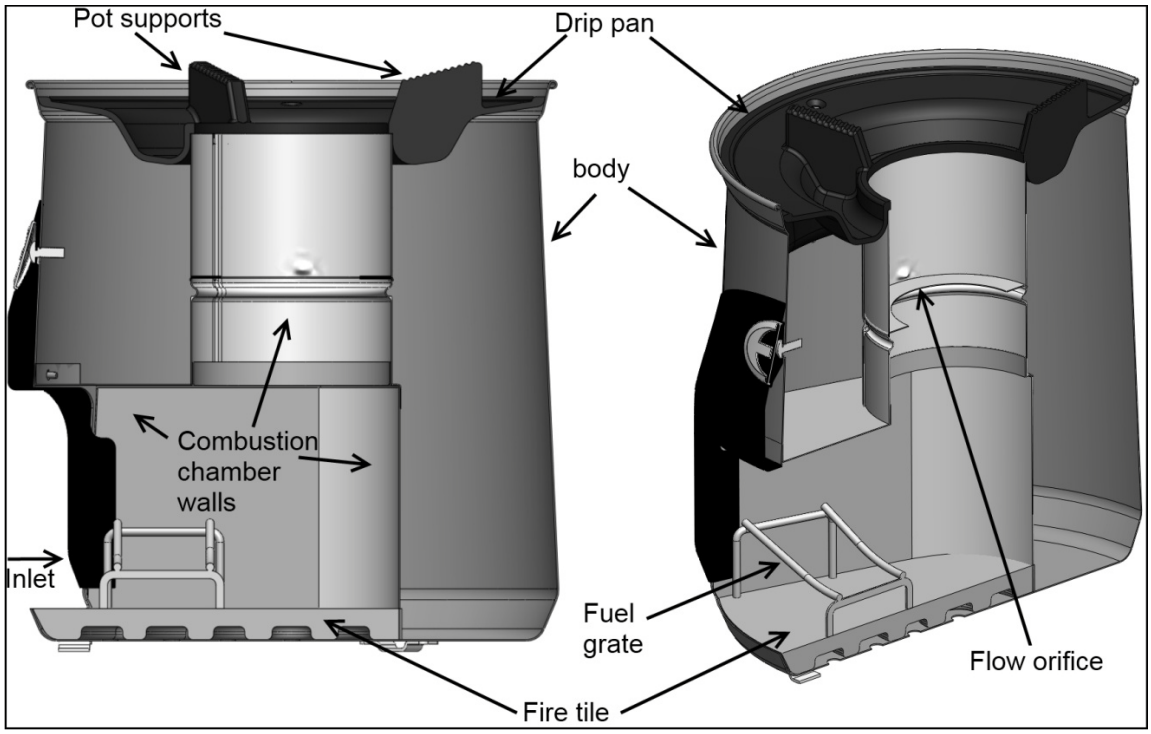

Figure 21: Detail cross-section view of G3300

The validation stove can be seen in Figure 22, and Figure 23 (fuel grate not included in image). Dimensions of the flow path are the same as those of the CFD simulation geometry model. The validation stove features a rotating upper section that allows for multiple planes of temperature to be resolved. The thermal mass of the validation stove was kept to a minimum through the use of 0.56 mm thick 304 stainless steel as the combustion chamber wall material. Insulation is composed of Unifrax Fiberfrax alumina-silicate refractory ceramic fiber, approximately 30mm thick. Table 10 includes the critical dimensions of the validation stove compared to the Envirofit G3300.

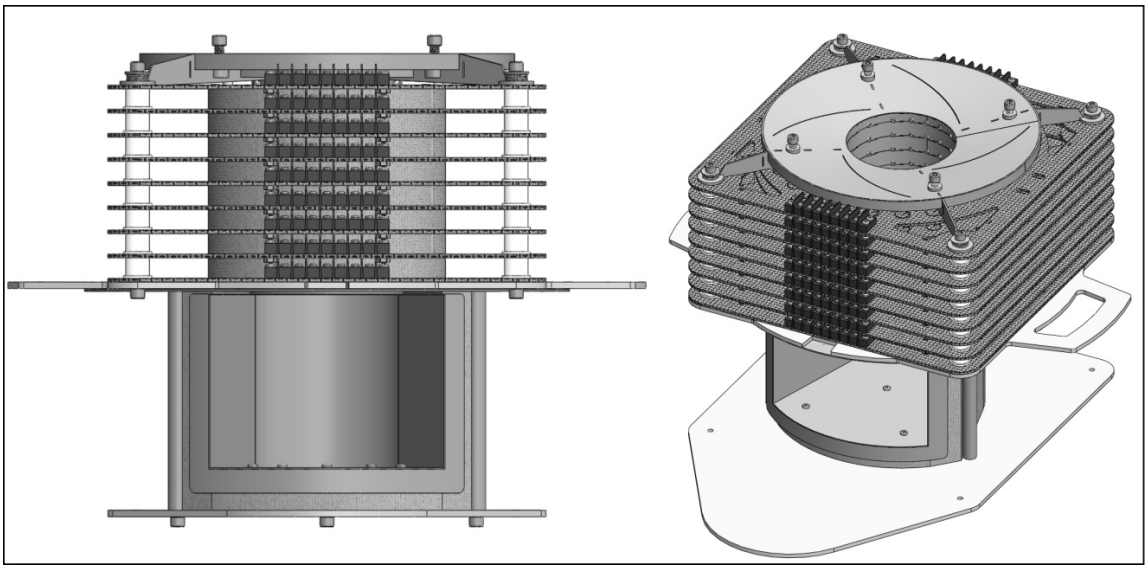

Figure 22: Instrumented experimental validation stove

Table 10: Critical dimensions of the Envirofit G3300 production stove vs. the experimental validation stove

	Envirofit G3300	Validation stove
Inner diameter of cylindrical combustion chamber:	slight variation, 100mm nom.	100mm
Combustion chamber material, thickness:	FeCrAl, 0.5mm	304 stainless, 0.56mm
Orifice inner diameter:	70mm	*none included*
Drip pan material, thickness:	cast iron, 3mm	304 stainless, 0.56mm
Pot gap planar distance:	8mm	adjustable, (8mm nom.)
Inlet height:	105.5mm	108mm
Fire tile material, thickness:	Clay fire tile, 15mm	*none included*
Fuel grate construction:	Steel wire	Steel sire
Fuel grate height above chamber bottom:	38mm	38mm
Insulation material in the radial direction:	AlSi (generic)	Unifrax Fiberfrax AlSi
Insulation thickness in radial direction:	varying, ~75mm nom.	~30mm
Insulation on bottom of chamber:	none except fire tile	25mm, Unifrax Fiberfrax

The lower portion of the validation stove is fixed in place, serving as a base for the upper, instrumented sections. The construction scheme is referred to as “plate and post” type, whereby

threaded standoffs offer ease of length/height change, and in this case easy slip-on assembly of the upper, instrumented levels of the stove. The combustion chamber is mounted to a base plate by way of 1" long ceramic standoffs to minimize conduction heat loss into the plate. The use of air gaps and thin insulation layers reduce heat loss out of the top of the lower combustion chamber into the layers above.

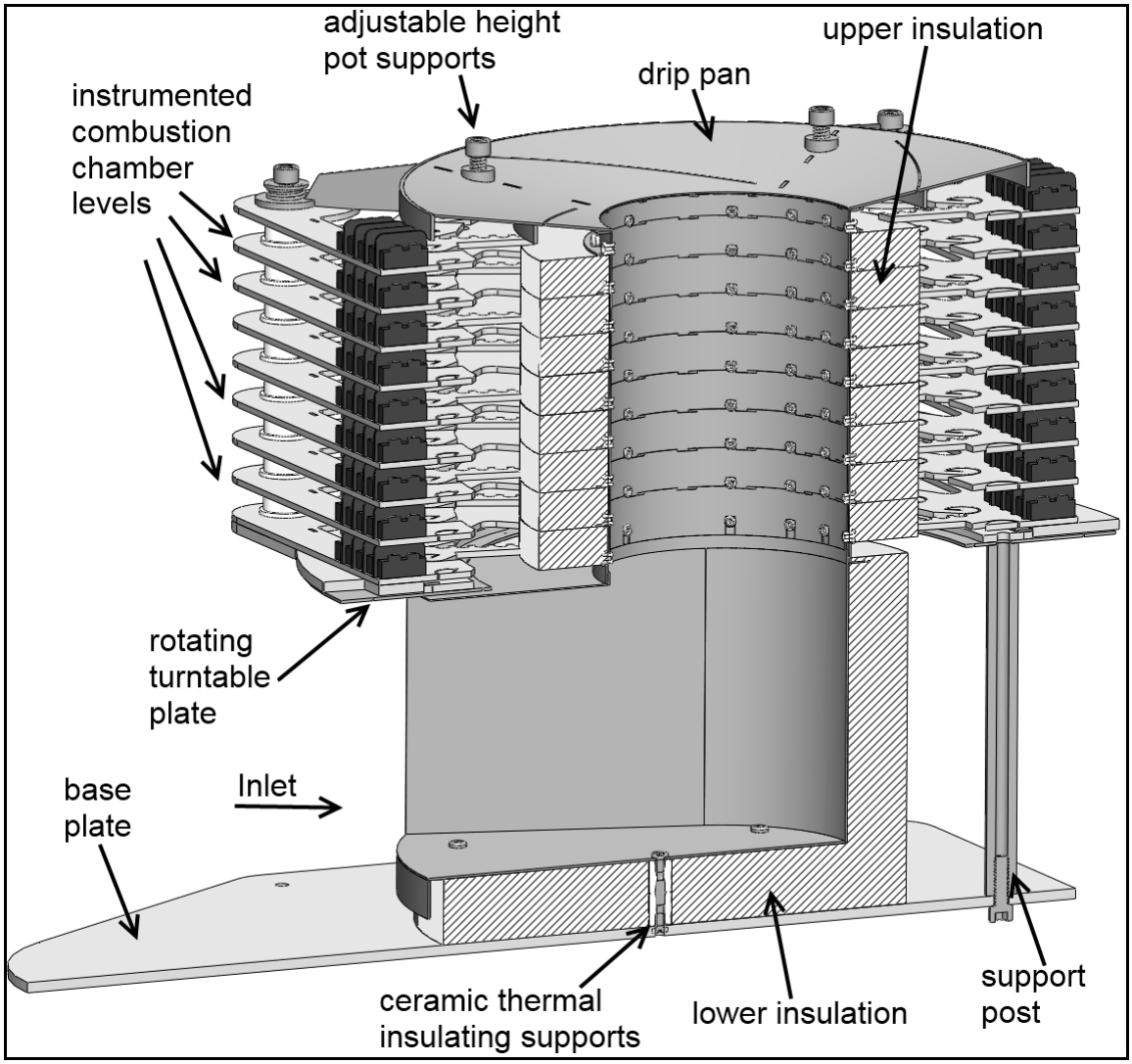

Figure 23: Detail cross-section view of validation stove

A rotating turntable plate support exists between the lower and upper levels of the stove, allowing for the orientation of the instrumented layers, and thereby the temperature-sensing plane, to be rotated to any orientation desired for temperature sampling of the flow. The upper

portion of the stove consists of nine instrumented combustion chamber sections stacked on top of the lower combustion chamber. Castellation of the bottom and top of each combustion chamber section prove radial and angular location, ensuring the combustion chamber sections stay connected and aligned. The top and bottom of these sections are different from the rest, with the top section being shorter to make the height match the G3300 and to interface to the drip pan, and the lower having a longer protrusion in order to connect with the lower combustion chamber, while allowing rotation.

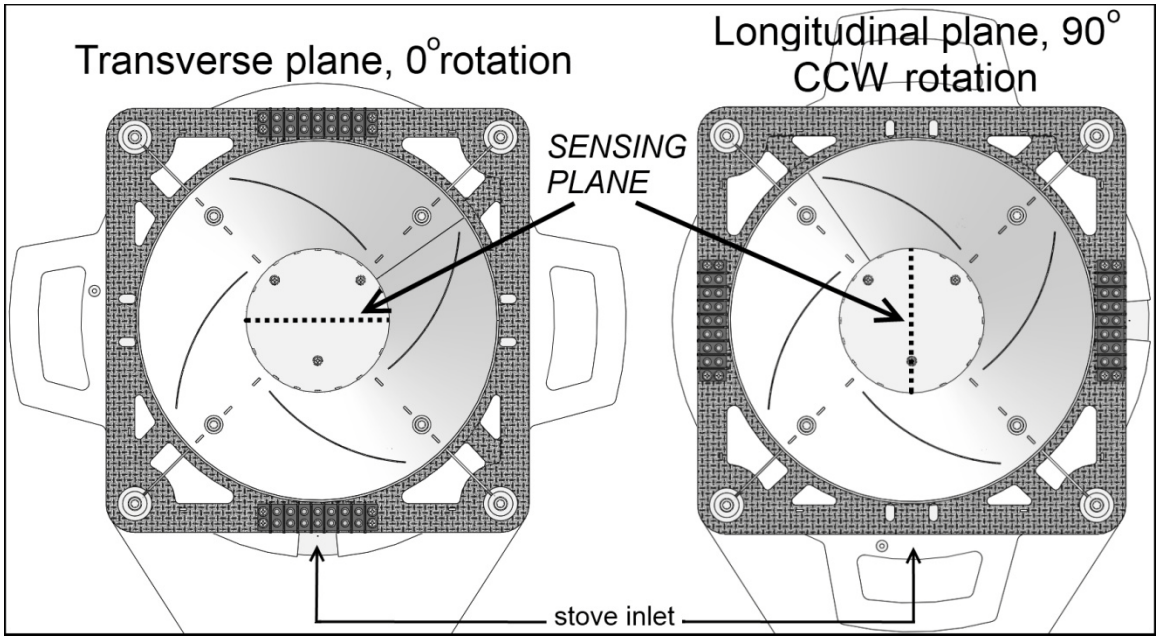

Figure 24: Instrument layer stacking within the validation stove

The method of stacking the instrumented layers in a "plate and post" arrangement allows for sections to be removed to shorten the height of the stove, or added to increase the height quickly, without requiring any significant manipulation. This allows for the height of the stove to be altered, the position of an orifice (should one be tested), to be relocated, etc, without significant alteration.

Each instrumented layer is essentially a self-supported section 15.1mm in axial thickness. A fiberglass deck constitutes a frame to which the other parts are mounted. The combustion

chamber section itself features a planar mounting ring with three arms having a shape designed to minimize conduction heat loss. These arms attach with screws to ceramic standoffs which are themselves attached to the fiberglass deck with screws. The fiberglass deck has spiral-shaped track features cut into it which the thermocouple wires thread through, providing proper separation. Plastic wire terminal blocks are also attached to the fiberglass deck with screws. The weight of the pot is transferred through the stack of combustion chamber sections down onto the lower combustion chamber, and also through the stack-up of fiberglass decks and nylon spacer at each of the four support posts down onto the base plate.

The sensing junctions for the seven thermocouples on each level fall on a single radial line and are separated from each other by 15mm, thus forming *sensing axes*. The axes from each instrumented level are thus parallel and aligned in a vertical plane, with each sensing axis separated from the neighboring one by 15.1mm. Together, the 7 x 9 qty array made of sensing junctions on a ~15mm x 15mm grid form a *sensing plane*. Sensing junctions also can be considered to form seven vertical axes. The sensing plane moves with any rotation of the top portion of the stove. The user can thus rotate this upper portion of the stove in order to acquire temperatures from any plane they choose.

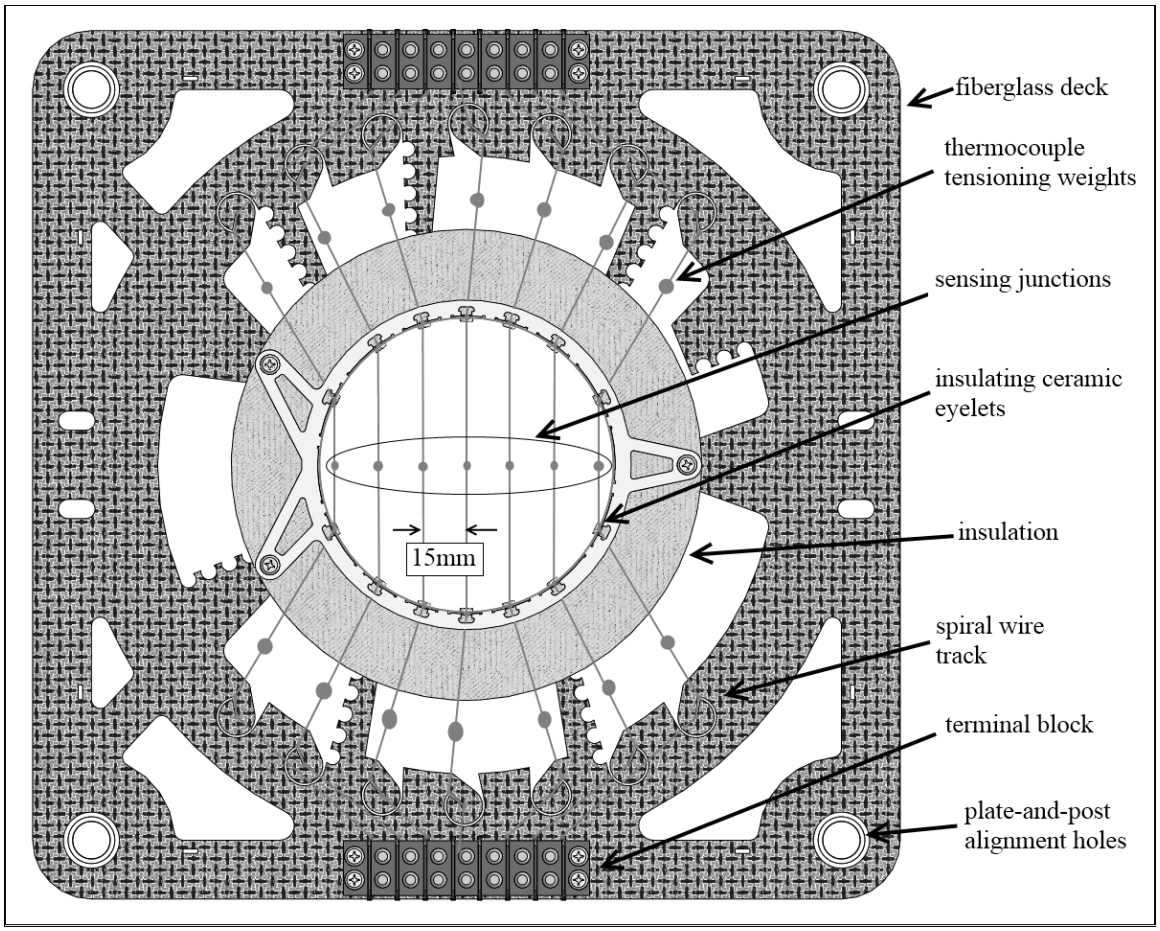

Figure 25: Detailed schematic of a single instrumented layer of validation stove

The two connected electrode wires of the thermocouple extend out perpendicularly from the sensing plane, routing through insulating ceramic eyelets snapped into features in the combustion chamber wall. The electrodes continue out between layers of Fiberfrax insulation towards the outer frame of the fiberglass deck. The electrodes thread through the spiral-shaped tracks in the fiberglass and then continue to the wire terminal where they are secured by a screw. Number three lead fishing weights are crimped onto the wires on both sides of the thermocouple, in the space between the insulation and the spiral-shaped tracks. These weights provide constant tension to the thermocouple wires during expansion and contraction of heating, keeping them slightly taught and thus holding the sensing junction where it is intended to be.

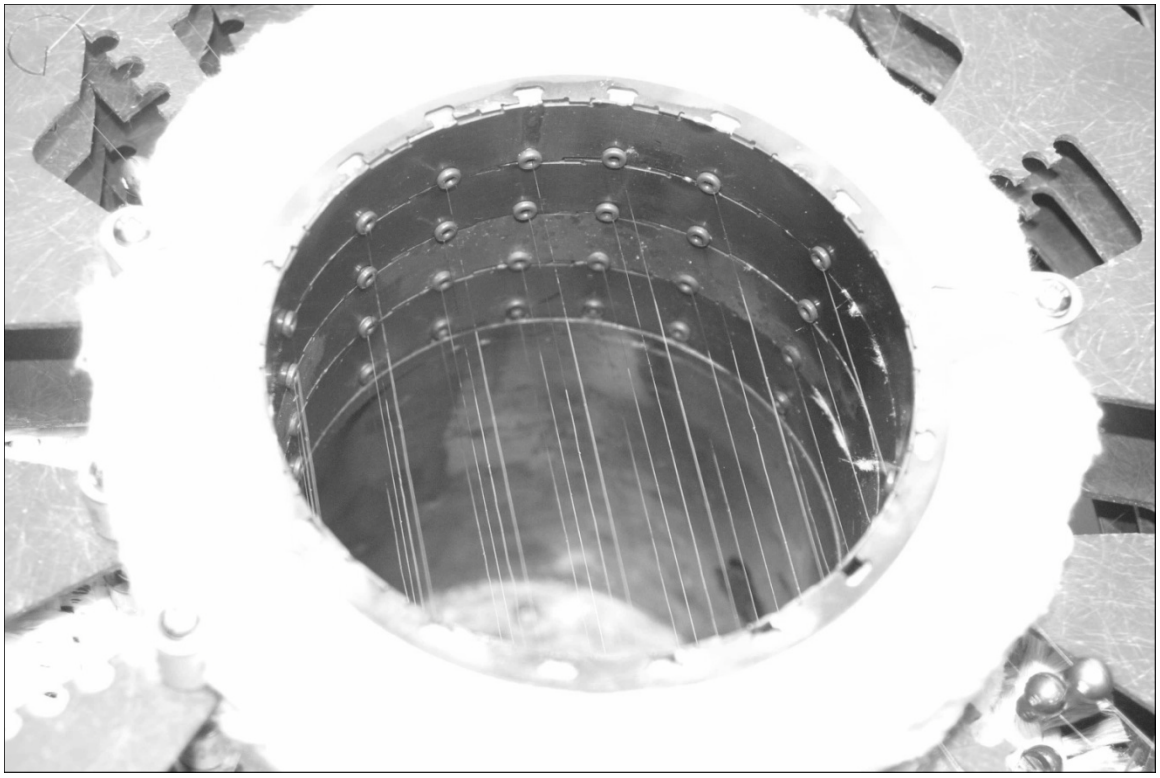

Figure 26: Close-up view of the thermocouple array of the instrumented validation stove

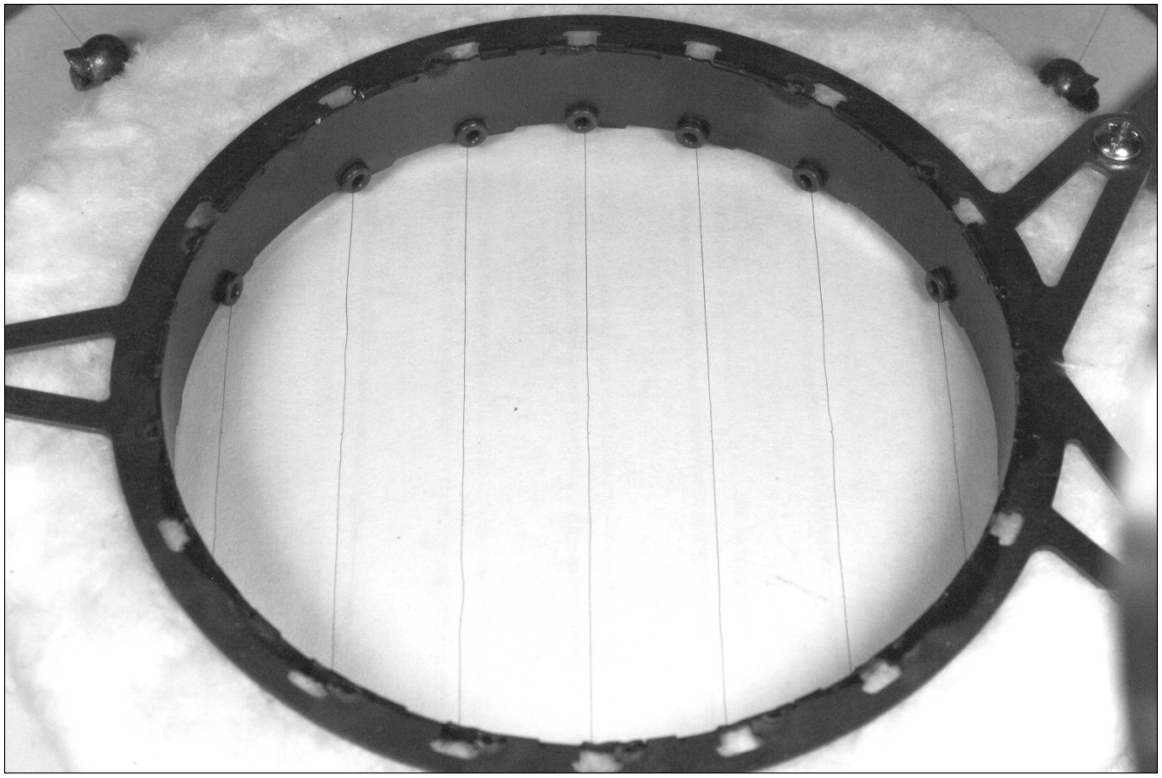

Figure 27: Close-up view of a single instrument layer of validation stove

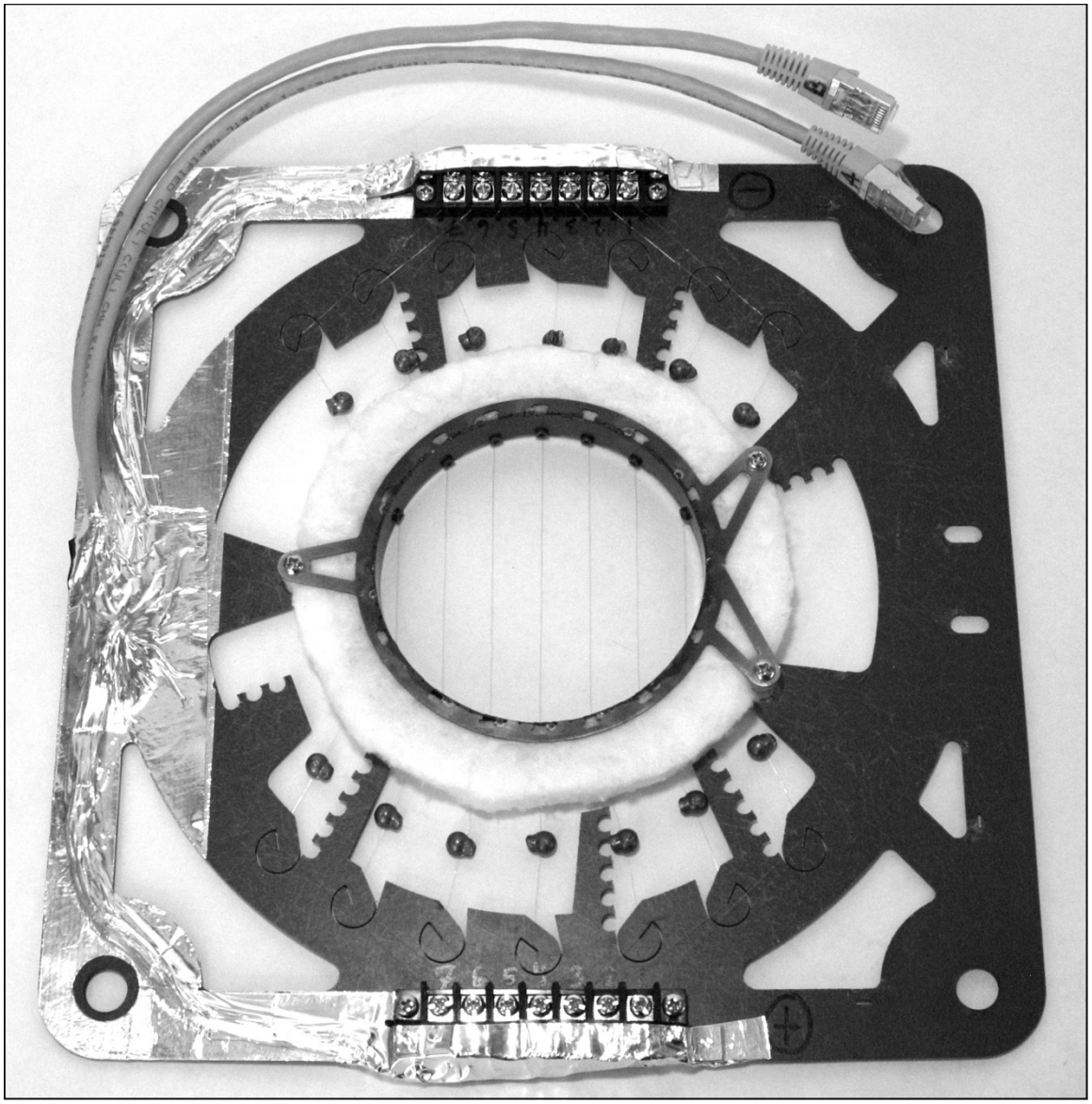

Figure 28: View of a complete instrumented layer of the validation stove, including signal leads

6.1.2 Thermocouple specification and calculations

An array of thermocouples as described in the previous section is employed to measure gas temperatures at array of planar locations in the flow field. The task of acquiring these temperatures is non-trivial due to concern of the effect of the thermocouples on the flow temperature and momentum, and the resulting feedback on measured temperature. Measurement of gas temperatures, especially transient ones, is somewhat invasive. By logic of the first law of

thermodynamics, energy must be conserved and as such heat transfer into and out of the thermocouple is required with a change of temperature. The thermocouple of course has mass, and as calculated by the specific heat and density has a heat capacity around three orders of magnitude higher than the gas. Thus, nearby gas will be significantly affected in this thermal energy transfer. Heat is transferred between the flow gas and the thermocouple by way of radiation and convection, and to a degree along the length of the wire via conduction. The development of a system to attain gas temperatures within the stove was conducted with these concerns in mind.

The works of Heitor and Moriera [38] and Kar et al. [95] provide a good discussion on this general topic. Sources of error are described in detail to include those of the temporal averaging of temperature due to the thermal inertia of the wire, error due to radiation transfer between the wire and locations far-field, artificial gas temperature reduction caused by the quenching of local reactions through heat loss to the wire, and from perturbation of the local flow momentum caused by the wire as an obstruction. The common maxim to all of this is to select a thermocouple wire of as fine a gauge as is practical. The logic behind this then becomes to balance the desired response performance of very fine-gauge wire thermocouples against the increased durability of those of a heavier gauge.

An initial exploratory experiment is conducted to evaluate the basic high-speed response of different fine-gauge thermocouples. N-type and K-type thermocouples manufactured by the Omega Corporation were acquired in 0.003”, 0.005” and 0.010” diameters. A porous-element burner was fed propane and air to produce a puffing flame with a very consistent ~6hz frequency. The thermocouples were mounted on a ring stand apparatus and positioned as seen in Figure 29, in a location above the burner such that the flame position would alternate between enshrouding the sensing junctions and ending below them. The thermocouples are mounted within several millimeters of each other and as such are assumed to be exposed to approximately the same

temperature profiles. The data acquisition system described in section 5.2.3 was used to measure the thermocouple voltage output as a function of time. Different sampling rates were used, varying between very low values and a high of 2000hz. Sample data seen in Figure 30 shows the difference in response of thermocouples of three different wire gauges. The effect of increased mass on the response is obvious, with the heavier 0.010" wire thermocouple showing much more temporal averaging than the 0.005" and 0.003" diameter wires, and still having the same approximate mean value. This exploratory investigation verifies that the finer thermocouples have a much faster response than the heavier ones, and also that they can survive the relatively high temperatures of a partially-premixed propane flame.

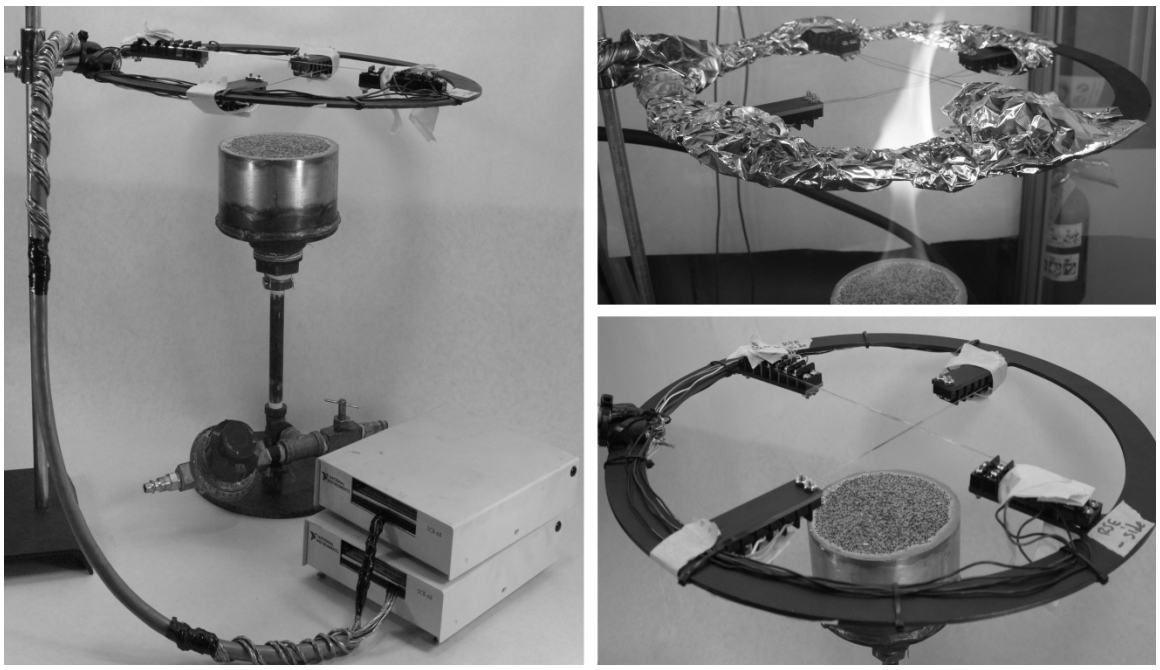

Figure 29: Apparatus for initial dynamic flame temperature measurement

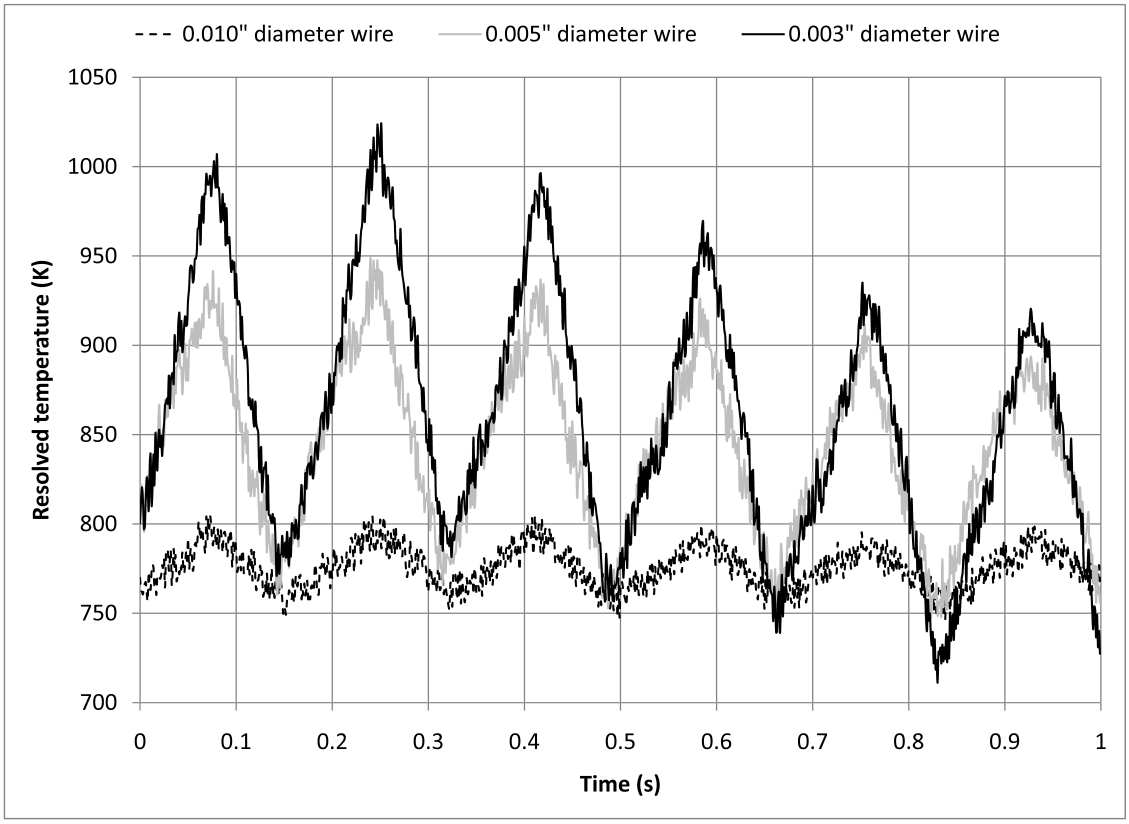

Figure 30: Signal trace from initial dynamic flame temperature measurement experiment

A search of commercially available thermocouples led to the decision to use 0.003" (7.62E-5 m) diameter, unshielded, parallel-welded N-type thermocouples manufactured by the Omega Corporation (part number OPON-003), as seen in Figure 31. N-type thermocouples are composed of a pair of trademarked alloys known as Nicrosil and Nisil, both approximated in calculations here as the thermocouple material Chromel. The transfer functions used for these N-type thermocouples is given in Table 11.

Table 11: Sensitivity and transfer function information for the N-type thermocouples

Type	Temperature range (°C)		Voltage output across range (V)	Voltage range of sensitivity (V)	Sensitivity (μV/°C)	Transfer function (°C/V)	Voltage sensing resolution (V)	Temperature sensing resolution (°C)
	Ref.	Max.						
N	0	1290	4.715E-02	4.00E-01	**36.552**	**27358**	**6.10E-06**	**0.1670**

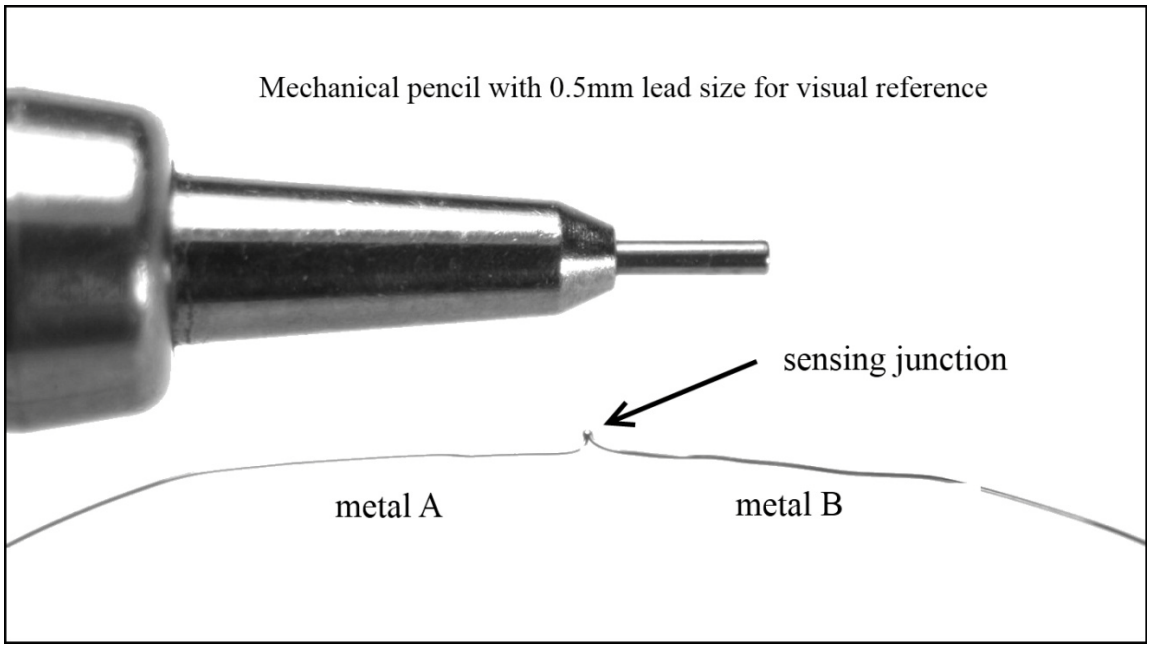

Figure 31: Photograph of 0.003" type N-thermocouple with mechanical pencil as size reference

Some analysis is warranted to understand how the thermocouples respond in various ways. The high and low Peclet number conditions at the thermocouples are considered in order to evaluate these aspects. Validation CFD simulations of the G3300 stove are then evaluated to gain average conditions at the thermocouple locations necessary to make required calculations. Fuel burn rates for the high firepower and low firepower validation cases were calculated as the average of hot start and simmer phase water boil test (WBT) benchmark data for the G3300, evaluated at the CSU Clean Cook Stove Laboratory, respectively, as seen in appendix E. CFD results yield an average thermocouple-zone gas temperature of 1148K at a flow velocity of $1.54*s^{-1}$ for the high firepower case, and 522K at $0.78m*s^{-1}$ for the lower firepower case.

An assessment of the temperature profile within the thermocouple is given by the Biot number as calculated for cylindrical bodies by equation 6.1 [96], which results from the Nusselt number of convection, and also the thermal conductivity of the gas and thermocouple wire. Under the standardized conditions explained above, the Biot numbers are 8.71E-4 and 5.61E-4 for the high and low firepower cases, respectively. Biot number values under ~0.1 suggest that heat transfer within the thermocouple is much faster than heat transfer at the sold/gas interface, with the latter defining the internal conditions. Thus, the temperature within the thermocouple can be considered isothermal, and the thermocouple in the hot gas treated as a lumped-capacitance system.

$$Bi = \frac{Nu * k_g}{4k_w} \tag{6.1}$$

where

Nu is the Nusselt number (dimensionless)

k_w = 17.4, the thermal conductivity of Chromel, the assumed thermocouple wire material $\left(\frac{W}{mK}\right)$

$k_g(T)$ is the conductivity of the gas $\left(\frac{W}{mK}\right)$

Thermocouple temperature lag transient response is another result of the fact thermocouples have mass. The thermocouple temperature will always lag behind changes in the gas temperature by a relation simply given by equation 6.2. Works by Duport et al. [97], Petit et al. [98], and Tagawa et al. [99], [96], [100], provide a very thorough development of many aspects of the transient response of thermocouple wires. The time constant of the system of a thermocouple wire in a gas stream of changing temperature is calculated in equation 6.3 [39], using material properties that are functions of temperature. Using equation 5.3) and the assumed high and low firepower stove conditions, the thermocouple wire has thermal time constants of 92 and 143 milliseconds, respectively. Subjected to an idealized step change in surrounding gas temperature the thermocouple wire temperature will increase to ~63.2% of final value in the

duration of one time constant. a simple and effective method of generating corrected temperature from frequency domain values, attainable through post-processing in modern numerical software packages such as MATLAB. A table including these inputs and results as seen in Table 12.

$$T_g = T_w + \tau \frac{dT_w}{dt} \tag{6.2}$$

where

T_g is the actual gas temperature, (K)

T_w is the thermocouple wire temperature (measured temperature), (K)

τ is the thermocouple time constant, (s^{-1})

$$\tau = \frac{\rho_w c_{p,w} d^2}{4 k_g Nu} \tag{6.3}$$

where

ρ_w = 8670 $\left(\frac{kg}{m^3}\right)$, the density of Chromel

d = 7.62E-5 (m), is the thermocouple wire diameter

$c_{p,w}$ = 444 $(\frac{J}{kgK})$, the specific heat of Chromel

Table 12: Inputs and calculations of major aspects of transient thermocouple response

	Parameter	High power case	Low power case
Standardized CFD inputs	Mass flow dry wood (g*s^{-1}):	2.25E-01	9.89E-02
	Idealized firepower (W):	4.23E+03	1.85E+03
Pertinent CFD results	Mean gas temperatue at thermocouples (K):	1149	522
	Mean wall temperature, cylindrical chamber (K):	706	512
	Mean flow velocity at thermocouples (m*s^{-1}):	1.537	0.775
Calculated thermocouple system values	Biot number (dimensionless):	8.713E-04	5.609E-04
	Peclet number (dimensionless):	0.515	0.739
	t, average time constant (s):	0.092	0.143

While thermocouple instrumentation of a flow will definitely perturb the flow momentum in ways that cannot be compensated for, the extensive nature of the temperature lends itself to correction. The thermocouple signal value can be corrected in post-processing for both effects of thermal inertia and undesired radiation losses. Transient thermal response correction was not attempted for the work reported in this thesis due to the complication the aforementioned signal noise would contribute. Considerable work was conducted in attempts to limit the initial, electronic pickup of the noise through the careful grounding and isolation of apparatus equipment, however the noise remained significant. Figure 32 shows the resolved temperature under null conditions (isothermal, room temperature air), sampled at 1000hz. The only alteration is the application of a linear voltage-to-temperature transfer function. The signal is stochastic, and unperiodic and thus a simple band-stop filter would not succeed in cleaning the signal. Close inspection of the data shows that in most but not all cases the outlying data are single events. The nature of this noise makes it difficult to discriminate the valid high frequency signal fluctuation from the signal noise itself. The amplitude of the noise was also quite high and thus needed special post-processing treatment that essentially made filtration very difficult. A considerable amount of work was done in National Labs DIAdem ™ software attempting to find a suitable filtration method for very high speed sampling. Some of these shortcomings are considered to be due to using non-thermocouple specific data acquisition hardware, a hypothesis discussed in section 6.4, and the conclusion. In response to these issues it is judged that the work required to properly condition these signals at very high speeds is outside the scope of the thesis and instead the sample rate was somewhat reduced to 500hz. The assumption is made that waveform fluctuations occurring at frequencies higher than around 10hz are erroneous and should be ignored. The concept of a sensed cutoff frequency can be applied here but is difficult to understand. Reversing fluctuations in the signal (such as a sinusoidal form) cannot be resolved at frequencies above the cutoff frequency. Inspection of the data at faster frequencies than this can however be made, bearing in mind the fact that the results contain significant, natural smoothing.

An example of the display of results at frequencies above cutoff can be had in the animation of contours, displayed at actual time speed, playing at 30 frames per second (30hz, which is higher than the ~10hz cutoff frequency).

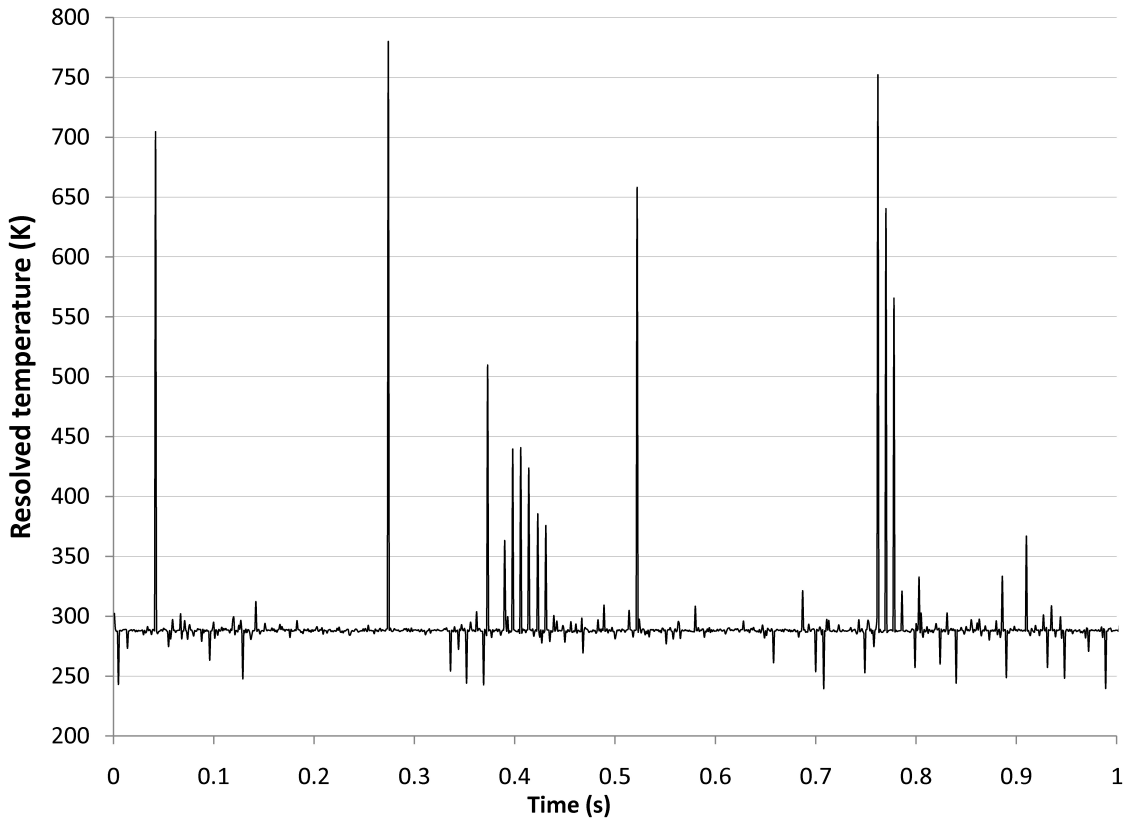

Figure 32: Typical unheated response of a thermocouple in the system including large noise signals.

Since the intent of the thermocouple is to measure the temperature of gas in the immediate vicinity, radiation transfer to and from other locations must be considered as a source of error. Such transfer in hot gas and flame temperature measurement is commonly approximated and corrected for. Kar et al. [95] gives a broad review of various approaches to achieving this.

A first law energy balance of the thermocouple, the surrounding gas, and a far field radiation source/sink is considered here, following the work of Maun [39]. The balance requires that convection and radiation be considered in a pure manner. The Nusselt number for pure convection without radiation for a wire in low Reynolds flow is correlated to the Peclet number

by Seiichi and Takura [101] in equation (6.4), and related to the convection heat transfer coefficient in equation (6.5).

$$Nu = [0.8237 - 0.5ln(Pe)]^{-1} \tag{6.4}$$

where

Pe is the Peclet number (dimensionless)

$$Nu = \frac{hd}{k_g} \tag{6.5}$$

where

d is the thermocouple wire diameter (m)

k_g is molecular thermal conductivity of the gas $\left(\frac{W}{mK}\right)$

$$h(T_g - T_w) = \sigma\varepsilon\left({T_w}^4 - {T_\infty}^4\right) - \frac{k_w d}{4}\frac{d^2T_s}{dx^2} \tag{6.6}$$

where

h is the convection coefficient, $\left(\frac{W}{m^2K}\right)$

σ = 5.669E-8$\left(\frac{W}{m^2K^4}\right)$ is the Stefan-Boltzman constant

ε = 0.863, emissivity of soot-covered thermocouple reported by Barnes et al. (dimensionless)

T_∞ is the temperature of far-field solid boundaries (combustion chamber) (K)

x is the direction of the axis of the thermocouple wire (m)

The first law energy balance is finally given by equation (6.6), where the left hand side is the convection term, the first term on the right hand side the radiation term, and the second right term being for conduction along the wire. Boundary conditions for the conduction term can be calculated rigorously with a method given by Tsuji et al. [102]. In the work reported in this thesis

neither the temperature gradient along the wire, nor the boundary conditions at the wire ends are known. Also unknown is the flow temperature profile in the plane perpendicular to the flow. Considering these facts, the conduction term cannot be calculated explicitly, nor estimated in a reliable manner. Studies by Tagawa [100] of wires of varying diameters (0.6-40μm) in fluctuating hot gas flows suggest that ignoring the conduction term will add some minor error in the range of low frequency fluctuations (0-100hz), which is the range of interest here. Pyrometry studies conducted by Maun [39] did yield temperature gradients along a 14μm diameter SiCO wire in a steady flame, and the conductive loss correction was calculated to be 320 times smaller than the radiation loss correction. These inferences suggest the error associated with ignoring the conduction term will be minor compared to other sources of error. The conduction term is thereby removed from equation (6.6).

The gas is assumed to be nitrogen for the calculation of molecular thermal conductivity using equation (6.7) as reported by Weast [103]. Equation (6.8) relates the Peclet, Reynolds and Prandtl numbers, with the Prandt number assumed to be a constant value of 0.7. Equation (6.9) is a definition for Reynolds number. Mills [104] gives the kinematic viscosity of nitrogen as a function of temperature in equation (6.10). Manipulations of equations (6.4) through (6.10) finally bring about equation (6.11), the simplified radiation correction.

$$k_g(T) = 5.107\text{E-}5T + 0.01141 \tag{6.7}$$

with T in (K)

$$Pe = RePr \tag{6.8}$$

where

Re is the Reynolds number (dimensionless)

Pr = 0.7 , the assumed constant Prandtl number (dimensionless)

$$Re = \frac{Vd}{\nu} \tag{6.9}$$

where

V is flow velocity $\left(\frac{m}{s}\right)$

ν is the kinematic viscosity $\left(\frac{m^2}{s}\right)$

$$\nu(T) = 6.2834\text{E-}11T^2 + 5.9794\text{E-}8T + 7.6259\text{E-}6 \tag{6.10}$$

with T in (K)

$$T_g = \frac{d\sigma\varepsilon\left({T_w}^4 - {T_\infty}^4\right)}{Nu\, k_g} + T_w \tag{6.11}$$

Equation (6.11) can now be used in post-processing to correct individual thermocouple temperatures for radiation effects. Major idealizations and assumptions are repeated here for clarity. A single, constant gas velocity to be used in calculation of the Reynolds number was evaluated through a CFD simulation as the average of velocities found at all thermocouple locations in both array planes. This procedure was repeated for both the high and low firepower validation cases. The validation CFD simulation was setup with respective high firepower and low firepower fuel burn rates specified as the average of fuel consumption found for hot-start and

simmer phase testing of the G3300 stove at the CSU Clean Cook Stove Laboratory. The velocity value used to calculate the Reynolds number is a constant, average value of the velocities at all thermocouple locations in both planes as reported by the CFD simulation of the validation cases. Conduction lengthwise along the thermocouple wire is ignored. The gas is idealized as nitrogen in the calculation of molecular thermal conductivity and kinematic viscosity. The final use of this procedure and additional idealizations and assumptions are explained in following section.

6.1.3 Data acquisition and post-processing

Electronic signals from the array of thermocouples need to be post-processed as explained in the previous section. Several levels of filtration and signal averaging are applied in both the DIAdem script that does initial conversion, and the MATLAB program that does arrangement of the matrices and creates the contour plots. Data is acquired using the hardware detailed in section 6.4. The data is then accessed with National Instruments DIAdem software. The following actions are taken by scripts run in DIAdem:

- A low-pass filter is applied to reduce spurious impulse noise.
- A running average of 10 data points is used to further smooth noise.
- The thermocouple scaling functions are applied to the array signals
- Scaling is applied to the heat exchanger pot water flow turbine as well as the heat-exchanger pot thermocouple signals
- Pot side and bottom heat flow calculations are made with the water flow and temperature data.

A program in MATLAB is then used to conduct final processing and display of the data, in the following steps:

- The data is split averaged over time bins per the specified interval.

- The data is arranged into matrices representational of the stove geometry, and flipped to the correct orientation.
- A standard deviation weighing method is used to reject data points out of range (bad signals, dead thermocouples).
- A Gaussian plotting technique is used to create the contours.

The DIAdem and MATLAB post-processing programs are included in appendix I and appendix J, respectively.

6.2 Instrumented heat exchanger cooking pot

The positive output of all stove testing is ultimately the useful heat. In stove testing, this useful heat is usually only considered in a bulk, time-integrated sense. This makes sense for the reason that the testing is in fact in bulk scale, having no spatial resolution within the stove, and relatively crude temporal resolution of bulk behavior. The addition of a CFD simulation with realistic zonal heat release and a thermocouple-instrumented stove change this fact, generating new questions on the finer scales of heat transfer. While the traditional measurement of the temperature rate of change of a pot of water does inherently give heating rate, the resolution limitations posed by the combination of the large thermal mass and the uncertainty of the temperature measurement limit that temporal resolution. Also, the pot is a single lumped target for the heat, with no discrimination made between its different zones (i.e. sides vs. bottom). Furthermore, the temperature of a pot of water increases as it is heated, hence adding another variable to an already complex measurement.

In the interest of addressing these issues, an instrumented heat exchanger cooking pot was designed, built and tested. This device provides the following function:

- It allows the measurement of useful heat flow in faster time scales.

- It adds minor spatial resolution to the measurement in the ability to discriminate between heat flowing into the bottom of the pot versus into the sides.
- It adds the option for the user to control the average pot temperature, within some practical limits.

The heat exchanger pot is the combination of the standard 5 liter pot and a heat exchanger insert consisting of a highly insulated plug with a coil of copper tubing wound in a spiral and helix around the outer surface. Images of the insert are seen in Figure 33 and Figure 34.

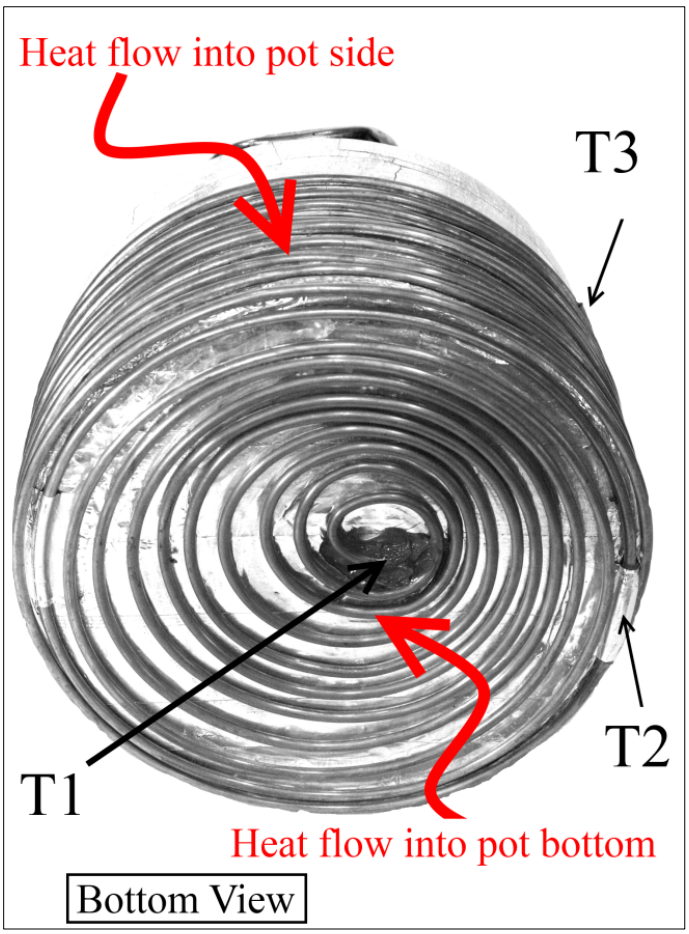

Figure 33: Bottom view of heat-exchanger insert

When inserted into the standard pot the coil essentially forms a spacer to the inner surface of the pot itself. The copper tubing has an OD of 3.175mm and an ID of 1.651mm, and a total length of approximately 15 meters. The coil begins in the center of the bottom of the pot and in

the direction of flowing water follows a spiral pattern to the outer edge of the bottom, where it then begins to wind in a helical pattern up the side of the pot, finally turning vertically, connecting to a drain line. The insulation on the inside of the plug is ½" thick aerogel, possessing a thermal conductivity of 0.02 $W*m^{-1}*K^{-1}$, practically eliminating any heat transfer out of the system except through the intended path via the water flowing in the coil. The insert was designed to displace as much water as possible out of the pot while providing maximum heat removal. With the insert fully installed, approximately 300g of water is poured into the gap between the insert and the outer pot, raising the upper level of the water to the level associated with 5 liters in the traditional arrangement. This water facilitates heat transfer into the system only over the area (height) that compares to the original 5 liter water level. The spacing of the coils and the cooling capacity make it so that the outer surface of the pot is very close to isothermal during operating conditions.

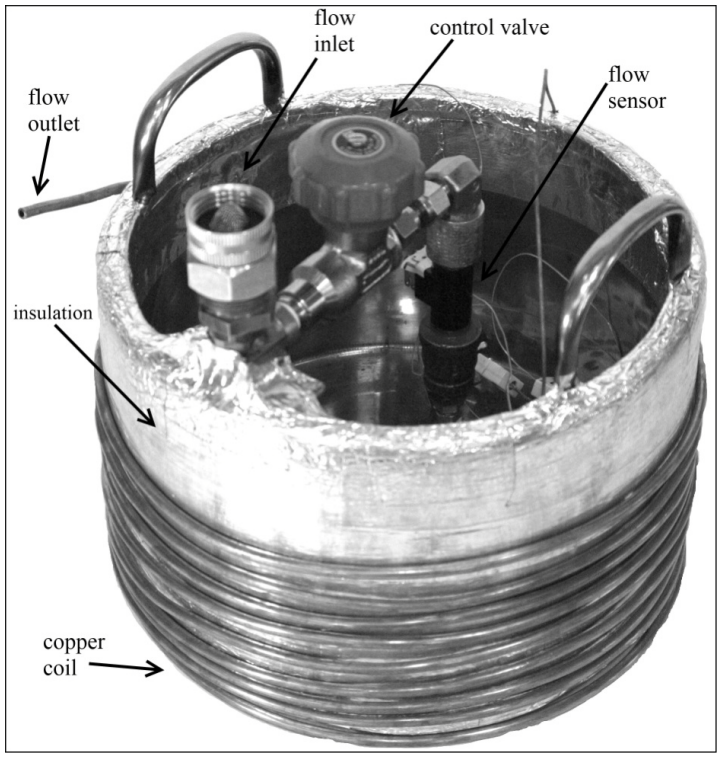

Figure 34: Diagrammed view of instrumented heat exchanger pot insert

A first thermocouple measuring temperature T_1 is attached to the coil at the location where the coil enters the pot bottom zone. A second thermocouple measuring temperature T_2 is mounted to the tubing in the gap region at the location where the tubing transitions from the pot bottom zone to the side zone. Thus, the difference between temperatures T_2 and T_1 give measurement of the temperature rise of the flowing water associated with heat flow into the pot bottom. A third thermocouple measures T_3 of the flowing water at the exit of the pot region, with the difference between T_3 and T_2 being the temperature rise associated with heat flow into the side of the pot. The thermocouples are insulated with small pieces of aerogel and waterproof silicone shrink tubing to provide good insulation and minimize the amount of heat flow into the coil from the outer surroundings. K-type thermocouples are used, with transfer functions given in Table 13.

Table 13: Sensitivity and transfer function information for the K-type thermocouples

Type	Temperature range (°C)		Voltage output across range (V)	Voltage range of sensitivity (V)	Sensitivity (μV/°C)	Transfer function (°C/V)	Voltage sensing resolution (V)	Temperature sensing resolution (°C)
	Ref.	Max.						
K	0	1370	5.480E-02	4.00E-01	**40.000**	**25000**	**6.10E-06**	**0.1526**

A turbine-style flow transducer measures volumetric flow. The operating principle is simple. The standard pot including the heat exchanger insert is placed on a stove as a regular pot would be. Water flow is driven by municipal water pressure with flow regulated by a valve. Flow and temperature differences allow the calculation of zone-averaged heat flow into the coil.

It is useful to consider the control volume of a cooking pot on a stove. Heat is transferred to and from the pot via convection, radiation, conduction, advection, condensation and evaporation as given in equation (6.12).

L'Orange [34], and DeFoort et al. [33] address the uncertainties associated with these aspects in standardized testing. The net effect of these terms is the heating of the pot and its contents, as given in equation (6.13). In the case of the actual water boil test the water mass is

5kg. The cooking pot typically used in stove performance testing is of a 5 liter nameplate capacity and having approximately equal diameter and height (it is not a well standardized item). A typical weight for this pot is approximately 0.75kg.

$$q_{convection} + q_{advection} + q_{radiation} + q_{condensation} + q_{evaporation} = 0 \tag{6.12}$$

$$Q_{absorbed} = Q_{water} + Q_{pot} \tag{6.13}$$

$$Q_{absorbed} = \int_{T_1}^{T_2} (m_{water}\, c_{p_{water}} + m_{pot}\, c_{p_{pot}}) dT \tag{6.14}$$

Equation (6.14) gives the thermal time constant for systems under convection heat transfer in a form useful to make a comparison of the response of the heat exchanger pot versus a traditional pot. The time constant was calculated for:

1. The heating of the pot in the configuration of the standard test method (pot with 5 liters of water).
2. The heating of the heat exchanger pot proposed here.
3. The forced cooling of the heat exchanger pot as proposed here.

Table 14: Inputs and resulting calculation of thermal time constants related to the heat exchanger pot insert

System parameters			
$h_{total\ heating}$, area-averaged total heat transfer coefficient, bottom of pot ($W*m^{-2}*K^{-1}$):	1194		
$h_{coil\ cooling}$, convection coefficient of water flow in copper tubing ($W*m^{-2}*K^{-1}$):	1.27E+07		
OD, outer diameter of copper tubing (m):	3.18E-03		
ID, inner diameter of copper tubing (m):	1.65E-03		
Cross sectional area of copper tubing solid (m^2):	5.78E-06		
Cross sectional area of copper tubing void (m^2):	2.14E-06		
Immersed length of tubing (m):	15		
$m_{dot,water}$, mass flow rate of water ($g*s^{-1}$):	15		
m_{pot}, mass of typical 5 liter pot (g):	750		
Pot surface area (m^2):	0.169		
Thermal time constant calculations			
Testing mode:	Standard water boil test	Heating of heat exchanger pot	Cooling of heat exchanger pot
m_{water}, mass of 5 liters of water (g):	5000	300	300
m_{copper}, mass of 15m of copper tubing (g):	n/a	775	775
τ, thermal time constant (s):	**108**	**11**	**6**

Calculated time constants are seen in Table 14. Heating the traditional pot, heating the heat exchanger pot, and cooling the heat exchanger pot have time constants of 108, 11, and 6 seconds, respectively. These thermal time constants directly relate to the relative response speeds and provide a proxy for additional discussion. The heat exchange pot can respond to, and then theoretically resolve impulses of heat approximately ten times faster than the traditional pot of water. The cooling rate time constant of the heat exchanger pot is almost half that of its heating rate time constant. This suggests that the pot can respond by removing impulses of incoming heat faster than they can be supplied. This also means that the cooling mechanism dominates the temperature of heat within the lumped mass of parts taking place in heat transfer, allowing the user a high degree of control over put surface temperatures.

6.3 Laboratory emissions measurement equipment

Emissions measurements were conducted in a fume hood at the EECL that was specifically engineered for the testing of stoves. The dimensions, geometry, and operating flow rate of the hood were selected to produce steady, fully developed flow without influencing the behavior of the stove. Inlet air is filtered to prevent unwanted infiltration of particulates. Air flow is maintained by a precisely controlled positive displacement Suterbilt Legend 4LP pump which is run by a Dayton 2Z267G 3hp AC motor. All doors and gaps to the fume hood are sealed through door sweeps and weather-stripping material. There are several small doors which allow the stove technician to tend to the stove safely without significantly affecting flow through the hood.

CO and CO2 are sampled from the hood via Siemens Ultramat 6 non-dispersive infrared (NDIR) analyzer systems which are calibrated and spanned according to EPA CFR Title 40 standards. Data is monitored and recorded through a PC that is running National Instruments LabVIEW version 8.2.1.

In order to calculate the air flow through the hood accurately, the air density must be determined with the correct temperature and pressure. Pressure is measured with an Omega PX209-015A5V pressure transducer while temperature is measured with an Omega k-type thermocouple which is connected to a NI-TC120 thermocouple module with cold-junction compensation.

A spiking test is conducted to find the delay between the generation of a spike of emissions in the test fume hood, and when they are sensed at the emissions measuring systems. This test consists of the introduction of fixed flow rate of marker gas into the fume hood at normal operating flow rate, and then the observation of the time of detection of that gas in the emission test data. This test has been conducted for both marker gasses of CO and CO2, with

both gasses having the same response times within the estimated error of measurement of approximately one second. Four tests of delay times using CO gas give 28, 26, 24 and 26 seconds delay. The mean value of 26 seconds is thus considered the standard delay, with an estimated uncertainty of plus/minus 1 second assumed. Figure 35 depicts the level of molar concentration of CO (PPM) from the analyzer in response to gas introduced by ignition of a fireball at t=0. The fireball duration was estimated at around one second. The time delay of ~26s to the start of the gain in value can plainly be seen but there is also a ~10 second lag to the signal peak. There is also a ~50s long decay down to ambient conditions. The dynamics of these transient responses are due to phenomena occurring between the source and the analyzer.

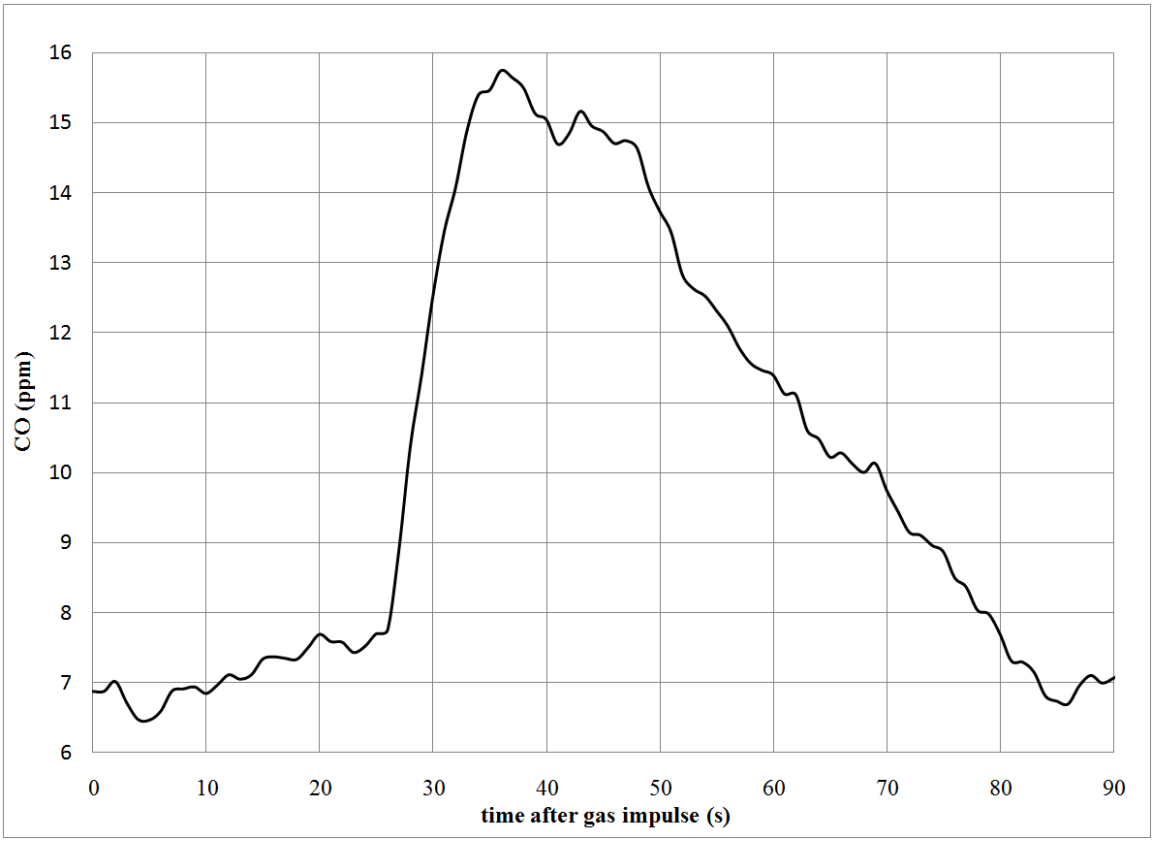

Figure 35: Carbon monoxide emission analyzer reading response (ppm CO) to a ~1s fireball created at t=0s.

Since firepower is calculated from instantaneous CO and CO2 emissions measurements that are themselves affected by these transient effects, the temporal resolution of the calculated

firepower is relatively low. The previously described emission sample delay time of approximately 26 seconds does not include clear information about the nature of diffusion and mixing that occur in the time and space between the emissions hood and the emission sensing equipment. Without a more rigorous analysis information about the transient nature of the firepower calculation cannot be known beyond a simple time delay figure. Calculated firepower values are considered as nominal, with the understanding that additional study is required to make more detailed claims.

6.4 Data acquisition for validation stove and heat-exchanger pot

Data acquisition (DAQ) and recording of the electronic signals from both the thermocouple-instrumented stove and the heat-exchanger pot is done with a National instruments PXI-1002 industrial PC computer with a PXI-6225, low-cost multifunctional DAQ board. The data consists of 63 channels of thermocouple signal from the stove, three thermocouple signals from the heat-exchanger pot, and one channel of signal from the turbine water flow meter. All circuits are wired into a pair of SCB-68 shielded I/O connector blocks.

A simple National Instruments Labview program code was created to parse and write the data to files. The program features a graphical user interface where the user selects the sampling frequency and the duration of signal to be recorded. The program writes streaming data into a memory buffer at the rate and size requested. The size of this buffer is of course a function of the frequency and duration specified by the user. When the user makes a ‘write’ command, data from the memory buffer is written to file, instantly. The execution of the ‘write’ command actually records data retroactive to the command, to file. The file is given a time stamp code that coincides with computer clock time. Thus, the data is retroactive to the time the ‘write’ command is given. Compensation for this effect is considered in previous sections. DAQ-related hardware and software is property of the CSU Engines and Energy Conversion Laboratory.

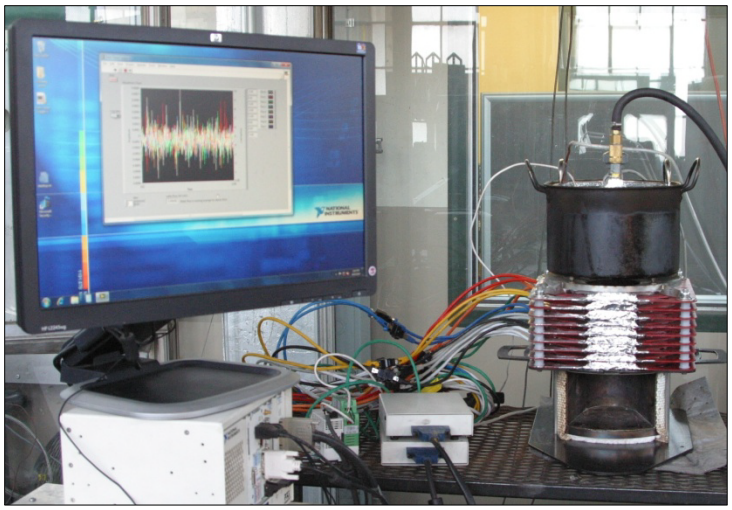

Figure 36: Full experimental apparatus including instrumented stove, heat-exchanger pot, and DAQ computer

7. Simulation and experiment results and discussion

The following section reports the results of CFD simulations and the physical experiments conducted to validate those simulations. Final CFD simulations have been conducted for the cases of a relatively low and relatively high firepower. Both the firepower and the surface area on the wood sticks which serve as the inlet for pyrolysis gas injection are defined by the fuel model developed in section 5.3. These simulations were run for up to 20 seconds of modeled time in order to get a good assessment of behavior. Results are considered in several ways, including in high resolution, in time and space-averaged values, and in the visual assessment of dynamic behavior. The latter is best observed in slow motion animations, and not adequately reported in the format of a paper thesis.

The two CFD simulation cases were based on the significantly evaluated behavior of Envirofit G3300 stove. Data has been previously collected in standardized water boil test (WBT) performance benchmark evaluations conducted at the CSU Clean Cook Stove Laboratory. This data serves both the purpose of defining the fuel consumption / firepower boundary conditions for the two CFD simulations, and also as an additional statistical reference to compare with both the validation experiment and the CFD simulation. The following mean values were calculated from this series of data, and can be seen in Table 15.

Table 15: Experimental basis for the establishment of the low and high firepower CFD simulation cases

CFD simulation case	CSU Clean Cook Stove Laboratory benchmark test	Mean dry wood feed rate	Mean char production rate	Actual firepower (LHV basis)	Mean time to boil	Mean CO production rate	Mean PM production rate
		($g*s^{-1}$)	($g*s^{-1}$)	(W)	(s)	($g*s^{-1}$)	($g*s^{-1}$)
high firepower	**WBT - hot start phase:**	2.253E-01	1.154E-02	3.743E+03	1.553E+03	5.161E-03	8.897E-04
low firepower	**WBT - simmer phase:**	9.888E-02	6.727E-03	1.593E+03	n/a	4.388E-03	1.689E-04

An experimental burn test in the instrumented validation stove is conducted at the CSU Clean Cook Stove Laboratory in the Engines and Energy Conversion Laboratory (EECL). The goal of the test was to acquire data necessary to resolve short time scales of the internal gas-temperature field and cooking pot heat flux along with longer time-scales of emissions (CO and CO2) data for calculation of firepower and consideration of those emissions. The test fire is representative of typical stove operation so as that the data can be comparable to the conditions targeted in the standardized testing that provided the statistical G3300 stove performance data. To this effect, the level of relative firepower is intentionally varied across the overall test such that individual test segments can later be correlated to the average operating points of *low (simmer phase)* and high *(hot start phase)* relative firepower G3300 benchmark performance test data.

The goal of achieving high temporal resolution of the internal temperature field requires high speed sampling of signals from the in-stove gas temperature thermocouple array. Signals from the heat-exchanger pot water temperature thermocouples and volumetric flow rate sensor are simultaneously recorded into the same data files as the thermocouple array signals, all at a sample rate of 500hz, using the aforementioned DAQ hardware and software. Emissions data of CO and CO2 concentrations (PPM) were recorded at a much slower sample rate of 1hz into a single, separate file spanning the entire burn duration. Together, this set of experimental data forms a partial set of the measurements needed to validate the CFD simulation. Figure 37 depicts the start times of the 64 individual data samples superimposed on the calculated instantaneous firepower vs. time. Data from the separate emissions file is corrected for the aforementioned

sample lag, synchronized, and appropriately sampled as to be matched with each individual test. Thus, thermocouple array temperature values, instrumented heat-exchanger heat flow values, and firepower and CO flow values are all pulled together for comparison in the following sections.

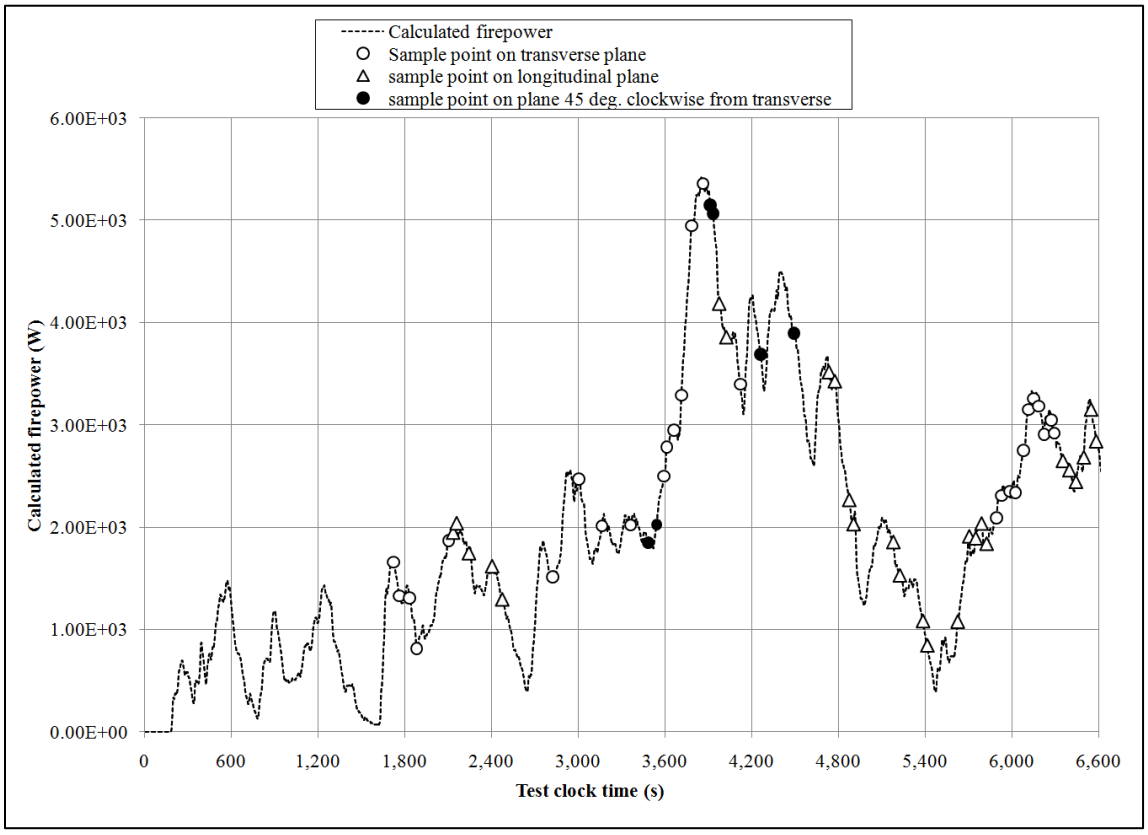

Figure 37: Plot of calculated firepower vs. validation test time, with sample points superimposed.

Results are reported in a variety of ways once again best distinguished with regard to their spatial and temporal scale. Table 16 describes the scale of these two aspects for each measurement in the evaluation. Data of higher resolution is always available in a less resolute form, with the details of the averaging method quite important. Results from the CFD simulation, data from the validation experiment and the statistical benchmark performance test data are compared within each of the following sections.

Table 16: Temporal and spatial resolution of the data resulting from the CFD simulation, validation experiment and CSU benchmark testing

Measurement	CFD simulation data		Validation experiment data		CSU benchmark data	
	Spatial resolution	Temporal resolution	Spatial resolution	Temporal resolution	Spatial resolution	Temporal resolution
In-stove temperature field	plane contours, thermocouple	0.001s	7 radial x 9 high 15mm grid	0.15s, resolved	*none*	*none*
Heat flux to pot bottom	surface contour, area integration	0.001s	Averaged for surface	10s, calculated	total pot lumped	entire test
Heat flux to pot side	surface contour, area integration	0.001s	Averaged for surface	10s, calculated		entire test
Total mass flow	contours, outlet area integration	0.001s	*none*	*none*	*no data*	*no data*
CO mass flow	contours, outlet area integration	0.001s	*none*	~30s	*none*	entire test
CO2 mass flow	contours, outlet area integration	0.001s	*none*	~30s	*none*	entire test
Soot production	contours, outlet area integration	0.001s	*none*	*none*	*none*	entire test

Sets of data acquired in the previously discussed sequence of test samples are evaluated by their average firepower as calculated from the emissions values. The samples are each 40 seconds long and as such can be considered by time averaging on several scales. Simuation and testing field results for the high firepower cases are reported here in greater detail than those of the lower firepower case since the behavior of the former is more interesting. The high firepower case results contain higher temperatures, and hence greater contour gradients that in turn offer a clearer demonstration of the concepts. Bulk results are reported for both cases in the same level of detail.

The mass flow rate of gas through a stove can be calculated from measured stack oxygen, acquired with a direct, point probe. Mass flow rates were not considered in the validation experiment as the unfortunate outcome of the testing plan. The complication of adding the oxygen measurement was to be added in a subsequent test which had to be canceled due to unexpected damage to the fine-gauge thermocouples sustained in the first test. Despite not being observed in the preliminary gas burner experiments nor in short, trial-run wood burns, accelerated

aging / damage of the thermocouples was experienced under the high temperature stresses of the high firepower case test. Hence, stack oxygen measurement was not conducted and mass flow rate cannot be verified. Considering that the flow exiting the stove is relatively asymmetric, as evaluated through proxies of unstable puffs of flame and soot, as seen as well in the CFD simulation, it is quite possible that an oxygen probe small enough not to be intrusive would preferentially sample the stack flow, leading to considerable error in calculated mass flow rate. It is a recommendation to pursue mass-flow measurements for validation purposes in the future.

PM emission production was not assessed during the validation experiment since the main focus was on the sweeping of firepower of that stove, which would complicate the >10 minute long samples required to attain enough mass of PM to allow for certain measurement. Also, efforts were made to minimize test durations in consideration of the rapidly deteriorating thermocouples. Instead of measuring PM production directly during the validation test, benchmark test data for the G3300 is considered for bulk result comparison.

Bulk results include extensive, time-averaged conditions that make for the easy, high-level performance assessment. Such data is acquired from the testing of the validation stove, and averaged, statistical performance data from the Envirofit G3300 stove, as tested at the CSU Clean Cook Stove Laboratory. Results of firepower, CO and PM mass flow, cooking pot heating rate, thermal efficiency, and mass and volumetric flow rates are available, but not for all stoves. A summary of this data is included in Table 17, and Table 18, for the low and high firepower case conditions, respectively. Appendix A contains the entire set of bulk data, including that from each individual sample considered in the two cases.

Table 17: Digested bulk result data from low firepower case CFD simulation, experiment, and benchmark data

Category:	Heat transfer					Emissions		Flow rates	
Parameter:	Sample firepower (LHV basis)	Heating rate, pot bottom	Heating rate, pot side	Heating rate, net TOTAL	Average thermal efficiency	Carbon monoxide mass flow	PM mass flow	Mass flow rate	Volumetric flow rate (@ ref)
Units:	(W)	(W)	(W)	(W)	(%)	($g*s^{-1}$)	($g*s^{-1}$)	($g*s^{-1}$)	(m^3*s^{-1})
G3300 simmer phase WBT mean:	1.59E+03	n/a	n/a	n/a	n/a	4.39E-03	1.69E-04	n/a	n/a
CFD, Low firepower case, time averaged:	1.79E+03	3.01E+02	-1.95E+01	2.82E+02	15.7%	1.91E-07	3.81E-13	2.16E+00	2.09E-03
Validation experiment, Low-firepower, mean:	1.90E+03	3.83E+02	1.21E+01	3.95E+02	21.1%	6.05E-03	n/a	n/a	n/a
Disagreement, CFD to G3300 (%):	12.6%	n/a	n/a	n/a	n/a	100.0%	100.0%	n/a	n/a
Disagreement, Val. To G3300 (%):	19.5%	n/a	n/a	n/a	n/a	37.8%	n/a	n/a	n/a
Disagreement, CFD to val (%):	5.8%	21.4%	261.5%	28.8%	25.8%	100.0%	n/a	n/a	n/a
Standard deviation, validation samples:	4.61E+02	6.81E+01	5.61E+01	9.13E+01	5.05E-02	2.54E-03	n/a	n/a	n/a

Table 18: Digested bulk result data from high firepower case CFD simulation, experiment, and benchmark data

Category:	Heat transfer					Emissions		Flow rates	
Parameter:	Sample firepower (LHV basis)	Heating rate, pot bottom	Heating rate, pot side	Heating rate, net TOTAL	Average thermal efficiency	Carbon monoxide mass flow	PM mass flow	Mass flow rate	Volumetric flow rate (@ ref)
Units:	(W)	(W)	(W)	(W)	(%)	($g*s^{-1}$)	($g*s^{-1}$)	($g*s^{-1}$)	(m^3*s^{-1})
G3300 hot start WBT mean:	3.74E+03	n/a	n/a	1.10E+03	n/a	5.16E-03	8.90E-04	n/a	n/a
CFD, High firepower case, time averaged:	4.09E+03	1.14E+03	-8.03E+00	1.13E+03	27.6%	2.88E-07	1.78E-14	2.85E+00	2.60E-03
Validation experiment, High-firepower, mean:	4.10E+03	8.25E+02	1.43E+02	9.69E+02	24.3%	5.02E-03	n/a	n/a	n/a
Disagreement, CFD to G3300 (%):	9.2%	n/a	n/a	n/a	n/a	100.0%	100.0%	n/a	n/a
Disagreement, Val. To G3300 (%):	9.6%	n/a	n/a	n/a	n/a	2.6%	n/a	n/a	n/a
Disagreement, CFD to val (%):	0.3%	37.7%	105.6%	16.6%	13.5%	100.0%	n/a	n/a	n/a
Standard deviation, validation samples:	7.81E+02	2.18E+02	1.15E+02	2.96E+02	8.53E-02	2.99E-03	n/a	n/a	n/a

It is immediately important to consider that both the high and low firepower case CFD simulation specified firepower levels are considerably different than the G3300 statistical firepower they were intended to match. This is due to a mistake made in the computation of the experimental firepower of the latter. Essentially, the char remainder was incorrectly considered. The G3300 hot start (high power) and simmer phase (low power) firepower values were lowered ~11% and ~8.6%, respectively, down from the levels of the corresponding CFD simulation cases.

By nature of having a three dimensional control volume, results of the CFD simulation can be reported at any location within it. Some results are in fact evaluated and displayed in the 3D space, including fluid flow path lines and various isosurfaces. Post-processed, experimental temperature results are available in a reduced, two dimensional planar format. Major CFD simulation results are thus reported in this same two dimensional form for the purpose of comparison to the experimental results.

These planes pass through the vertical axis central to the cylindrical portion of the combustion chamber, and are termed *transverse* and *longitudinal*, as defined relative to the CFD simulation geometry in Figure 38. The longitudinal plane is a plane of geometric symmetricity for the stove while the transverse plane is not. Path lines of flow moving along both the horizontal inlet and vertical section of the stove are parallel to the longitudinal plane whereas only flow lines in the vertical portion of the stove run parallel to the transverse plane.

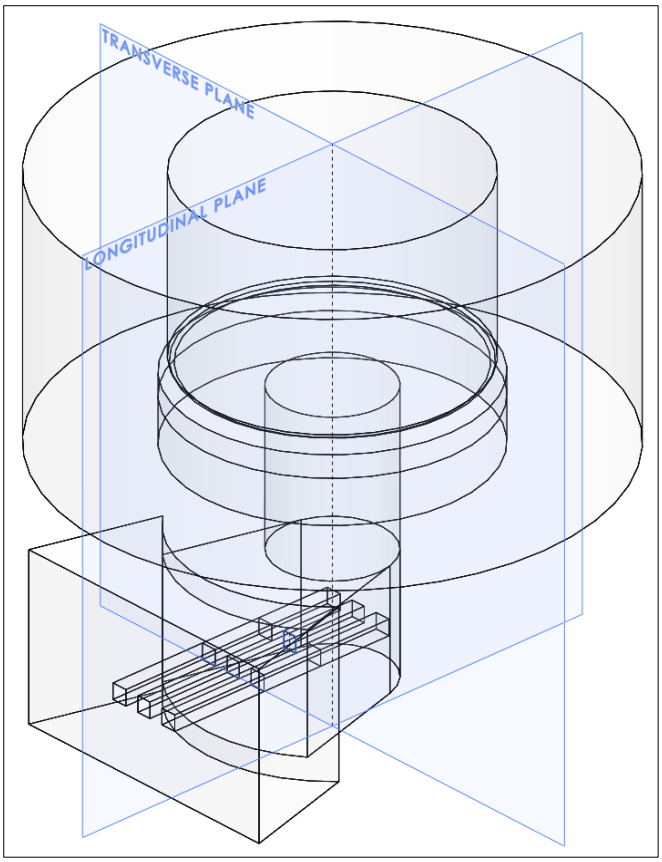

Figure 38: Major reporting planes in CFD simulation and from validation experiment thermocouple array.

7.1 Gas temperature field results

Both the CFD simulation and the experimental validation using the instrumented stove yield temperatures in relatively fine spatial and temporal resolution. The CFD simulation naturally gives temperature and all tracked metrics at the spatial resolution of the mesh (~1-

7mm), and the temporal resolution of the time step (0.001s). Thus, resolution is not a limiting factor in consideration of the CFD results. The experiment gives temperatures at the 63 locations (7qty radial x 9 qty axial) on a 15mm grid, sampled at a frequency of 500hz over 40 second samples. The thermocouple system is not corrected for thermal inertia and thus the resolution of the experimental data is limited to the approximate cutoff frequency around 15hz. The challenge with reporting and communicating the results of works that have produced high spatial and temporal resolution data is the clear identification of the relevant information. The results here have been reduced down to the simplest elements possible for a clear display of the concept. The fine resolution data is processed and configured for consideration in plane resolved temperature contours and in linear temperature rakes.

The CFD simulation results have a clear visual reference in the fact the domain holds the shape of the stove, as seen also in Figure 39. The resolved validation experiment temperatures come from the featureless, axisymmetric cylindrical region within the stove and thus there is no inherent visual reference to cylindrical coordinates or other parts of the stove. The scheme for identifying the orientation of these results relative to the physical stove can be seen in Figure 39. In the reporting of both the CFD simulation and validation experiment results, the left side of a figure coincides with the front side of a longitudinal plane, and the left side of a transverse plane as seen in Figure 40 and Figure 41, respectively.

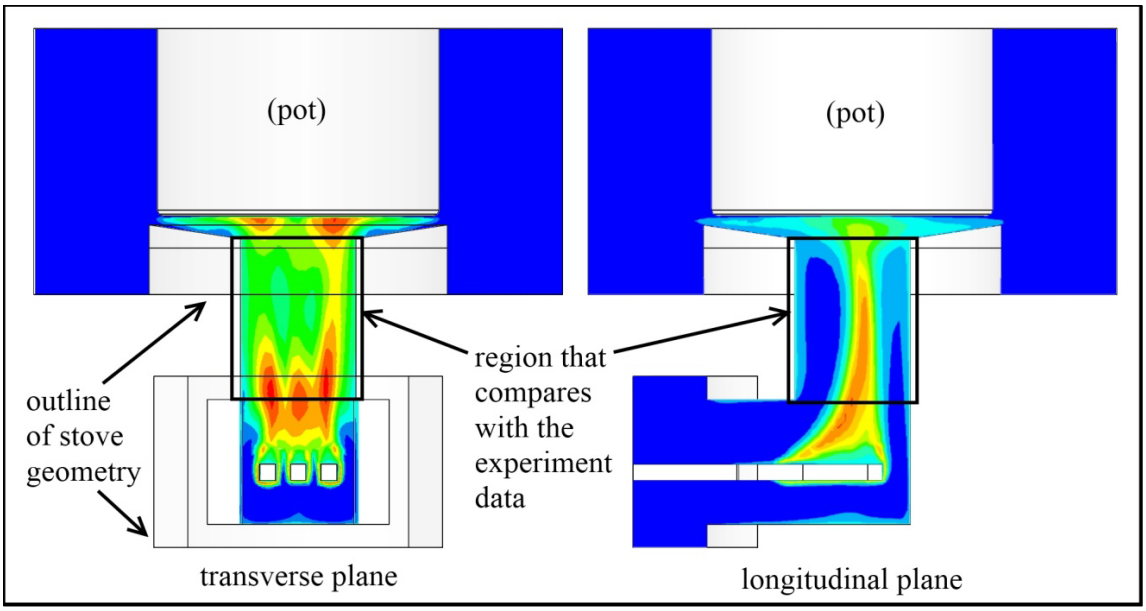

Figure 39: Position and orientation of the sensed zone of the thermocouple array in both transverse and longitudinal plane orientation.

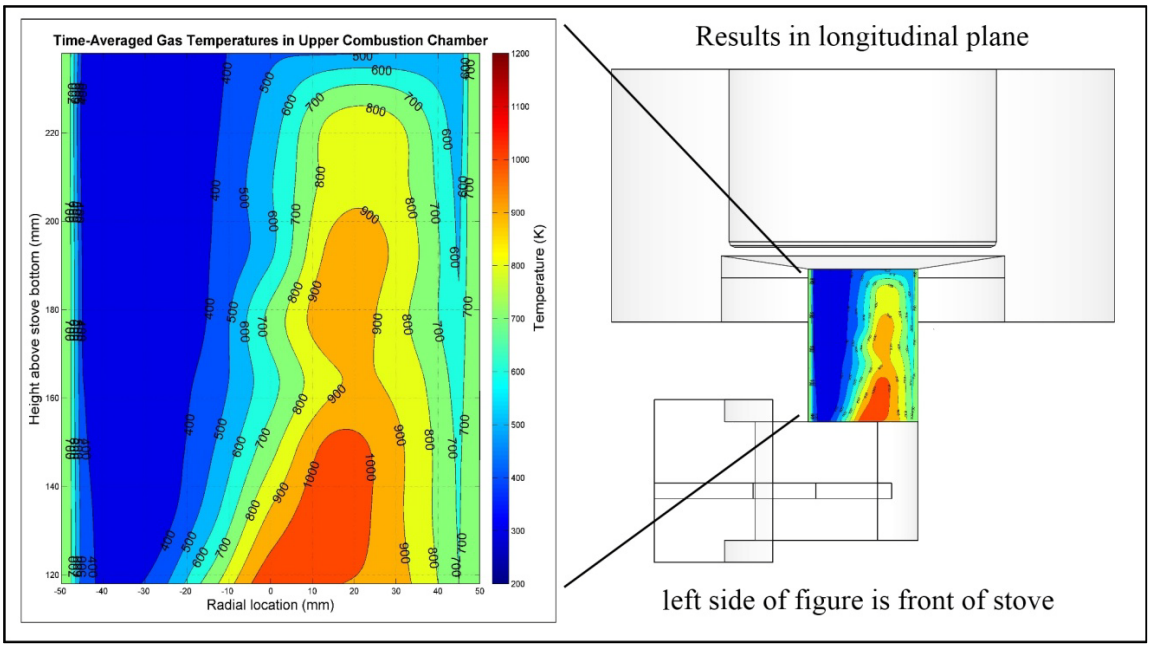

Figure 40: Visual example of the graphical orientation of the resulting contour plot for the longitudinal sensing plane, relative to the domain geometry.

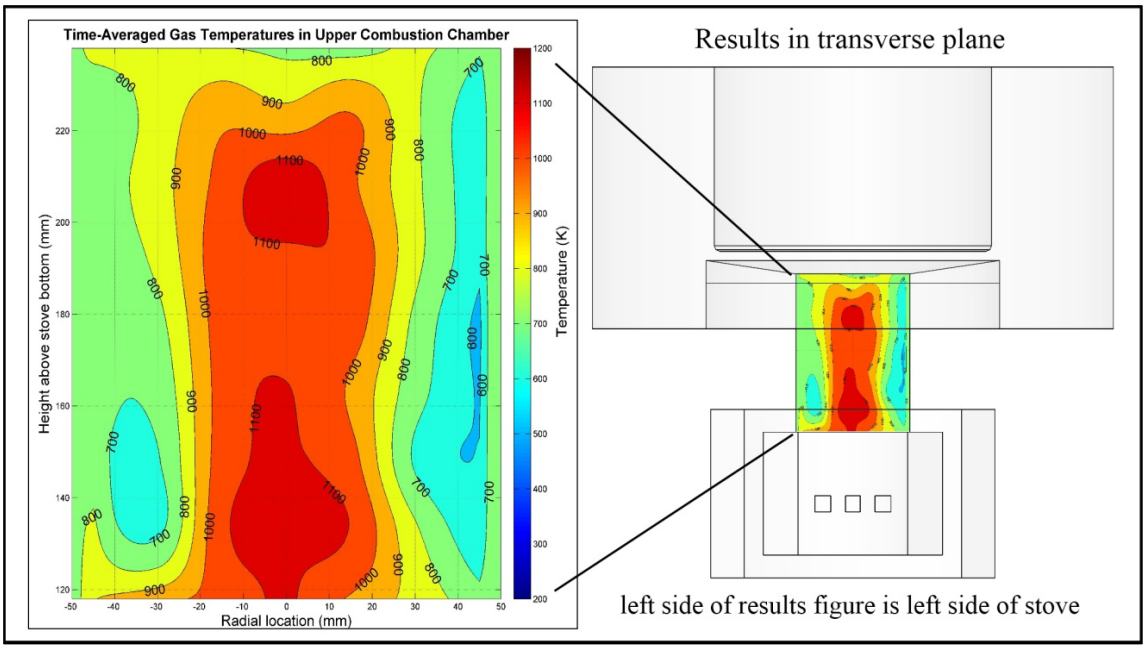

Figure 41: Visual example of the graphical orientation of the resulting contour plot for the transverse sensing plane, relative to the domain geometry.

It must be noted that while the CFD simulation results are reported at the mesh resolution of a ~6-7mm grid across the entire cylindrical combustion chamber zone, the validation stove experimental data is recorded at 63 locations at a 15mm x 15mm grid resolution. The experimental data is then considered by the procedure outlined in section 6.4, which includes the Gaussian contour plotting. The difference in resolution will definitely contribute to differences in how the raw temperature data is presented between the CFD simulation and the experiment, however, the author finds that other factors contribute much more significantly to the interpreted differences. The experimental data temperature signals are known to have significant amounts of error that require the conditioning and post processing described in sections 6.1.2 and 6.1.3. These effects can be well-seen in animations of the experimental data (not seen in this thesis, naturally). The author notes that the results can be significantly affected by the adjustment of any of the error-rejection, averaging, or smoothing settings and coefficients. Thus the mesh resolution is judged to be a minor element of disagreement between the experimental and CFD simulation data.

7.1.1 High-temporal resolution

Results data from the CFD simulation and validation experiment can be considered on a variety of time scales, ranging from the finest resolution as given in Table 16, to time-averaged results of any span of interest. This thesis reports results in a practical range, from 0.015s on the fine-scale end of this spectrum to 40s averages on the other end. CFD simulation results are available at resolutions down to the time-step increment of ~0.001s, but such time steps are not visually perceptible or particularly useful. As explained in section 6.1.2, the estimated cutoff frequency of the thermocouple array is around 10hz, as calculated as the inverse of the system time constant of around 0.1s. Contours of temperature results are displayed at a shorter time step of 0.015s (~67hz), which is faster than the cutoff frequency. Therefore, any fluctuations occurring on time scales shorter than the cutoff frequency are not resolved, but their effect averaged.

Instantaneous temperature contours give a freeze-frame representation of the transient temperature field without any intentionally added temporal and spatial averaging. Such contours give a visual form of the data in the highest available spatial and temporal resolution. The capability of viewing the instantaneous temperature field frozen in time may be useful to the combustion scientist and stove designer. Viewing a chronological succession of these contours gives an understanding of the flow dynamics in much the same way as watching a moving flame, or a simulation animation would, but giving the viewer more time to inspect the conditions.

Figure 42 and Figure 43 depict two contours at a 0.015s time step for the low firepower simulation case, on longitudinal and transverse planes, respectively. The sequential contours are significantly more different and the temperature field not as symmetric about the longitudinal plane in the high firepower case vs. the low firepower case. This behavior supports the idea that relatively high firepower operation has greater fluctuations and is less stable than lower firepower operation, in the case of this particular stove.

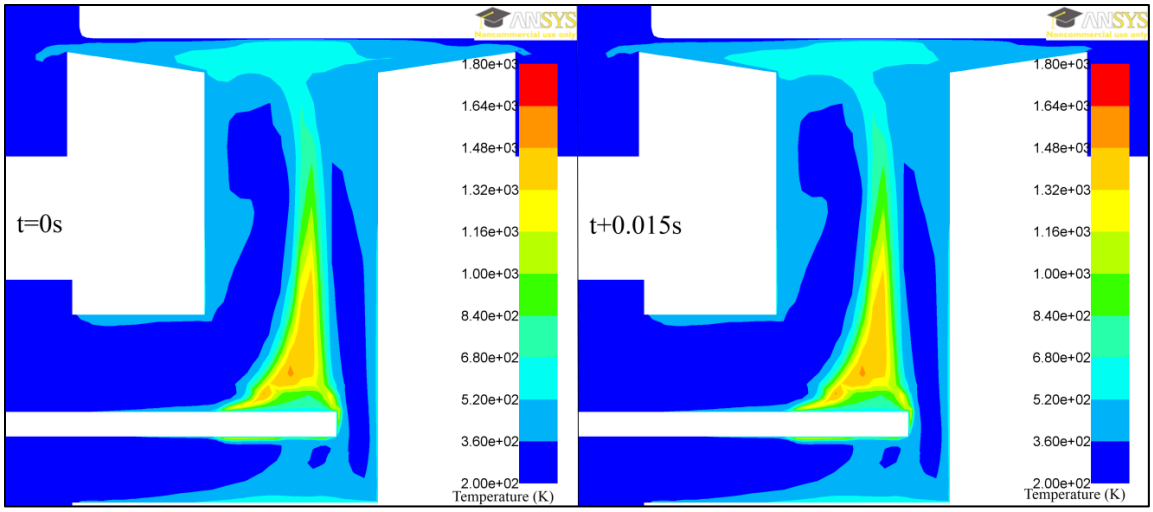

Figure 42: Low firepower CFD simulation longitudinal plane temperature contours at 0.015s time step.

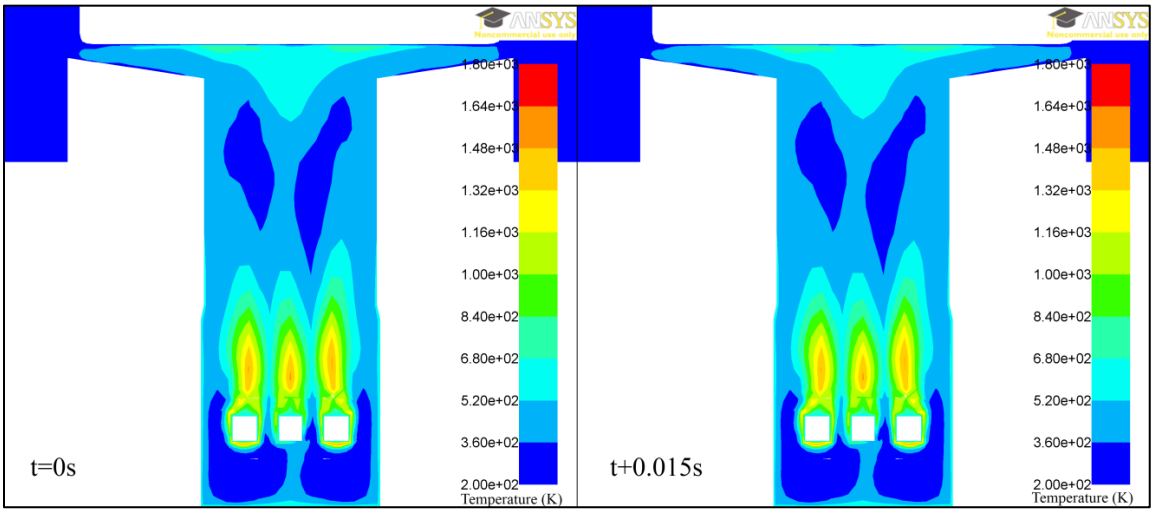

Figure 43: Low firepower CFD simulation transverse plane temperature contours at 0.015s time step.

Figure 44 below depicts a succession of two instantaneous temperature contours for the longitudinal and transverse planes of the high firepower simulation case, respectively. The time difference between the two contours in each figure is approximately 0.015s. Note that these contours are all scaled from 200 to 1800K across the contour range.

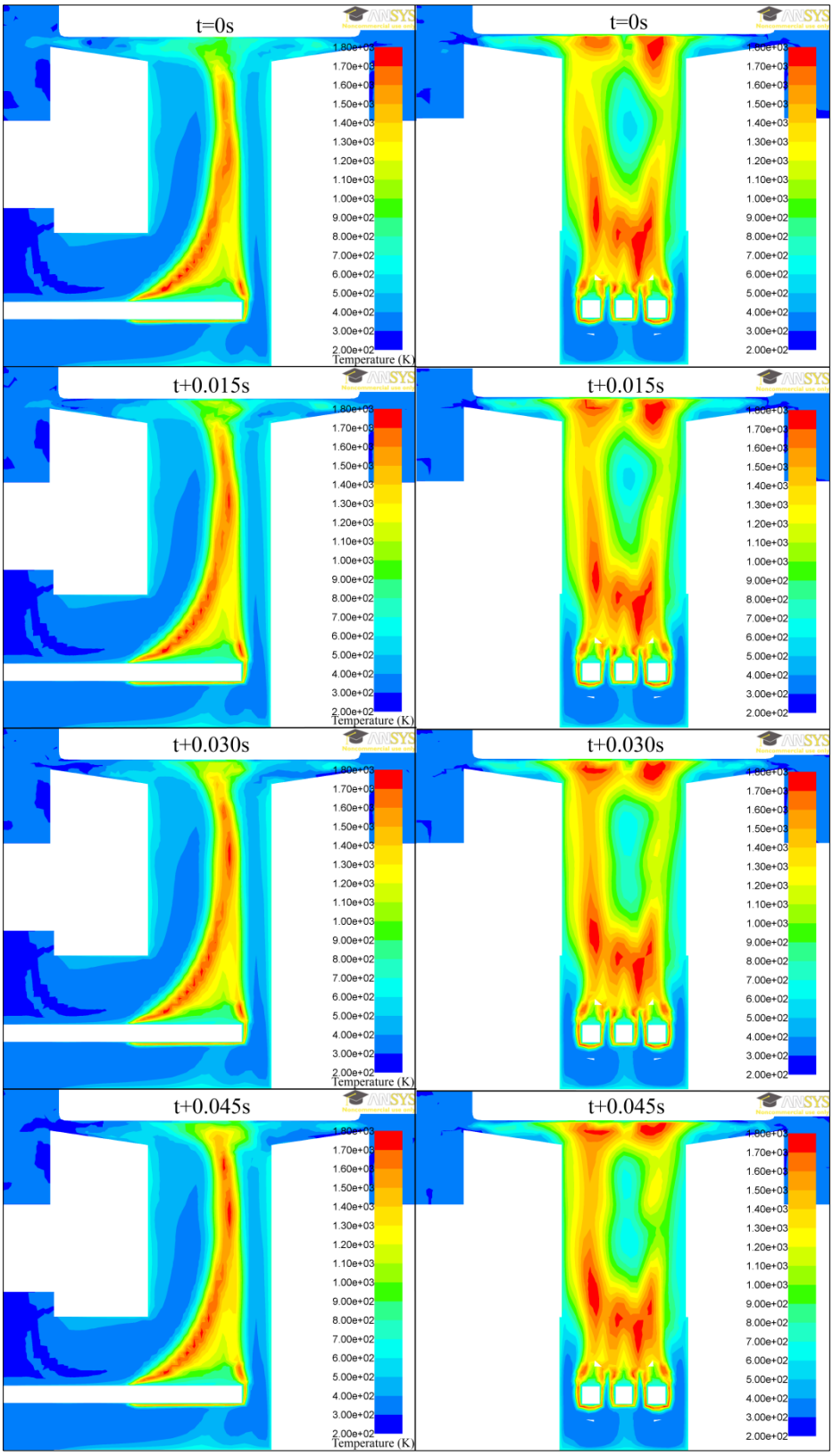

Figure 44: High firepower case CFD simulation temperature contour results at 0.015s time steps, on longitudinal (left) and transverse planes (right).

The left-hand column of plots in Figure 45 is simply a recreation of the transverse plane CFD simulation results of figure 1, cropped to highlight the region that is thermocouple-instrumented in the validation stove, for the purpose of comparison to the experimental results. Note the coordinate system grid for ease of making pinpoint comparisons. As in previous contour plots, the left hand side of the plot the left hand side of the stove in the transverse plane view, or the front of the stove in the longitudinal plane view. Contour plots making up the right hand column of Figure 45 provide a sequence of instantaneous resolved temperature contours from longitudinal plane of the experimental stove in validation experiment sample F25. The calculated average firepower across this sample point is 4.05kW, a value very close to the 4.09kW implicitly specified firepower of the CFD simulation.

The two columns of contours are thus directly comparable, yet such a comparison has very little statistical significance, considering the stochastic, transient nature of both the actual fire and the CFD simulation. Figure 45 thus serves to illustrate that both the CFD simulation and the instrumented stove can resolve short time-scale behavior of a fire. Comparison of a single, or even multiple sequences such as these does not provide validation of the CFD simulation, but merely supports the idea that the CFD simulation is able to capture some degree of dynamic fire behavior. Sequences of temperature field results acquired at a high speed on short time steps may also be displayed in animated form. The purpose for this is to observe this dynamic behavior in a way difficult to perceive in stopped motion.

Many sequences such as the ones depicted in Figure 45 exist in the results of the CFD simulation and the validation experiment. A visual assessment of these sequences of contours suggests that the CFD simulation does provide reasonably authentic prediction of the short time-scale dynamics of the temperature fields. More quantitative analysis of the CFD simulation exists in the time-averaged assessment of the temperature fields.

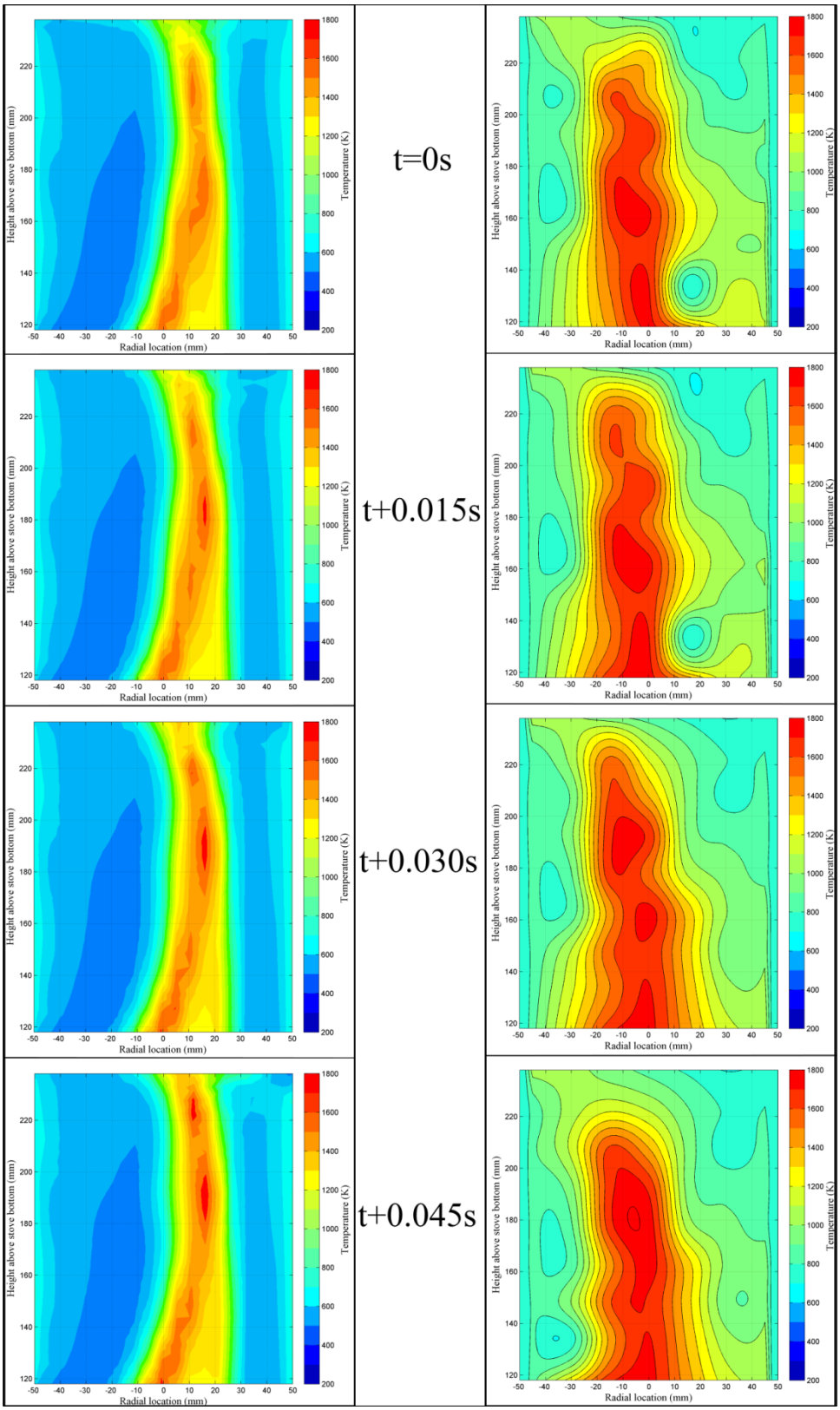

Figure 45: Consecutive temperature contours of *longitudinal* planes under high firepower combustion plotted at 0.015s time steps. 4.09kW CFD simulation (left) vs. 4.05kW validation experiment sample F25 (right).

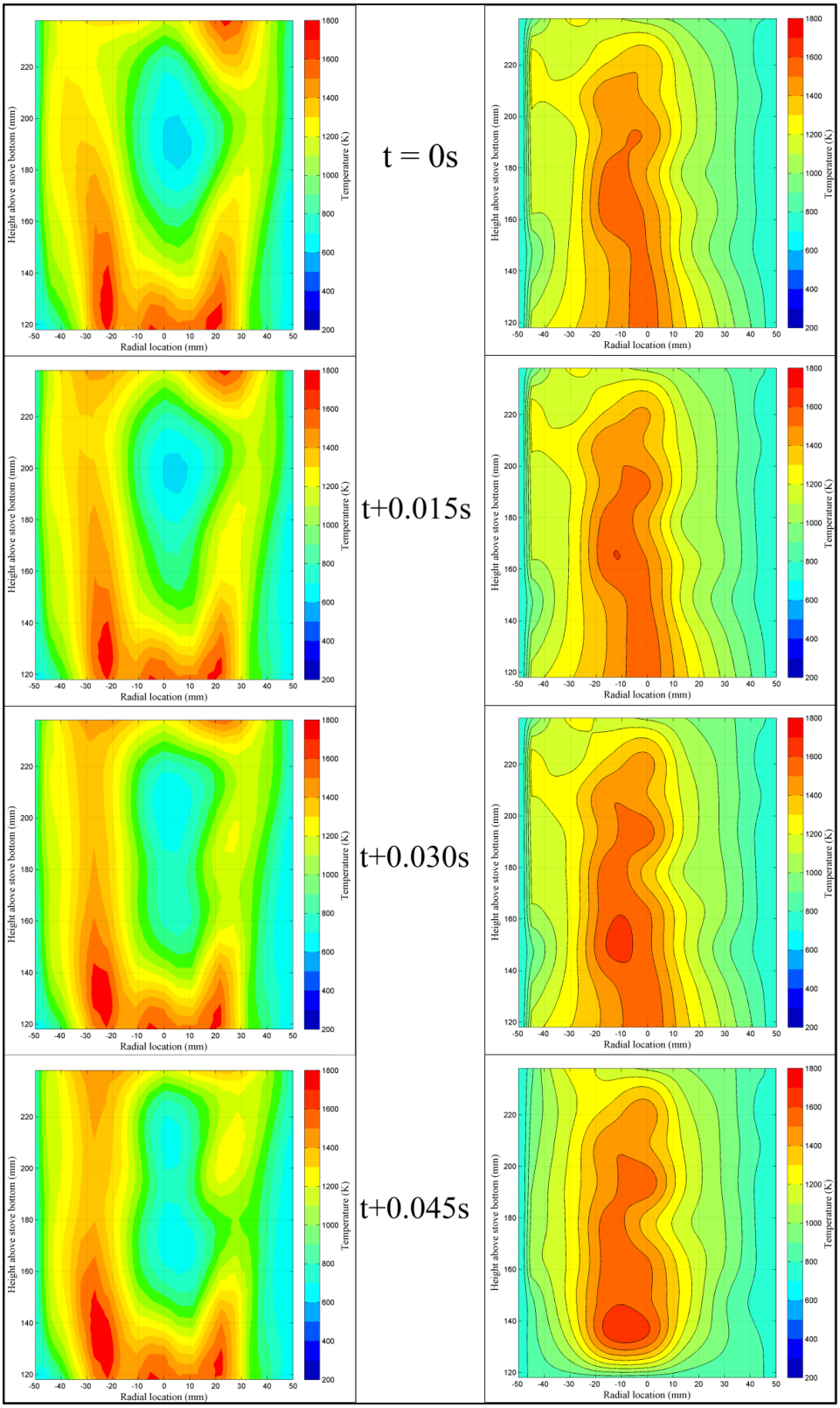

Figure 46: Consecutive temperature contours of *transverse* planes under high firepower combustion plotted at 0.015s time steps. 4.09kW CFD simulation (left) vs. 5.31kW validation experiment sample F22 (right).

The sources of the disagreement between the CFD simulation results and those of the experiment are thought to be a combination of thermocouple signal error, inconsistent signal conditioning and post-treatment due to said error being itself inconsistent, and also the fact that there are unsteady perturbations to the system in physical reality that are not represented in the CFD simulation. The first listed source was minimized as much as possible but still proved to be significant. The reason for so much electronic signal noise may be the use of low-cost, general purpose data acquisition cardThese include inlet air flow turbulent energy and unsteady spatial and temporal variation in the pyrolysis reaction. Furthermore, despite efforts during the experimental validation to arrange the fuel symmetrically over the longitudinal axis, it could never be perfect. Asymmetric fuel conditions no doubt contribute to additional flow instability. Future work further developing the CFD simulation could include additional sensitivity studies on these perturbations. Mixture fraction variance could be increased on the fuel condition, as could the inlet air turbulence values, both of which are left at null values in the simulation work presented here.

7.1.2 Time averaged temperature fields

Time-averaged temperature results are useful for understanding the general effect a combustion chamber has on the flow path and the stretch and position of flames, and for the optimization of heat transfer (to be considered in combination with surface heat flux results). Studying the time-averaged temperature fields acquired from the validation experiment is also a more effective way to attain validation of the CFD simulation.

The fact that the transverse plane result doesn't match the CFD simulation result as well is not surprising, since the flame structure is expected to have inconsistencies due to the gaps between the sticks, which having a 1-2cm distance are not well resolved by a 15mm spaced array of thermocouples. The expected effect in such cases is the averaging of the natural gradient.

Figure 47 and Figure 48 depict CFD simulation result contours of 5 second temporally-averaged temperature fields on the same longitudinal and transverse planes for the low and high firepower cases, respectively.

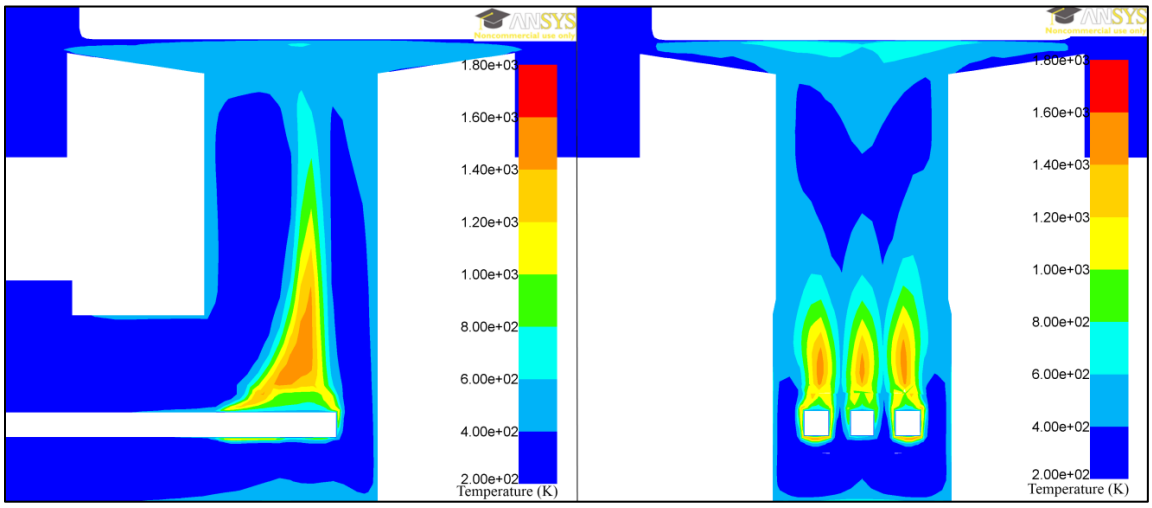

Figure 47: Low firepower case CFD simulation temporally averaged temperature contours for the longitudinal (l) and transverse (r) planes.

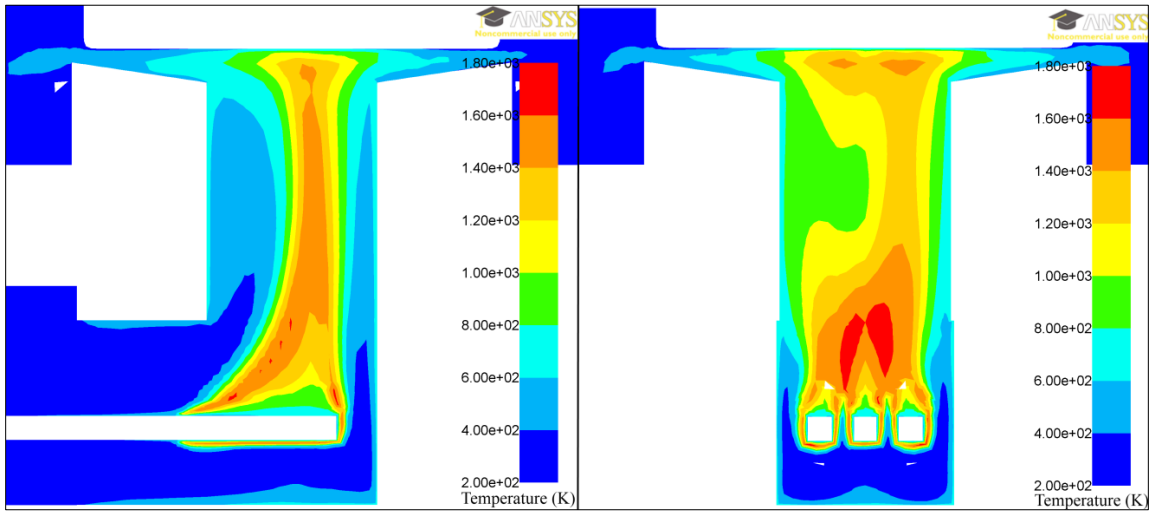

Figure 48: High firepower case CFD simulation temporally averaged temperature contours for the longitudinal (l) and transverse (r) planes.

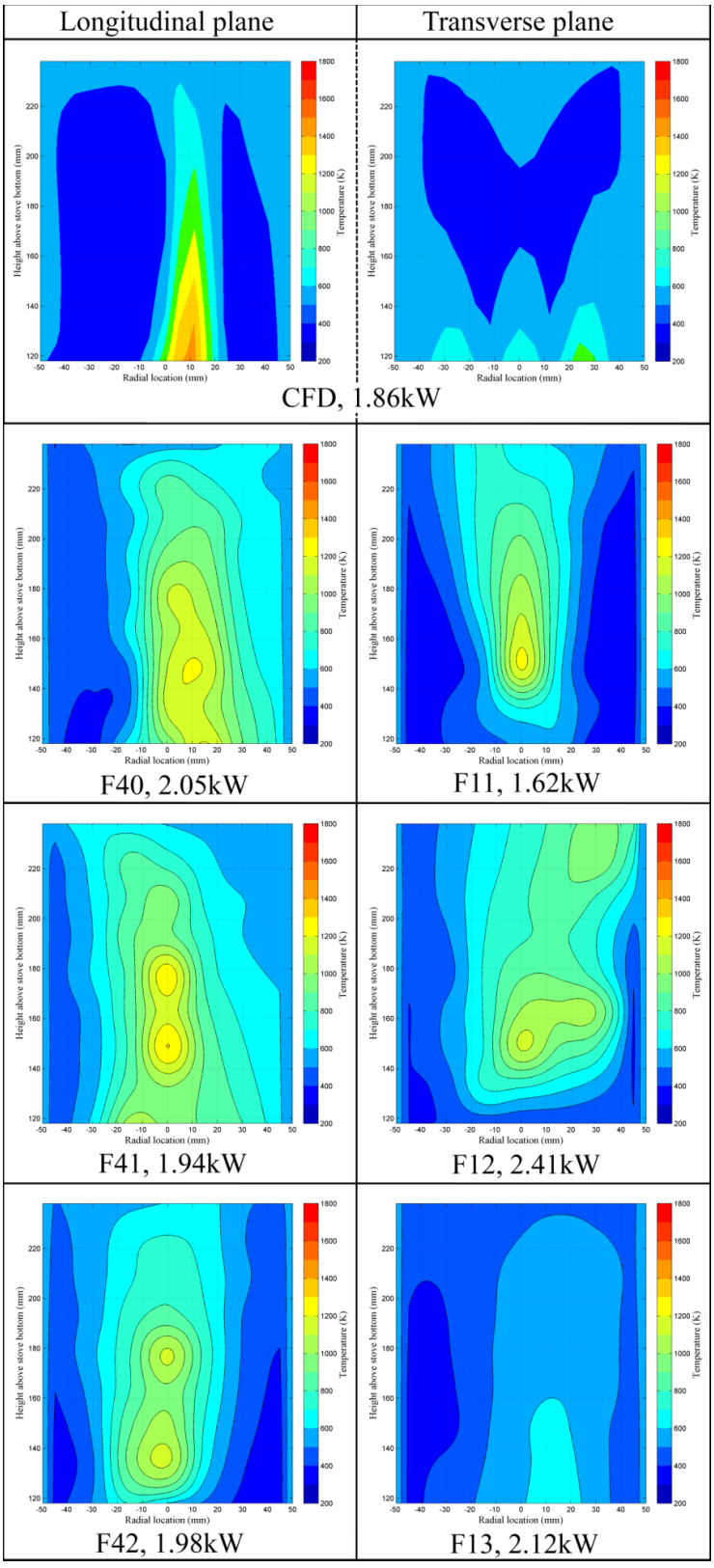

Figure 49: Comparison of 10s CFD simulation contour averages (top) to 40s averages from validation experiment, on longitudinal planes (left) and transverse planes (right). Sample ID and mean firepower listed.

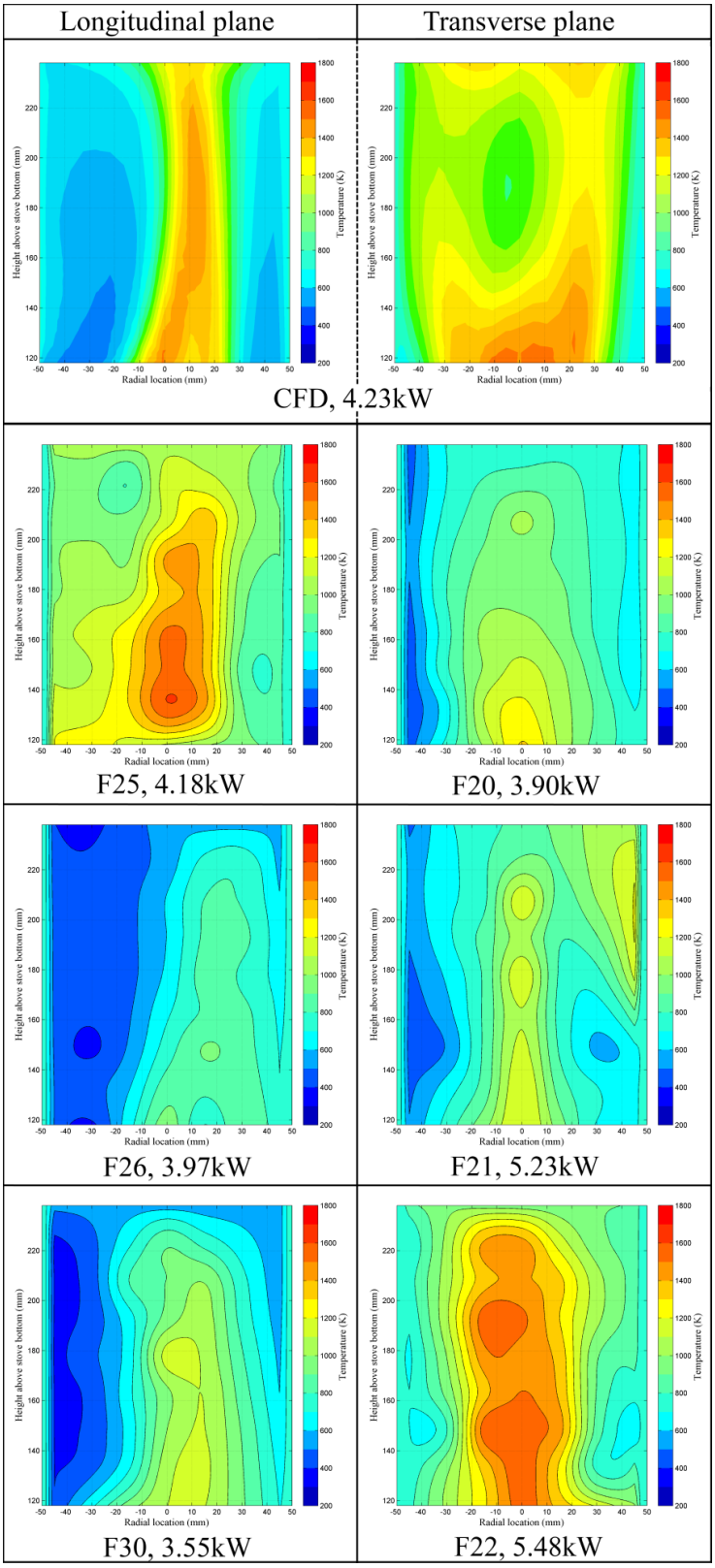

Figure 50: Comparison of 10s CFD simulation contour averages (top) to 40s averages from validation experiment, on longitudinal planes (left) and transverse planes (right). Sample ID and mean firepower listed.

A more elaborate statistical analysis of these fields could provide additional meaning to the combustion scientist or stove designer. For example, analysis of the variation of temperature in the field by way of plotting the standard deviation or perhaps range of the temperature could suggest things about flame position stability and hence possibly emission formation. Post-processing with software such as MATLAB would allow interpretation such as this.

7.2 Velocity field results

Velocity vector field plots are resolved in the CFD simulation but not in the case of the validation stove due to the lack of any equipment to measure velocity. A velocity vector plot is a graphical representation of a field of local flow vectors, usually defined in a particular plane of interest, but can be displayed in three dimensional space. These arrows are usually located at mesh nodes or face centers, and are depicted pointing in the direction of the flow at that location. The length of the arrow represents the relative magnitude of the velocity, as does its color, in reference to a contour colormap.

Results are produced here for the longitudinal and transverse planes. Figure 51 depicts instantaneous vector plots for the longitudinal and transverse planes of the low firepower case. Figure 52 gives a set of four, sequential velocity vector plots for the two major planes in the high firepower case, generated at 0.015s time steps. In this view the flow is fully developed and unsteady flow motions are minimal, yet the difference in the vector plots from one to the next frame is detectable.

A few things are obvious from looking at even static (non-animated) results. The flow acceleration due to buoyant force acting on the heating gas can be seen in both plane views, with the speed increasing as it climbs. Results for steps proceeding backwards or forwards in time give a sense of the flow motion in the stove. Flow circulation can be seen in zones where it naturally occurs, such as at the exit of the pot gap or behind an orifice in the vertical section (not involved

here). Circulating flow structures (eddies), or flows with highly curvilinear paths increases flow residence time. Knowledge of the velocity field is important for consideration of emission formation.

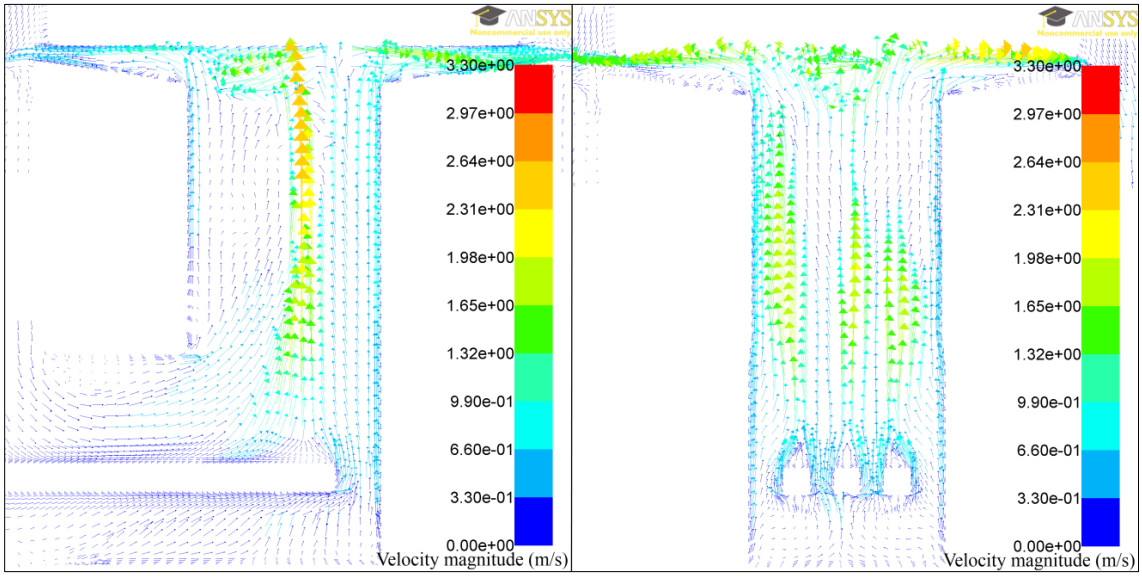

Figure 51: Vector plots of the instantaneous velocity fields on the longitudinal (left) and transverse (right) planes of the low firepower case CFD simulation.

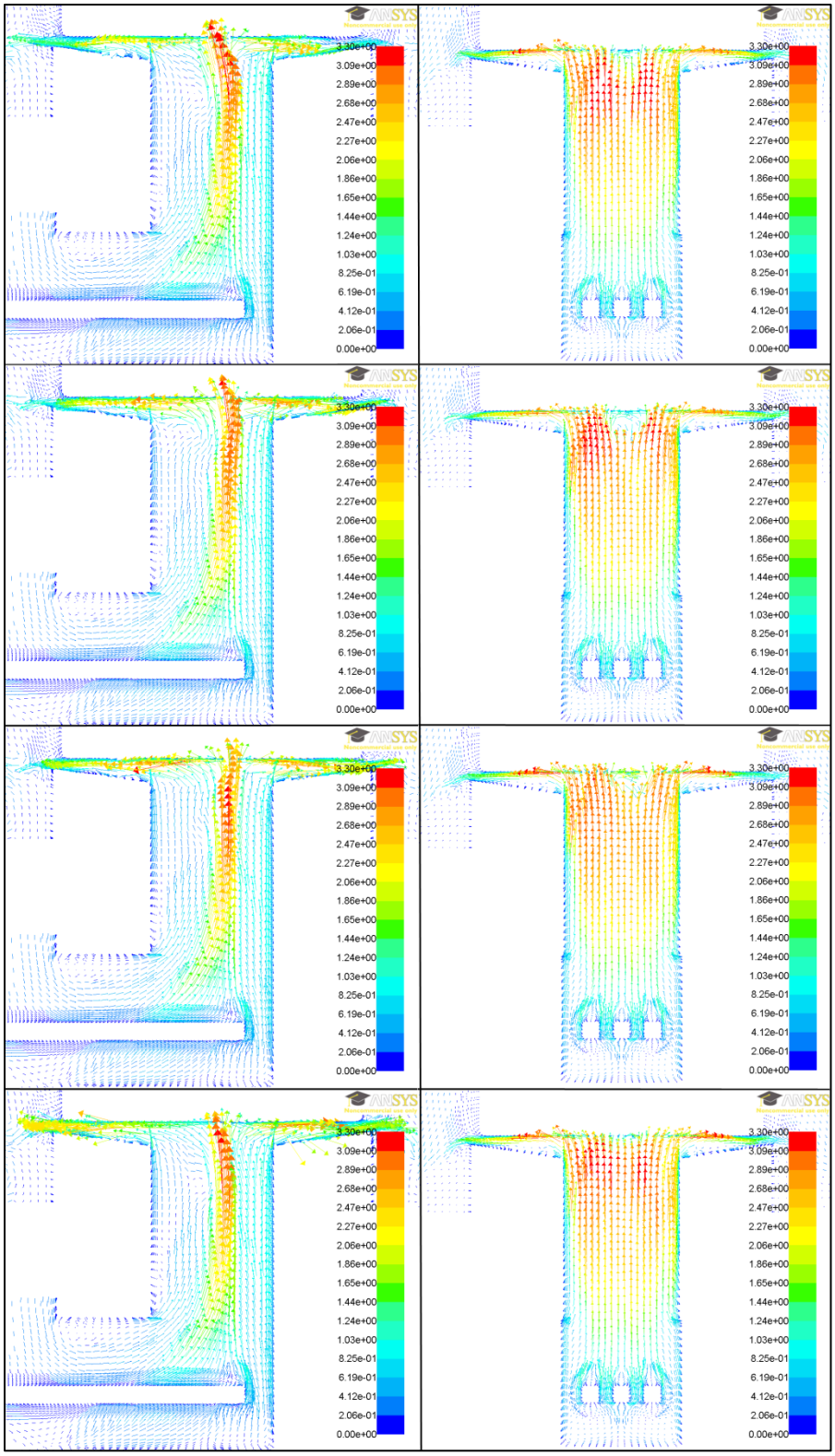

Figure 52: Sequence of instantaneous velocity vector field plots on longitudinal (left) and transverse (right) planes for high-firepower case. Sequence proceeds from top down on 0.015s time steps.

Significant differences can be seen between the velocities in the two firepower cases. This is expected due to the large difference in heating rate, and subsequent volumetric expansion and buoyant motion. Velocity profiles are important and useful to the stove designer. Even without the access to heat transfer results the designer can estimate heat transfer considering the Blasius condition for stagnating flow. The better controlled and directed the flow of gas against the pot, the more useful heat transferred.

7.3 Heat transfer to pot

Bulk heat transfer results are given for the low firepower case in Table 19, and high firepower case in Table 20. Heat transfer rates are comparable between the high firepower case CFD simulation and the hot start G3300 test average, however the difference in firepower must be noted. Considering that the three firepower values are relatively close, the regime of heat transfer can be assumed to be comparable, and the thermal efficiencies considered with greater scrutiny.

Table 19: Final bulk heat transfer results for the low firepower case

Category:	Heat transfer				
Parameter:	Sample firepower (LHV basis)	Heating rate, pot bottom	Heating rate, pot side	Heating rate, net TOTAL	Average thermal efficiency
Units:	(W)	(W)	(W)	(W)	(%)
G3300 simmer phase WBT mean:	1.59E+03	n/a	n/a	n/a	n/a
CFD, Low firepower case, time averaged:	1.79E+03	3.01E+02	-1.95E+01	2.82E+02	15.7%
Validation experiment, Low-firepower, mean:	1.90E+03	3.83E+02	1.21E+01	3.95E+02	21.1%
Disagreement, CFD to G3300 (%):	12.6%	n/a	n/a	n/a	n/a
Disagreement, Val. To G3300 (%):	19.5%	n/a	n/a	n/a	n/a
Disagreement, CFD to val (%):	5.8%	21.4%	261.5%	28.8%	25.8%
Standard deviation, validation samples:	4.61E+02	6.81E+01	5.61E+01	9.13E+01	5.05E-02

Table 20: Final bulk heat transfer results for the high firepower case

Category:	Heat transfer				
Parameter:	Sample firepower (LHV basis)	Heating rate, pot bottom	Heating rate, pot side	Heating rate, net TOTAL	Average thermal efficiency
Units:	(W)	(W)	(W)	(W)	(%)
G3300 hot start WBT mean:	3.74E+03	n/a	n/a	1.10E+03	n/a
CFD, High firepower case, time averaged:	4.09E+03	1.14E+03	-8.03E+00	1.13E+03	27.6%
Validation experiment, High-firepower, mean:	4.10E+03	8.25E+02	1.43E+02	9.69E+02	24.3%
Disagreement, CFD to G3300 (%):	9.2%	n/a	n/a	n/a	n/a
Disagreement, Val. To G3300 (%):	9.6%	n/a	n/a	n/a	n/a
Disagreement, CFD to val (%):	0.3%	37.7%	105.6%	16.6%	13.5%
Standard deviation, validation samples:	7.81E+02	2.18E+02	1.15E+02	2.96E+02	8.53E-02

The highest heat transfer / thermal efficiency of 29.5% is seen in the benchmark data from the G3300 stove. This is a statistically significant value considering the strict methodologies used in the standardized testing and on the fact that the data is calculated from mean values based on fourteen individual samples. The CFD simulation result is considerably close at 27.6%. The CFD simulation data cannot be considered in any statistical manner besides the implication that

can be made in scrutiny of the model itself. It is possible that the assumed pot-to-water heat transfer coefficient may be too low, and hence a significant source of error. Secondly, there are differences between the drip pan regions of the G3300 and validation stove which could make for different gas-to-pot heat transfer. These differences are very hard to evaluate without very detailed experimentation or modeling. The most straightforward way to inspect this may be to conduct a CFD simulation of the validation stove geometry with the drip pan altered to the same as the G3300. The difference in results could be attributed to the drip pan. The validation experiment heat transfer efficiency comes out as the lowest of the three. The reason for this cannot be told without additional, careful study. One possibility is that the validation stove loses more heat through the combustion chamber walls due to having only 30mm of AlSi insulation. That would leave less heat available for transfer to the pot. Finally, it must be noted that the instrumented heat-exchanger pot was itself not rigorously validated. Considering the complications of the transient response, it would be a significant challenge to establish the experimental uncertainty of the device.

Figure 53 depicts critical relations associated with heat transfer during one of the sixty-four, forty-second samples during the experimental validation test. Included is the firepower (LHV basis) as calculated from the delay-corrected emissions stream along with the calculated heating rates into the bottom and side of the instrumented heat-exchanger pot. Thermal efficiency is calculated from these two curves. Fluctuation in firepower and efficiency may be explained by any transient response effects previously discussed in section 6.3, and the transient element of the response of the heat-exchanger pot measurement, itself, also previously discussed in section 6.2. Figures presenting this data from the other sample points can be seen in appendix F.

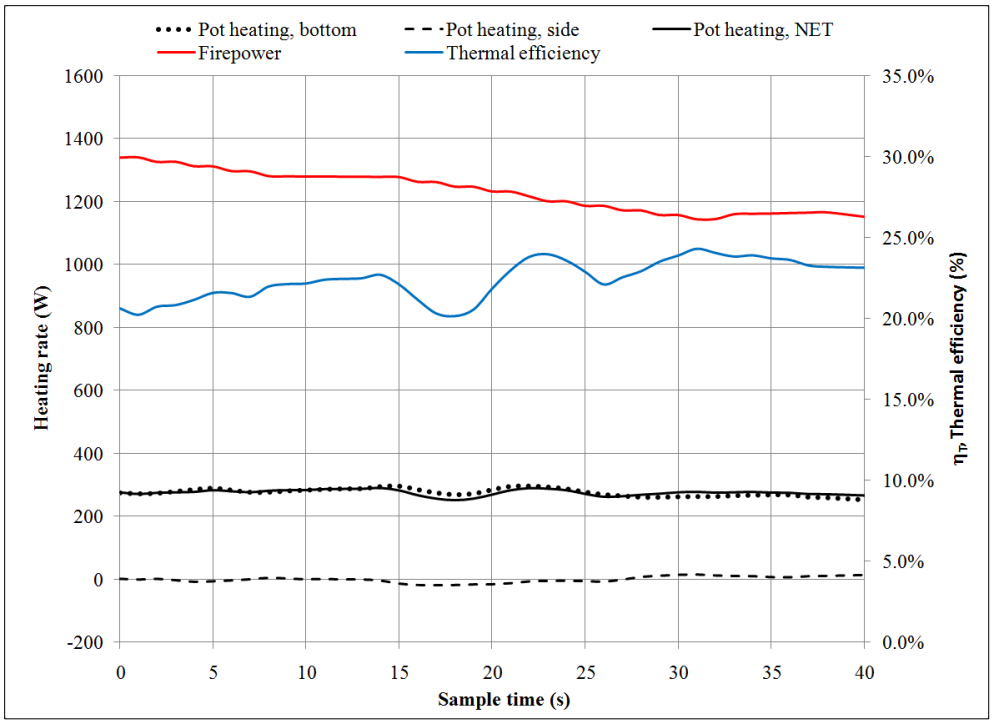

Figure 53: Resolved firepower calculated by emissions, measured heat flux via heat-exchange pot, and the resultant calculated thermal efficiency over the duration of low-firepower sample F10.

Instantaneous heat transfer to the pot is seen in Figure 54. Time-averaged surface heat flux to the cooking pot bottom can be seen in Figure 55, for the high firepower case (~4.1kW). Heat flowing out of the system is in this convention termed a negative flow. Hence, heat flow out of the control volume and into the pot holds a negative sign. The highest heat transfer rates seen in this figure are hence at the two dark zones in the pot center, reaching values of approximately 1.5E5 $W \bullet m^{-2}$. Heat transfer to the pot is an indirect measure of the thermal efficiency of a stove and as such is very important. The pattern seen on the pot bottom is expected to be left/right symmetric. There are several likely sources of asymmetricity to discuss here. The most significant source is likely that a 15 second run time is not quite long enough to get an absolute left/right balance of the unsteady flow fluctuations, and hence and secondarily that the numerical solution is influenced by asymmetricity in the mesh and the flow upstream from the pot surface.

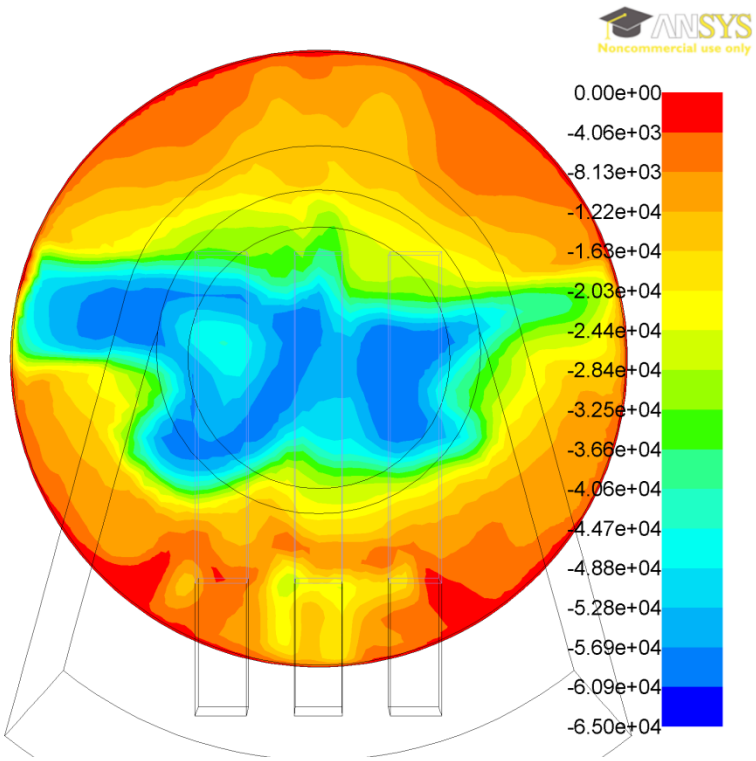

Figure 54: Instantaneous surface heat flux (W•m^{-2}) to bottom of cooking pot for the high firepower case.

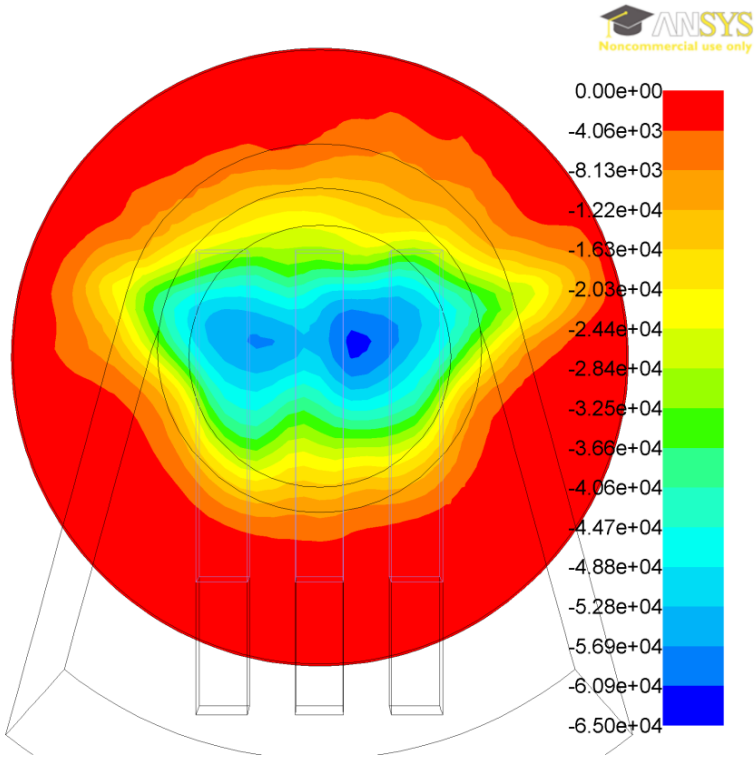

Figure 55: Temporally-averaged surface heat flux (W•m^{-2}) to bottom of cooking pot for the high firepower case.

7.4 Emissions

Emissions formation rates can be seen for the low and high firepower rates in Table 21, and Table 22, respectively. Carbon monoxide values are vastly underpredicted due to the involvement of the mixture fraction formulation for combustion. It can immediately be seen by the As discussed in section 5.4, the mixture fraction approximation holds that reactions proceed from reactants to products as directed by the turbulence-enhanced progress variable. Intermediate products are predicted, in the case of the settings chosen here, by equilibrium chemistry tables, mitigated by non-adiabatic heat-flow considerations. Mixture fraction is known to predict heat release quite well (as explained in section 5.4) since the most energetic and exothermic reactions which define flame position are very fast, and an infinitely-fast reaction approximation is quite useful. Unfortunately, some major players in combustion reactions are not well accounted for by these assumptions. This is definitely the case for carbon monoxide, known in the literature and seen here to be significantly underpredicted with the equilibrium chemistry assumption. One highlight is that the high firepower validation CO production values is only 2.6% off of the benchmark data.

The particular matter emission model failed to even remotely match the experimental data, with reported values for soot prediction approximately ten orders of magnitude low. This is thought to be the result of a lack of accuracy of the chemical species that are specified as the reaction precursors, which are in this case benzene and ethylene. It was thought beforehand that the use of a mixture fraction formulation combustion model may contribute to significant error. Furthermore, the Moss-Brookes soot model was developed to work with methane flames, but the gas composition specified here contains only ~8% methane, by mass. It is not known if the relatively low fraction of methane, or the nature of the mixture fraction formulation, or perhaps other model parameter specifications, are to blame for this severe underprediction.

Table 21: Emission formation for low firepower case

Category:	Emissions	
Parameter:	Carbon monoxide mass flow	PM mass flow
Units:	($g*s^{-1}$)	($g*s^{-1}$)
G3300 simmer phase WBT mean:	4.39E-03	1.69E-04
CFD, Low firepower case, time averaged:	1.91E-07	3.81E-13
Validation experiment, Low-firepower, mean:	6.05E-03	n/a
Disagreement, CFD to G3300 (%):	100.0%	100.0%
Disagreement, Val. To G3300 (%):	37.8%	n/a
Disagreement, CFD to val (%):	100.0%	n/a
Standard deviation, validation samples:	2.54E-03	n/a

Table 22: Emission formation for high firepower case

Category:	Emissions	
Parameter:	Carbon monoxide mass flow	PM mass flow
Units:	($g*s^{-1}$)	($g*s^{-1}$)
G3300 hot start WBT mean:	5.16E-03	8.90E-04
CFD, High firepower case, time averaged:	2.88E-07	1.78E-14
Validation experiment, High-firepower, mean:	5.02E-03	n/a
Disagreement, CFD to G3300 (%):	100.0%	100.0%
Disagreement, Val. To G3300 (%):	2.6%	n/a
Disagreement, CFD to val (%):	100.0%	n/a
Standard deviation, validation samples:	2.99E-03	n/a

8. Conclusion

A unique application-specific CFD simulation has been developed for use in evaluating relatively fine-scale behaviors within small cook stoves burning wood sticks in a relatively high firepower mode of flaming combustion. This modeling scheme is suitable for computation on a common, desktop workstation, within a practical timeframe on the order of one to several days. An experimental validation stove and heat-exchanger pot were designed and constructed to provide quantitative assurance that the CFD simulation was usefully accurate. The initial results are encouraging, suggesting that more development is justified.

A literature review of stove simulations and combustion CFD, and knowledge of the processes of modern stove design for high performance suggests that an accurate, finely resolved flow field may be emphasized at the expense of long time scale phenomena such as stove body heating and a transient fuel condition. This distinction is significant as it suggests that a finely resolved domain is most important to the designer, and is one not presently addressed in most stove simulation techniques. The fine resolution of boundary layers and resulting accurate calculation of heat transfer is very useful for optimizing geometry such as that of the pot-gap region.

A fuel model was selected from the literature considering a steady, time-averaged, lumped, one-step global reaction for the pyrolysis of relatively large particles of wood experiencing fire-level feedback heating. The selected method of calculating the primary pyrolysis gas composition as a simple function of the fuel specific area and not any extensive quantities occurring during reaction is attractive for several reasons. The fuel state can be

configured previous to, and without iterative feedback from the CFD simulation. The effect of different sizes of fuel can be investigated through simulation.

An additional concept is of a fire simulation burner with physical dimensions and parameters identical to the boundary conditions in the CFD model. This burner would feature a porous element from which gas similar to actual net pyrolysis gas could be injected into the stove. A more direct and certain validation of the CFD simulation could be achieved using this simulation burner, featuring parameters that closely match the fuel conditions calculated in the stand-alone lumped fuel model and used in the CFD. The simulation burner would also provide a useful tool for physical testing, with the novel utilities being the ability to control the operating characteristics to be a close surrogate for an actual biomass fire. The concept of this burner, coupled with the demonstrated heat-exchanger pot offer opportunities for further advancement of the improved stove design process.

The study behind this thesis definitely motivates the author and others working at the CSU Clean Cook Stove Laboratory to pursue quantitative, high technology design tools. In light of this the author makes the following recommendations:

- The mixture fraction formulation has been very useful for this initial development but is limited in the amount of reaction fidelity it offers. Work should be done to develop CFD simulations built around higher-fidelity combustion models such as Arrhenius-rate based chemical kinetics, and models featuring more complex mixing and turbulence interactions, such as the eddy-dissipation concept type model.
- Apply a more rigorous study of periodic conjugate heat transfer in order to further develop the technique of using reduced-mass boundaries to attain relevant, stabilized heat transfer values.
- If a high-fidelity combustion model is selected, an adaptive mesh refinement technique will be needed to finely-resolve only the flame front region as needed,

leaving a coarser mesh in other areas. Such an approach is necessary as the computational cost of resolving a flame front is very high.

- Further experimental validation should be conducted with the simplified fuel condition used here. Perhaps bench-scale pyrolysis experiments could be used for this validation, possibly contributing to the development of an additionally stove-specific fuel model.
- Along with the development of an accurate combustion model, specific emission codes may be necessary, especially for the prediction of particulate matter. The chemical composition of the net pyrolysis gas is unique enough that present soot models may never be appropriate. More investigation is needed.
- Further develop the thermocouple-instrumented validation stove. Increase the robustness by employing slightly-heavier gauge thermocouples. Switch to using thermocouple-specific DAQ equipment for lower signal error. Develop a streamlined system for post processing the data, possibly providing real-time computer display for the user. Include the thermal mass transient response correction that as discussed in section 6.1.2. Further develop the testing protocol.
- Continue development of the heat-exchanger cooking pot. Attempt to further reduce the thermal mass and possible develop some correction for the remaining response lag. Rigorously study the error associated with this device.
- Further investigate the error in calculated firepower that is attributable to the transient behavior of exhaust gas within the testing fume hood and emissions equipment. Consider the development of a stove-top emission-probe to minimize the associated concerns.
- Repeat the validation procedure introduced here including stove-top oxygen probe to provide data necessary to validate mass flow through the stove.

9. References

[1] M. Ezzati and D. M. Kammen, "The health impacts of exposure to indoor air pollution from solid fuels in developing countries: knowledge, gaps, and data needs.," *Environmental Health Perspectives*, vol. 110, no. 11, pp. 1057-1068, Nov. 2002.

[2] N. Bruce, R. Perez-Padilla, and R. Albalak, "Indoor air pollution in developing countries: a major environmental and public health challenge," *Bulletin of the World Health Organization*, vol. 78, pp. 1078–1092, 2000.

[3] H. E. S. Mestl, K. Aunan, and H. M. Seip, "Health benefits from reducing indoor air pollution from household solid fuel use in China -- Three abatement scenarios," *Environment International*, vol. 33, no. 6, pp. 831-840, Aug. 2007.

[4] A. Gaye, *Human Development Report 2007/2008 Fighting climate change: Human solidarity in a divided world*. United Nations Development Programme, 2007.

[5] S. Mehta and C. Shahpar, "The health benefits of interventions to reduce indoor air pollution from solid fuel use: a cost-effectiveness analysis," *Energy for Sustainable Development*, vol. 8, no. 3, pp. 53-59, Sep. 2004.

[6] R. A. Cabraal, D. F. Barnes, and S. G. Agarwal, "Productive Uses of Energy for Rural Development," *Annual Review of Environment and Resources*, vol. 30, no. 1, pp. 117-144, 2005.

[7] K. R. Smith, "Biomass combustion and indoor air pollution: the bright and dark sides of small is beautiful," *Environmental Management*, vol. 10, no. 1, pp. 61-74, Jan. 1986.

[8] D. A. Tillman, A. J. Rossi, and W. D. Kitto, *Wood combustion. Principles, processes, and economics.* New York, NY: Academic Press, 1981.

[9] F. Shafizadeh, "Introduction to pyrolysis of biomass," *Journal of Analytical and Applied Pyrolysis*, vol. 3, no. 4, pp. 283-305, Apr. 1982.

[10] A. Demirbas, "Combustion characteristics of different biomass fuels," *Progress in Energy and Combustion Science*, vol. 30, no. 2, pp. 219-230, 2004.

[11] C. Di Blasi, "Modeling and simulation of combustion processes of charring and non-charring solid fuels," *Progress in Energy and Combustion Science*, vol. 19, no. 1, pp. 71-104, 1993.

[12] B. M. Jenkins, L. L. Baxter, T. R. Miles, and T. R. Miles, "Combustion properties of biomass," *Fuel Processing Technology*, vol. 54, no. 1, pp. 17–46, 1998.

[13] D. Mohan, C. U. Pittman,, and P. H. Steele, "Pyrolysis of Wood/Biomass for Bio-oil: A Critical Review," *Energy & Fuels*, vol. 20, no. 3, pp. 848-889, 2006.

[14] A. Demirbas, "Calculation of higher heating values of biomass fuels," *Fuel*, vol. 76, no. 5, pp. 431-434, Apr. 1997.

[15] T. Sonobe and N. Worasuwannarak, "Kinetic analyses of biomass pyrolysis using the distributed activation energy model," *Fuel*, vol. 87, no. 3, pp. 414-421, Mar. 2008.

[16] J. J. M. Orfão, F. J. A. Antunes, and J. L. Figueiredo, “Pyrolysis kinetics of lignocellulosic materials--three independent reactions model,” *Fuel*, vol. 78, no. 3, pp. 349-358, Feb. 1999.

[17] B. Agarwal, “Diffusion of rural innovations: Some analytical issues and the case of wood-burning stoves,” *World Development*, vol. 11, no. 4, pp. 359-376, Apr. 1983.

[18] D. Barnes, K. Openshaw, K. R. Smith, and R. van der Plas, *What Makes People Cook with Improved Biomass Stoves? A comparative International Review of Stove Programs*. The World Bank, 1994.

[19] M. Arnold and R. Persson, “Reassessing the fuelwood situation in developing countries,” *International Forestry Review*, vol. 5, no. 4, pp. 379-383, 2003.

[20] M. Arnold, G. Köhlin, and R. Persson, “Woodfuels, livelihoods, and policy interventions: Changing Perspectives,” *World Development*, vol. 34, no. 3, pp. 596-611, Mar. 2006.

[21] H. W. de Koning, K. R. Smith, and J. M. Last, “Biomass fuel combustion and health,” *Bulletin of the World Health Organization*, vol. 63, no. 1, pp. 11-26, 1985.

[22] K. R. Smith, “Health, energy, and greenhouse-gas impacts of biomass combustion in household stoves,” *Energy for Sustainable Development*, vol. 1, no. 4, pp. 23-29, Nov. 1994.

[23] N. Panwar, A. Kurchania, and N. Rathore, “Mitigation of greenhouse gases by adoption of improved biomass cookstoves,” *Mitigation and Adaptation Strategies for Global Change*, vol. 14, no. 6, pp. 569-578, 2009.

[24] T. Phuket, “Wood Energy, Climate and Health: International Expert Consultation.”

[25] L. Mugerwa, *How to Build the Improved Household Stoves: A Construction Guide for the Rocket - Lorena and Shielded Fire Stoves*. Energy Advisory Project, Ministry of Energy and Mineral development, Republic of Uganda, 2004, pp. 1-35.

[26] P. Scott, *Introduction of Rocket Stove Cooking Devices in Uganda*. Kampala, Uganda: Aprovecho Research Center, 2003, pp. 3-44.

[27] P. Scott, *Rocket Stove Design Guide*. Aprovecho Research Center: Aprovecho Research Center, pp. 1-9.

[28] “Rocket Stove Design Base - Design Tool,” *Rocket Stove Design Base*. [Online]. Available: http://www.rocketstove.org/index.php?option=com_wrapper&Itemid=65. [Accessed: 24-Apr-2010].

[29] S. Baldwin, *Biomass Stoves: Engineering Design, Development, and Dissemination*. Princeton University: Volunteers in Technical Assistance, 1987.

[30] H. Burnham-Slipper, *Eritrean Stove Optimization: Literature Review*. University of Nottingham, 2005.

[31] H. Burnham-Slipper, “Breeding a better stove: The use of Computational Fluid Dynamics and Genetic Algorithms to optimise a wood burning stove for Eritrea,” doctoral dissertation, University of Nottingham, 2008.

[32] R. Bailis, “The Water Boiling Test (WBT),” *Shell Foundation*, 2007.

[33] M. Defoort, B. Willson, and C. L'Orange, “Influence of Testing Parameters on Biomass Stove Performance: Evaluation of Testing Methodologies,” 2010.

[34] C. L'Orange, “Testing methodologies for biomass cook stoves and their effects on emissions,” Colorado State University, 2009.

[35] M. Y. Choi, G. W. Mulholland, A. Hamins, and T. Kashiwagi, “Comparisons of the soot volume fraction using gravimetric and light extinction techniques,” *Combustion and Flame*, vol. 102, no. 1, pp. 161–169, 1995.

[36] G. Tanda and F. Devia, “Application of a schlieren technique to heat transfer measurements in free-convection,” *Experiments in Fluids*, vol. 24, no. 4, pp. 285–290, 1998.

[37] C. Alvarez-Herrera, D. Moreno-Hernández, B. Barrientos-Garc\'ıa, and J. A. Guerrero-Viramontes, “Temperature measurement of air convection using a Schlieren system,” *Optics and Laser Technology*, vol. 41, no. 3, pp. 233–240, 2009.

[38] M. Heitor and A. Moreira, “Thermocouples and sample probes for combustion studies,” *Progress in Energy and Combustion Science*, vol. 19, no. 3, pp. 259-278, 1993.

[39] J. D. Maun, P. B. Sunderland, and D. L. Urban, “Thin-filament pyrometry with a digital still camera,” *Applied Optics*, vol. 46, no. 4, pp. 483-488, Feb. 2007.

[40] C. Di Blasi, “Combustion and gasification rates of lignocellulosic chars,” *Progress in Energy and Combustion Science*, vol. 35, no. 2, pp. 121-140, Apr. 2009.

[41] A. TenWolde, J. D. McNatt, and L. Krahn, *Thermal properties of wood and wood panel products for use in buildings*. 1988.

[42] M. Balat, “Mechanisms of Thermochemical Biomass Conversion Processes. Part 1: Reactions of Pyrolysis,” *Energy Sources, Part A: Recovery, Utilization, and Environmental Effects*, vol. 30, no. 7, pp. 620-635, 2008.

[43] C. Brage, Q. Yu, and K. Sjöström, “Characteristics of evolution of tar from wood pyrolysis in a fixed-bed reactor,” *Fuel*, vol. 75, no. 2, pp. 213-219, Jan. 1996.

[44] C. Di Blasi, G. Signorelli, C. Di Russo, and G. Rea, “Product Distribution from Pyrolysis of Wood and Agricultural Residues,” *Industrial & Engineering Chemistry Research*, vol. 38, no. 6, pp. 2216-2224, Jun. 1999.

[45] E. Cetin, B. Moghtaderi, R. Gupta, and T. F. Wall, “Influence of pyrolysis conditions on the structure and gasification reactivity of biomass chars,” *Fuel*, vol. 83, no. 16, pp. 2139–2150, 2004.

[46] O. Senneca, “Kinetics of pyrolysis, combustion and gasification of three biomass fuels,” *Fuel Processing Technology*, vol. 88, no. 1, pp. 87-97, Jan. 2007.

[47] M. J. Spearpoint and J. G. Quintiere, “Predicting the burning of wood using an integral model,” *Combustion and Flame*, vol. 123, no. 3, pp. 308-325, Nov. 2000.

[48] B. Moghtaderi, V. Novozhilov, D. Fletcher, and J. H. Kent, “An integral model for the transient pyrolysis of solid materials,” *Fire and Materials*, vol. 21, no. 1, pp. 7-16, 1997.

[49] J. N. Agenbroad, “A Simplified Model for Understanding Natural Convection Driven,” Colorado State University, 2010.

[50] G. Cox and R. Chitty, “Some stochastic properties of fire plumes,” *Fire and Materials*, vol. 6, no. 3, pp. 127-134, 1982.

[51] G. Heskestad, “Dynamics of the Fire Plume,” *Philosophical Transactions: Mathematical, Physical and Engineering Sciences*, vol. 356, no. 1748, pp. 2815-2833, Dec. 1998.

[52] E. Zukoski, B. Cetegen, and T. Kubota, “Visible structure of buoyant diffusion flames,” *Symposium (International) on Combustion*, vol. 20, no. 1, pp. 361-366, 1985.

[53] F. Liu and J. X. Wen, “The effect of turbulence modelling on the CFD simulation of buoyant diffusion flames,” *Fire Safety Journal*, vol. 37, no. 2, pp. 125–150, 2002.

[54] Y. Liu, K. Lee, R. Perez-Padilla, N. Hudson, and D. Mannino, "Outdoor and indoor air pollution and COPD-related diseases in high- and low-income countries [State of the Art Series. Chronic obstructive pulmonary disease in high- and low-income countries. Edited by G. Marks and M. Chan-Yeung. Number 2 in the series]," *The International Journal of Tuberculosis and Lung Disease*, vol. 12, pp. 115-127, Feb. 2008.

[55] P. Chatterjee, J. L. de Ris, Y. Wang, and S. B. Dorofeev, "A model for soot radiation in buoyant diffusion flames," *Proceedings of the Combustion Institute*, vol. 33, no. 2, pp. 2665-2671, 2011.

[56] J. L. Rhatigan, H. Bedir, and J. S. T'ien, "Gas-phase radiative effects on the burning and extinction of a solid fuel," *Combustion and Flame*, vol. 112, no. 1, pp. 231-241, Jan. 1998.

[57] S. Bhattacharjee and W. L. Grosshandler, "Effect of radiative heat transfer on combustion chamber flows," *Combustion and Flame*, vol. 77, no. 3, pp. 347-357, Sep. 1989.

[58] S. B. Kausley and A. B. Pandit, "Modelling of solid fuel stoves," *Fuel*, vol. 89, no. 3, pp. 782-791, Mar. 2010.

[59] A. Horvat and Y. Sinai, *Validation of two-equation turbulence models for heat transfer applications*. Didcot, UK: ANSYS CFX, 2003.

[60] D. T. CONROY and S. G. L. SMITH, "Endothermic and Exothermic Chemically Reacting Plumes," *Journal of Fluid Mechanics*, vol. 612, pp. 291-310, 2008.

[61] H. Xue, J. C. Ho, and Y. M. Cheng, "Comparison of different combustion models in enclosure fire simulation," *Fire Safety Journal*, vol. 36, no. 1, pp. 37-54, Feb. 2001.

[62] D. Menghini, T. Marchione, G. Martino, F. S. Marra, C. Allouis, and F. Beretta, "Numerical and experimental investigations to lower environmental impact of an open fireplace," *Experimental Thermal and Fluid Science*, vol. 31, no. 5, pp. 477–482, 2007.

[63] D. Menghini, F. S. Marra, C. Allouis, and F. Beretta, "Effect of excess air on the optimization of heating appliances for biomass combustion," *Experimental Thermal and Fluid Science*, vol. 32, no. 7, pp. 1371–1380, 2008.

[64] M. R. Ravi, A. Jhalani, S. Sinha, and A. Ray, "Development of a semi-empirical model for pyrolysis of an annular sawdust bed," *Journal of Analytical and Applied Pyrolysis*, vol. 71, no. 1, pp. 353-374, Mar. 2004.

[65] M. Ravi, S. Kohli, and A. Ray, "Use of CFD simulation as a design tool for biomass stoves," *Energy for Sustainable Development*, vol. 6, no. 2, pp. 20-27, Jun. 2002.

[66] M. Bojko and M. Branc, "A definition of the mathematical model of combustion process in the stove," *Journal of applied science in the thermodynamics and fluid mechanics*, vol. 3, 2009.

[67] K. M. Bryden and D. S. McCorkle, "Evolutionary optimization of energy systems using population graphing and neural networks," *Advances in Engineering Software*, vol. 35, no. 5, pp. 289–299, 2004.

[68] K. M. Bryden, D. A. Ashlock, D. S. McCorkle, and G. L. Urban, "Optimization of heat transfer utilizing graph based evolutionary algorithms," *International Journal of Heat and Fluid Flow*, vol. 24, no. 2, pp. 267–277, 2003.

[69] G. L. Urban, K. M. Bryden, and D. A. Ashlock, "Engineering optimization of an improved plancha stove," *Energy for Sustainable Development*, vol. 6, no. 2, pp. 9-19, Jun. 2002.

[70] H. Y. Wang, M. Coutin, and J. M. Most, “Large-eddy-simulation of buoyancy-driven fire propagation behind a pyrolysis zone along a vertical wall,” *Fire Safety Journal*, vol. 37, no. 3, pp. 259-285, Apr. 2002.

[71] S. Hostikka and K. B. McGrattan, “Large eddy simulation of wood combustion,” in *Proceedings of the Ninth International Interflam Conference*, pp. 755–762.

[72] G. H. Yeoh and K. K. Yuen, *Computational fluid dynamics in fire engineering theory, modelling and practice*. Amsterdam ;: Elsevier/Academic Press, 2009.

[73] ANSYS, Inc., “ANSYS FLUENT Theory Guide, Release 13.0,” ANSYS, Inc., Nov-2010.

[74] R. Bailis, D. Ogle, N. MacCarty, and D. Still, *The Water Boiling Test (WBT)*. 2007, pp. 36-38.

[75] G. Ballard-Tremeer and H. H. Jawurek, “Comparison of five rural, wood-burning cooking devices: Efficiencies and emissions,” *Biomass and Bioenergy*, vol. 11, no. 5, pp. 419-430, 1996.

[76] D. Zube, “Heat transfer efficiency of biomass cookstoves,” Colorado State University.

[77] T. Fujii and H. Imura, “Natural-convection heat transfer from a plate with arbitrary inclination,” *International Journal of Heat and Mass Transfer*, vol. 15, no. 4, pp. 755-764, IN5-IN6, 765-767, Apr. 1972.

[78] S. W. Churchill and H. H. S. Chu, “Correlating equations for laminar and turbulent free convection from a vertical plate,” *International Journal of Heat and Mass Transfer*, vol. 18, no. 11, pp. 1323-1329, Nov. 1975.

[79] “Fiberfrax Refractory Ceramic Fiber - Fiberfrax High Temperature Insulation.” [Online]. Available: http://www.fiberfrax.com/. [Accessed: 17-Mar-2011].

[80] B. Moghtaderi, “The state-of-the-art in pyrolysis modelling of lignocellulosic solid fuels,” *Fire and Materials*, vol. 30, no. 1, pp. 1-34, 2006.

[81] M. Miltner, A. Makaruk, M. Harasek, and A. Friedl, “Computational fluid dynamic simulation of a solid biomass combustor: modelling approaches,” *Clean Technologies and Environmental Policy*, vol. 10, no. 2, pp. 165-174, 2008.

[82] R. Zanzi, K. Sjöström, and E. Björnbom, “Rapid high-temperature pyrolysis of biomass in a free-fall reactor,” *Fuel*, vol. 75, no. 5, pp. 545-550, Apr. 1996.

[83] H. Thunman, F. Niklasson, F. Johnsson, and B. Leckner, “Composition of Volatile Gases and Thermochemical Properties of Wood for Modeling of Fixed or Fluidized Beds,” *Energy & Fuels*, vol. 15, no. 6, pp. 1488-1497, Nov. 2001.

[84] C. Di Blasi, E. G. Hernandez, and A. Santoro, “Radiative Pyrolysis of Single Moist Wood Particles,” *Industrial & Engineering Chemistry Research*, vol. 39, no. 4, pp. 873-882, Apr. 2000.

[85] M. J. Spearpoint and J. G. Quintiere, “Predicting the piloted ignition of wood in the cone calorimeter using an integral model -- effect of species, grain orientation and heat flux,” *Fire Safety Journal*, vol. 36, no. 4, pp. 391-415, Jun. 2001.

[86] C. K. Law, *Combustion Physics*, 1st ed. Cambridge University Press, 2006.

[87] J. E. Floyd, “CFD Fire Simulation Using Mixture Fraction Combustion and Finite Volume Radiative Heat Transfer,” *Journal of Fire Protection Engineering*, vol. 13, no. 1, pp. 11-36, 2003.

[88] J. E. Floyd and K. B. McGrattan, “Multiple Parameter Mixture Fraction with Two-step Combustion Chemistry for Large Eddy Simulation,” in *Proceedings of 10th Interflam conference, London*, 2007.

[89] K. B. McGrattan and J. E. Floyd, *A mixture fraction combustion model for large scale fire simulation*. National Institute of Standards and Technology, 2001, pp. 1-5.

[90] Y. Xin, J. Gore, K. McGrattan, R. Rehm, and H. Baum, “Fire dynamics simulation of a turbulent buoyant flame using a mixture-fraction-based combustion model,” *Combustion and Flame*, vol. 141, no. 4, pp. 329-335, Jun. 2005.

[91] B. Böhm, J. Brübach, C. Ertem, and A. Dreizler, “Experiments for Combustion-LES Validation,” *Flow, Turbulence and Combustion*, vol. 80, no. 4, pp. 507-529, 2008.

[92] W. Kays, M. Crawford, and B. Weigand, *Convective Heat and Mass Transfer*, 4th ed. New York, NY: McGraw-Hill, 2005.

[93] S. J. Brookes and J. B. Moss, “Predictions of soot and thermal radiation properties in confined turbulent jet diffusion flames,” *Combustion and Flame*, vol. 116, no. 4, pp. 486–503, 1999.

[94] J. B. Moss, C. D. Stewart, and K. J. Young, “Modeling soot formation and burnout in a high temperature laminar diffusion flame burning under oxygen-enriched conditions,” *Combustion and Flame*, vol. 101, no. 4, pp. 491-500, Jun. 1995.

[95] K. Kar, S. Roberts, R. Stone, M. Oldfield, and B. French, “Instantaneous Exhaust Temperature Measurements Using Thermocouple Compensation Techniques,” presented at the SAE 2004 World Congress & Exhibition, Detroit, MI, 2004.

[96] M. Tagawa, K. Kato, and Y. Ohta, “Response compensation of temperature sensors: Frequency-domain estimation of thermal time constants,” *Review of Scientific Instruments*, vol. 74, no. 6, p. 3171, 2003.

[97] A. Duport, P. Paranthoen, J. C. Lecordier, and P. Gajan, “Influence of temperature on the frequency response of fine-wire thermocouples over the range (300K-800K) in airflows,” *Journal of Physics E: Scientific Instruments*, vol. 17, no. 9, pp. 808-812, 1984.

[98] C. Petit, P. Gajan, J. C. Lecordier, and P. Paranthoen, “Frequency response of fine wire thermocouple,” *Journal of Physics E: Scientific Instruments*, vol. 15, no. 7, pp. 760-770, 1982.

[99] M. Tagawa and Y. Ohta, “Two-thermocouple probe for fluctuating temperature measurement in combustion—Rational estimation of mean and fluctuating time constants,” *Combustion and Flame*, vol. 109, no. 4, pp. 549–560, 1997.

[100] M. Tagawa, K. Kato, and Y. Ohta, “Response compensation of fine-wire temperature sensors,” *Review of Scientific Instruments*, vol. 76, no. 9, p. 094904, 2005.

[101] N. Seiichi and O. Takuro, “Heat transfer from a horizontal circular wire at small reynolds and grashof numbers--I: Pure convection,” *International Journal of Heat and Mass Transfer*, vol. 18, no. 3, pp. 387-396, Mar. 1975.

[102] T. Tsuji, Y. Nagano, and M. Tagawa, “Frequency response and instantaneous temperature profile of cold-wire sensors for fluid temperature fluctuation measurements,” *Experiments in Fluids*, vol. 13, no. 2, pp. 171-178, 1992.

[103] R. Weast, *CRC handbook of chemistry and physics*, 3rd ed. Boca Raton, FL: CRC Press, LLC, 1978.

[104] A. F. Mills, *Basic heat and mass transfer*, 1st ed. Chicago: Irwin, 1995.

APPENDIX A – Full set of bulk result data

Category:	Heat transfer					Emissions		Flow rates	
Parameter:	Sample firepower (LHV basis)	Heating rate, pot bottom	Heating rate, pot side	Heating rate, net TOTAL	Average thermal efficiency	Carbon monoxide mass flow	PM mass flow	Mass flow rate	Volumetric flow rate (@ ref)
Units:	(W)	(W)	(W)	(W)	(%)	($g*s^{-1}$)	($g*s^{-1}$)	($g*s^{-1}$)	(m^3*s^{-1})
G3300 simmer phase WBT mean:	**1.59E+03**	n/a	n/a	n/a	n/a	**4.39E-03**	**1.69E-04**	n/a	n/a
CFD, Low firepower case, time averaged:	**1.79E+03**	**3.01E+02**	**-1.95E+01**	**2.82E+02**	**15.7%**	**1.91E-07**	**3.81E-13**	**2.16E+00**	**2.09E-03**
Validation experiment, Low-firepower, mean:	**1.90E+03**	**3.83E+02**	**1.21E+01**	**3.95E+02**	**21.1%**	**6.05E-03**	n/a	n/a	n/a
Disagreement, CFD to G3300 (%):	**12.6%**	n/a	n/a	n/a	n/a	**100.0%**	**100.0%**	n/a	n/a
Disagreement, Val. To G3300 (%):	**19.5%**	n/a	n/a	n/a	n/a	**37.8%**	n/a	n/a	n/a
Disagreement, CFD to val (%):	**5.8%**	**21.4%**	**261.5%**	**28.8%**	**25.8%**	**100.0%**	n/a	n/a	n/a
Standard deviation, validation samples:	**4.61E+02**	**6.81E+01**	**5.61E+01**	**9.13E+01**	**5.05E-02**	**2.54E-03**	n/a	n/a	n/a
Validation sample F10	1.19E+03	2.74E+02	1.69E+00	2.76E+02	21.3%	7.280E-03	n/a	n/a	n/a
Validation sample F11	1.56E+03	4.16E+02	-9.28E+01	3.23E+02	20.6%	2.147E-03	n/a	n/a	n/a
Validation sample F12	2.33E+03	5.15E+02	-4.16E+00	5.11E+02	22.0%	6.790E-03	n/a	n/a	n/a
Validation sample F13	2.05E+03	4.16E+02	9.80E+01	5.14E+02	25.1%	3.814E-03	n/a	n/a	n/a
Validation sample F17	2.70E+03	3.85E+02	6.29E+01	4.48E+02	16.6%	2.555E-03	n/a	n/a	n/a
Validation sample F35	1.44E+03	3.97E+02	5.71E+01	4.54E+02	31.6%	6.712E-03	n/a	n/a	n/a
Validation sample F40	1.99E+03	3.18E+02	-2.75E+01	2.91E+02	14.6%	7.907E-03	n/a	n/a	n/a
Validation sample F41	1.99E+03	3.46E+02	-1.67E+00	3.44E+02	17.3%	8.614E-03	n/a	n/a	n/a
Validation sample F42	1.87E+03	3.81E+02	1.52E+01	3.96E+02	21.2%	8.597E-03	n/a	n/a	n/a

Category:	Heat transfer					Emissions		Flow rates	
Parameter:	Sample firepower (LHV basis)	Heating rate, pot bottom	Heating rate, pot side	Heating rate, net TOTAL	Average thermal efficiency	Carbon monoxide mass flow	PM mass flow	Mass flow rate	Volumetric flow rate (@ ref)
Units:	(W)	(W)	(W)	(W)	(%)	($g*s^{-1}$)	($g*s^{-1}$)	($g*s^{-1}$)	(m^3*s^{-1})
G3300 hot start WBT mean:	**3.74E+03**	n/a	n/a	**1.10E+03**	n/a	**5.16E-03**	**8.90E-04**	n/a	n/a
CFD, High firepower case, time averaged:	**4.09E+03**	**1.14E+03**	**-8.03E+00**	**1.13E+03**	**27.6%**	**2.88E-07**	**1.78E-14**	**2.85E+00**	**2.60E-03**
Validation experiment, High-firepower, mean:	**4.10E+03**	**8.25E+02**	**1.43E+02**	**9.69E+02**	**24.3%**	**5.02E-03**	n/a	n/a	n/a
Disagreement, CFD to G3300 (%):	**9.2%**	n/a	n/a	n/a	n/a	**100.0%**	**100.0%**	n/a	n/a
Disagreement, Val. To G3300 (%):	**9.6%**	n/a	n/a	n/a	n/a	**2.6%**	n/a	n/a	n/a
Disagreement, CFD to val (%):	**0.3%**	**37.7%**	**105.6%**	**16.6%**	**13.5%**	**100.0%**	n/a	n/a	n/a
Standard deviation, validation samples:	**7.81E+02**	**2.18E+02**	**1.15E+02**	**2.96E+02**	**8.53E-02**	**2.99E-03**	n/a	n/a	n/a
Validation sample F20	3.76E+03	5.63E+02	2.94E+01	5.92E+02	15.8%	7.514E-03	*n/a*	*n/a*	*n/a*
Validation sample F21	5.06E+03	5.81E+02	9.80E+01	6.79E+02	13.4%	9.844E-03	*n/a*	*n/a*	*n/a*
Validation sample F22	5.31E+03	1.02E+03	3.75E+01	1.06E+03	20.0%	6.846E-03	*n/a*	*n/a*	*n/a*
Validation sample F25	4.05E+03	1.12E+03	2.40E+02	1.36E+03	33.6%	2.698E-03	*n/a*	*n/a*	*n/a*
Validation sample F26	3.84E+03	9.65E+02	3.06E+02	1.27E+03	33.1%	2.432E-03	*n/a*	*n/a*	*n/a*
Validation sample F27	3.29E+03	8.11E+02	2.39E+02	1.05E+03	32.0%	2.755E-03	*n/a*	*n/a*	*n/a*
Validation sample F30	3.43E+03	7.15E+02	5.17E+01	7.67E+02	22.4%	3.085E-03	*n/a*	*n/a*	*n/a*

APPENDIX B – Fuel model calculation spreadsheet

Ave. Pyrolysis front temp (K):	800
Reference temperature (K):	298
Boiling water temperature (K):	368.33
Dry wood mass flow rate ($g*s^{-1}$):	2.253E-01
Wood water mass fraction, $Y_{water,\ dry\ basis}$:	0.07
Heat release at complete combustion, LHV basis (W):	4.089E+03
Fuel specific area (m^{-1}):	319
Derived heat of gasification, end-grain ($J*g^{-1}$):	1.600E+03
Derived heat of gasification, cross-grain ($J*g^{-1}$):	2.900E+03
Average surface heat flux ($W*m^{-2}$):	4.500E+04

Steady flow mass balance	
Dry wood, IN ($g*s^{-1}$):	2.253E-01
Intrinsic water, IN ($g*s^{-1}$):	1.577E-02
O2 for CO oxidation, IN ($g*s^{-1}$):	6.551E-02
Primary (dry wood) pyrolysis gas, OUT ($g*s^{-1}$):	1.761E-01
CO from heterogeneous reaction, OUT ($g*s^{-1}$):	1.147E-01
Vaporized intrinsic water, OUT ($g*s^{-1}$):	1.577E-02
NET BALANCE ($g*s^{-1}$):	4.637E-06

Steady flow energy balance - dry wood to PRIMARY pyrolysis gas	
$E\_dot_{reactants,primary}$ ($J*s^{-1}$):	*3585*
$E\_dot_{products,primary}$ ($J*s^{-1}$):	*-897*
$E\_dot_{net,primary}$ ($J*s^{-1}$):	*4481*
$E\_dot_{dev.,Spearpoint}$, from empirical findings of Spearpoint ($J*s^{-1}$):	**-617**

***Another option is consideration of the Spearpoint heat of pyrolysis**			
Parameter (Y_a/Y_b)	**Symbol, R_i**	**mass ratio (Y_a/Y_b)**	**Function of**
Char/dry wood	R_1	2.18E-01	Specific area
H2/P.D.G.	R_2	6.00E-03	Explicit
T.H.C./CO_2	R_3	1.23E+00	Specific area
(CH_4+C_2H_4)/CO_2	R_4	1.05E+00	nominal, fixed range
CH_4/C_2H_4	R_5	2.50E+00	nominal, fixed range
CO/CO_2	R_6	2.32E+00	Specific area
H_2O/CO_2	R_7	9.82E-01	Specific area

***Light = C_2H_4+CH_4**

Primary dry total products (dry wood -> primary pyrolysis gas + char)				
	$Y_{PDT,i}$	$X_{PDT,i}$	$m\_dot_{arbitrary\text{-}PDT,i}$ (CO^2=1)	$m\_dot_{PDT,i}$ ($g*s^{-1}$)
H_2*	0.005	0.045	3.339E-02	1.057E-03
H_2O	0.138	0.149	9.816E-01	3.107E-02
CH_4	0.105	0.128	7.500E-01	2.374E-02
C_2H_4	0.042	0.029	3.000E-01	9.495E-03
C_6H_6	0.026	0.006	1.835E-01	5.808E-03
CO	0.325	0.226	2.316E+00	7.331E-02
CO_2	0.140	0.062	*1.000E+00*	3.165E-02
Char, C(s)	0.218	0.354	(direct ratio)	4.917E-02
SUM:	**1.000**	**1.000**	**N/a**	**2.253E-01**

Primary dry gas (primary pyrolysis product)							
	$Y_{PDG,i}$	$X_{PDG,i}$	$m\_dot_{PDG,i}$ ($g*s^{-1}$)	$X_{PDG,i} * MW_i$ ($g*mol^{-1}$)	$Y_{PDG,i} * HHV_i$ ($J*g^{-1}$)	$Y_{PDG,i} * h^0_{,i}$ ($j*g^{-1}$)	$Y_{PDG,i} * c_{p,i}$ ($j*g^{-1}*K^{-1}$)
H_2*	0.006	0.070	1.057E-03	1.413E-01	8.507E+02	0	8.780E-02
H_2O	0.176	0.231	3.107E-02	4.155E+00	0.000E+00	-2368	3.543E-01
CH_4	0.135	0.198	2.374E-02	3.175E+00	7.484E+03	-629	4.198E-01
C_2H_4	0.054	0.045	9.495E-03	1.270E+00	2.712E+03	100	1.219E-01
C_6H_6	0.033	0.010	5.808E-03	7.767E-01	1.394E+03	35	6.084E-02
CO	0.416	0.350	7.331E-02	9.804E+00	4.204E+03	-1643	4.519E-01
CO_2	0.180	0.096	3.165E-02	4.233E+00	0.000E+00	-1607	1.853E-01
SUM:	**1.000**	**1.000**	**1.761E-01**	**2.355E+01**	**1.665E+04**	**-6.111E+03**	**1.682E+00**

Net control volume gas (lumped reaction product)							
	$Y_{NCVG,i}$	$X_{NCVG,i}$	$m\_dot_{NCVG,i}$ ($g*s^{-1}$)	MW_i ($g*mol^{-1}$)	$Y_{NCVG,i} * HHV_i$ ($J*g^{-1}$)	$Y_{NCVG,i} * h^0_{,i}$ ($j*g^{-1}$)	$Y_{NCVG,i} * c_{p,i}$ ($j*g^{-1}*K^{-1}$)
H_2*	0.003	0.042	1.057E-03	8.490E-02	4.888E+02	0	5.044E-02
H_2O	0.153	0.209	4.684E-02	3.763E+00	0.000E+00	-2051	3.069E-01
CH_4	0.077	0.119	2.374E-02	1.907E+00	4.300E+03	-361	2.412E-01
C_2H_4	0.031	0.027	9.495E-03	7.629E-01	1.558E+03	58	7.006E-02
C_6H_6	0.019	0.006	5.808E-03	4.666E-01	8.009E+02	20	3.495E-02
CO	0.613	0.539	1.880E-01	1.510E+01	6.193E+03	-2420	6.657E-01
CO_2	0.103	0.058	3.165E-02	2.543E+00	0.000E+00	-923	1.064E-01
SUM:	**1.000**	**1.000**	**3.06571E-01**	**2.463E+01**	**1.334E+04**	**-5.677E+03**	**1.476E+00**

SUM description: Sum check = 1.000 ɹm check = 1.000

Upper flammability limit as calculated by Le Chatelier's principle				
	$X^{ND}_{NCVG,i}$	$X^{D}_{NCVG,i}$	$X^{ND}_{NCVG,i}/UFL_i$	$X^{D}_{NCVG,i}/UFL_i$
H_2*	0.005	0.042	6.178E-03	5.615E-02
H_2O	0.000	0.209		
CH_4	0.104	0.119	6.505E-01	7.430E-01
C_2H_4	0.042	0.027	1.156E-01	7.554E-02
C_6H_6	0.025	0.006	3.265E-01	7.658E-02
CO	0.824	0.539	1.114E+00	7.286E-01
CO_2	0.000	0.058		
SUM:	1.000	1.000	**4.520E-01**	**5.953E-01**

Composition		Properties					
Phase	Species	MW (g/mol)	HHV (J/g)	LHV (J/g)	UFL (X_i) w/ air	h^0, Enthalpy of formation @ 298.15K (J*mole^{-1})	h^0, Enthalpy of formation @ 298.15K (J*g^{-1})
Gas	**H_2***	2.016	141790	121000	0.750	0	0
	H_2O	18.016	0	0	*0.000*	-241845	-13424
	CH_4	16.043	55528	50000	0.160	-74831	-4664
	C_2H_4	28.054	50313	47175	0.360	52283	1864
	C_6H_6	78.113	42277		0.078	82927	1062
	CO	28.010	10100	10100	0.740	-110541	-3946
	CO_2	44.011	0	0	*0.000*	-393546	-8942
	O_2	31.999	0	0	0.000	0	0
Solid	**C(s) (graphite)**	12.011	32808	32808	N/a	0	0
	Dry wood	99.197	19470	18072	N/a	1578233	15910
	Wet wood	-	18196	17436	N/a	N/a	N/a

*From Thunman

*CSA B415.1-10

Model name		Status	Bulk Size (mm)	misc desc.	Interpolation model
SENSITIVITY	1	Fail	7	rounded sticks	none - started from initiations
SENSITIVITY	2	Fail	6	rounded sticks	none - started from initiations
SENSITIVITY	3	Fail	7	rounded sticks	none - started from initiations
SENSITIVITY	4	Complete	7	removed stick rounds	none - started from initiations
SENSITIVITY	5	Fail	7	larger rounds	SENSITIVITY-004-6_375-interpolate
SENSITIVITY	6	Fail	7	single large stick	SENSITIVITY-004-6_375-interpolate
SENSITIVITY	7	Complete	7	1st successful size function	SENSITIVITY-004-6_375-interpolate
SENSITIVITY	8	Complete	6	Successful size function with smaller bulk	SENSITIVITY-004-6_375-interpolate
SENSITIVITY	9	Fail	8	-	SENSITIVITY-004-6_375-interpolate
SENSITIVITY	10	Complete	7	growth function off pot bottom and outlets	SENSITIVITY-004-6_375-interpolate
SENSITIVITY	11	Complete	7	Excellent-looking behavior at top	SENSITIVITY-004-6_375-interpolate
SENSITIVITY	12	Complete	6	Computational repeatability study - Additonal 8s run of model 08, statistics reset	SENSITIVITY-004-6_375-interpolate
SENSITIVITY	13	Complete	8	GF1 from outlet, GF2 from pot bottom - trying to meet wall Y+ range	SENSITIVITY-004-6_375-interpolate
SENSITIVITY	14	.9s	8	GF1 from outlet, GF2 from pot bottom - trying to meet wall Y+ range	SENSITIVITY-004-6_375-interpolate
SENSITIVITY	15	unstarted	8		SENSITIVITY-004-6_375-interpolate
SENSITIVITY	16	unstarted	8	Dual GF's like 014 but includes a BL at pot bottom	SENSITIVITY-004-6_375-interpolate
SENSITIVITY	17	Complete	8	Cooper-meshed hex mesh on entire upper half, BL from 0.2mm	SENSITIVITY-004-6_375-interpolate
SENSITIVITY	18	Complete	8	Cooper-meshed hex mesh on entire upper half, BL from 0.1mm	SENSITIVITY-004-6_375-interpolate
SENSITIVITY	19	Complete	<8	Similar to 17, 18. BL 1st layer 0.15mm, more square chimney elements	SENSITIVITY-004-6_375-interpolate
SENSITIVITY	20	Complete	var.	(Continuation of 19 w/ short time step) (results questionable - could be mixed up with 019)	none - continuation of model 19
SENSITIVITY	21	Complete	var.	Repeat of model 19,20. Statistical study on normalization and data average	SENSITIVITY-INTERPOLATION-019
SENSITIVITY	22	unstarted	<10	Same BL variation as 19, but higher radial resolution (~8mm)	
SENSITIVITY	23	3.1 s	9		
SENSITIVITY	24	unstarted	9	Eliminated inlet reservoir. Refined BL (0.1mmx1.2x6), cooper hex top, tet elsewhere	
SENSITIVITY	25	Complete	7	Cooper mesh top and chimney, tet meshed lower portion	Started from scratch

		GROWTH FUNCTIONS									
Model name		SF from...	start size 1 (mm)	growth rate 1	start size (mm) 2	growth rate 2	inlet res	outlet res	# of elements	time step size (s)	max iterations per time step
SENSITIVITY	1	Outlet face	3	1.1	-	-	yes	no		0.005	N/A
SENSITIVITY	2	Outlet face	3	1.1	-	-	yes	no		0.005	N/A
SENSITIVITY	3	N/A	-	-	-	-	yes	no		0.005	N/A
SENSITIVITY	4	N/A	-	-	-	-	yes	no		0.005	200
SENSITIVITY	5	N/A	-	-	-	-	yes	no		0.005	200
SENSITIVITY	6	N/A	-	-	-	-	yes	no		0.005	200
SENSITIVITY	7	Outlet face	3	1.1	-	-	yes	no		0.005	200
SENSITIVITY	8	Outlet face	3	1.1	-	-	yes	no	214494	0.005	200
SENSITIVITY	9	Outlet face	3	1.1	-	-	yes	no		0.005	200
SENSITIVITY	10	Outlet & Pot Bottom Face	4	1.1	-	-	yes	no	175313	0.005	200
SENSITIVITY	11	Outlet & Pot Bottom Face	2.5	1.1	-	-	yes	no	333306	0.005	200
SENSITIVITY	12	Outlet face	3	1.1	-	-	yes	no	214494	0.005	200
SENSITIVITY	13	Outlet face	3	1.1	2	1.4	yes	no	325000	0.005	200
SENSITIVITY	14	Outlet face	3	1.1	0.4	1.4	yes	no	2489358	0.005	200
SENSITIVITY	15		3	1.1	0.6	1.4	yes	no		0.005	200
SENSITIVITY	16									0.005	200
SENSITIVITY	17	Faces							217229	0.005	200
SENSITIVITY	18								235543	0.005	200
SENSITIVITY	19								276377	0.005	200
SENSITIVITY	20								276377	0.0025	200
SENSITIVITY	21								276377	0.005	200
SENSITIVITY	22								399017	0.005	
SENSITIVITY	23								632786	0.005	200
SENSITIVITY	24								327228	0.005	200
SENSITIVITY	25								127670	0.005	250

Model name		Computer run on	# threads	Run time (s)	Computer processor time (hr)	Compute wall time (hr)	Compute wall time per second run (hr/s)	results misc comments
SENSITIVITY	1	1.0			fail	fail	fail	didn't run
SENSITIVITY	2	1.0			fail	fail	fail	didn't run
SENSITIVITY	3	1.0			fail	fail	fail	didn't run
SENSITIVITY	4	1.0		8		55.7	7.0	able to run
SENSITIVITY	5	1.0			fail	fail	fail	able to run, interesting but user terminated due to info learne
SENSITIVITY	6	1.0			fail	fail	fail	no improvement in convergence, stopped before completion
SENSITIVITY	7	1.0					fail	Converges before 200i to default residual criteria!
SENSITIVITY	8	1.0	8				fail	Converges before 200i to default residual criteria!
SENSITIVITY	9	1.0			fail	fail	fail	stopped running after a 5 seconds
SENSITIVITY	10	1.0					#DIV/0!	Converges before 200i to default residual criteria!
SENSITIVITY	11	1.0					#DIV/0!	Converges before 200i to default residual criteria!
SENSITIVITY	12	1	8	8	report error	report error	report error	Converges before 200i to default residual criteria!
SENSITIVITY	13	2	8	8	1725.7	101.6	12.7	Converges before 200i to default residual criteria!
SENSITIVITY	14	2	8	8	report error	report error	report error	
SENSITIVITY	15	2		8			0.0	
SENSITIVITY	16	2		8			0.0	
SENSITIVITY	17	2	8	8	report error	report error	report error	
SENSITIVITY	18	2	16	8	?	?	#VALUE!	Converges before 200i to default residual criteria!
SENSITIVITY	19	2		8	916	54	6.8	Converges before 200i to default residual criteria!
SENSITIVITY	20	2	16	8	1522	89.7	11.2	Converges before 200i to default residual criteria!
SENSITIVITY	21	2	16	12	2172	127.9	10.7	
SENSITIVITY	22	2					#DIV/0!	
SENSITIVITY	23	2					#DIV/0!	
SENSITIVITY	24	2	16				#DIV/0!	
SENSITIVITY	25	2	16	10	712	47	4.7	

Model name		Pot bottom Wall Y+				Pot area (m^2)	Unsteady statistics			MF N2	MF O2	Temporal average mass outlet flow rate (kg/s)	Instantaneous outlet mass flow rate (kg/s)f(t)
		min	max	mean	median		Instantaneous heat transfer (W)f(t)	Convective heat transfer to pot (W)	Radiative heat transfer to pot (W)				
SENSITIVITY	1	fail	fail	fail				fail	-				fail
SENSITIVITY	2	fail	fail	fail				fail	-				fail
SENSITIVITY	3	fail	fail	fail				fail	-				fail
SENSITIVITY	4	3.1	11.1	7.6				667.5	-				2.69E-03
SENSITIVITY	5	fail	fail	fail				fail	-				fail
SENSITIVITY	6	fail	fail	fail				fail	-				fail
SENSITIVITY	7	2.4	9.8	6.1				603.2	-				3.30E-03
SENSITIVITY	8	2.4	8.3	5.4			834.5	744.7	-	1.88E-03	5.72E-04	2.64E-03	2.83E-03
SENSITIVITY	9	fail	fail	fail				fail	-				fail
SENSITIVITY	10						817.5	847.0	-	1.80E-03	5.48E-04	2.54E-03	2.85E-03
SENSITIVITY	11			2 to 5				739.1	-	1.87E-03	5.68E-04	2.63E-03	3.84E-03
SENSITIVITY	12						773.0	739.0	-	2.22E-03	6.74E-04	3.08E-03	2.60E-03
SENSITIVITY	13						1032.0	865.0	-	1.82E-03	5.54E-04	2.56E-03	2.62E-03
SENSITIVITY	14							165.6	-	2.41E-03	7.20E-04	3.32E-03	2.50E-03
SENSITIVITY	15								-				
SENSITIVITY	16								-				
SENSITIVITY	17	0.223	1.894	0.778	0.758			1522.0	-	2.01E-03	6.11E-04	2.81E-03	2.81E-03
SENSITIVITY	18	0.081	3.017	0.456	0.432		2302.4	2174.3	-	2.05E-03	6.24E-04	2.86E-03	2.96E-03
SENSITIVITY	19	0.116	3.620	0.601	0.593		2454.0	1849.1	-	2.01E-03	6.13E-04	2.81E-03	2.87E-03
SENSITIVITY	20	0.067	3.665	0.572	0.573		1883.7	1652.2	-	1.93E-03	5.87E-04	2.70E-03	2.53E-03
SENSITIVITY	21												
SENSITIVITY	22								-				
SENSITIVITY	23												
SENSITIVITY	24												
SENSITIVITY	25	0.106	0.888	0.575	0.582	0.039	1782.0	2872.0	-				

APPENDIX D – Water flow sensor calibration data

Calibration date: 9/20/2010
Calibration personel: Dan Lionberg
Density of water (@20C) [kg*m^3]: 998.2
Pulses per liter: 4600
Full scale frequency [hz]: 150.00
Full scale voltage [V]: 10.00
Correction factor: 0.939
K_f, mass flow multiplier (K_f*V_m=m_dot [g*s^{-1}]): 3.056492

Reference measurement data							Calculated by sensor V_m	
V_L Low voltage [V]	V_H High voltage [V]	V_m Mean voltage [V]	Mass [g]	Time [s]	Mass flow rate [g*min^{-1}]	Volumetric flow rate [ml*min^{-1}]	Mass flow rate [g*min^{-1}]	Mass flow rate percent of reading disagreement [%]
0.900	0.760	0.83	886	304.6	175	175	152	12.8%
1.170	1.030	1.10	1096	298.2	221	221	202	8.5%
1.560	1.450	1.51	954	204.3	280	281	276	1.5%
1.740	1.580	1.66	1556	298.3	313	314	304	2.7%
2.100	1.780	1.94	1790	294.3	365	366	356	2.5%
2.500	2.330	2.42	2623	354.5	444	445	443	0.2%
3.350	3.110	3.23	1613	165.3	585	587	592	-1.2%
3.450	3.210	3.33	2919	287.6	609	610	611	-0.3%
4.720	4.510	4.62	4109	297.0	830	832	846	-2.0%
5.300	5.220	5.26	2126	133.1	958	960	965	-0.7%
6.180	5.840	6.01	4672	259.0	1082	1084	1102	-1.8%
7.940	7.780	7.86	4529	189.3	1435	1438	1441	-0.4%

*Data in grey highlight is below the sensor extended flow sensitivity range of 0.25-15 l/min

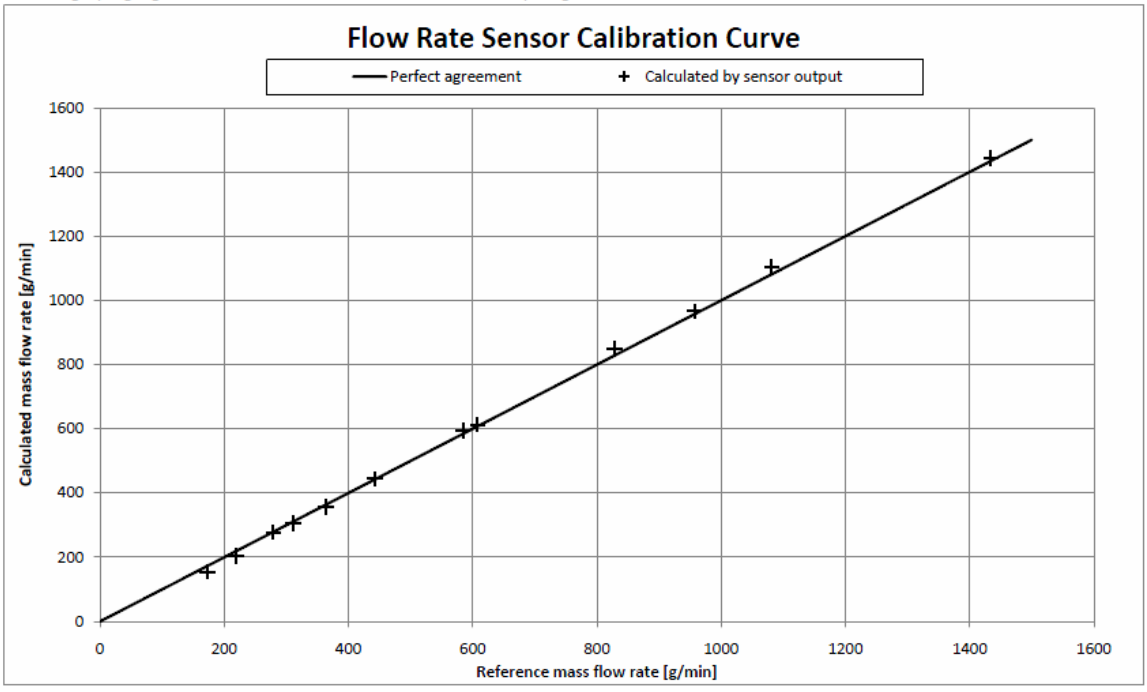

Stove Model	Version Number	Test Type	Test Date	HS: TTB (min)	HS: Wood (g)	HS: WOOD/TIME (g/s)	HS: CO (g)	HS: PM (mg)	CS: Char Accumulation (g)	SMR: Wood (g)	SMR: WOOD/TIME (45 minutes = 2700s)	SMR: CO (g)	SMR: PM (mg)	SMR: Char Accumulation (g)	Thermal Efficiency	Char Accumulation Average
G3300 P2	1	EPTP	4/21/2010	22.6	327.5	2.418E-01	6.1	862.9	18.0	267.6	**9.910E-02**	12.7	288.4	18.3	30.1	18.0
G3300 AS	1	EPTP	6/10/2010	20.0	319.6	2.663E-01	3.8	759.0	15.0	262.6	**9.726E-02**	9.2	368.0	13.0	31.9	14.0
G3300 AS	1	EPTP	6/11/2010	21.0	301.9	2.396E-01	5.1	740.0	18.0	246.7	**9.137E-02**	9.3	477.0	16.0	31.3	17.0
G3300 AS	1	EPTP	6/14/2010	25.9	329.0	2.117E-01	4.4	x	18.0	282.2	**1.045E-01**	7.5	x	17.0	32.4	17.5
G3300 AS	1	EPTP	6/22/2010	22.0	298.1	2.258E-01	5.8	933.0	22.0	257.9	**9.552E-02**	x	488.0	18.0	31.9	20.0
G3300 AS	1	EPTP	6/23/2010	22.0	348.6	2.641E-01	11.2	1835.0	16.0	303.7	**1.125E-01**	14.5	724.0	26.0	29.4	21.0
G3300 AS	1	EPTP	6/1/2010	24.0	366.4	2.544E-01	8.1	x	22.0	281.3	**1.042E-01**	14.1	x	19.0	30.9	20.5
G3300 AS Redo	1	EPTP	7/2/2010	41.0	401.9	1.634E-01	10.8	x	14.0	239.3	**8.863E-02**	11.8	x	23.0	29.2	18.5
G3300 AS Redo	1	EPTP	7/7/2010	26.0	353.3	2.265E-01	9.3	1511.0	15.0	264.5	**9.796E-02**	10.6	606.0	18.0	26.6	16.5
G3300 AS Redo	1	EPTP	7/8/2010	33.0	371.0	1.874E-01	9.2	1525.0	15.0	321.5	**1.191E-01**	9.9	768.0	20.0	25.9	17.5
G3300 AS Redo	1	EPTP	7/8/2010	30.0	366.4	2.036E-01	8.8	1305.0	16.0	276.6	**1.024E-01**	12.4	426.0	17.0	25.0	16.5
G3300 AS	2	EPTP	7/12/2010	25.0	370.1	2.467E-01	6.6	1208.0	15.0	242.1	**8.967E-02**	11.7	346.0	14.0	32.6	14.5
G3300 AS	2	EPTP	7/13/2010	24.0	266.4	1.850E-01	12.0	2586.0	23.0	229.9	**8.515E-02**	12.7	215.0	17.0	30.1	19.0
G3300 AS	2	EPTP	7/13/2010	26.0	371.0	2.378E-01	10.3	1197.0	24.0	261.7	**9.693E-02**	17.6	309.0	18.0	25.7	21.0
Mean values of all G3300 data:				**25.9**	**342.2**	**2.253E-01**	**8.0**	**1314.7**	**17.9**	**267.0**	**9.888E-02**	**11.8**	**455.9**	**18.2**	**29.5**	**18.0**

APPENDIX F – Validation experiment firepower and heat transfer result figures

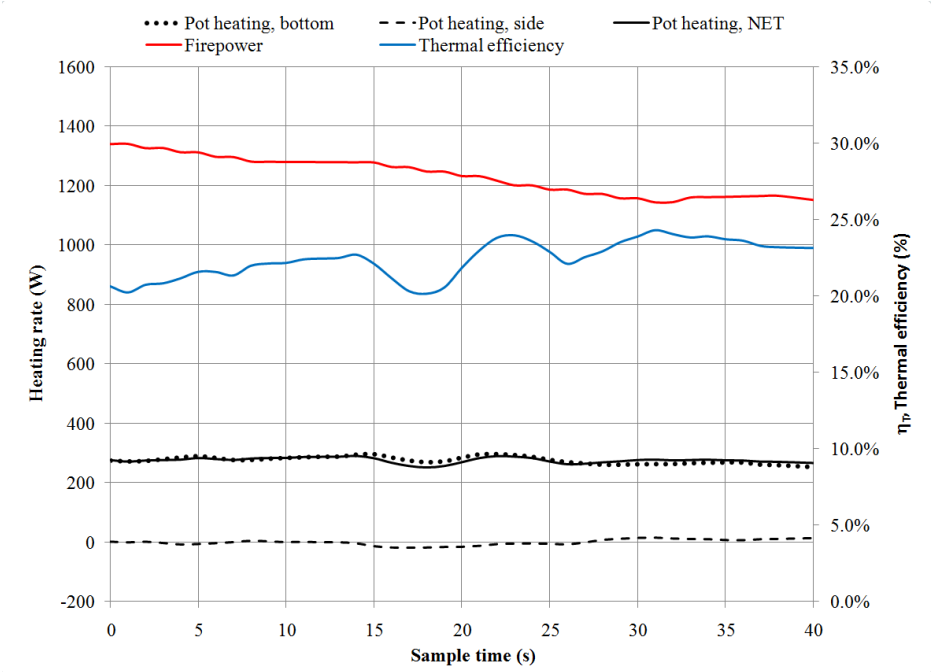

Sample F10

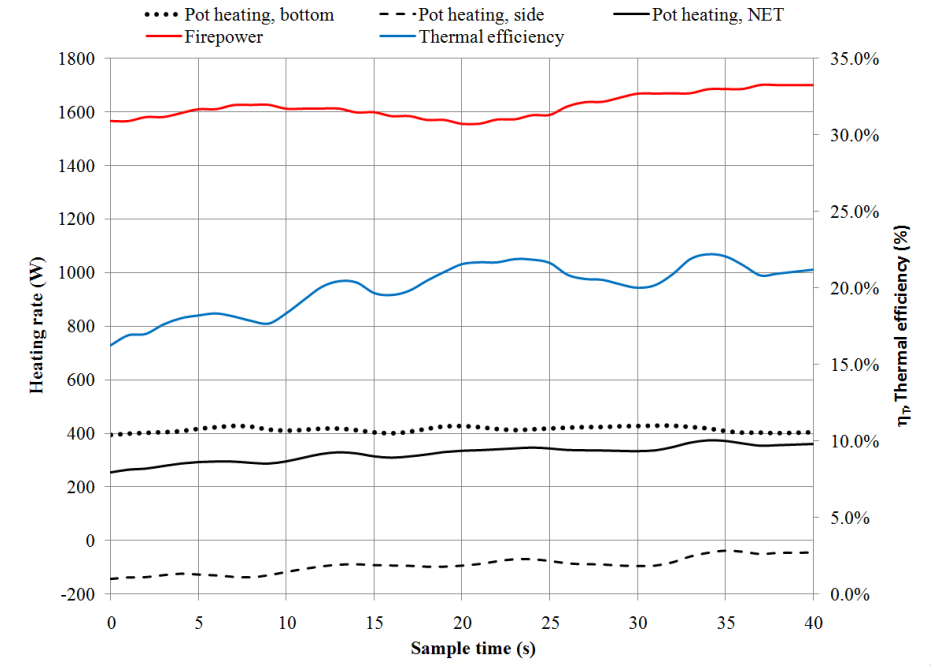

Sample F11

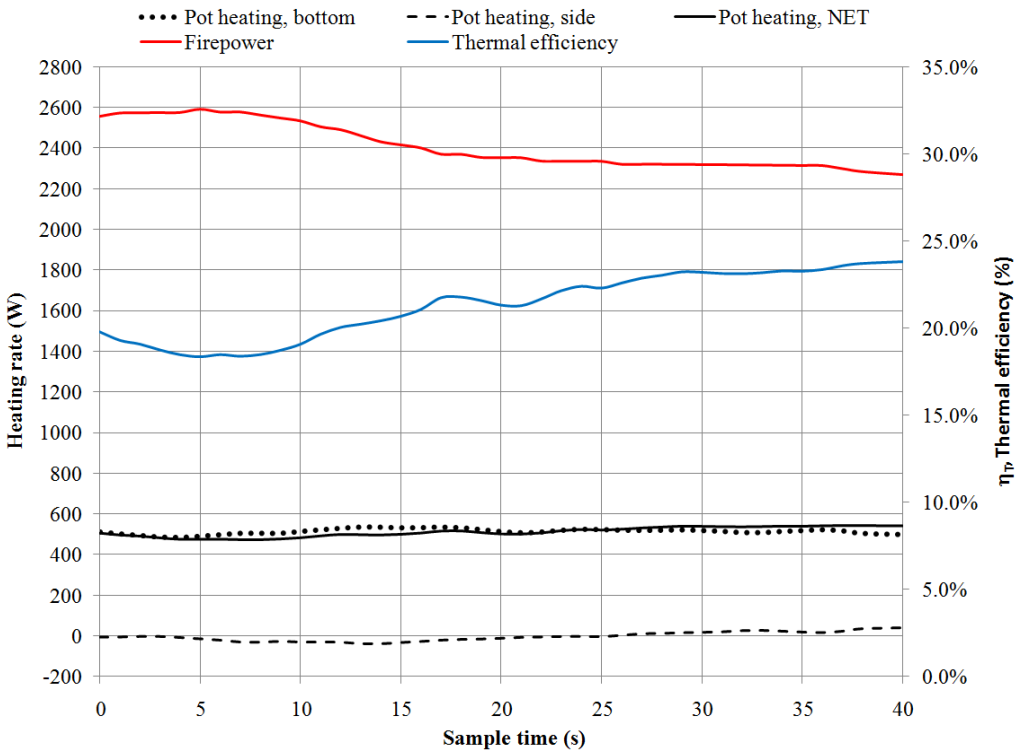

Sample F12

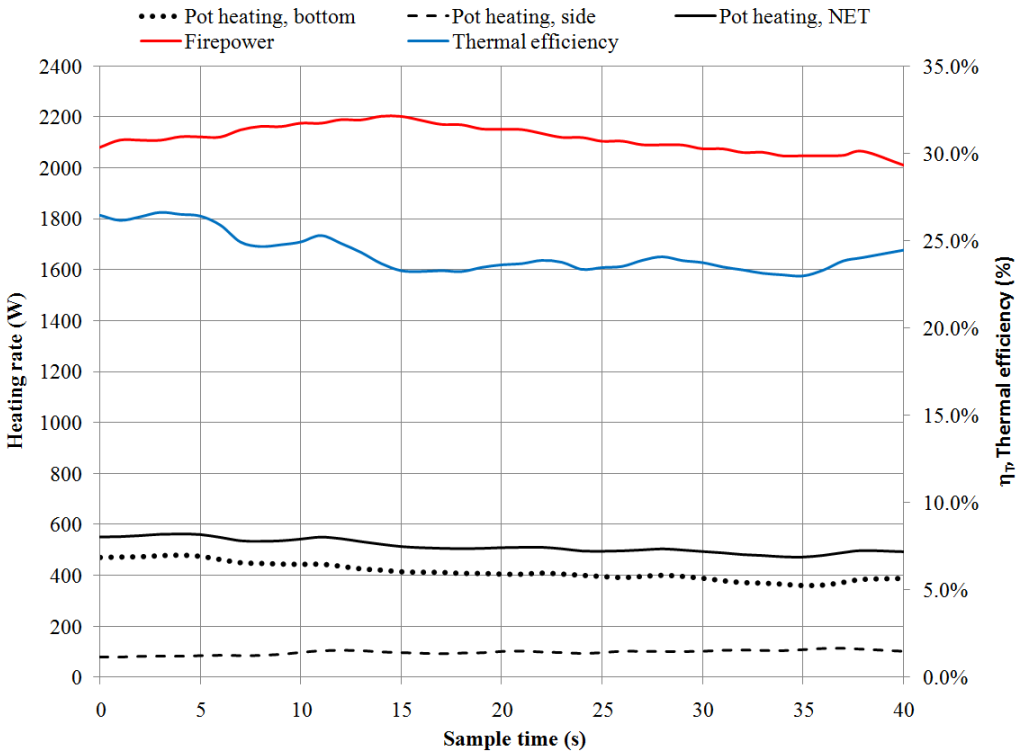

Sample F13

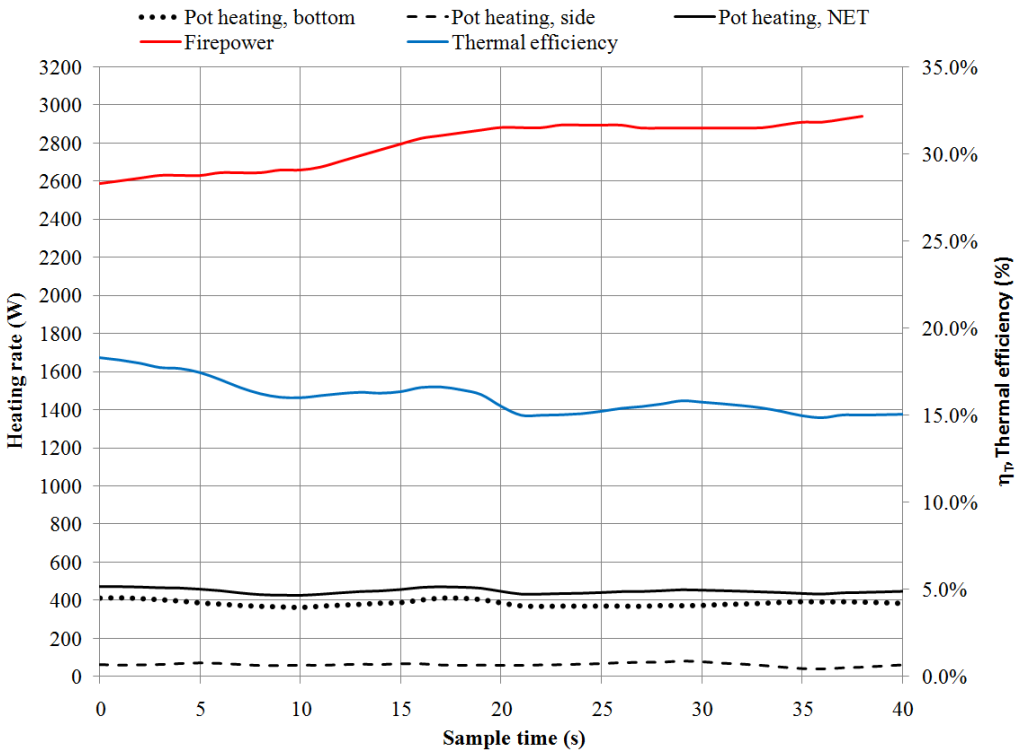

Sample F17

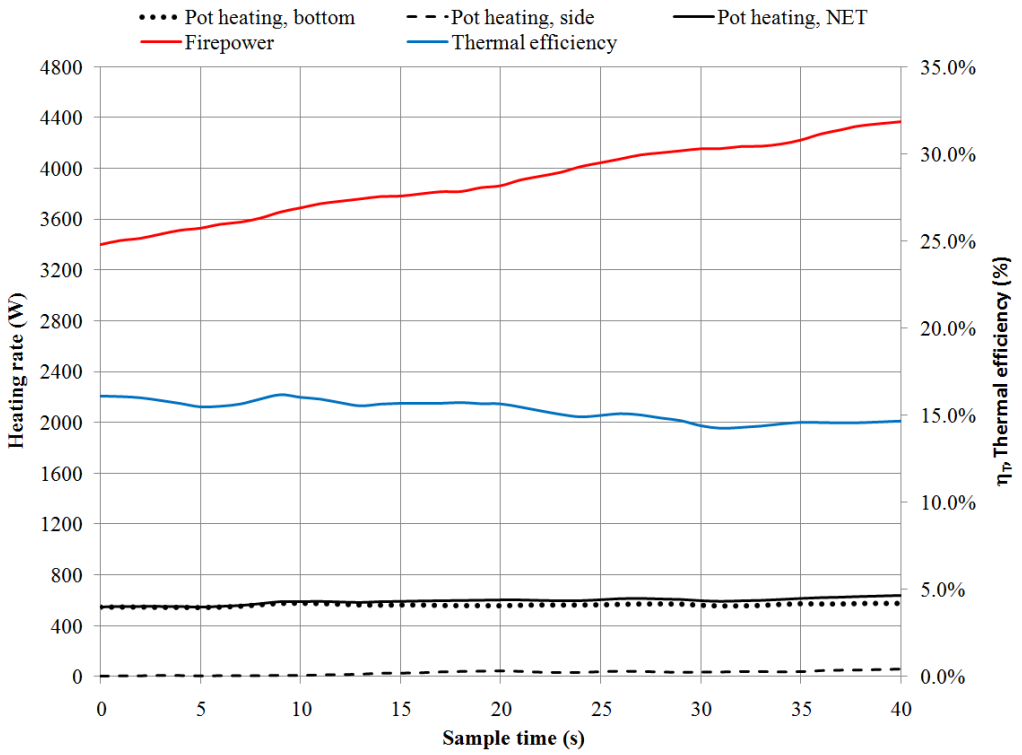

Sample F20

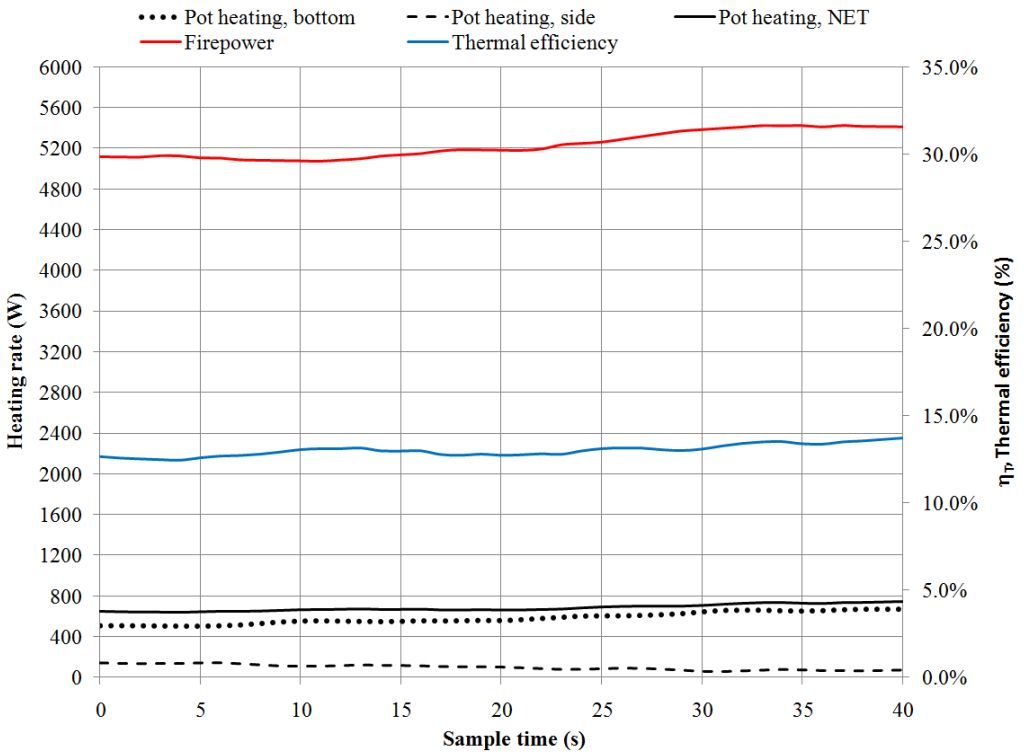

Sample F21

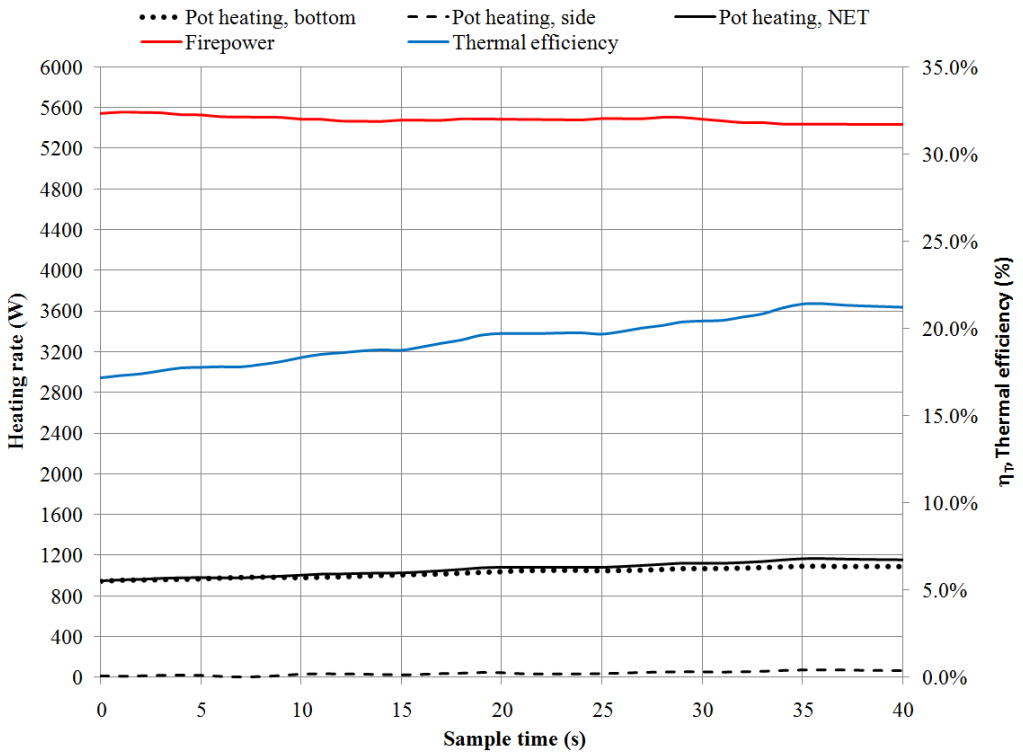

Sample F22

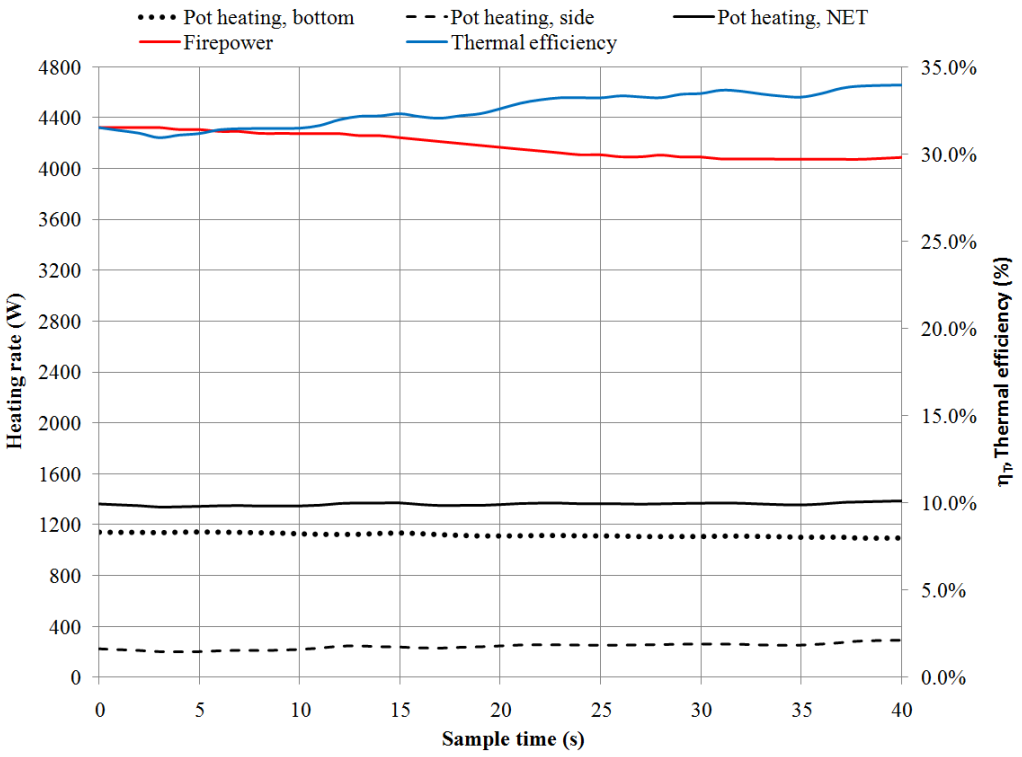

Sample F25

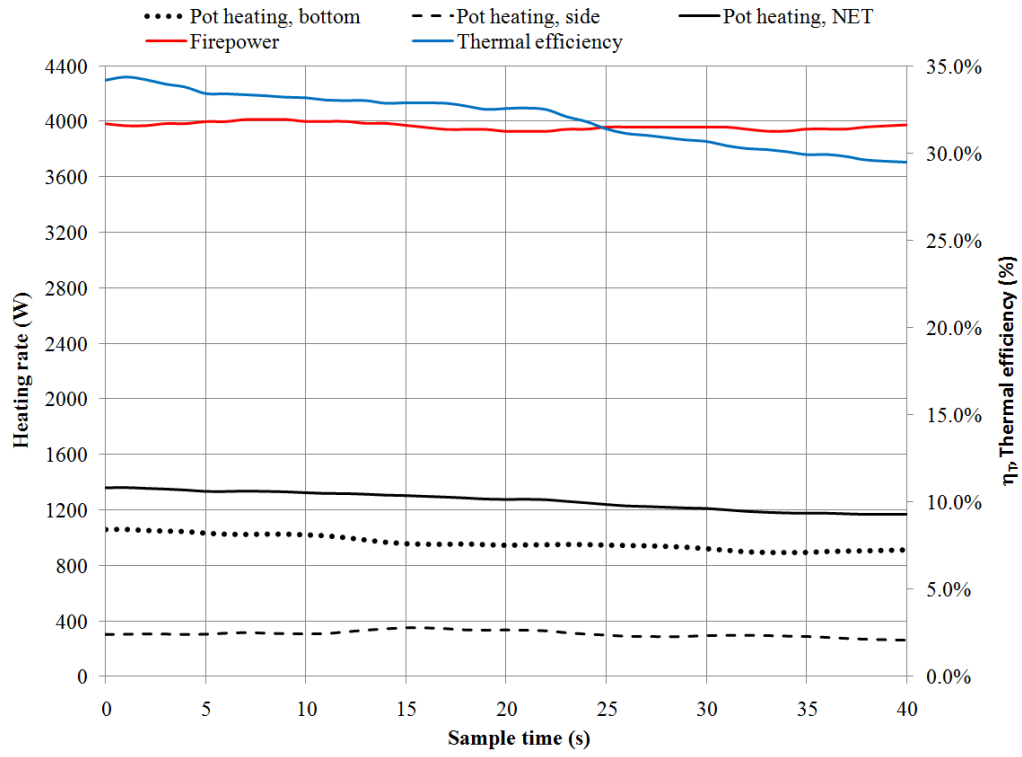

Sample F26

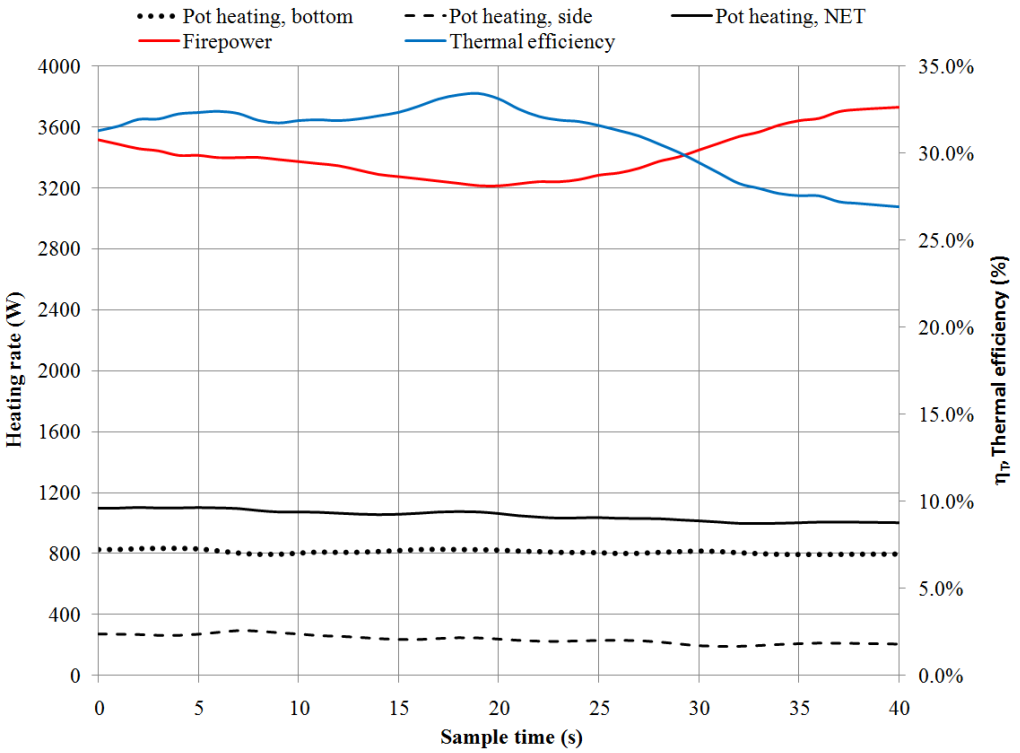

Sample F27

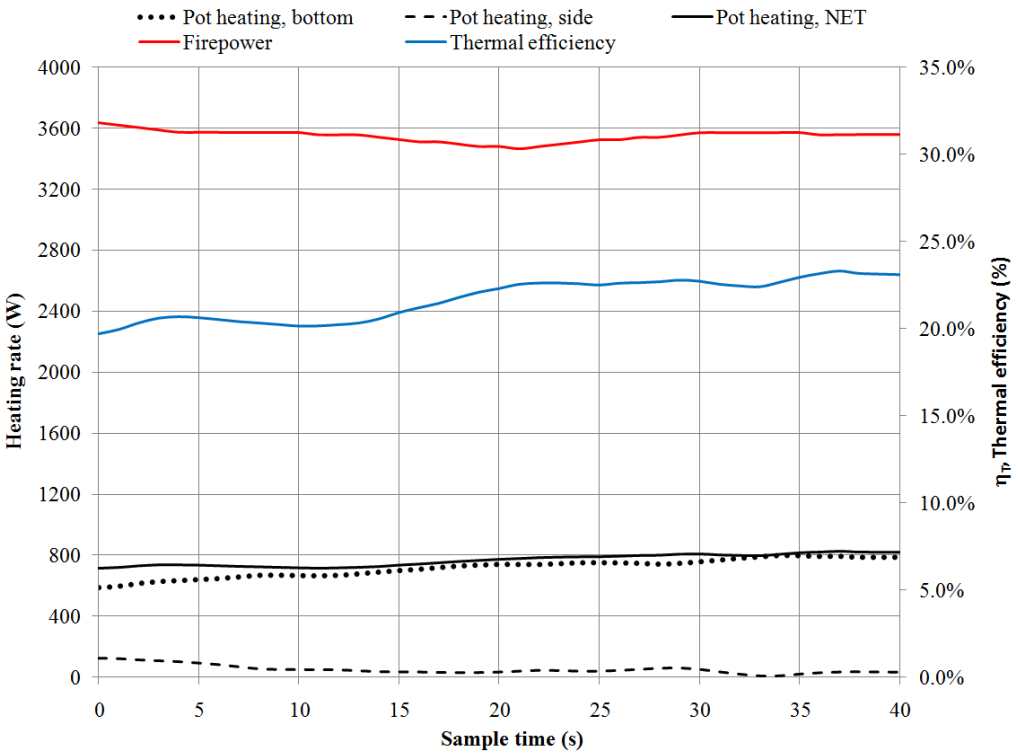

Sample F30

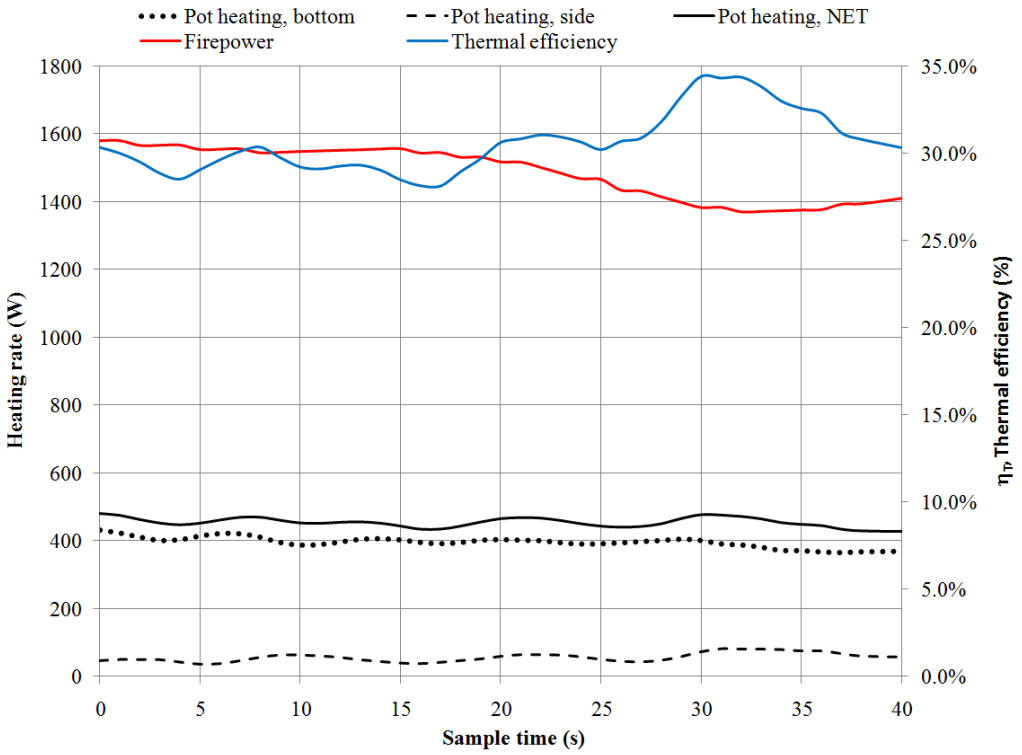

Sample F35

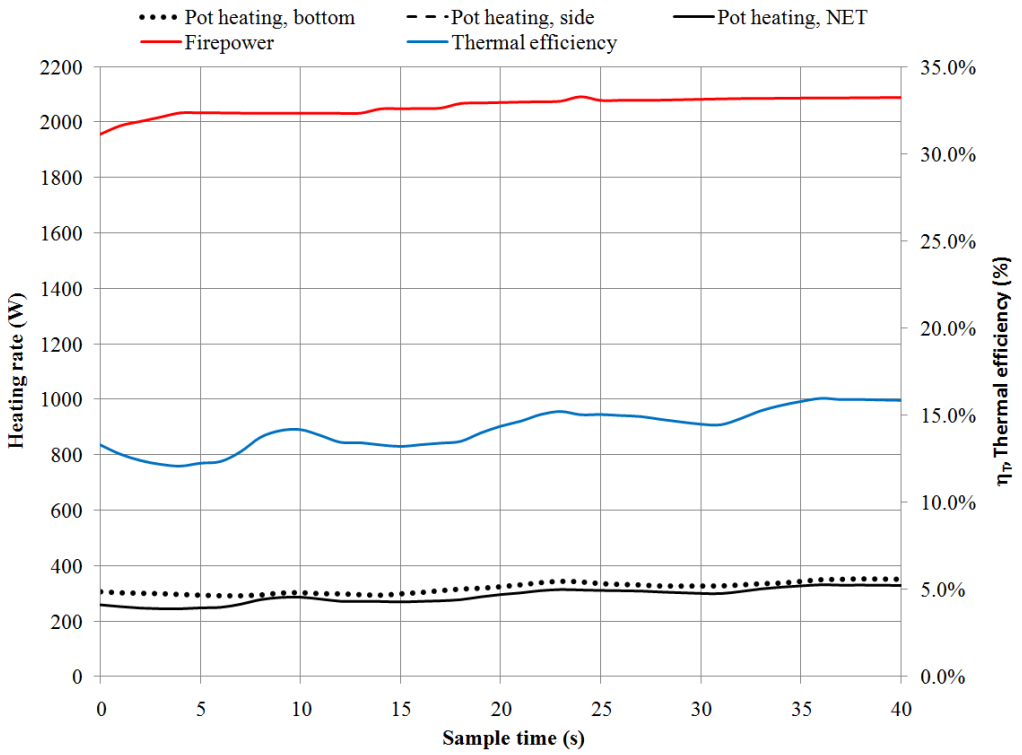

Sample F40

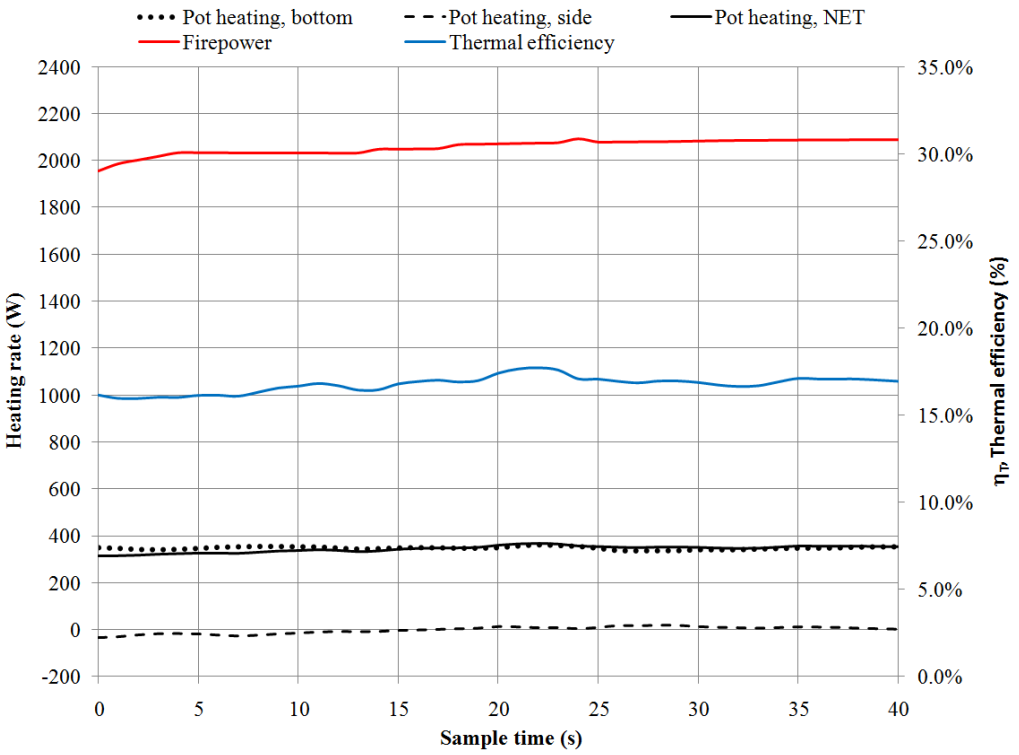

Sample F41

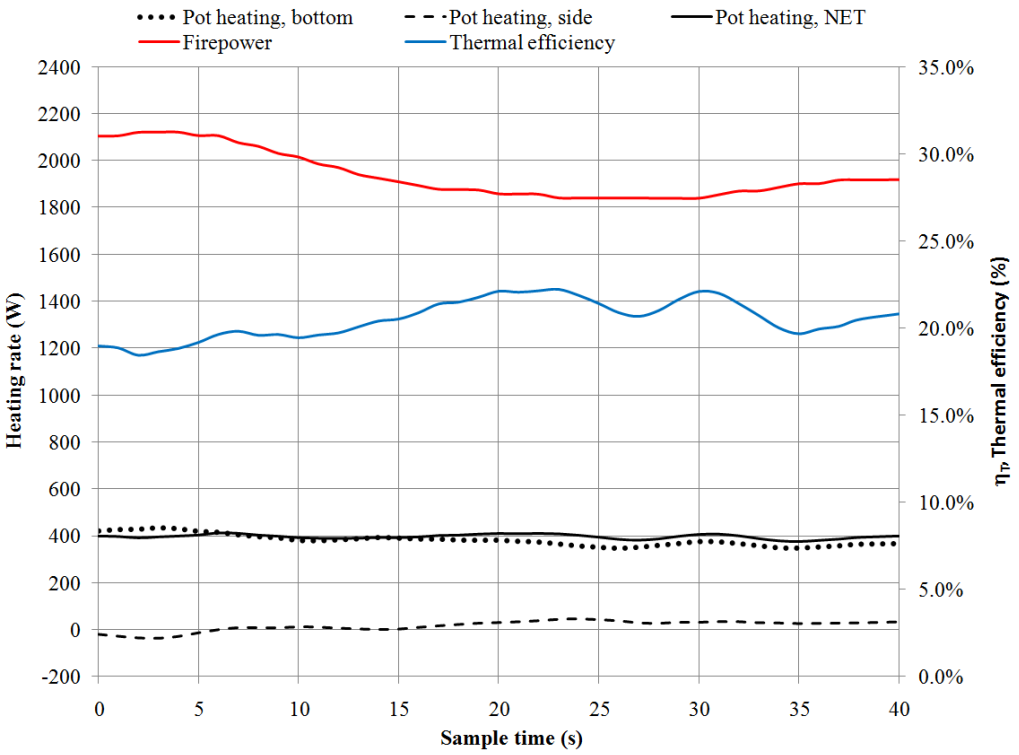

Sample F42

APPENDIX G – ANSYS Workbench mesh setup

Details of "Mesh"	
Defaults	
Physics Preference	CFD
Solver Preference	Fluent
Relevance	0
Sizing	
Use Advanced Size Fu...	On: Fixed
Relevance Center	Fine
Smoothing	High
Min Size	0.10 mm
Max Size	25.60 mm
Growth Rate	3.0
Minimum Edge Length	13.0 mm
Inflation	
Use Automatic Inflation	None
Inflation Option	Smooth Transition
Transition Ratio	0.272
Maximum Layers	5
Growth Rate	1.5
View Advanced Options	Yes
Collision Avoidance	Layer Compression
Fix First Layer	No
Gap Factor	0.4
Maximum Height o...	1
Growth Rate Type	Geometric
Maximum Angle	140.0 °
Fillet Ratio	1
Use Post Smoothing	Yes
Smoothing Iterations	7
CutCellMeshing	
Active	Yes
Feature Capture	Program Controlled
Tessellation Refinement	Program Controlled
Statistics	
Nodes	207150
Elements	198376
Mesh Metric	Aspect Ratio
Min	1.0021
Max	698.06
Average	4.70877879733604
Standard Deviation	6.63048435640756

Mesh control for all stick surfaces	
Scope	
Scoping Method	Geometry Selection
Geometry	38 Faces
Definition	
Suppressed	No
Type	Element Size
Element Size	4.3 mm
Behavior	Soft
Growth Rate	3.0

Mesh control for cylindrical chamber	
Scope	
Scoping Method	Geometry Selection
Geometry	1 Face
Definition	
Suppressed	No
Type	Element Size
Element Size	8. mm
Behavior	Soft
Growth Rate	1.10

Mesh control for cylindrical chamber	
Scope	
Scoping Method	Geometry Selection
Geometry	5 Faces
Definition	
Suppressed	No
Type	Element Size
Element Size	9. mm
Behavior	Soft
Growth Rate	1.70

Mesh control for drip pan and pot bottom	
Scope	
Scoping Method	Geometry Selection
Geometry	2 Faces
Definition	
Suppressed	No
Type	Element Size
Element Size	8. mm
Behavior	Soft
Growth Rate	1.80

Mesh control for pot radius (rollover from bottom to side of pot)	
Scope	
Scoping Method	Geometry Selection
Geometry	2 Faces
Definition	
Suppressed	No
Type	Element Size
Element Size	3.5 mm
Behavior	Soft
Growth Rate	2.50

Mesh control for pot sides and upper stove body	
Scope	
Scoping Method	Geometry Selection
Geometry	3 Faces
Definition	
Suppressed	No
Type	Element Size
Element Size	13. mm
Behavior	Soft
Growth Rate	2.0

Mesh control for outlet surfaces	
Scope	
Scoping Method	Geometry Selection
Geometry	9 Faces
Definition	
Suppressed	No
Type	Element Size
Element Size	26. mm
Behavior	Soft
Growth Rate	3.0

APPENDIX H – ANSYS FLUENT 13.0 solver settings

FLUENT
Version: 3d, dp, pbns, pdf22, LES, transient (3d, double precision, pressure-based, 22 species pdf, large eddy simulation, transient)
Release: 13.0.0
Title:

Models
Space 3D
Time Unsteady, 2nd-Order Implicit
Viscous Large Eddy Simulation
Sub-Grid Scale Model Smagorinsky-Lilly
Heat Transfer Enabled
Solidification and Melting Disabled
Radiation None
Species Non-Premixed Combustion ((ch4 h2 n2 o2 c6h6 co2 co h2o c2h4 ch2o h hcooh oh ho2 hono o h2o2 c<s> c2h6 cho hco hoco) species)
Coupled Dispersed Phase Disabled
NOx Pollutants Disabled
SOx Pollutants Disabled
Soot Enabled
Mercury Pollutants Disabled

Solver Settings

Equations

Equation	Solved
Flow	yes
Soot	yes
Nuclei	yes
Energy	yes
Pdf	yes

Numerics

Numeric	Enabled
Absolute Velocity Formulation	yes

Unsteady Calculation Parameters

Time Step (s)	0.001
Max. Iterations Per Time Step	100

Relaxation

Variable	Relaxation Factor
Pressure	0.3
Density	0.89999998
Body Forces	0.89999998
Momentum	0.7
Soot	0.9
Nuclei	0.9
Energy	0.89999998
Temperature	0.89999998
Mean Mixture Fraction	0.89999998

Linear Solver

Variable	Solver Type	Termination Criterion	Residual Reduction Tolerance
Pressure	V-Cycle	0.1	
X-Momentum	Flexible	0.1	0.7
Y-Momentum	Flexible	0.1	0.7
Z-Momentum	Flexible	0.1	0.7
Soot	Flexible	0.1	0.7
Nuclei	Flexible	0.1	0.7
Energy	Flexible	0.1	0.7
Mean Mixture Fraction	Flexible	0.1	0.7

Pressure-Velocity Coupling

Parameter	Value
Type	SIMPLE

Discretization Scheme

Variable	Scheme
Pressure	Second Order
Density	Bounded Central Differencing
Momentum	Bounded Central Differencing
Soot	Second Order Upwind
Nuclei	Second Order Upwind

Energy	Third-Order MUSCL
Mean Mixture Fraction	Second Order Upwind

Solution Limits

Quantity	Limit
Minimum Absolute Pressure	1
Maximum Absolute Pressure	5e+10
Minimum Temperature	1
Maximum Temperature	5000
Maximum Turb. Viscosity Ratio	100000

APPENDIX I – National Instruments DIAdem scripts

Process_init.VBS - Initialization script

```
'--------------------------------------------------------------------------------
-
'-- VBS script file
'-- Created on 10/17/2010 14:12:57
'-- Author: ---
'-- Comment: ---
'--------------------------------------------------------------------------------
-
Option Explicit  'Forces the explicit declaration of all the variables in a
script.

Dim MyFolders(), Process_MAIN
Call InitMyFolders
'--------------------------------------------------------------------------------
-
Sub InitMyFolders
  ReDim MyFolders(3)
  MyFolders(0)="W:\Experiments\Data\VAULT\Test fire\working\RAW\"
  MyFolders(1)="W:\Experiments\Data\VAULT\Test fire\working\FORMATTED\"
  MyFolders(2)="W:\Experiments\Data\VAULT\Test fire\working\CSV\"
End Sub
'--------------------------------------------------------------------------------
-
Call DataFileLoad(MyFolders(0)&"01.tdms","","") '...
DataFilename,FileImportFilter,ImportAction
Scriptstart "Process_MAIN"
Call DataFileSave(MyFolders(1)&"F01.tdms","TDMS") '...
DataFilename,FileExportFilter
Call DataFileSave(MyFolders(2)&"F01.csv","CSV") '...
DataFilename,FileExportFilter
Call Data.Root.ChannelGroups.Remove("Untitled")

Call DataFileLoad(MyFolders(0)&"02.tdms","","") '...
DataFilename,FileImportFilter,ImportAction
Scriptstart "Process_MAIN"
Call DataFileSave(MyFolders(1)&"F02.tdms","TDMS") '...
DataFilename,FileExportFilter
Call DataFileSave(MyFolders(2)&"F02.csv","CSV") '...
DataFilename,FileExportFilter
Call Data.Root.ChannelGroups.Remove("Untitled")

Call DataFileLoad(MyFolders(0)&"5gas-01.tdms","","") '...
DataFilename,FileImportFilter,ImportAction
Call Data.Root.ChannelGroups("5-Gas Data").Channels.Remove("THC [ppm]")
Call Data.Root.ChannelGroups("5-Gas Data").Channels.Remove("O2 [%]")
Call Data.Root.ChannelGroups("5-Gas Data").Channels.Remove("NOx [ppm]")
Call Data.Root.ChannelGroups("5-Gas Data").Channels.Remove("NO [ppm]")
Call Data.Root.ChannelGroups("5-Gas Data").Channels.Remove("NO2 [ppm]")
Call Data.Root.ChannelGroups("5-Gas Data").Channels.Remove("Time")
```

```
Call Data.Root.ChannelGroups("5-Gas Data").Channels.Remove("Time[sec]")
Call DataBlDel("'5-Gas Data/CO2 [%]' - '5-Gas Data/CO [ppm]'",1,69,1) '...
ChnNoStr,ChnRow,ValNo,ValDelOnly
Call DataFileSave(MyFolders(1)&"5gas-01.tdms","TDMS") '...
DataFilename,FileExportFilter
Call DataFileSave(MyFolders(2)&"5gas-01.csv","CSV") '...
DataFilename,FileExportFilter
Call Data.Root.ChannelGroups.Remove("5-Gas Data")

Call DataFileLoad(MyFolders(0)&"03.tdms","","") '...
DataFilename,FileImportFilter,ImportAction
Scriptstart "Process_MAIN"
Call DataFileSave(MyFolders(1)&"F03.tdms","TDMS") '...
DataFilename,FileExportFilter
Call DataFileSave(MyFolders(2)&"F03.csv","CSV") '...
DataFilename,FileExportFilter
Call Data.Root.ChannelGroups.Remove("Untitled")
```

Process_MAIN.VBS script (subroutine below initialization)

```
'------------------------------------------------------------------------------
-
'-- VBS script file
'-- Created on 10/10/1510 23:02:41
'-- Author: ---
'-- Comment: ---
'------------------------------------------------------------------------------
-
Option Explicit  'Forces the explicit declaration of all the variables in a
script.
Call Data.Root.ChannelGroups("Untitled").Activate()
Dim Process_ZERODEADTC, Process_N_SCALING

'Generate time channel for use in differentiation calculations
Call ChnGenTime("/TimeGenerated","millisecond",0,0,2,"StartStepNo",20000) '...
E,GenTimeUnit,GenTimeXBeg,GenTimeXEnd,GenTimeStep,GenTimeMode,GenTimeNo
Call
Data.Move(Data.Root.ChannelGroups("Untitled").Channels("TimeGenerated"),Data.Ro
ot.ChannelGroups("Untitled").Channels,2)
Call Data.Root.ChannelGroups("Untitled").Channels.Remove("Untitled")

Data.Root.ChannelGroups("Untitled").Channels("Untitled 1").Name = "working"
Scriptstart "Process_N_SCALING"
Call
Data.Move(Data.Root.ChannelGroups("Untitled").Channels("working"),Data.Root.Cha
nnelGroups("Untitled").Channels,3)
Data.Root.ChannelGroups("Untitled").Channels("working").Name = "Gas Temp 1"
```

(last 6 lines repeated for all thermocouple channels…)

```
'Processing the two channels of the water flow meter output'

'Untitled 64 - Flow meter gain signal (+)
Call ChnSmooth("Untitled/Untitled 64","/flow signal 1",1000,"maxNumber") '...
Y,E,SmoothWidth,SmoothType
'Call ChnFiltCalc("Untitled/TimeGenerated","Untitled/Untitled 64","/flow signal
1","IIR","Bessel","Low pass",3,0.5,0,0,1.2,25,"Hamming",1,1) '...
XW,Y,E,FiltStruc,FiltStyle,FiltType,FiltDegree,FiltLimit,FiltLowLimit,FiltUppLi
mit,FiltWave,FiltSamples,FiltWndFct,FiltZeroPhase,FiltCorrection
Call Data.Root.ChannelGroups("Untitled").Channels.Remove("Untitled 64")
```

```
'Untitled 65 - Flow meter ref signal (~0V)
Call ChnSmooth("Untitled/Untitled 65","/flow signal 2",1000,"maxNumber") '...
Y,E,SmoothWidth,SmoothType
'Call ChnFiltCalc("Untitled/TimeGenerated","Untitled/Untitled 65","/flow signal
2","IIR","Bessel","Low pass",3,0.5,0,0,1.2,25,"Hamming",1,1) '...
XW,Y,E,FiltStruc,FiltStyle,FiltType,FiltDegree,FiltLimit,FiltLowLimit,FiltUppLi
mit,FiltWave,FiltSamples,FiltWndFct,FiltZeroPhase,FiltCorrection
Call Data.Root.ChannelGroups("Untitled").Channels.Remove("Untitled 65")

'May have to reverse flow signal 1 and flow signal 2 below here...
Call ChnSub("Untitled/flow signal 1","Untitled/flow signal 2","/Water m_dot")
'... Y,Y1,E
Call ChnFiltCalc("Untitled/TimeGenerated","Untitled/Water m_dot","/Water
m_dot","IIR","Bessel","Low pass",3,0.2,0,0,1.2,25,"Hamming",1,1) '...
XW,Y,E,FiltStruc,FiltStyle,FiltType,FiltDegree,FiltLimit,FiltLowLimit,FiltUppLi
mit,FiltWave,FiltSamples,FiltWndFct,FiltZeroPhase,FiltCorrection
Call ChnLinScale("Untitled/Water m_dot","/Water m_dot",3.0565,0) '...
Y,E,ChnScaleFactor,ChnScaleOffset

'Now converting the three channels for pot water themocouples wired in RSE
configuration

'Applying progressive 0.2 and 2 second averages to temperature signals
Call ChnSmooth("Untitled/Untitled 66","/Water T1",500,"maxNumber") '...
Y,E,SmoothWidth,SmoothType
Call ChnSmooth("Untitled/Water T1","/Water T1",1000,"maxNumber") '...
Y,E,SmoothWidth,SmoothType
Call ChnSmooth("Untitled/Untitled 68","/Water T2",500,"maxNumber") '...
Y,E,SmoothWidth,SmoothType
Call ChnSmooth("Untitled/Water T2","/Water T2",1000,"maxNumber") '...
Y,E,SmoothWidth,SmoothType
Call ChnSmooth("Untitled/Untitled 70","/Water T3",500,"maxNumber") '...
Y,E,SmoothWidth,SmoothType
Call ChnSmooth("Untitled/Water T3","/Water T3",1000,"maxNumber") '...
Y,E,SmoothWidth,SmoothType

Call Data.Root.ChannelGroups("Untitled").Channels.Remove("Untitled 66")
Call Data.Root.ChannelGroups("Untitled").Channels.Remove("Untitled 68")
Call Data.Root.ChannelGroups("Untitled").Channels.Remove("Untitled 70")

Call ChnLinScale("Untitled/Water T1","/Water T1",25000,300) '...
Y,E,ChnScaleFactor,ChnScaleOffset
Call ChnLinScale("Untitled/Water T2","/Water T2",25000,300) '...
Y,E,ChnScaleFactor,ChnScaleOffset
Call ChnLinScale("Untitled/Water T3","/Water T3",25000,300) '...
Y,E,ChnScaleFactor,ChnScaleOffset

Call ChnSub("Untitled/Water T2","Untitled/Water T1","/Water deltaTa") '...
Y,Y1,E
Call ChnSub("Untitled/Water T3","Untitled/Water T2","/Water deltaTb") '...
Y,Y1,E

If CalculationSet.CalculationGroups("heat
flux").Calculations("Heat_flux_bottom").Validate() Then
  Call CalculationSet.CalculationGroups("heat
flux").Calculations("Heat_flux_bottom").Run()
End If
If CalculationSet.CalculationGroups("heat
flux").Calculations("Heat_flux_side").Validate() Then
  Call CalculationSet.CalculationGroups("heat
flux").Calculations("Heat_flux_side").Run()
End If
```

```
Call ChnAdd("Untitled/Q1","Untitled/Q2","/Q_total","W") '... Y,CALCYChn,E

'Removing other unused channels
Call Data.Root.ChannelGroups("Untitled").Channels.Remove("Untitled 67")
Call Data.Root.ChannelGroups("Untitled").Channels.Remove("Untitled 69")
Call Data.Root.ChannelGroups("Untitled").Channels.Remove("Untitled 71")
Call Data.Root.ChannelGroups("Untitled").Channels.Remove("flow signal 1")
Call Data.Root.ChannelGroups("Untitled").Channels.Remove("flow signal 2")
```

Process_N_SCALING - Subroutine to scale N-type thermocouple signals

```
'-------------------------------------------------------------------------------
-
'-- VBS script file
'-- Created on 10/12/2010 08:32:56
'-- Author:
'-- Comment:
'-------------------------------------------------------------------------------
-
Option Explicit  'Forces the explicit declaration of all the variables in a
script.
Call
ChnDifferentiate("Untitled/TimeGenerated","Untitled/working","Untitled/Differen
tiatedX","Untitled/DifferentiatedY") '... XW,Y,E,E
Call Calculate ("Ch(""Untitled/DifferentiatedY"")=
Abs(Ch(""Untitled/DifferentiatedY""))")
L1 = CNo("Untitled/working")
L2 = CNo("Untitled/DifferentiatedY")
Call FormulaCalc("Ch(L1):= Ch(L1) + NoValue*(Ch(L2)>0.18)")
Call FormulaCalc("Ch(L1):= Ch(L1)*(Ch(L2)<=0.18)")
Call ChnToWfChn("Untitled/TimeGenerated","Untitled/working",0) '...
X,ChnNoStr,XChnDelete Call
ChnToWfChn("Untitled/TimeGenerated","Untitled/Untitled 1",0) '...
X,ChnNoStr,XChnDelete
Call WfChnToChn("Untitled/working") '... ChnNoStr
Call
ChnNovHandle("Untitled/TimeGenerated1","Untitled/working","Interpolate","XY",1,
0,0) '... CALCXChn,CALCYChn,NovMeth,NovCtrlChn,ChnNovIP,NoVChnX,NovReplaceVal
Call Data.Root.ChannelGroups("Untitled").Channels.Remove("TimeGenerated1")
Call Data.Root.ChannelGroups("Untitled").Channels.Remove("DifferentiatedY")
Call Data.Root.ChannelGroups("Untitled").Channels.Remove("DifferentiatedX")
Call
ChnFiltCalc("Untitled/TimeGenerated","Untitled/working","/working","IIR","Besse
l","Low pass",3,15,0,0,1.2,25,"Hamming",1,1) '...
XW,Y,E,FiltStruc,FiltStyle,FiltType,FiltDegree,FiltLimit,FiltLowLimit,FiltUppLi
mit,FiltWave,FiltSamples,FiltWndFct,FiltZeroPhase,FiltCorrection
Call ChnLinScale("Untitled/working","Untitled/working",27358,285) '...
Y,E,ChnScaleFactor,ChnScaleOffset
```

Process_ZERODEADTC.VBS Subroutine to zero dead thermocouple channel signals

```
'-------------------------------------------------------------------------------
-
'-- VBS script file
'-- Created on 10/16/2010 16:06:57
'-- Author: ---
'-- Comment: ---
'-------------------------------------------------------------------------------
-
```

```
Option Explicit  'Forces the explicit declaration of all the variables in a
script.

Call StatBlockCalc("Channel","1-","Untitled/working") '...
StatDirec,RowNoStr,ChnNoStr

Dim j, k, oMyGrp, oMyChn
If StatArithMean<50 Then
  Call Data.Root.ChannelGroups("Untitled").Channels.Remove("working")
  Set oMyGrp = Data.Root.ActiveChannelGroup
  Set oMyChn = oMyGrp.Channels.Add("working", DataTypeFloat64)
    For j = 1 to 20000
    oMyChn.Values(j) = NoValue
    Next
Else If
  If oMyChn.Values(k)>1600 Then
    oMyChn.Values(k)=NoValue
  End If
  If oMyChn.Values(k)<353 Then
    oMyChn.Values(k)=NoValue
  End If
Next
```

APPENDIX J – MATLAB thermocouple conditioning and display script

(example settings here)

```
clear all
close all
clc

%Values to be adjust per case:
filename='f27.csv';
xyz=filename(1:3)
cw=0; %If sample plane orientation was rotated CW = 1 otherwise =0
V=0.772; %Average flow field velocity (operating point specific)
n=200; %Number of data points per second desired.
ts=0; %(between 0-40) Post-process START time
tf=0.5; %(between 0-40, must be greater than ts) Post-process END time.
s=1.5; %Weighting factor for standard deviation outlier rejection
T1=512; %C, Wall temperature (and T_infinity for radiation correction)
T2=T1+7; %C, Next location in on assumed boundary layer
T3=T2+5; %C, Last location in on assumed boundary layer
lower_ind_limit=200; %K, Lower rejection temp for INDIVIDIDUAL values.
upper_ind_limit=1700; %K, Upper rejection temp for INDIVIDIDUAL values.
lower_ave_limit=200; %K, Lower rejection temp for AVERAGE values.
upper_ave_limit=1700; %K, Upper rejection temp for AVERAGE values.

coords = importdata('TCcoords.csv');
vars = fieldnames(coords);
for i = 1:length(vars)
    assignin('base', vars{i}, coords.(vars{i}));
end

DIAdem_tempdata = importdata(filename);
%Note that "DIAdem data" is composed of two different variables:
%"data" is the numerical variable and "test" is the heading string
variable
% Create new variables in the base workspace from those fields.
vars = fieldnames(DIAdem_tempdata);

for i = 1:length(vars)
    assignin('base', vars{i}, DIAdem_tempdata.(vars{i}));
end

L=size(data,1); %Returns the number of temporal data points in entire
file.
rate=500; %(hz) Raw data sample frequency.
emm=0.863; %Average emissivity for soot-coated nickel wire (ref.
Barnes)
dia=7.62E-5; %(m) thermocouple wire diameter
Pr=0.7; %(dimensionless) Assumed Prandtl number
```

```
sigma=5.669E-8; %Stefan-Boltzman constant
z=floor(rate/n); %Down-rounded integer of sample points per averaging
bin.

ia=floor((ts/40)*(L/z));
if ia<1
    ia=1
end
ib=ceil((tf/40)*(L/z));

for i = 1:L
    for j = 1:63
        if data(i,j)<lower_ind_limit;
            data(i,j)=NaN;
        end
        if data(i,j)>upper_ind_limit;
            data(i,j)=NaN;
        end
    end
    clear j
end
clear i

%This block will replace an entire temperature channel value with NaN
value
%if the mean value of the sample is outside the range limits.
T_channel_mean = nanmean(data);
for j = 1:63
    if T_channel_mean(1,j)<lower_ave_limit ||
T_channel_mean(1,j)>upper_ave_limit;
       for i = 1:L
           data(i,j) = NaN;
       end
    end
end

for i = ia:ib %length of desired new data matrix
    for j = 1:63 %skipping first two time columns
        T_reduced(i,j) = nanmean(data((z*(i-1)+1:z*(i-1)+z),j));
        %calculating mean values within the time bin
        T_rad(i,j)=((dia*sigma*emm*((T_reduced(i,j))^4-T1^4)*(0.8237-
0.5*log((V*dia)*Pr/(6.2834E-11*(T_reduced(i,j))^2+5.9795E-
8*(T_reduced(i,j))+7.6259E-6))))/(5.107E-
5*(T_reduced(i,j))+0.01141))+T_reduced(i,j);
    end
end

for k = ia:ib
    for i = 1:9 %number of horizontal rows of thermocouples
        for j = 1:7 %number of vertical columns of thermocouples
            temp1a{k}(i,j) = T_rad(k,(i-1)*7+j) %Time averaged-reduced
            %channel columns are now arranged into the spatial matrix
        end
    end
    %temp1b{k}=flipud(temp1a{k}); %Matrix flipped vertically to align.
    if cw==1
```

```
        temp1c{k}=fliplr(temp1a{k}); %If CW orientation, flip on
vertaxis
    else temp1c{k}=temp1a{k}; %If CCW orientation, DON'T flip on
vertaxis
    end
    temp1d{k}=inpaint_nans(temp1c{k},2); %Original NaNs are filled in.
    meancol{k}=nanmean(temp1d{k}); %Row vector of vertical column mean
    %values is created for use in signal error removal
    stdev{k}=std(temp1d{k},0,1); %Row vector of vertical column
    %standard deviation values is created for use in signal error
removal.
    temp1e{k}=temp1d{k};
    for i=1:9
        for j=1:7
            if abs(temp1e{k}(i,j)-meancol{k}(1,j)) >
(1/s)*stdev{k}(1,j)
            temp1e{k}(i,j) = NaN;
            end
        end
    end
    temp1f{k}=inpaint_nans(temp1e{k},2);
end


for i = 1:9 %writing rows of data
    for j = 1:7 %writing rows for contour
        xoriginal1(i,j) = coords.data((i-1)*7+j,1)
        yoriginal1(i,j) = coords.data((i-1)*7+j,2)
    end
end
xoriginal=flipud(xoriginal1);
yoriginal=fliplr(yoriginal1);

%clear i
%clear j
%clear k
%clear n
%clear vars
%clear textdata
%clear rate
%clear tempcontour
%clear data
%clear xdims1
%clear ydims1

[y1,x1] = ndgrid(118:0.3342617:238.01,-50:0.35842276:50.01);
y=flipud(y1)
x=fliplr(x1)

%clear xoriginal1
%clear yoriginal1
%clear x1
%clear y1

for i = ia:ib
    TNaN{i} = interp2(xoriginal,yoriginal,temp1f{i},x,y,'cubic')
```

```
    for j = 1:360
        TNaN{i}(j,1)=T1;
        TNaN{i}(j,3)=T2;
        TNaN{i}(j,6)=T3;
        TNaN{i}(j,276)=T3;
        TNaN{i}(j,278)=T2;
        TNaN{i}(j,280)=T1;
    end
    T{1,i}=inpaint_nans(TNaN{1,i},2)
end

vidObj = VideoWriter('mymovieVW.avi');
vidObj.FrameRate = 15 % Set and view the frame rate.
vidObj.Quality = 70 % Set and view the frame rate.
open(vidObj);


%load('ANSYS200-1200','mycmap')
load('ANSYS200-1800','mycmap')
%rect=[0 0 530 635]
record=[-50 -40 530 635] %[left bottom width height]
display=[0 0 780 710]
display2=[50 50 780 710]
set(gcf, 'PaperOrientation', 'portrait');
set(gcf, 'PaperPosition',display);
set(gcf, 'OuterPosition',display);
set(gcf, 'Position',display2);

for i=ia:ib
set(gcf, 'PaperOrientation', 'portrait');
colordef white
v=[0;100;200;300;400;500;600;700;800;900;1000;1100;1200;1300;1400;1500;
1600;1700;1800];
%v=[200;400;600;800;1000;1200;1400;1600;1800;2000];
[C,h] = contourf(x,y,T{1,i},v);
set(gcf,'Colormap',mycmap)
%colormap(jet(16));
caxis([200 1800]);
%clabel(C,h,v,'FontSize',20);
colorbar('FontSize',10,'location','northoutside');
grid on
set(gca,'DataAspectRatio',[1 1 1])
xlabel('Radial location (mm)','fontsize',13,'FontName','Times New
Roman')
ylabel('Height above stove bottom (mm)','fontsize',13,'FontName','Times
New Roman')
xlim([-50 50])
ylim([118,238])
%title('Time-Averaged Gas Temperatures in Upper Combustion
Chamber','FontWeight','bold','fontsize',10,'FontName','Times New
Roman')
text(-13,255,'Temperature (K)','fontsize',13,'FontName','Times New
Roman')
set(gcf, 'Units', 'pixels');
%figurename=[xyz '-' mat2str(i)]
%print('-f1','-r100','-dtiff',figurename);
```

```
F=getframe(gca,record);
writeVideo(vidObj,F);
end
%movie(F)
close(vidObj);
```

LIST OF ABBREVIATIONS

AGW – anthropogenic global warming

AIP - indoor air pollution

aka – also known as

BC – Boundary condition

CFD – computational fluid dynamic (model)

CDR – convective-diffusive-reactive (system)

DO – discret ordinates (radiation model)

FAO - Food and Agriculture Organization (of the United Nations)

FEM – finite element method

FVM – finite volume method

GA – genetic algorithms

GBEA – graph based evolutionary algorithm

Hz – Hertz, units of cycles per second

HHV – Higher heating value

LHV – Lower heating value

NGOs - non-governmental organizations

NIST – National Institute of Standards and Technology (U.S.A.)

PDG – pyrolysis dry gas

RANS – Reynolds-averaged Navier Stokes

U^+ - Dimensionless velocity (in the boundary layer)

UN - United Nations

UNDP – United Nations Development Programme

VHS – Volumetric Heat Source

WBT – Water boil test

WHO - World Health Organization

Y^+ - Dimensionless distance from the wall (in the boundary layer)